

University of Warwick institutional repository: <http://go.warwick.ac.uk/wrap>

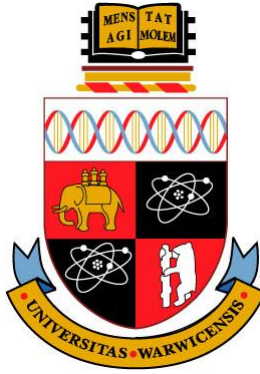
**A Thesis Submitted for the Degree of PhD at the University of Warwick**

<http://go.warwick.ac.uk/wrap/3749>

This thesis is made available online and is protected by original copyright.

Please scroll down to view the document itself.

Please refer to the repository record for this item for information to help you to cite it. Our policy information is available from the repository home page.



# **Towards Rapid 3D Direct Manufacture of Biomechanical Microstructures**

Philip Huw King BSc (Hons)

*Submitted in fulfillment of the requirements  
for the degree of Doctor of Philosophy*

University of Warwick  
School of Engineering

**December 2009**

# Contents

---

List of Figures	<i>viii</i>
List of Tables	<i>xvi</i>
Acknowledgements	<i>xviii</i>
Declaration	<i>xix</i>
Summary	<i>xx</i>
List of Author's Publications	<i>xx</i>
Conferences	<i>xxi</i>
Abbreviations	<i>xxii</i>

<b>1</b>	<b>Introduction</b>	<b>1</b>
1.1	Stereolithography for Microstructures	1
1.2	Project Objectives	3
1.3	Thesis Outline	3
1.4	References	5
<b>2</b>	<b>Polymeric Micropumps - Materials and Fabrication</b>	<b>6</b>
2.1	Introduction	6
2.2	Micro Nomenclature	7
2.3	The Rise of Polymeric Microfluidics	7
2.4	Polymeric Materials - Their Properties and Applications	10
2.4.1	Poly(methyl methacrylate) - PMMA	10
2.4.2	Polyimide	12
2.4.3	PDMS	13
2.4.4	SU-8 and Epoxy Resins	15
2.4.5	Other Materials	16

2.5	Fabrication Techniques	18
2.5.1	Machining	18
2.5.2	Micromachining	21
2.5.3	Moulding	26
2.5.4	Soft Lithography and Multi-Layer Soft Lithography	28
2.5.5	LIGA (X-ray Lithography)	30
2.5.6	<i>In-situ</i> Photopolymerisation	32
2.5.7	Other	34
2.5.8	Stereolithography	35
2.6	Conclusion	36
2.7	References	36
<b>3</b>	<b>Polymeric Micropumps – Design and Actuation</b>	<b>45</b>
3.1	Introduction	45
3.2	Valve Mechanisms	45
3.3	Passive Microvalves	46
3.3.1	Passive Membrane Hole Valves	46
3.3.2	Passive Float Valves	47
3.3.3	Passive Flaps	47
3.3.4	Ball Valves	49
3.3.5	Nozzle/Diffuser Elements	49
3.4	Active Valves	51
3.4.1	Active Membrane Valves	51
3.4.2	Active Plug Valves	52
3.4.3	Throttle Valves	52
3.5	Pump Mechanisms	53
3.6	Reciprocating Displacement Micropumps	55
3.6.1	Membrane Micropumps	55



3.6.2	Reciprocating Piston	59
3.6.3	Rotary	59
3.6.4	Air Detonators	60
3.7	Dynamic Micropumps	60
3.7.1	Centrifugal Micropumps	60
3.7.2	Special Effect Devices	61
3.8	Actuation Techniques	61
3.8.1	Piezoelectric	62
3.8.2	Magnetic	64
3.8.3	Electrostatic	65
3.8.4	Pneumatic	66
3.8.5	Thermopneumatic	68
3.8.6	Hydrogel	70
3.8.7	Cardiomyocytes	71
3.9	Conclusion	72
3.10	References	74
<b>4</b>	<b>Additive Layer Manufacture</b>	<b>80</b>
4.1	Introduction	80
4.2	Classification of Additive Layer Manufacture	81
4.3	ALM System Selection	82
4.4	Stereolithography	84
4.5	EnvisionTEC	90
4.5.1	Company Profile	90
4.5.2	ALM System Range	90
4.5.3	Digital Light Procession Technology and the DMD Chip	92
4.5.4	Enhanced Resolution Module (ERM)	93
4.6	Additive Layer Materials	95

4.7	SLA System Operation	96
4.7.1	Machine Build Operations	97
4.7.2	Post Processing Operations	98
4.7.3	Calibration	99
4.8	Software	103
4.8.1	SolidWorks	103
4.8.2	EnvisionTEC Perfactory Start Centre	104
4.8.3	Materialise Magics	111
4.9	Conclusion	114
4.10	References	115
<b>5</b>	<b>SLA Capabilities</b>	<b>116</b>
5.1	Introduction	116
5.2	Macroscale Components	116
5.2.1	Demonstration Parts	117
5.2.2	Microchannel Arrays	119
5.2.3	Overhanging Structures	120
5.3	Microscale Components and Features	122
5.3.1	Meshes	122
5.3.2	Microscale Test Build	127
5.3.3	Single Pixel Structures	128
5.4	Surface Patterning	129
5.5	Fabrication Time	130
5.6	Biocompatibility Testing	131
5.7	Projector Output	132
5.8	Conclusion	133
5.9	References	135

<b>6</b>	<b>Microneedles</b>	<b>136</b>
6.1	Introduction	136
6.1.1	The Oral Route	136
6.1.2	The Tropical Route	137
6.1.3	The Intravenous Route	137
6.2	Human Skin	139
6.2.1	Structure	139
6.2.2	Mechanical Properties of Skin	142
6.3	Current Microneedle Research	142
6.3.1	Classification	142
6.3.2	Solid Microneedles	147
6.3.3	Hollow Microneedles	150
6.3.4	Safety and Pain Response	153
6.4	Conclusion	154
6.5	References	155
<b>7</b>	<b>Microneedle Arrays by Microstereolithography</b>	<b>158</b>
7.1	Introduction	158
7.2	Microneedle Design	158
7.3	Modelling Skin/Microneedle Interaction	163
7.4	MSL Fabrication of Microneedles	165
7.5	Testing of MSL Microneedle Array	169
7.5.1	FEM Analysis	169
7.5.2	Mechanical Testing	171
7.6	Hollow Microneedles by MSL	174
7.7	Conclusion	176
7.8	References	177

<b>8</b>	<b>Microstereolithography for Active Microfluidic Systems</b>	<b>178</b>
8.1	Introduction	178
8.2	Fabrication of SLA Membranes	179
8.2.1	Design, Build and Post-Processing Parameters	179
8.2.2	Membrane Characterisation	181
8.2.3	Membrane Thickness	184
8.3	Selection of Micropump Design and Actuation	185
8.3.1	Mechanism and Rectification	185
8.3.2	Thermopneumatic Actuation	185
8.3.3	Pneumatic Actuation	187
8.4	Initial Pneumatic Micropump Design and Test Rig Development	189
8.4.1	Early Experimentation	189
8.4.2	Test System Setup	190
8.4.3	SLA Micropump Reliability - Part 1	197
8.4.4	Further Pneumatic Micropump Development	199
8.4.5	Backpressure Measurements	200
8.5	Data and Device Reliability	202
8.5.1	Swept-Frequency Flowrate Data Reliability	202
8.5.2	SLA Micropump Reliability - Part 2	204
8.6	MSL Micropump - Final Designs	205
8.6.1	Mk5 Single-Membrane - Manual Data	205
8.6.2	Beyond Single Membranes for Nozzle/Diffuser Designs	207
8.6.3	Multi-Membrane Self-Priming Designs	210
8.7	Nozzle/Diffuser Optimisation	213
8.8	Towards an Integrated SLA Microfluidic System	218
8.9	Conclusion	219
8.10	References	220

<b>9</b>	<b>Conclusions and Future Work</b>	<b>222</b>
9.1	Conclusions	222
9.2	Microneedles	222
9.3	Active Microfluidic Components	223
9.4	Future Work	227
9.5	References	229

## **Appendices:**

<b>A</b>	<b>Circuit Diagrams</b>	<b>230</b>
A.1	Capacitive Sensor - Oscillator Circuit	231
A.2	Capacitive Sensor - Filter Circuit	232
A.3	Micropump Control - Voltage-to-Frequency Convertor	233
<b>A</b>	<b>Error Analysis</b>	<b>234</b>

# List of Figures

---

Figure 2.1	Structure presented by Khoo et al, with the fabrication process leading to micromachined permalloy microstructures being embedded in a flexible PDMS membrane for use in a magnetic micropump device. Further detail in main text.....	22
Figure 2.2	(a) Fabrication technique used by Yang et al to make their “spiral electrode” electrohydrodynamic pump, seen in situ in (b).....	24
Figure 2.3	Fabrication process used by Lei et al to create SU-8 microimpellers shown in (b).....	26
Figure 2.4	Multilayer soft lithography approach used by Unger et al to fabricate pneumatically-actuated active microfluidic components. The PDMS material (shown as the “hollow” boxes) is moulded using pre-fabricated SU-8 “soft” moulds, shown in the shaded areas. The assembled device is mounted on a flat substrate (dotted area).....	29
Figure 3.1	Overview of classification of passive and active microvalves seen in the literature....	46
Figure 3.2	Operational mechanisms of passive microvalves, showing membrane hole, float, flap, ball and nozzle diffuser valves in open and closed states. In the case of nozzle/diffuser valves, there isn’t a specific “closed” state; the working fluid is simply more likely to move in one direction than the other when pressure is applied.....	48
Figure 3.3	PDMS microstructures employed as active throttle valves by Johnson et al. The arrow points to one of the gaps in the structure, just 20 $\mu\text{m}$ across. These gaps are closed by the action of a piezoelectric disc placed over the throttle structure.....	53
Figure 3.4	Classification system for micropumps put forward by Laser and Santiago.....	54
Figure 3.5	Basic operational principles employed by single-membrane reciprocating displacement micropump designs.....	56
Figure 3.6	Working principal employed by device published by Tracey et al.....	57
Figure 3.7	The working principle of a thermopneumatic 3-membrane peristaltic micropump, taken from Jeong et al.....	58
Figure 3.8	Working principle of a reciprocating displacement piston-based micropump, utilising a ferrofluidic plug. A mobile rare earth magnet is use to move the ferrofluid. Taken from Yamahata et al.....	59
Figure 3.9	Effect of stress on different molecules: A—Centrosymmetric, stress produces no polarisation; B—Polarisation parallel to stress; C—Polarisation perpendicular to stress. Taken from Pointon et al.....	60
Figure 3.10	Multiple micrographs showing the sequential peristaltic action of the novel pneumatic micropump presented by Wang et al. The serpentine-shape pneumatic microchannel is visible over the working fluid channel, separated by a thin PDMS membrane. A pulse of pneumatic pressure is fed into the device via the input port (upper) through to the outlet port (lower), deflecting each membrane created as the pneumatic channel passes over the working fluid channel. This causes a peristaltic movement in the working fluid, as shown in the movement of the red-coloured liquid in (a)-(f).....	67
Figure 3.11	Microvalve device presented by Xu et al. (a) A pair of air pockets are trapped in microfluidic structures either side of a fluidic channel, just before a narrowing in the channel. (b) Localised heating by an upstream (left) microhotplate causes the expansion of the air, until the bubbles block the channel.....	69
Figure 3.12	Working principle of thermopneumatic “trapped bubble” micropump presented by Jun et al. The working fluid chamber is specifically shaped to take advantage of the surface tension effects present at small scales – the chamber, shown full of the blue working fluid in (a), is around 5 mm long, including the inlet and outlet nodes. In (b) the microheaters, seen on both sides of the working fluid chamber, are activated, expanding the air trapped within them. Ultimately this leads to the discharge stroke as the expanding bubbles meet across the chamber (c). Finally, the hotplates are deactivated, cooling the air which returns to its normal volume. Due to the shape of the chamber, the returning movement during the suction stroke (d) is mainly in the	70

	forward direction.....	
Figure 4.1	Classification of additive layer manufacture (ALM) systems, as found in Liou 2008.	81
Figure 4.2	Steps used in laser-based stereolithography. In (a), a laser cures a thin layer of resin between previously cured resin and the top of the resin vat. The build platform subsequently lowers by a layer thickness (b), and a sweeper blade then moves across the surface of the resin and freshly cured polymer (c). The process then repeats, as the laser cures the next layer of resin (d).....	84
Figure 4.3	Mechanism employed by dual-photon SLA systems. Main process details in text. Cut-out shows the secondary photon release (yellow) causing the initiation of curing within the resin.....	86
Figure 4.4	“Micro-bull” presented by Kawata et al in 2001. The structure is just 10 $\mu\text{m}$ long and 7 $\mu\text{m}$ tall (length scale bar = 1 $\mu\text{m}$ ), and was fabricated using a urethane-acrylate resin exposed to a primary infra-red laser beam focussed in 3 dimensions. The resolution of the proprietary system was 150 nm, and the structure was fabricated over a period of 3 hours.....	86
Figure 4.5	Steps used in projector-based stereolithography. The Z-axis mobile build platform (a) moves down into the resin tray, creating a layer of resin which is subsequently cured by the masked output of a projector mounted below the tray (a). The build platform moves up one layer thickness, and the process is repeated (b). This sequence is repeated until the final build rises out of the resin tray (c).....	87
Figure 4.6	Comparison of (a) single chip and (b) 3-chip DLP projection systems. Taken from DLP.com.....	93
Figure 4.7	Demonstration of the effect of the enhanced resolution module (ERM) fitted as an option on a number of EnvisionTEC Perfactory ALM systems. (a) shows the image mask generated for a layer in a build processed by the EnvisionTEC Perfactory RP software. (b) shows the complementary mask produced for the ERM mode, with the pixel mesh offset diagonally by half a pixel diagonal width. (c) shown the composite image of (a) and (b), giving a smoother edge. (d) shows the limitations of the system, with the minimum solid feature size still being one pixel (white squares, top left), whilst the theoretical hole size is $\frac{1}{4}$ the area (black squares, middle right), which can be extended to decrease the minimum trench width and minimum wall width (lower right).....	96
Figure 4.8	Photograph of the EnvisionTEC Perfactory Mini Multi-Lens rapid manufacturing system purchased by the Sensors Research Laboratory in 2007. It has a 20 $\times$ 20 $\times$ 25 $\mu\text{m}$ X/Y/Z resolution.....	89
Figure 4.9	Workflow for fabrication of components using the EnvisionTEC Perfactory Mini Multi-Lens system. Explanation in text.....	97
Figure 4.10	EnvisionTEC Perfactory Mini Multi-Lens system with calibration plate inserted in place of the resin tray. Also pictured is the integrated light sensor.....	100
Figure 4.11	Screenshot of the front end of the Perfactory RP software, provided by EnvisionTEC for use with the Perfactory Mini Multi-Lens system. Part shown is Mk9 self-priming micropump. The brown area represents the build are of the system.....	105
Figure 4.12	Support settings available via the Perfactory RP program, with defaults shown for R11.....	106
Figure 4.13	Processes used during peeling and levelling steps of the fabrication mechanism employed by the EnvisionTEC Perfactory Mini Multi-Lens system. (a) shows the first layer being cured by a masked output from the projector, resulting in a cured layer of resin trapped between the resin tray and build platform (b), along with unexposed liquid resin. (c) shows the peeling process, where the resin tray tilts (shown from the side for clarity; is from the back of the tray in reality), peeling the fabricated layer from the resin tray. (d) the build platform moves up one layer thickness. (e) the resin tray levels to its original position, and the mechanism is ready for the projector to cure the next layer.....	108
Figure 4.14	Geometry conditions where support structures are required. (a) shows a CAD geometry that is impossible if built from the bottom up, with the resultant build (b) missing the double-back overhanging structure. (c) shows the CAD geometry with the required supports (purple structure), resulting in a complete structure shown in	112

	(d). The support structures can be snapped off once the build has been removed from the glass build platform.....	
Figure 5.1	(a) Photograph and (b) SEM electron micrograph of miniature football World Cup fabricated by the Perfactory Mini Multi-Lens system.....	117
Figure 5.2	Demonstration parts fabricated using the Perfactory Mini Multi-Lens SLA system. (a) 1,200 $\mu\text{m}$ tall Homer Simpson figure, with hollow donut and drinks can. (b) Head of Scooby Doo character, fabricated in 50 $\mu\text{m}$ layer thickness, with layers clearly visible. (c) Rook chess piece build, with UK 20 p piece for scale. (d) Top-down view of rook, showing internal spiral staircase.....	118
Figure 5.3	Microchannel array fabricated using the Perfactory Mini Multi-Lens SLA system. The structure measures 27 mm across and 20 mm deep/tall, and features a pair of integrated pipe fittings. The total channel length was in the order of 3 metres, with the channel width being 500 $\mu\text{m}$ .....	119
Figure 5.4	A pair of test membranes fabricated using the Perfactory Mini Multi-Lens system. Both components were built from the bottom of the figure upwards, thus requiring supports for the overhanging pneumatic ports. The left-hand component had supports constructed, and a layer of burr can be seen beneath the cylindrical overhang. The right-hand component had no supports, and therefore the lower edge of the cylinder has been pulled up by the repeated peeling forces. Both parts were functional.....	121
Figure 5.5	Angled overhang tests. Features 500 $\mu\text{m}$ in width were projected 2 mm out from a series of angled bases, from 0° (horizontal) to 45°, in 5° steps. (a) and (b) are micrographs of the completed part, taken from each side due to the low focal length of the microscope making taking images of the whole structure impossible. (c) and (d) are the corresponding CAD structures used to create the component.....	121
Figure 5.6	Angled pipe fittings integrated into a micropump design (see following chapter). The fittings are angled in order to avoid the use of supports, and are angled at 45° from horizontal.....	122
Figure 5.7	Photographs of a circular mesh test piece fabricated using the Perfactory Mini Multi-Lens SLA system. (a) Mesh with UK 20p piece for scale. (b) Close-up of the mesh, which is 100 $\mu\text{m}$ thick, built in 25 $\mu\text{m}$ layers, with 100 $\mu\text{m}$ wide holes in a 50 $\mu\text{m}$ wide mesh. It was found that a 100 $\mu\text{m}$ wide “superstructure” mesh increased the mesh yields to close to 100%, resisting the fabrication forces.....	123
Figure 5.8	SEM electron micrographs of a 100 $\mu\text{m}$ mesh with 100 $\mu\text{m}$ holes. Although the structure itself was reasonably regular, the mesh can be seen to have delaminated..	123
Figure 5.9	Structure designed in SolidWorks as a potential scaffold for tissue engineering, in collaboration with Dr. Judith Hoyland of the School of Medicine at Manchester University.....	125
Figure 5.10	Resultant structure fabricated using the Perfactory Mini Multi-Lens SLA system, from the CAD data shown in Figure 5.10. The structure is 30 mm across its widest point.....	125
Figure 5.11	Mesh sphere fabricated using the Perfactory Mini Multi-Lens SLA system. It is composed of a hexagonal lattice of 70 $\mu\text{m}$ -thick struts.....	126
Figure 5.12	100 $\mu\text{m}$ thin mesh structures built on a vertical plane, with (a) 200 $\mu\text{m}$ and (b) 100 $\mu\text{m}$ diameter holes. It is noticeable that the horizontal struts of the mesh have built wider than the vertical features. The struts in the CAD file were of the same size.....	127
Figure 5.13	SEM electron micrographs of test build designed to probe the minimum feature sizes of the Perfactory Mini Multi-Lens system. (a) A microstructure, with 100 $\mu\text{m}$ wide beams meshed together. The structure stands 645 $\mu\text{m}$ tall, and is 700 $\mu\text{m}$ wide. (b) A bridge structure, once again with 100 $\mu\text{m}$ wide struts. The structure is 300 $\mu\text{m}$ tall and 900 $\mu\text{m}$ long. (c) 20 $\mu\text{m}$ wide, 200 $\mu\text{m}$ tall wall structure, a single pixel width wide. (d) Failed tree-like structure, standing around 700 $\mu\text{m}$ tall (was designed as 900 $\mu\text{m}$ ). The central post was designed to have 3 offset “branches”, which were hollow with 20 $\mu\text{m}$ wide outer walls.....	128
Figure 5.14	Pyramidal microstructure fabricated using the Perfactory Mini Multi-Lens system. The structure is 100 $\mu\text{m}$ wide and 125 $\mu\text{m}$ tall, and has a point of 20 $\times$ 20 $\mu\text{m}$ area that is the output curing of a single projector pixel.....	129



Figure 5.15	SEM electron micrograph of bulk cured resin surface, as fabricated by the Perfactory Mini Multi-Lens system. A 20 × 20 μm grid-like pattern in the surface roughness is clearly visible.....	130
Figure 5.16	Build time comparison for a simple 10 mm “bulk material” cube fabricated using standard factory settings for peel speed vs. a more complex part, of the same size, containing a thin membrane that requires a half peel speed setting for maximum fabrication yield.....	131
Figure 5.17	Stem cells growing on a tissue scaffold fabricated from R11 using the Perfactory Mini Multi-Lens System. Clumps of cells are marked. Courtesy of Dr. J. Hoyland of Manchester University School of Medicine.....	131
Figure 5.18	Spectra obtained from EnvisionTEC Perfactory Mini Multi-Lens system.....	132
Figure 5.19	Chemical structure (a) and absorption profile (b) of Ciba® Irgacure® 369 photoinitiator found in EnvisionTEC R11 photosensitive resin. Taken from chemical datasheet.....	133
Figure 6.1	Schematic overview of the architecture and cytologic constituents of normal human skin. This projection demonstrates the cellular components of the epidermis and superficial dermis in greater detail, with epidermal strata denoted numerically. 1, stratum basalis (subcutis hypodermis); 2, stratum spinosum (dermis); 3, stratum granulosum (epidermis, basal layer); 4, stratum corneum (epidermis, horny layer). AC, eccrine acrosyringium; AP, arrector pili muscle; B, follicular bulb; DC, perivascular dendritic cell; E, epidermis; EC, coil of eccrine gland; ED, dermal eccrine duct; EN, endothelial cell; F, fibroblast; IN, follicular infundibulum; IS, follicular isthmus; LC, Langerhans cell; MC, mast cell; Mφ, macrophage; PD, papillary dermis; RD, reticular dermis; S, sebaceous gland; SF, subcutaneous fat; V, vessel. Taken from Velazquez and Murphy, 2004.....	140
Figure 6.2	Histograms of the skin, showing the dermis and epidermis (boxout), which itself is composed of the basal layer and the stratum corneum. Adapted from Velazquez and Murphy, 2004.....	141
Figure 6.3	Drawing showing the principles used by microneedle devices. An array of microstructures 5 to 100 μm tall pierces the skin through the stratum corneum and into the basal layer of the epidermis. The microneedles are hollow (not shown in figure) and connect to a shared reservoir containing the drug. Taken from Gerstel and Place, 1976.....	143
Figure 6.4	In-plane microneedles developed by Lin et al.....	144
Figure 6.5	Scanning electron micrographs of microneedles made by the reactive ion etching technique. Taken from Henry et al.....	145
Figure 6.6	Schematic of drug delivery using different designs of microneedles: (a) solid microneedles for permeabilizing skin via formation of micron-sized holes across stratum corneum. The needle patch is withdrawn followed by application of drug-containing patch, (b) solid microneedles coated with dry drugs or vaccine for rapid dissolution in the skin, (c) polymeric microneedles with encapsulated drug or vaccine for rapid or controlled release in the skin, (d) hollow microneedles for injection of drug solution. Taken from Arora et al.....	146
Figure 6.7	Permeability of human skin treated with different microneedle protocols in vitro. Increases of 3 to 4 orders of magnitude were observed for microneedles (1) inserted and left in skin, (2) inserted for 10 s and then removed, and (3) inserted for 1 h and then removed. Such large increases in skin permeability have the potential to significantly increase the number and types of drugs which can be delivered across the skin. Each data point represents the average of 7 to 9 experiments. Standard deviation bars are shown. Taken from Henry et al.....	147
Figure 6.8	Solid microneedles fabricated out of silicon, polymer, and metal imaged by scanning electron microscopy. (A) Silicon microneedle 150 μm tall from a 400-needle array etched out of a silicon substrate. (B) Section of an array containing 160,000 silicon microneedles (25 μm tall). (C) Metal microneedle (120 μm tall) from a 400-needle array made by electrodepositing onto a polymeric mould. (D–F) Biodegradable polymer microneedles with bevelled tips from 100-needle arrays made by filling polymeric moulds. (D) Flat-bevel tip made of polylactic acid (400 μm tall). (E)	148

	Curved-bevel tip made of polyglycolic acid (600 $\mu\text{m}$ tall). (F) Curved-bevel tip with a groove etched along the full length of the needle made of polyglycolic acid (400 $\mu\text{m}$ tall). Taken from McAllister et al 2003.....	
Figure 6.9	(a) Scanning electron micrograph of solid metal microneedles shown next to the tip of a 27-gauge hypodermic needle. The complete microneedle array contains 105 needles, each measuring 1000 $\mu\text{m}$ in length, 50 $\mu\text{m}$ by 200 $\mu\text{m}$ in cross section at the base, and tapering to a sharp tip with an angle of 20°. (b) Changes in blood glucose level in diabetic, hairless rats after insulin delivery using microneedles ( $\blacktriangle$ ), subcutaneous hypodermic injection of 0.05 U ( $\diamond$ ), 0.5 U ( $\square$ ), or 1.5 U ( $\circ$ ) of insulin, or passive delivery across untreated skin ( $\times$ ). Microneedles were inserted into skin for 10 min and then removed. Insulin solution was applied to the skin immediately after microneedle insertion and left on the skin for 4 h (as shown by arrow). Subcutaneous injections took a few seconds to perform. The pharmacodynamic effect of insulin delivery by microneedles was bounded by that of 0.05-0.5 U injected subcutaneously. Data are expressed as mean values ( $n \geq 3$ ) with average standard deviation associated with each data point of 14%. Blood glucose levels have been normalised relative to average pretreatment levels. From Martanto et al.	149
Figure 6.10	Process flow for hollow microneedles presented in Chun et al. (a) Silicon wafer is patterned. (b) Silicon is etched as deep as 100 $\mu\text{m}$ . (c) The entire wafer is the reoxidised 1 to 2 $\mu\text{m}$ . (d) A Pyrex glass substrate is drilled and etched in BHF. (e) The silicon part is bonded anodically with a processed Pyrex glass. (f) Back-side silicon etching in TMAH solution. (g) Tip oxide etching in buffered HF. (h) Silicon etching in TMAH. (i) Hollow microcapillaries, 30 $\mu\text{m}$ long, approximately 5 $\mu\text{m}$ in diameter, and 1 $\mu\text{m}$ in thickness. (j) Cross-sectional view of hollow microcapillaries. (k) Top view. (l) Close-up view of (j).....	151
Figure 6.11	Microneedles fabricated by Gardiniers et al. (i) Microneedle fabrication sequence. The drawings on the left give a cross section of the structure after each processing step, along the dotted line in the top view drawings that are shown on the right. The thick black line represents a silicon nitride coating that is used as a protection layer during KOH etching. (ii) The slot and flow channel, bound by silicon nitride walls that are resistant against KOH etching, after step 4 of the process sequence in (i). (iii) SEM picture of a 350 $\mu\text{m}$ high microneedle, with a base of 250 $\mu\text{m}$ (measured in widest direction). The elliptical flow channel is 70 $\mu\text{m}$ in its widest direction.....	152
Figure 6.12	SEM images of side-opened microneedles, the hole beginning approximately 50 $\mu\text{m}$ above the base of the needle. The length of the structure is 210 $\mu\text{m}$ . Taken from Griss and Stemme.....	152
Figure 7.1	Microneedle array structures, designed using SolidWorks CAD package. (a) Conical, (b) asymmetric pyramid, (c) stepped cone, (d) symmetric pyramid and (e) inverted trumpet.....	159
Figure 7.2	Key variables for microneedle geometries tested. Another available variable is the spacing of the array, between microneedle structures.....	159
Figure 7.3	Graphical representations of needle failure force, with respect to microneedle tip and bored radius. All forces in Newtons and are per needle. All radii in micron. Simulated microneedle material is EnvisionTEC e-Shell 100, with a tensile strength of 47.8 MPa.....	162
Figure 7.4	Microneedle array and skin model assembly, after simulation. The microneedle array and skin model are shown separately for clarity.....	164
Figure 7.5	Initial unsuccessful prototype microneedle array. The material used was R11, with machine parameters set at factory defaults (1000 $\mu\text{m/s}$ peeling speed) with a 50 $\mu\text{m}$ layer thickness.....	166
Figure 7.6	Second unsuccessful fabrication attempt, using a Z-axis resolution of 25 $\mu\text{m}$ .....	166
Figure 7.7	Successful prototype build of MSL microneedles, showing (a) inverted trumpet, (b) symmetric pyramid and (c) stepped cone geometries. (d) is a close up of the damage caused by a bubble formed in the resin during fabrication.....	167
Figure 7.8	SEM close-ups of microneedles fabricated using MSL. (a) is a 400 $\mu\text{m}$ tall stepped cone geometry, (b) is a 400 $\mu\text{m}$ tall inverted trumpet geometry, (c) is a 200 $\mu\text{m}$ tall	167

	inverted trumpet, and (d) is a 125 $\mu\text{m}$ tall symmetric pyramid. Fabrication layers can be clearly seen, each being an average of 25 $\mu\text{m}$ thick.....	
Figure 7.9	Microneedle arrays produced for mechanical testing. (a) shows an array of inverted trumpet geometries, (b) an array of stepped cone geometries, (c) and (e) show inverted trumpet designs from two angles, (d) and (f) show the same for the stepped cone designs. Significant debris and needle damage can be seen in (a), although it is unclear if this was caused by factors during or after fabrication. The arrays were arranged in straight $9 \times 9$ grids, and each structure was 400 $\mu\text{m}$ tall. The array separation was 750 $\mu\text{m}$ .....	168
Figure 7.10	Microneedle arrays after simulation. The colour spectrum indicates the stress distribution throughout the needle structures. (a) is an array of stepped cone geometry microneedles, (b) shows an array of inverted trumpet structures.....	170
Figure 7.11	Representation of simulated failure mode of microneedles under axial load. (a) is an array of stepped cone geometry microneedles, (b) shows an array of inverted trumpet structures.....	171
Figure 7.12	Apparatus for mechanical testing of MSL fabricated microneedle arrays. (a) Microneedle sample site, (b) displacement control, (c) Schneeberger Frictionless Table, (d) spring load, (e) TESA Displacement Sensor, (f) TESA Numerical Display, (g) top mounted optical microscope.....	172
Figure 7.13	Graphical representation of results gathered from mechanical test rig. The figure compares simulated failure forces (red) to measured failure forces (blue, line indicates average) for (a) inverted trumpet and (b) stepped cone geometries.....	173
Figure 7.14	Hollow microneedles with a central 80 $\mu\text{m}$ bore, showing build failure in the upper part of the microneedle structure.....	174
Figure 7.15	SEM images of MSL fabricated hollow microneedle structures with offset 80 $\mu\text{m}$ diameter internal bore. (a), (b), and (c) – inverted trumpet geometry in array, single needle and aerial view; (d), (e), (f) – same for stepped cone geometry.....	175
Figure 8.1	(a) photograph of test component, showing the membrane in rest (upper) and pressurised (lower) positions; (b) plot of pneumatic pressure vs. membrane deflection measured using a Tallysurf surface profiler in manual mode. A maximum deflection of just less than 1.2 mm was achieved with a pneumatic pressure of 3.5 PSIG.....	181
Figure 8.2	Schematic of long-term membrane reliability test setup. A 3-way Clippard pneumatic valve was used to digitally (on/atmospheric) control a pneumatic pressure provided by a pressure port and controlled by a regulator. The pressure was read by a Honeywell 26PC-series pressure sensor, which counted the on/off pulses in LabVIEW 7.1 via an NI USB-6009 DAQ device. If a membrane broke during testing, the peak pressure would not reach the set threshold, and the last recorded count number was used to determine the number of cycles reached.....	182
Figure 8.3	(a) photograph of initial micropump design, a reciprocating displacement thermopneumatic device rectified by a pair of active membrane valves; (b) wireframe 3D representation of pump, in an exploded view showing the separate components that were built on the SLA machine and later manually assembled, showing the 2 membrane hole valves with (i) collared distal fluidics, the three working fluid chambers linked by (ii) $500 \times 300 \mu\text{m}$ cross-section fluidic channels, the (iii) thermopneumatic actuation chamber, separated from the working fluid chamber by the membrane, and (iv) the separately fabricated MSL pipe fittings. The device measures $28 \times 10 \times 11 \text{ mm}$ , not including heater PCBs and pipe fittings.....	186
Figure 8.4	Actuation pattern of thermopneumatic micropump, from (i) to (vi). Although in theory a simpler pattern of (i) to (v) could be used, the step at (vi) makes sure that at no point is the pump in a position where at least one of the valves is not closed, increasing the backpressure created by the actuation motion.....	187
Figure 8.5	(a) schematic of initial nozzle/diffuser micropump design, produced using the EnvisionTEC Perfactory Mini Multi-Lens SLA system, details in text. (b) initial flowrate vs. frequency test results for this design.....	189
Figure 8.6	Final test rig used to characterise both the flowrate and backpressure characteristics of the MSL fabricated micropumps. Further details in main text.....	191

Figure 8.7	Details of PCB capacitive plates used in final test rig setup. (a) Plate dimensions and layout, including position of soldered pin placed through the PCB facing outwards from the gold strip, allowing connection to the rig electronics. (b) Positioning of plates to form the capacitor, with the C-Flex tubing internal bore (1.6 mm diameter) placed along the horizontal 80 mm gold strip on the plates. This arrangement was held together using a series of customised MSL-fabricated components. Two sets of plates containing the tubing were used, with one connected to the output of the micropump, and the other left dry as a reference device.....	192
Figure 8.8	Test setup used to obtain flowrate data from the pneumatic SLA micropumps. Details of operation in text.....	195
Figure 8.9	Interface of LabView 7.1 program used to control the test system and the devices during characterisation. Output indicators for the capacitive sensor voltage and pressure sensor, along with inputs for pump actuation frequency, data file name and test status are visible.....	196
Figure 8.10	Final single-membrane nozzle-diffuser rectified pneumatic micropump (Mk5) fabricated using the EnvisionTEC Perfactory Mini Multi-Lens SLA system.....	198
Figure 8.11	Flowrate data collected from the Mk5 SLA-fabricated micropump using the frequency-sweep mode in the LabView software. This data was published in poster form at Eurosensors '09.....	198
Figure 8.12	Typical backpressure and flowrate data collected using the test setup described in section 8.3.5.....	202
Figure 8.13	Data collected from the original Mk5 device via manual, single-frequency flowrate measurements, in comparison to the flowrate data collected via the swept-frequency method shown in Figure 8.8.....	203
Figure 8.14	Backpressure data collected from the original Mk5 SLA-fabricated micropump via the manual, single-frequency method.....	203
Figure 8.15	Averaged flow rate data collected from 4 identical Mk5 pneumatic single-membrane nozzle/diffuser micropumps. The devices were post-processed using the drying period described in the main text, rather than the use of conformal coating...	206
Figure 8.16	Averaged flow rate data collected from 4 identical Mk5 pneumatic single-membrane nozzle/diffuser micropumps. The devices were post-processed using the drying period described in the main text, rather than the use of conformal coating...	206
Figure 8.17	Dual-membrane “boxer” nozzle-diffuser rectified pneumatic micropump (Mk6) fabricated using the EnvisionTEC Perfactory Mini Multi-Lens SLA system. This device required support structures (concept described in Chapter 4) attached to the bottom surface in order to build – the slight roughness visible on the bottom surface either side of the central pneumatic port are where the support teeth met the device before being removed during post-processing.....	208
Figure 8.18	Dual-membrane nozzle-diffuser rectified pneumatic micropump (Mk7) fabricated using the EnvisionTEC Perfactory Mini Multi-Lens SLA system.....	208
Figure 8.19	Averaged flow rate data collected from 3 identical Mk6 pneumatic dual-membrane nozzle/diffuser micropumps. The devices were post-processed using the drying period described in the main text, rather than the use of conformal coating.....	209
Figure 8.20	Averaged flow rate data collected from 3 identical Mk6 pneumatic dual-membrane nozzle/diffuser micropumps. The devices were post-processed using the drying period described in the main text, rather than the use of conformal coating.....	209
Figure 8.21	3-membrane pneumatic SLA-fabricated micropump, consisting of a pair of active membrane valves sandwiching a central pump membrane.....	210
Figure 8.22	Backpressure and flowrate data from Mk9, a monolithic 3-membrane pneumatic SLA-fabricated micropump.....	211
Figure 8.23	Simulation process: (a) DXF 3D CAD file exported from SolidWorks of device fluidics; b) model walls and subdomains defined, with the curved pump chamber walls defined as velocity inlets, the end walls (top and bottom) defined as zero-pressure outlets, and the remaining surfaces defined as non-slip. The subdomain was defined as having a density of $1000 \text{ kg/m}^3$ and a dynamic viscosity of $0.001 \text{ Pa.s}$ ; c) the subdomain was meshed (8640 elements per model); d) the result of the simulation, expressing high pressure as red to low pressure in dark blue. The upper element is	214

	the diffuser (pump outlet) and the lower the nozzle (pump inlet); e) velocity data collected from diffuser side-outlet; f) velocity data collected from nozzle-side outlet, showing the fluid leaving the device faster on the diffuser side, as expected.....	
Figure 8.24	Simulation results, plotting maximum velocity differential between nozzle and diffuser outlets against the nozzle/diffuser centreline divergence, along with the maximum flowrate found for Mk5 pumps using 6°, 8° and 10° divergence.....	214
Figure 8.25	Flowrate collected from Mk5 nozzle/diffuser micropump with nozzle/diffuser elements with 6° centreline divergence. The maximum flowrate of 995 µl/min was reported at 60 Hz and an actuator pressure of 2.5 PSIG.....	216
Figure 8.26	Backpressure collected from Mk5 nozzle/diffuser micropump with nozzle/diffuser elements with 6° centreline divergence.....	216
Figure 8.27	Flowrate data collected from Mk5 nozzle/diffuser micropump with nozzle/diffuser elements with 10° centreline divergence. The maximum flowrate of 802 µl/min was reported at 75 Hz and an actuator pressure of 2.5 PSIG.....	217
Figure 8.28	Backpressure data collected from Mk5 nozzle/diffuser micropump with nozzle/diffuser elements with 10° centreline divergence.....	217
Figure 8.29	Test device fabricated using the EnvisionTEC Perfactory Mini Multi-Len SLA system, featuring a solid microneedle array positioned over an internal chamber, 1 mm deep. 4 0.5 mm diameter holes lead from the array to the chamber. The chamber is connected to an integrated 3-membrane pneumatic micropump by a serpentine channel. The device could be used in the analysis of blood coagulation.....	218

# List of Tables

---

Table 2.1	Material properties of substances commonly used in the literature in the fabrication of plastic-based micropumps and microvalves, with values for single- and polycrystal silicon for comparison. Source: most of the values are taken from either the polymer data handbook or Microsensors, MEMS and Smart Devices unless otherwise indicated. These values are thought to be accurate to the best knowledge of the author, although many polymers exist in a range of forms and validation against a primary source is always advised.....	9
Table 4.1	Costs of ownership for EnvisionTEC Perfactory Mini Multi-Lens projector-based MSL system, and a range of competing laser-based systems produced by 3D Systems. 3D Systems Viper and iPro 8000 “Min Resin Fill” cost based on lowest cost resin available and the quoted fill; iPro 9000XL resin capacity is not quoted directly and is therefore estimated in comparison to the iPro 8000 build envelope. Perfactory “Min Resin Fill” cost based on a full resin tray of 500 ml, and a cost of £225 per 1.5 litres. All costs listed without value added tax (V.A.T.) and were correct as of Q1 2010.....	83
Table 4.2	Summary of the range of EnvisionTEC rapid manufacture SLA systems. In the case of systems with multiple resolution options, the highest resolution system specification is shown. Additional derived options listed on the company website are simply application-targeted versions of the machines above – see text for further information. The specification of the 2007 Perfactory® Mini Multi-Lens used in the Sensors Research Laboratory. ERM = Enhanced Resolution Module; DSP = Digital Shell Printer (hearing aid industry specification).....	91
Table 4.3	Summary of materials evaluated by the Sensors Research Laboratory using the EnvisionTEC Perfactory Mini Multi-Lens rapid manufacturing system. Data taken from EnvisionTEC data sheets.....	95
Table 4.4	Parameters configurable using the Perfactory RP software. Explanation in text. * Minimum value for burn-in layers is 20,000 ms.....	107
Table 5.1	Design parameters taken from test builds fabricated using the EnvisionTEC Perfactory Mini Multi-Lens SLA system. All values in micron unless otherwise indicated. The “theoretical” values represent the highest resolution obtainable by the machine. “Expert User” values are those that can be in practice achieved under ideal conditions by an experienced system operator, whereas “Novice User” values are those that will nearly always resolve if included in a device design without advanced optimisation or changing of build parameters.....	135
Table 6.1	Functions of the skin. Adapted from Hunter et al 2002.....	141
Table 6.2	Mechanical properties of human skin. Taken from Diridollou et al.....	142
Table 7.1	Range of variables considered in this study, compared to previous work in the literature.....	158
Table 7.2	Simulated failure forces for six microneedle geometries in arrays of 3 × 3 needles. Forces are expressed in Newtons and are per needle.....	161
Table 7.3	Typical material properties for a number of EnvisionTEC Perfactory resins available at the time of this study. Data for PMMA, a common microengineering polymer, are also displayed for comparative purposes.....	165
Table 7.4	Tabulated failure values for each microneedle design, as calculated in FEM analysis..	170
Table 7.5	Data collected from MSL microneedle arrays via mechanical testing, via the test rig shown in Figure 11.....	172
Table 9.1	Summary of active microfluidic devices presented in this thesis. Dimensions are of device body without pipe fittings.....	217

*To my parents and to Angela*

# Acknowledgements

---

I would like to thank Dr. James Covington for his guidance, support and patience throughout my PhD. I would also like to thank Professor Christopher Dowson of the University of Warwick Department of Biological Sciences for introducing me to the Sensors Research Laboratory. I would also like to acknowledge the Engineering and Physical Sciences Research Council (EPSRC) for their funding of my project.

I would also like to thank the following people:

Mr. Frank Courtiney and Mr. Ian Griffith for their excellent technical support work, often without much notice but always of the highest quality;

Professor Julian Gardner, Dr. Marina Cole and Dr. Nigel Stocks of my PhD review panel for their much appreciated advice and guidance;

Mr. Faraz Abulhawa and Miss Ekta Jakasania for their work on the modelling of the microneedle structures and their mechanical testing;

Mr. Christopher Purcell and Mr. Max Joseph for their spectrographic data collected from the EnvisionTEC Perfactory Mini Multi-Lens SLA system.

Finally, I would like to thank my parents, friends and family for their continued love and support.



# Declaration

---

This thesis is presented in accordance with the regulations for the degree of Doctor of Philosophy.

The work described by the author is entirely original and my own unless otherwise stated.

# Summary

---

The field of stereolithography has developed rapidly over the last 20 years, and commercially available systems currently have sufficient resolution for use in microengineering applications. However, they have not as yet been fully exploited in this field. This thesis investigates the possible microengineering applications of microstereolithography systems, specifically in the areas of active microfluidic devices and microneedles. The fields of micropumps and microvalves, stereolithography and microneedles are reviewed, and a variety of test builds were fabricated using the EnvisionTEC Perfactory Mini Multi-Lens stereolithography system in order to define its capabilities.

A number of microneedle geometries were considered. This number was narrowed down using finite element modelling, before another simulation was used to optimise these structures.  $9 \times 9$  arrays of 400  $\mu\text{m}$  tall, 300  $\mu\text{m}$  base diameter microneedles were subjected to mechanical testing. Per needle failure forces of 0.263 and 0.243 N were recorded for the selected geometries, stepped cone and inverted trumpet. The 90  $\mu\text{m}$  needle tips were subjected to between 30 and 32 MPa of pressure at their failure point - more than 10 times the required pressure to puncture average human skin.

A range of monolithic micropumps were produced with integrated 4 mm diameter single-layer 70  $\mu\text{m}$ -thick membranes used as the basis for a reciprocating displacement operating principle. The membranes were tested using an oscillating pneumatic actuation, and were found reliable (>1,000,000 cycles) up to 2.0 PSIG. Pneumatic single-membrane nozzle/diffuser rectified devices produced flow rates of up to 1,000  $\mu\text{l}/\text{min}$  with backpressures of up to 375 Pa. Another device rectified using active membrane valves was found to self-prime, and produced backpressures of up to 4.9 kPa.

These devices and structures show great promise for inclusion in complex, fully integrated and active microfluidic systems fabricated using microstereolithography alone, with implications for both cost of manufacture and lead time.

# List of Author's Publications

---

F.K. Che Harun, P.H. King, J.A. Covington and J.W. Gardner, "Novel gas chromatographic microsystem with very large sensor arrays for advanced odour discrimination", *IEEE Sensors 2007 Conference, Atlanta*, 1361-1363, 2007.

P.H. King and J.A. Covington, "A novel monolithic microactuator fabricated by 3D rapid direct manufacture", *Proc. Eurosensors XXIII Conference, Lausanne, Switzerland*, 1163-1166, 2009.

M.E. Snowden, P.H. King, J.A. Covington, J.V. Macpherson and P.R. Unwin, "Fabrication of versatile channel flow cells for quantitative electroanalysis using prototyping", *Analytical Chemistry*, 82 (8), 3124-3131, 2010.

P.H. King and J.A. Covington, "A multi-membrane self-priming micropump fabricated using a single process commercial microstereolithography system", *Submitted for peer review (Journal of Micromechanics and Microengineering)*, 2010

P.H. King and J.A. Covington, "Novel monolithic micropumps fabricated using commercial 3D rapid direct manufacture", *Submitted for peer review (Sensors and Actuators A: Physical)*, 2010.

# Conferences

---

P.H. King and J.A. Covington, "A novel monolithic microactuator fabricated by 3D direct manufacture", *Proceedings of the Eurosensors XXIII Conference, Lausanne*, 1163-1166, 2009.

# Abbreviations

---

3DP	3D Printing
4-HBA	4-hydroxylbutyl acrylate
AC	Alternating Current
ACEO	Alternating Current Electroosmotic
ALM	Additive Layer Manufacture
aPTT	Activated Partial Thromboplastin Time
BT	Bleeding Time
CAD	Computer Aided Design
CAM	Computer Aided Machining
CCD	Charged-Couple Device
CNC	Computer Numerical Control
COC	Cyclic Olefin Copolymer
DC	Direct Current
DLD	Direct Laser Deposition
DLP	Digital Light Processing
DRIE	Deep Reactive Ion Etching
EBM	Electron Beam Melting
EHD	Electrohydrodynamic
EOS	Electro Optical Systems GmbH
ERM	Enhanced Resolution Module
FDM	Fused Deposition Modelling
IBM	International Business Machines

IDT	Interdigital Transducer
INR	International Normalised Ratio
ISI	International Standardised Index
LIGA	X-ray Lithography
LOM	Laminated Object Manufacture
MEMS	Micro Electrical Mechanical Systems
MSL	Microstereolithography
μTAS	Micro Total Analysis System
NI	National Instruments
NIDAQ	National Instruments Data Acquisition
NSL	Nanostereolithography
PC	Polycarbonate
PDMS	Poly(dimethylsiloxane)
PEEK	Poly(ether ether ketone)
PEG	Polyethylene Glycol
PMMA	Poly(methyl methacrylate)
POC	Point-Of-Care
PR	Prothrombin Ratio
PSU	Polysulphone
PT	Prothrombin Time
PTFE	Poly(tetrafluoroethylene)
PVC	Polyvinylchloride
PVDF	Polyvinylidene Fluoride

RIE	Reactive Ion Etching
RP	Rapid Prototyping
RPM	Revolutions Per Minute
SAW	Surface Acoustic Wave
SEM	Scanning Electron Microscope
SL	Stereolithography
SLA	Stereolithography Apparatus
SLS	Selective Laser Sintering
SMA	Shape Memory Alloy
STL	Stereolithography File Format
TCT	Thrombin Clotting Time
TF	Tissue Factor
USB	Universal Serial Bus
UV	Ultraviolet
vWF	Von Willebrand Factor

# Chapter 1

---

## 1 Introduction

### 1.1 Stereolithography for Microstructures

The process of stereolithography was first developed by 3D Systems Corporation in 1987 [1]. The system produced was the first example of an additive layer manufacture (ALM) machine, and lead to the development of a large range of other systems based upon the same principles in the decades since. ALM systems are defined by the production of components in an additive fashion, normally by slicing the component to be built into a series of horizontal layers, which are then fabricated sequentially to produce a final component. In the case of stereolithography, the additive material is a photo-sensitive resin, normally acrylate or epoxy, which, when exposed to light of the correct frequency, polymerises to form a solid material.

Stereolithography has now progressed to the point that micro- and even potentially nano-scale features are possible, and some systems can now be seen as an automated form of micromachining [2]. They are now common commercial tools, used for a wide range of prototyping and rapid machining requirements.

SLA systems have been used to create microfluidic devices in the past, usually in combination with other microengineering techniques. However, stereolithography has yet to emerge as a widely-used fabrication technique in microengineering. For example, only a few examples are reported in the literature of micropumps using ALM as part of their fabrication [3-5], and in these cases only the device body is produced – the active components were produced using other, more standard microengineering techniques.

The majority of SLA devices are laser-based, and although this allows a high resolution, it does increase the cost of the systems greatly. An alternative mechanism has been developed by EnvisionTEC with their Perfactory range of SLA systems [6]. These machines instead use a projector to create the masks for each layer, rather than using a rastering laser. This has the advantage of making the machines cheaper and faster, but also confers some unique capabilities in terms of the features it is able to fabricate.

In theory, the curing of each layer in a single exposure allows for the fabrication of thin membranes, crossing larger distances unsupported than with other SLA devices. This technique has been used previously in the production of membranes for ultrasonic sensors [7]. Researchers in the Sensors Research Laboratory of the University of Warwick have also previously used SLA systems to create low-headspace, customisable sensor covers, along with complex and compact gas chromatography columns [8].

Another field in which SLA systems have not been used extensively is the nascent area of microneedles. This is perhaps because of the sometimes unfavourable material properties of cured light-sensitive materials. However, material development is perhaps the area where the majority of research into SLA systems is based currently, and it can be expected that suitable materials are on the horizon.

There are a number of advantages that SLA brings to the field of microengineering, making research in this area promising. The first is process lead time and expense. SLA machines are often known as “rapid prototyping” systems, capable of building complex components at around 4-5 mm per hour. They also do not require expensive cleanroom facilities in order to function. Finally, their ease of use means that the designer can fabricate the device easily and quickly themselves, rather than potentially having to rely on technical staff.



## **1.2 Project Objectives**

In this thesis, the potential applications of SLA systems, specifically the EnvisionTEC Perfactory Mini Multi-Lens system, will be examined. Particular areas of interest are in microneedle and microfluidic device fabrication, towards the production of integrated medical devices. Reviews of both these fields will be presented, along with an overview of ALM technology, its advantages and limitations.

In the area of microneedle fabrication, the viability of SLA as a fabrication technique will be examined by the development of a series of microneedle arrays. These structures will be developed using FEA (finite element analysis) modelling, followed by mechanical testing.

The potential of SLA technology in the fabrication of microfluidic systems will also be examined via the development of micropumps fabricated entirely using the SLA system. These devices will include the integrated thin membranes mentioned previously. These devices will be fully characterised, requiring the development of an electronic test system. These devices will then be assessed for suitability for integration into more complex microfluidic systems.

## **1.3 Thesis Outline**

Chapter 2 reviews the materials and fabrication methods used in the literature to produce micropumps and microvalves, with a particular focus on polymer-based devices and the development of polymeric fabrication methods as an alternative to more traditional silicon micromachining techniques

Chapter 3 follows on from chapter 2 by outlining the state of the art in terms of polymer-based micropump and microvalve design, working principles and actuation. It

highlights the way that the use of polymeric materials in the production of active microfluidic devices affects both the design and performance of such devices.

Chapter 4 briefly outlines the field of ALM systems, before examining in more detail the working principles of the EnvisionTEC Perfactory Mini Multi-Lens system used in the development of the devices presented in this thesis.

Chapter 5 examines the capabilities of the EnvisionTEC Perfactory Mini Multi-Lens SLA system, and aims via a series of test builds, and components built in collaboration with other projects, to demonstrate the minimum feature sizes and variety of microstructures available for use in microfluidic device fabrication.

Chapter 6 aims to review the field of microneedles as vectors for drugs into the body and for the retrieval of blood samples from the body, focussing on the fabrication techniques and materials reported in the literature.

Chapter 7 charts the development of arrays of SLA-fabricated microneedles, including FEA modelling to select and refine the needle geometries, and mechanical testing to validate the models and characterise the fabricated structures.

Chapter 8 focuses on the development of a series of SLA-fabricated micropump devices, starting with the testing and characterisation of membranes produced using the EnvisionTEC Perfactory Mini Multi-Lens SLA system. The devices produced are characterised in detail using an electronic test system based on the LabView programming language. A simple FEA model is also produced in an attempt to optimise one of the micropump geometries.

Chapter 9 draws together the principle conclusions from the data collected in this thesis. Possible future work is also discussed.

## 1.4 References

- [1] L. Wood, "Rapid Automated Prototyping: An Introduction," *Industrial Press Inc.*, 1993.
- [2] J. W. Gardner, V. J. Varadan, and O. Awadelkarim, "Microsensors, MEMS and Smart Devices," *John Wiley & Sons Ltd, Chichester*, 2001.
- [3] M. C. Carrozza, N. Croce, B. Magnani, and P. Dario, "A Piezoelectric-Driven Stereolithography-Fabricated Micropump," *Journal of Micromechanics and Microengineering*, vol. 5, pp. 177-179, Jun 1995.
- [4] A. Han, M. Graff, O. Wang, and A. B. Frazier, "An approach to multilayer microfluidic systems with integrated electrical, optical, and mechanical functionality," *Ieee Sensors Journal*, vol. 5, pp. 82-89, Feb 2005.
- [5] T. Hasegawa, K. Nakashima, F. Omatsu, and K. Ikuta, "Multi-directional micro-switching valve chip with rotary mechanism," *Sensors and Actuators a-Physical*, vol. 143, pp. 390-398, May 16 2008.
- [6] EnvisionTEC, "EnvisionTEC Computer Aided Modelling Devices," [online], vol. Available: <http://www.envisiontec.de/> [accessed 16th July 2009], 2009.
- [7] R. J. Bradley, D. R. Billson, and D. A. Hutchins, "P3R-5 Novel Capacitive Ultrasonic Transducers Fabricated Using Microstereolithography," *Ultrasonics Symposium, 2006, IEEE*, pp. 2381-2384, 2006.
- [8] F. K. Che Harun, P. H. King, J. A. Covington, and J. W. Gardner, "Novel gas chromatographic microsystem with very large sensor arrays for advanced odour discrimination," *IEEE SENSORS 2007*, pp. 1361-1363, 2007.

# Chapter 2

---

## 2 Polymeric Micropumps – Materials and Fabrication

### 2.1 Introduction

As the drive of technological miniaturisation pushes devices ever smaller, the need for systems that can accurately handle small volumes of gas or liquids becomes greater. Review papers in the field of micropumps [1-5] reveal a large number of current and potential applications across a wide range of fields, such as biological analysis [6-8], drug delivery [6, 7] and in medical devices [8-10]. Many microfluidic systems rely on silicon, either in their construction, or as moulds for forming additional parts. Even though there have been many successes using these techniques, devices are limited by the material properties of silicon. Silicon processing requires extensive facilities, with multiple processing steps, which can result in a high unit cost. These developments have ridden predominantly on the back of the meteoric rise of the silicon chip. Clearly, alternative methods and materials for use in the fabrication of microfluidic devices are available with many routes to future commercialisation.

The purpose of this chapter is to give an overview of the advantages and disadvantages of polymer materials in the fabrication and performance of microfluidic devices. The focus will be on micropumps and microvalves, or combinations thereof. It should be noted that microvalve designs are often overlooked in reviews of the field, and are discussed in detail in these chapters.

In this chapter, a brief history of polymer micro-fluidics is given, followed by an overview of the requirements of pumps and valves. The materials available to researchers

in the field will be discussed, along with the major fabrication techniques used in the literature. Finally, the types of polymer micropumps and valves, with emphasis on how the material use affects the final design and working principles (including actuation techniques) are discussed.

## **2.2 Micro Nomenclature**

The definition of whether or not a device can be considered a micropump or microvalve is one that varies depending on the context of the paper. In their review of the field in 1994, Shoji and Esashi [1] defined microflow devices as “very small devices controlling or sensing flow in the order of  $\mu\text{l}/\text{min}$ .” On the other hand, the 1993 review by Gravensen *et al* [2] concentrated on devices made using microfabrication techniques previously defined in the literature. Laser and Santiago [3] in 2004 preferred to “adhere to the convention for micro electrical mechanical systems, with the prefix *micro* considered to be appropriate for devices with prominent features having length scales of order  $100\ \mu\text{m}$  or less.” However, often the working definition of a micro device, such as a microsensor, is a device “that has at least one physical dimension at the sub millimetre level”, quoted from Gardner *et al*, 2001 [11]. For the purposes of this chapter, the latter definition will be used, as this allows the widest range of devices to be considered.

## **2.3 The Rise of Polymeric Microfluidics**

One of the main driving forces behind the first developments in micropump research was an application familiar to the public – the inkjet printer. A patent granted to IBM in 1974 [12] describes an electrosmotic inkjet printer head, which could be defined as a simple valveless special effect micropump. Early discrete micropump designs relied on traditional machining of the pump chamber [13-15]. However, the nascent field of the

micromachining of silicon soon became the focus of research. Early examples include papers by Van Lintel *et al* [16] and Esashi *et al* [17], both reporting the use of piezoelectrically-actuated devices. In follow-up work from the former, Vandepol *et al* [18] detailed the thermopneumatic actuation method for microfluidic devices, subsequently leading to the production of a working micropump [19]. This was based in part on earlier work on thermopneumatic microvalves by Zdeblick *et al* [20], and work on peristaltic 3-membrane piezoelectric micropumps by Smits *et al* [21].

Vandepol's design utilised a silicon-micromachined actuation membrane. These stiff membranes work well with piezoelectric drivers, which have low deflection, high force and high frequency. However, they are less than ideal for thermopneumatic actuation, which has a lower frequency and stroke force capability, leading to low stroke volumes and thus low flow rates with the stiff glass and silicon membranes normally used in silicon-micromachined devices. It was obvious that new, more flexible polymeric materials would need to be utilised in order for thermopneumatic devices to be efficient.

The first micropump to utilise a polymer material as an integral part of the actuation method was also the first to have the entire structure fabricated from polymer. In their conference paper of 1994, Büstgens *et al* [22] presented a micropump fabricated using a combination of thermoplastic moulding and membrane techniques. The thermoplastic moulded pump case and fluidics are made from polyvinylidene fluoride (PVDF) and polysulphone (PSU), patterned using a machined brass substrate. The final device had lateral dimensions of 7 by 10 mm and incorporated a 2.5  $\mu\text{m}$  polyimide membrane.

*Table 2.1—Material properties of substances commonly used in the literature in the fabrication of plastic-based micropumps and microvalves, with values for single— and polycrystalline silicon for comparison. Source: most of the values are taken from either the Polymer Data Handbook [27] or Microsensors, MEMS and Smart Devices [11] unless otherwise indicated. These values are thought to be accurate to the best knowledge of the author, although many polymers exist in a range of forms and validation against a primary source is always advised.*

Material	Density $\rho_m$ (kg m <sup>-3</sup> )	Maximum Working Point T <sub>max</sub> (°C)	Thermal Conductivity $\kappa$ (W/m/K)	Specific Heat Capacity $C_p$ (J/K/kg)	Temperature Expansivity (10 <sup>-5</sup> /K)	Dielectric Constant $\epsilon_r$	Young's Modulus $E_m$ (GPa)	Tensile Strength $\gamma_m$ (Mpa)
PDMS	970	-	0.16	1350-1510	9.0	2.75	0.36-0.87	10.80
PMMA	1170-1200	138 <sup>5,7</sup>	-	-	-	3.5-3.7	3.1	48-76
Polyimide <sup>1</sup>	1380	-	0.24	1100	3.6	17.3	5.2	117.20
PEEK	1400	200	0.25	3700	16.1	3.3 <sup>9</sup>	3.56	92.00
PTFE	2100-2300	260	0.24-0.25	1050	10.0	2.0	0.4	10-31
Polythene	926-941	71-93	0.33-0.42	1900	14-16	2.3	0.4-1.3	8-24
Polycarbonate	1200	200-235	0.19	3200	26.0	3.17	2.38	62.10
PVC	1300-1400	70-74	0.16	840-1170	5-18	3.0-4.0	2.9	34-62
PVDF	1750-1780	150	0.10	-	5-14	2.9	2.1	36-56
Polypropylene <sup>2</sup>	900-910	-	0.12-0.22	-	6.6	2.2-2.3	1.389	35.1 <sup>10</sup>
Su-8	1200 <sup>6</sup>	200 <sup>5,8</sup>	0.2 <sup>8</sup>	-	5 <sup>8</sup>	3 <sup>8</sup>	4.4 <sup>8</sup>	73.1 <sup>11</sup>
Polyester <sup>3</sup>	-	~75 <sup>5</sup>	0.19	2175	-	-	-	17.6-20.6
Polystyrene <sup>4</sup>	1040-1065	240 <sup>5</sup>	0.116	-	-	2.49-2.55	0.31	3.2-4.2
Si(c)	2330	~1400 <sup>5</sup>	168	678	0.26	11.7	190	6900
Poly-Si	2320	-	34	678	0.2-0.28	-	161	-

<sup>1</sup> Torlon 4000T unfilled

<sup>2</sup> Isotactic

<sup>3</sup> Polychloroprene

<sup>4</sup> Amorphous

<sup>5</sup> Melting point

<sup>6</sup> memscyclopedia.org/su8.html

<sup>7</sup> Kitayama *et al* 1990

<sup>8</sup> www.geocities.com/guerinlj

<sup>9</sup> Rajani *et al* 2008

<sup>10</sup> Lyakhovich *et al* 1974

<sup>11</sup> Feng *et al* 2003

However, an earlier paper by Sjölander *et al* in 1991 [23] details the first use of a polymer in a microvalve, with a silicone rubber membrane sandwiched between moulded high-density polystyrene plates. Another early example of polymer use was a paper by Shoji *et al* in 1992 [24], which is the first instance of a silicone rubber compound used in a microvalve. From this point on there has been an explosion of polymer micro-pumps and valves formed in a range of fabrication techniques and from a variety of materials, the full spectrum of which are investigated here.

## **2.4 Polymeric Materials - Their Properties and Applications**

There are a large number of different polymer materials available to researchers developing microfluidics components. *Table 2.1* shows a number of the materials commonly found in use in polymer-based micropumps and microvalves.

Early polymer micropumps tended to use a mixture of poly(methyl methacrylate) (PMMA), polycarbonate, polyimide and generic silicone rubber compounds, often fabricated using moulding and machining techniques. However, as fabrication techniques evolved, pushing features size ever smaller, so the materials had to evolve. The development of soft lithography and therefore multi-layer soft lithography detailed in papers such as Xia and Whitesides [25] and Unger *et al* [26], respectively, shifted the balance significantly towards polydimethylsiloxane (PDMS), and the majority of devices post 2000 use PDMS and multilayer soft lithography in some part of their construction.

### **2.4.1 Poly(methyl methacrylate) – PMMA**

As mentioned, PMMA was one of the original polymer materials used by researcher developing polymer microfluidics. It is a thermoplastic, optically transparent material, more commonly known as Plexiglas, Perspex or Lucite. It is commonly used as a



lighter, less brittle alternative to glass in a wide variety of macro engineering applications [27]. PMMA is also versatile microengineering material, and can be shaped using thermoplastic moulding [8, 9, 28-32], traditional machining [33-39] and masked powder blasting [37-42]. However, due to its relatively brittle nature in comparison with other polymeric microengineering materials, PMMA is used in the literature only for fluidic channels and fittings, as opposed to membranes or movable components.

PMMA is also an X-ray-sensitive material, and therefore is often used as the working material for LIGA (lithographie, galvanoförmung, abformung, or X-ray lithography) fabricated devices [7, 43]. Further information on this application can be found in the LIGA section later in this chapter.

After components of a microfluidic system have been fabricated, they must be bonded together. A number of papers used conventional adhesive in this application [7-9, 32, 35], or use mechanical pressure via bolts [30, 31, 44, 45]. Yamahata *et al* [37-40] produced a series of micropumps using PMMA for the body material, and used the polymerisation of the monomer triethylene glycol dimethacrylate, which is cured in a hotpress at 70°C to bond the components. Shen *et al* [41, 42] also used this procedure. Chloroform is a solvent for PMMA, and has been used to bond components in Irawan *et al* [46]. Hsu *et al* [47] analysed different PMMA solvent bonding techniques, and found that although a combination of 24.5 kPa at 100°C for 9 minutes with ethanol as the solvent produced the strongest bonding, a method using 24.5 kPa at 60°C for 5 minutes with isopropanol as the solvent produced the least shrinkage. Alternatively, Wei *et al* [48] bonded 2 traditionally machined PMMA plates together by applying a pressure of 1.5 MPa at 108°C for 10 minutes with no solvent.

### 2.4.2 Polyimide

One of the more popular pre-PDMS materials was polyimide. There are a number of polyimides available, which are sold under a variety of trade names. Poly(amine imide) is known as Torlon<sup>®</sup>, and is often used in macroscale injection moulding. Poly(ether imide) is sold as Ultem<sup>®</sup> and is used in printed circuit boards. Poly(pyromellitimide-1,4-diphenyl ether) is thankfully also known as either Kapton<sup>®</sup> (a thin-film commercial product), Vespel<sup>®</sup> or Apical<sup>®</sup>. It is a high-performance polymeric material used in a wide variety of industrial applications, including wire and cable wrap and automotive polymer parts. Some polyimides are thermoplastic materials, meaning they can be heated until melting, before being cooled to set solid, while other formulations are photocurable [27].

Polyimide has been used in a large number of polymer-based micropumps, in most cases as a membrane material [49-52]. The aforementioned Büstgens *et al* [22], who described the first all-polymer micropump, employing a photocurable polyimide material to form a pump and valve membrane just 2.5  $\mu\text{m}$  thick. The sheet was fabricated with an integrated titanium microhotplate using a combination of membrane transfer and micromachining techniques, and was bonded onto the separately fabricated pump body components using adhesive. A later paper by the same group used similar techniques to create a thermopneumatic microvalve system [8]. Also by the same group, Goll *et al* [32] in 1996 documented an interesting microvalve design using a 25  $\mu\text{m}$  thick polyimide membrane. The membrane had a central silicone rubber platelet integrated to aid valves sealing. The membrane is made bi-stable, only requiring energy input to switch between on/off states, by becoming buckled during assembly. The adhesive process used to fix the membrane between the moulded PMMA valve body components requires heating, which shrinks the PMMA, causing the polyimide to deform advantageously. Finally, Goll *et al*

[53] in 1997 produced an interesting electrostatic microvalve concept, using a membrane composed of a pair of 1  $\mu\text{m}$  thick polyimide layers insulating a central gold layer, fabricated using micromachining techniques.

Fluorinated polyimide can be used as a substrate for reactive ion etching (RIE), as demonstrated by Furuya *et al* [54], who used the technique to create a microgrid of 100  $\mu\text{m}$  tall fingers. This grid was subsequently metalized to form the electrodes of a special effect ion drag micropump. The thermal insulation properties of the material were employed by Kawada *et al* [55], who used a micromachined polyimide comb structure to isolate a Ni/Si cantilever from the rest of the microvalve structure. Heating of the cantilever via an integrated microhotplate caused the cantilever to deform, opening and closing the microvalve.

### 2.4.3 PDMS

Polydimethylsiloxane, or PDMS, has influenced the way micropumps and microvalves are designed more than any other polymer material. Since Unger *et al* [26] and the advent of multilayer soft lithography, devices have often shifted away from designs with discrete valve and pump chambers and membranes, to simply employing channels with membranes incorporated into their ceilings. The flexibility of PDMS in thin films allows pneumatic actuators to inflate the membranes like a balloon, filling even square channels entirely. On the other hand, thicker structures are reasonably strong, allowing PDMS to be used as a bulk structural material for microfluidic devices.

PDMS is used in a range of macro-scale applications, such as in release agents, in sealants and gaskets and in adhesives. It is favoured for its thermal stability, minimal thermal expansion and high UV radiation tolerance. However, it is known as being

permeable to gas [27]. In the literature searches used for this review, over 70 published papers were found using PDMS as a functional part of a micropump or valve. The majority (50+) of these use multilayer soft lithography as the fabrication technique, and these will be discussed later in this chapter. However, other fabrication techniques have been applied, including micromoulding [56-61], micromachining [62-64] and macroscale machining [65].

The use of PDMS with micromachining techniques allows the integration of actuator components into thin, strong PDMS membranes. Khoo *et al* [62] produced a PDMS membrane with integral permalloy blocks, in a process discussed later in this chapter. Similarly, Yin *et al* [63] integrated a planar metal coil into their PDMS membrane as part of their electromagnetic micropump. Tracey *et al* [66] demonstrated a PDMS-based piezoelectric pump with a glass membrane. Under normal conditions, PDMS does not bond to glass, but adhesion was achieved using a UV-ozone treatment of both surfaces, followed by a 2-hour bake at 90°C.

Some of the industrial properties of PDMS described have been utilised on the micro scale. For example, Chung *et al* [67] used a PDMS gasket in their otherwise traditionally-machined piezoelectric microvalve. The gas permeability was exploited by Eddings *et al* [68] in their dynamic microfluidic devices, which used a thin membrane of PDMS to step down a macro-scale pressure to one useable at a micro level. This permeability is however in some applications not advantageous. Hansen *et al* [69] found PDMS to be inefficient as a body material for their electroosmotic special effect micropump. Electroosmotic micropumps require ions dissolved in the working fluid to function, and it was found these ions would leech out of solution and into the PDMS

during operation. Wang *et al* [70] found their magnetohydrodynamic special effect pump suffered from the same problem, and solved it by coating the PDMS micropump channels with a thin layer of SU-8.

Samel *et al* published a pair of papers [71, 72] in which they mixed PDMS with expandable microspheres, a mixture they called PDMS-XB. The two papers demonstrated a single-shot drug delivery system and a thermoexpansion-actuated micropump. In both cases, the cured PDMS-XB mixture was heated, expanding the microbeads and causing displacement in the working fluid.

### **2.4.4 SU-8 and Epoxy Resins**

SU-8 is a ubiquitous microengineering material, manufactured by MicroChem Corporation. It is an epoxy compound, mixed with a triarylium sulphonium salts as a photoinitiator. This forms an acid upon exposure to ultraviolet (UV) radiation, which polymerises the mixture with a high cross-linking rate. Using the lithographic techniques of micromachining, along with a post-exposure high-temperature baking step, SU-8 cures into a solid with excellent material properties, water insolubility and chemical inertness. It is also capable of high aspect ratio microstructures, and as such forms the basis of surface micromachining techniques [73]. SU-8 itself is not used outside of microengineering applications, although epoxy compounds are used in a wide range of situations, such as in adhesives and protective coatings [27].

The micromachining techniques used to fabricate device elements using SU-8 are discussed below. The use of SU-8 as a simple photoresist material in the micromachining of silicon and glass substrates is not discussed; although this is by far the most prevalent use of the material. It has been used in the field of micropumps and valves in a variety of

applications, including as a structural, device body material [36, 74-78], in passive microvalve flap and plug structures [33, 35, 44, 79, 80] and in the impellers of dynamic centrifugal micropumps [30, 31]. All of these examples used standard micromachining techniques, except Li *et al* [74] who used an innovative focused laser approach, that allowed the fabrication of *in-situ* microstructures including cantilever beams that were used in the mechanism of a passive microvalve.

There have been examples of device being produced using other epoxy compounds. Bohm *et al* [81] used reactive injection moulding to form the body of their micropump, where the epoxy pre-polymer and initiator are injected separately into a mould. The pre-polymer and initiator mix and form the cured device component. Boden *et al* [49] used another UV-curable epoxy, to form the body of their micropump. The epoxy material was chosen over SU-8 as it didn't require the high-temperature baking steps needed for curing SU-8 after the initial UV radiation exposure.

### 2.4.5 Other Materials

A number of other polymer materials used in the fabrication of micropumps and valves have been reported in the literature. Poly(ether ether ketone) (PEEK) exhibits numerous useful material properties, including abrasion resistance, resistance to solvents and excellent thermal stability, making it a material of choice for high temperature applications [27]. Richter *et al* [82] used machined PEEK as the body material for their chemical-resistant piezoelectric micropump, along with a PDMS gasket. Truckenmuller *et al* [82] used micro ultrasonic welding to fuse both PEEK and PMMA components of their piezoelectric micropump.

Cyclic olefin copolymer (COC) is a relatively new polymer material, with properties including optical clarity, low shrinkage and low moisture absorption [83]. Ahn *et al* [84] produced an innovative  $\mu$ TAS using COC, citing the material's polar solvent resistance and wide spectrum UV transmission as advantages over other common injection-moulding materials such as PMMA and polycarbonate. Another advantageous property specific to the injection moulding process employed was the ability of COC to be injected at nearly double the flow rate of both PMMA and polycarbonate. Das *et al* [85] also used COC in their microfluidic device, citing similar reasons to Ahn *et al*.

An early thermopneumatic micropump design presented in a pair of papers by Büstgens *et al* [22] and Schomburg *et al* [52] was fabricated from polysulphone (PSU) and poly(vinylidene fluoride) (PVDF). Despite being widely used in macroscale industry, neither material has since been used in the fabrication of either micropumps or valves.

Miles *et al* [86] used 50  $\mu$ m thick polypropylene sheets to form the fluidics of their micropump device, shaped using micro vacuum forming techniques. The sheets were subsequently joined using laser welding. Munyan *et al* [29] used modified polypropylene laboratory plasticware surrounded by a PDMS matrix in their microfluidic device.

Inman *et al* [87] used a 25  $\mu$ m thick polyurethane membrane in their peristaltic pneumatic micropump. Finally, the previously discussed Sjölander *et al* [23] used moulded polystyrene (presumably high density) plates to create their microvalves. The plates were subsequently joined by ultrasonic welding.

## **2.5 Fabrication Techniques**

There is a wide variety of potential fabrication techniques available when working with polymer materials, some of which are by their nature are not possible with conventional microengineering materials such as silicon. In this section, the fabrication techniques documented in this review will be discussed and defined.

It should be noted that the fabrication techniques described only include those used to manipulate polymer materials found as a final component of the device. Other techniques may have been used in the fabrication of non-polymer parts of the device, but these techniques are not included here. Additionally, the use of temporary polymeric masks such as SU-8 is not discussed, as this is used in nearly all micromachined silicon devices. However, devices in which such materials are present in the final mechanism as functional components are commented upon in the micromachining section.

### **2.5.1 Machining**

The use of conventional machining techniques, such as drill bits and lathes, is obviously limited by the scale of the devices being fabricated. However, as microfabrication technology has advanced, so have macro-scale tools. The development of high-resolution CAD/CAM systems utilising precision drill bits or lasers, driven to an extent by the clockwork wristwatch industry, allows far finer detail to be achieved. There are also a number of examples of devices in which traditional hand tools, normally drills, have been used with precision drill bits to create microfluidic features.

The original micropump designs in the literature used machining techniques [13, 15]; however, their use since in polymer devices has been limited. Some micro-scale devices have been reported, being generally simple in design, which have been entirely



fabricated in polymer using macro-scale techniques. Interestingly, PMMA or some other form of acrylic is used in nearly all the reported devices that use a machined polymer as part of their design.

Yuen *et al* in 2000 [88] presented a simple, semi-disposable membrane microvalve, consisting of two CNC (computer numerical control) machined Plexiglas (PMMA) layers containing the fluidics. The fluidics were cut using a 250  $\mu\text{m}$  end mill, resulting in channels 250  $\mu\text{m}$  wide and 100  $\mu\text{m}$  deep. The fluidic layers sandwiched a flexible polymer membrane, which was a commercially available 3M tape. The valve was normally open, with pressure in the working fluid pushing the membrane up over a weir. Positive pressure applied to the membrane, via an actuation method not expanded upon, closed the valve. Inman *et al* in 2007 [87] also presented a CNC-machined PMMA device, a pneumatically actuated single membrane displacement pump with a pair of active pneumatic membrane valves. The device also consisted of a pair of acrylic layers containing the fluidics, with a purchased 25  $\mu\text{m}$  polyurethane membrane sandwiched between them. The fluidics were cut with a 0.4 mm ball mill, giving channels 190  $\mu\text{m}$  deep.

An alternative method of machining uses a high-power laser instead of a physical tool. Irawan *et al* [46] used a CO<sub>2</sub> laser cutting machine in the fabrication of their centrifugal micropump. The 40 W laser had a wavelength of 10.6  $\mu\text{m}$ , and followed 2D patterns defined by a computer graphics package over an area of 610  $\times$  305 mm. A microfan of diameter 2.5 mm and a channel 1000  $\times$  500  $\mu\text{m}$  in area were ablated in both PMMA and PVC substrates.

Machining techniques can have a number of advantages over purely micro-scale techniques. When working with larger device components such as pump bodies and connecting fluidics, fabrication can be far quicker and cheaper than micro-scale techniques. When prototyping a system, it may be favourable to produce a test device via machining before the final micro-scale device is fabricated. For example, Yin *et al* [89] produced a test device to explore the expansion of bubbles in a blinking-bubble device, using laser machining tools to produce the required 125  $\mu\text{m}$  microchannel in PMMA. The test device can be in an entirely different material to the final design. Yamahata *et al* [39] used laser cutting of metal to produce a prototype of the nozzle/diffuser valves used in their magnetically actuated micropump; the final device was produced from PMMA using masked powder blasting and machining techniques.

However, the highest resolution and accuracy cannot be achieved without expensive CAD/CAM equipment or skilled technical staff, although the investment required for this is still considerably less than for silicon processing facilities. Therefore the best solution in terms of price, speed of manufacture and fabrication resolution is often a mix of both traditional and micro-scale fabrication processes. Tsuei *et al* [7] used a conventionally machined acrylic layer, with 250  $\mu\text{m}$  diameter flow channels, as a base for their off-axis X-ray exposure fabricated microvalve. Nguyen and Truong [35, 44] used multiple machined PMMA layers with 0.6 mm fluidic holes as part of their microvalves, where the valve structures were micromachined in SU-8. Finally, Yamahata *et al* [38-40] used machined PMMA as part of their electromagnetically actuated pumps, along with a range of other techniques such as masked powder blasting and moulding.

### 2.5.2 Micromachining

Micromachining commonly describes a number of techniques involving the two-dimensional patterning and development of photoresist materials on top of a substrate to form temporary masks. As a technique it forms the basis of silicon chip technology, as well as MEMS (Micro Electrical Mechanical Systems) and microsensors work, including silicon micropump fabrication [11, 90, 91].

There are two main forms of micromachining, known as “bulk” and “surface”. Bulk micromachining uses the photoresist pattern to define areas to be etched in the silicon, or built up using deposition techniques. The final device will be found within the bulk of the silicon substrate. Surface micromachining also uses the photoresist pattern to define an area on the substrate, but this is instead used to define the deposition of a secondary material. The final device is normally found above the surface of the substrate. Etching of the substrate, which does not have to be silicon, is often not employed.

Micromachining as outlined above is predominantly used as a silicon/metal-based process. However, polymers can be implemented into the final design, most often using a surface micromachining approach. Devices using polymer materials are found with silicon (e.g. [59, 61, 62, 92-97]) and glass substrates [10, 98-107], along with devices using both materials (e.g. [108-112]). A large number are mainly silicon-based, but use PDMS as a membrane material. Devices using thermopneumatic [93, 104, 108-111], pneumatic [59, 106], piezoelectric [92], magnetic [62, 94-98], electrowetting [78, 107] and hydrogel [61, 112] actuation are reported using PDMS as the membrane material, although other materials including polyimide [50, 51, 113] and parylene [58] are used in a similar way. In the case of thermopneumatic devices, the use of micromachining allows direct

integration of the required microheaters. In some devices, the silicon or glass substrate is only used as a base of the microheater, and the rest of the device is fabricated using other techniques [100-103]. Glass micromachined substrates can also be utilised for their optical properties, allowing remote analysis of the working fluid [114, 115]. Polymer micro total analysis systems ( $\mu$ TAS) systems, also known as lab-on-a-chip devices, are also reported with integrated micromachined microsensors [116-119].

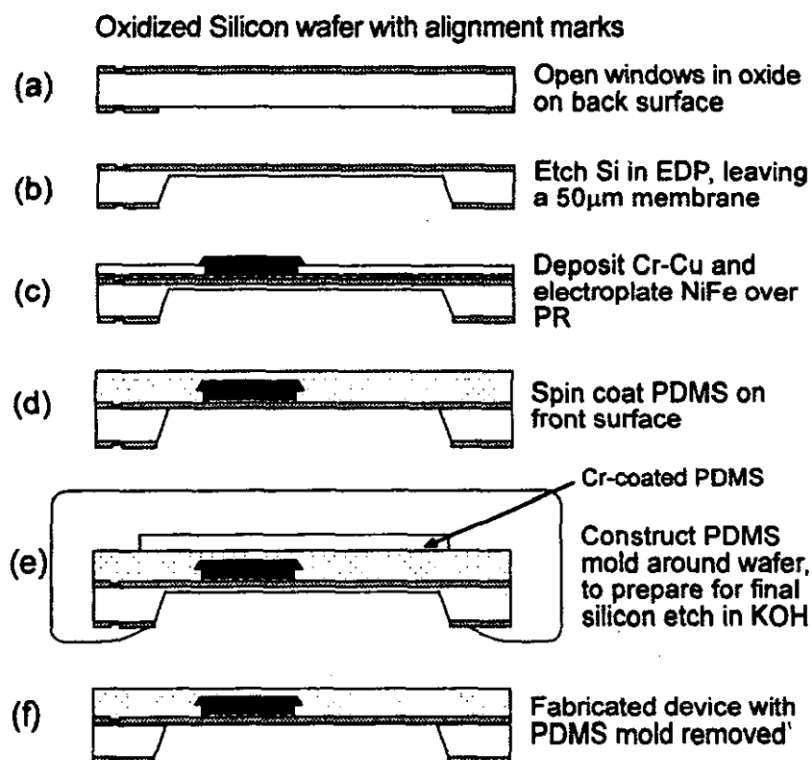


Figure 2.1 – Structure presented by Khoo et al [62], with the fabrication process leading to micromachined permalloy microstructures being embedded in a flexible PDMS membrane for use in a magnetic micropump device. Further detail in main text.

A good example of a surface micromachined device with polymer components is Khoo *et al* [62], with the fabrication steps shown in Figure 2.1. To fabricate the device, a silicon wafer is oxidised except for a 2 × 2 mm window on the back face. This window is then etched through so a 50  $\mu$ m thick silicon membrane is left. The front side of the wafer is coated in a thin layer of chromium and copper, to aid a later electroplating step, before

a 10  $\mu\text{m}$  layer of photoresist is patterned on top. A permalloy material (Ni80Fe20) is then electroplated on top of the chromium/copper, through the photoresist pattern. This forms the permanent magnet strips that will later actuate the pump membrane. The permalloy is over-electroplated to create a “mushroom” shape partially over the photoresist, the rim of which helping the strips to mechanically hang onto the final membrane. The photoresist is removed, and the chromium/copper layer etched away, before PDMS is spin coated onto the top surface of the wafer to a thickness of 40  $\mu\text{m}$ . This covers the permalloy strips, embedding them within the membrane. Finally, the silicon membrane, which was kept to hold the membrane structure together during fabrication, is etched away. In order to achieve this without etchant diffusing through the thin PDMS membrane, the entire structure is coated in a thicker layer of PDMS, except for the back window etched earlier in the wafer. A 1 mm thick piece of chromium-coated PDMS is placed on top of the membrane before this coating is applied to prevent strong PDMS-PDMS bonding occurring during the curing process. The silicon membrane is etched, freeing the PDMS/permalloy membrane, and the PDMS mould is removed.

An interesting variation on the manipulation of glass using micromachining can be found in Yang *et al* from 2007 [80]. In this paper, a glass tube is coated with a photoresist, and then is exposed through a static mask with repeating diagonal lines (see *Figure 2.2a*). The stage below the tube moves, rolling the tube between itself and the mask, leaving a spiral pattern in the developed photoresist. The exposed glass is then primed with a Ti/Au seeding layer, before being coated with a Ni layer that acts as the electrode. Finally, the tube is surrounded by an SU-8 photoresist layer, and the glass etched away to form a

photoresist tube with internal spiral electrode. This forms the basis of an electrohydrodynamic micropump, shown in *Figure 2.2b*.

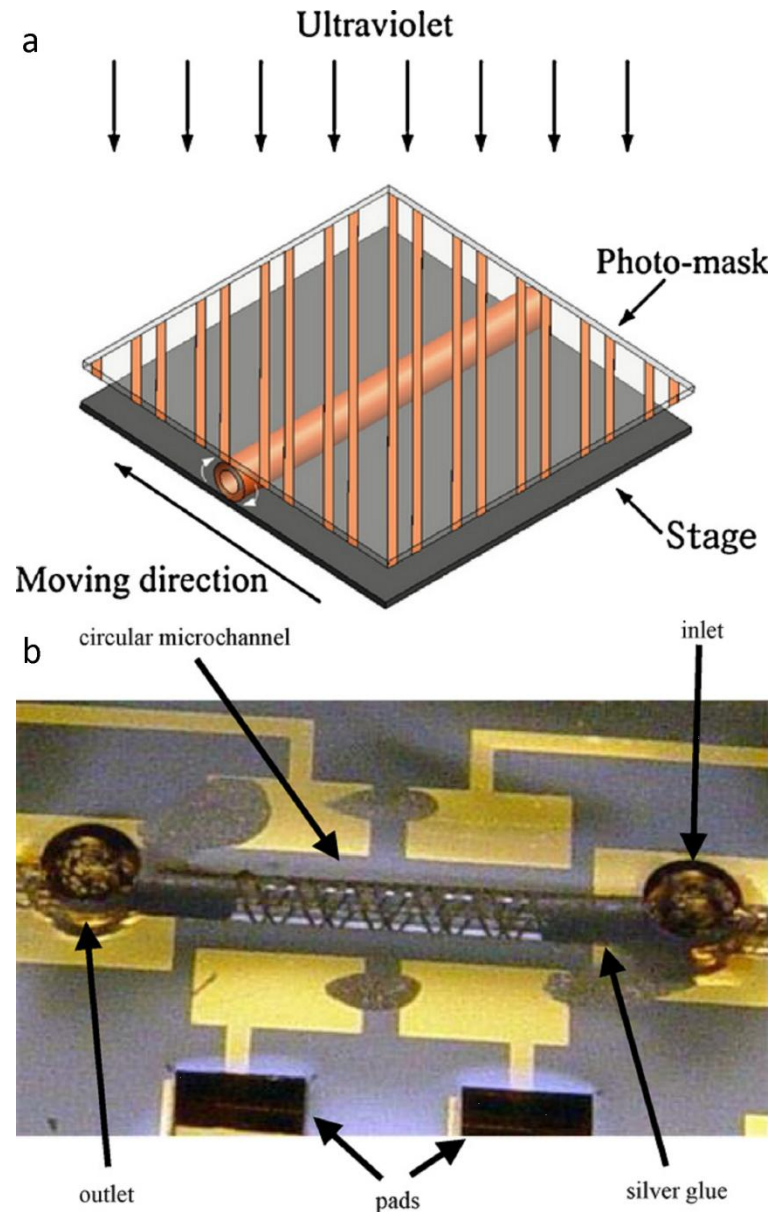


Figure 2.2 – (a) Fabrication technique used by Yang et al [80] to make their “spiral electrode” electrohydrodynamic pump, seen in situ in (b).

Whereas most bulk micromachining usually uses a “wet” chemical etch to remove volumes of silicon, there are also dry etch techniques available. One of these techniques is reactive ion etching (RIE), in which the substrate to be etched is placed upon an RF-powered electrode (cathode). Plasma is created above the substrate, and ions are

accelerated from this onto the substrate by the self-bias that emerges between the plasma and substrate. The resulting ion bombardment can lead to chemical changes, but also sputters molecules from the substrate surface, thus etching the substance away in a highly anisotropic process [11].

RIE is normally used within the field of MEMS to etch silicon substrates. For example, Thruiller *et al* [59] used both traditional micromachining and DRIE (deep reactive ion etching) to create micromoulds that defined a 100  $\mu\text{m}$  microvalve channel in PDMS. However, RIE has also been used to pattern polymeric materials, specifically fluorinated polyimide. Furuya *et al* [54] used magnetically controlled-RIE (MC-RIE) to create 100  $\mu\text{m}$  tall, 15  $\mu\text{m}$  wide fingers out of fluorinated polyimide, which were then metallised to create electrodes for use in a dynamic ion drag (electrostatic) micropump. Geng *et al* [92] used both RIE and chemical etching to produce separate versions of their piezoelectrically-actuated micropump. The chemical etch was used to create angled nozzle diffuser elements, whilst RIE was used to create parallel tubes in a different type of micropump. This anisotropic etching property, where the side walls of the etch are not parallel but are predictable, have been used in other devices to create nozzle/diffuser elements [120].

As noted above, the use of polymer photoresist material such as SU-8 during the fabrication stages does not allow a device to be defined as “polymeric” in this review, as the material is not present in the final device. However, some designs do use photoresist materials in functional parts. One of the first papers reporting the use of polymer materials in a microvalve was Shoji *et al* in 1992 [24]. The valve design consists of a micromoulded silicone rubber plug, suspended across a complimentary anisotropically-

etched hole in a silicon substrate by four SU-8 arms. Pan *et al* [79] presented a flap valve made of micromachined SU-8 that rectified flow through an opening. Yun *et al* [77] used SU-8 as a bulk layer material, whilst Li *et al* [74] used a pulsed laser to create bridge structures in SU-8 that were used as valve flaps. Lam *et al* [30] and Lei *et al* [31, 121, 122] reported the development of an all-polymer dynamic centrifugal micropump, with a PMMA body and a micromachined SU-8 impellor. Finally, a pair of papers by Nguyen *et al* explore the use of patterned SU-8 as the functional layer of a passive flap microvalve [33, 44].

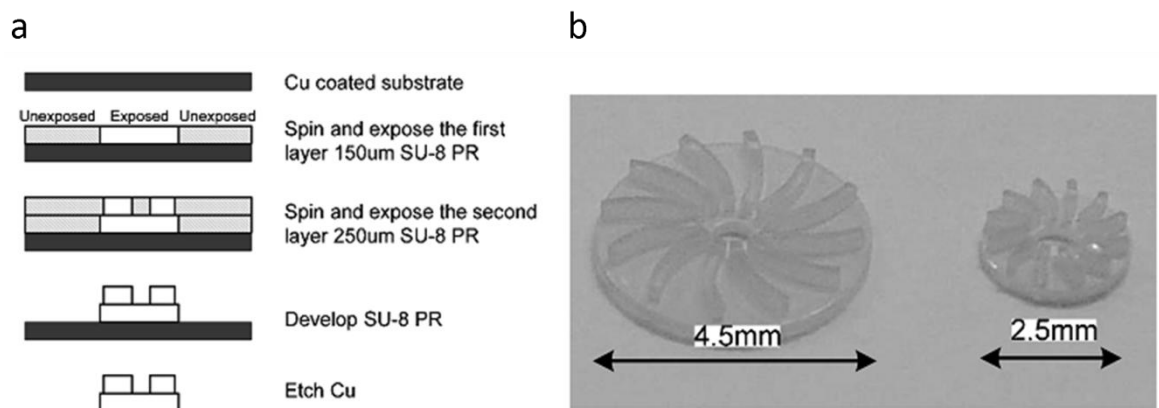


Figure 2.3 – (a) Fabrication process used by Lei *et al* [121] to create SU-8 microimpellers shown in (b).

### 2.5.3 Moulding

The vast majority of macroscale polymer items are formed by moulding techniques, rather than bulk machining. Many polymer materials are available in liquid pre-polymer form, and can be cured using either heat, light, or (normally) UV. Other materials can be altered in their solid form by the melting of the bulk material or smaller parts of it. In either case, the final shape of the material is defined by the mould or stamp used during the cooling or curing process.

The definition of a “moulded” or “micromoulded” polymer part relies more on the fabrication techniques used to make the mould than the dimensions of the final



component. A number of papers have used moulds made with conventional machining techniques, shaping materials such as PDMS [39, 123, 124], epoxy [81] and polystyrene [23]. The moulds are made of a variety of materials, including aluminium [81, 123] and epoxy [124]. Metallic moulds are preferable for PDMS moulding, as the PDMS does not bond to metal surfaces post curing [125]. Alternatively, the casting can be performed around pre-prepared components as a matrix to hold them together [29]. Commercially produced tubing and other purchased components such as metal pins can be used in such processes to create channels and other features [56].

Micromoulded devices on the other hand have moulds fabricated using silicon micromachining, giving the advantages in resolution that micromachining confers. The processes used are similar to PDMS multilayer soft lithography, except the mould is permanently fabricated into the silicon rather than defined in SU-8 on top of the silicon substrate. The silicon moulds are normally fabricated using wet etching, although, as mentioned above, RIE has also been used [59]. Without exception, the micromoulded material used in the literature is PDMS [57-59, 93, 126, 127]. This ubiquity is due to the ability PDMS to take even micron-scale features fabricated in the silicon mould, along with its other favourable properties such as high elasticity and strength.

Injection moulding is most commonly used in the production of macroscale mass-produced polymer items, and there have been some developments in using the technique at micro scales in the field of microfluidic devices. Injection moulding involves the melting of thermoplastic polymeric materials into a liquid form, which is then forced into a multi-part mould. The polymer sets within the mould, which in macroscale industry is often water cooled to speed up the setting of the polymer. The mould pieces are then pulled

apart, releasing the formed item. A small number of papers report microfluidic actuators produced using injection moulding, using materials such as COC [84] and polyimide [53]. Reactive injection moulding has also been used [128], where both parts of a two-part thermosetting polymer, typically polyurethane, are injected and mixed in the mould cavity. Injection moulding is sometimes listed as having the potential for commercially-aimed microfluidic devices, due to its use in polymer mass-production [69, 129].

#### **2.5.4 Soft Lithography and Multi-Layer Soft Lithography**

The process of soft lithography is one that has only been in general use in microengineering for around a decade. It exists in two main forms, single- and multi-layer. In their review paper of 1998, Xia and Whitesides [25] defined a number of single-layer soft lithography techniques all sharing a common two-stage fabrication. A mould is created on a silicon substrate using a photoresist material, which is in turn used to mould an elastomeric substrate, normally PDMS. This elastomer part is peeled off the substrate, and is then used as a mould or a stamp to pattern a thin layer of elastomer on a substrate.

However, in their paper of 2000, Unger *et al* [26] produced a device using a multi-layer approach, outlined in *Figure 2.4*. This technique uses a number of layers of PDMS, each created in a one-step process where the photoresist-moulded elastomer part was used directly in the device. This multi-layer approach is the basis for a large number of subsequent devices. Soft lithography has a number of advantages over micromoulding, primarily in that it does not require the training, expertise, facilities and time that the manufacture of micromachined micromoulds requires. Multiple soft lithography stamps for different layers of a device can be patterned on a single wafer or quickly on separate

substrates. This technique lowers the device fabrication costs, although, as a technique, it probably lacks the process simplicity required for use in mass production.

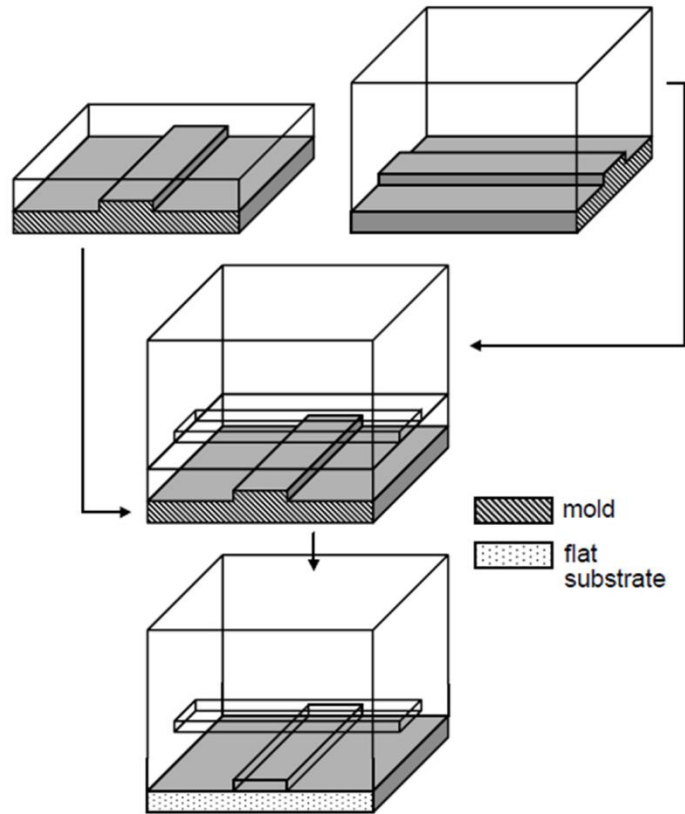


Figure 2.4 – Multilayer soft lithography approach used by Unger et al [26] to fabricate pneumatically-actuated active microfluidic components. The PDMS material (shown as the “hollow” boxes) is moulded using pre-fabricated SU-8 “soft” moulds, shown in the shaded areas. The assembled device is mounted on a flat substrate (dotted area).

Due to the ubiquitous nature of the technique, there are a large number of papers that document the exact steps used in multilayer soft lithography, each with slight variations dependant on the exact application. However, the overall process can be briefly summarised. First, the photoresist (normally SU-8) is spin coated onto the silicon or glass substrate, patterned with UV through a mask, developed and baked (though only thick layers are possible when patterning onto glass). The PDMS mixture is degassed, before being poured onto the photoresist mould. The PDMS is cured at around 65°C for 12 hours before being separated from the mould. Multiple layers can be fabricated in this

way using a variety of different moulds. To bond the layers together, the PDMS surfaces are treated using oxygen plasma, before being pressed together for around 15 minutes. This achieves a permanent bond, resulting in what is essentially a monolithic component.

In order to assist the transfer process from the photoresist mould, the glass or silicon substrate is treated in such a way to make it non-adhesive. Treatments include coating substrate with a  $\text{CHF}_3$  plasma polymerised polymer [130] or gold [56]. Polished stainless steel has also been used as a substrate; as mentioned earlier, silicone rubber compounds do not stick to metallic surfaces once cured [124].

Most soft lithography-based micropumps use pneumatic actuation [131-138], taking advantage of the elastic nature of PDMS with large stroke volumes at lower actuation rates. A number of active valves with pneumatic actuation are also reported [139-142]. Other reported devices use thermopneumatic [143-147], special effect [148, 149], hydrogel [6, 150, 151], piezoelectric [152-155], mechanical [156, 157] and biological [158] actuators.

### 2.5.5 LIGA (X-ray Lithography)

LIGA is the German acronym for **L**ithographie (lithography), **G**alvanoformung (electroforming) and **A**bformung (moulding), also known as X-ray lithography. It can be used to create microstructures, with parallel sides perpendicular to the substrate, that are much deeper than those created through bulk micromachining. First, a metal stamp is created. A several hundred micron thick resist is exposed through a mask to X-rays from a synchrotron, and this resist is developed and electroplated, filling the resist mould. The remaining resist is then removed, leaving a metallic structure attached to the substrate [91]. In non-polymer devices, this is where the process stops; however, the metallic

microstructure can also be used to pattern a polymeric material, using thermoplastic moulding [9] and injection moulding [28] techniques.

PMMA is often used as both an X-ray resist material and as a part of the final device. Exposure of PMMA to X-rays causes chain scission of cross-links within the polymer, allowing etching of selectively exposed areas with solvents. PMMA is also a good material for thermoplastic moulding, having a low glass transition temperature [9].

Guber in 1995 [28] presented, along with a number of other devices, the first example of a LIGA-fabricated polymer microvalve. The structure was produced in PMMA using injection moulding against a LIGA-produced mould. The valve was actuated pneumatically, and was only 3 mm in diameter. Ruzzu *et al* [9] followed up on this work with a very similar device. Kar *et al* [43] presented a micropump in which the planar microfluidics, including a pair of nozzle/diffuser microvalves, were fabricated using direct X-ray lithography in PMMA. However, the X-rays used were “soft” (i.e. non-collimated), meaning a smaller radiation source could be used. The fluidics were found to be 50  $\mu\text{m}$  deep, with the nozzle/diffuser sections 30  $\mu\text{m}$  and 300  $\mu\text{m}$  wide at the outlet and inlet respectively. Despite the soft nature of the radiation, the channel walls were found to be vertical, as the source had a high aspect ratio output.

Another distinct X-ray lithography technique was reported by Tsuei *et al* [7]. A simple PMMA plug microvalve fabricated by off-axis X-ray exposure was presented. The plug and plug hole were defined by direct exposure and subsequent development of the PMMA (much as with Kar *et al* [43]), with the tapered plug edges defined by rotating the material relative to the X-ray plane. However, the technique has not been used subsequently in this field.

It is noticeable however in the literature the lack of papers in the last decade. This is due to the rise of other techniques such as soft lithography, which is cheaper than LIGA and can give similar high-resolution, high aspect-ratio structures. Access to the synchrotron X-ray facilities required to produce the collimated radiation required for most LIGA is limited, and the process itself is therefore prohibitively expensive [90, 91].

### 2.5.6 *In-situ* Photopolymerisation

There are a number of situations where it is beneficial to be able to cure a polymer within an otherwise complete device. This is especially true of polymers that are damaged or destroyed by the high temperatures or the use of solvents required by the later fabrication steps used during the construction of the device, such as the baking of SU-8. The main field in which *in-situ* photopolymerisation has been developed is in the fabrication of devices actuated by hydrogels.

The precise nature of hydrogels and their mechanisms of actuation are discussed in the next chapter. There are however a number of papers that focus directly on the processes of *in-situ* photopolymerisation. The first example in the literature employing the technique in the fabrication of a polymer-based micropump was Liu *et al* [150] in 2002. This paper describes 4 separate devices, all hydrogel actuated, in this case by an acrylic acid material. All the hydrogel actuators are fabricated by *in-situ* photopolymerisation within pre-fabricated PDMS devices. All the devices are forms of valves, apart from one that is closer in mechanism to a throttle. The throttle device uses a novel laminar flow method to produce two layers of solidified hydrogel on either side of a microfluidic channel. A flowing layer of glycerine was used to separate two flows of hydrogel inserted from either side of the throttle channel. The hydrogel flows were cured

using a UV light source, creating the actuation layers. Further devices were created using simple masking techniques, creating precision-fabricated hydrogel features. Eddington *et al* [6] also describe a device actuated using *in-situ* photopolymerised hydrogel features, including a microvalve and a pump chamber.

Kim *et al* [155] describes a complete system for producing features within PDMS microfluidics devices. This consists of an optical microscope with a CCD camera, connected to a computer to visualise the mask and prefabricated device. The microscope and camera are mounted on a rotating frame along with a UV source, which can be rotated into position above the device once the mask has been aligned using an X/Y mobile stage. The mask is stationary while the device is manoeuvred into position with the stage. Both the device and the mask are held in place using negative pressure from a vacuum pump. The liquid pre-polymer, in this case 4-hydroxylbutyl acrylate (4-HBA), is inserted into the microfluidic channels using a syringe pump. The pre-polymer is cured using the UV source, before the unused material is flushed from the finished device by deionised water. Using these techniques, Kim *et al* fabricated passive check valves to rectify flow in a micropump device, and fabricated the actuation pillar for a bi-fluid active plug microvalve.

A pair of later papers by the same group [159, 160] demonstrated a method of creating hydrogel spheres for use in microfluidic devices. Liquid prepolymer 4-HBA was slowly injected into a sheath flow of mineral oil using a sharp pipette. This formed droplets of the prepolymer within the sheath flow, which were carried with the flow downstream. The droplets then passed through a UV source, which cured the pre-polymer. Polymer beads of diameters between 100 and 200  $\mu\text{m}$  were produced by

varying the sheath fluid flow rate. The beads were then used to produce a pH-sensitive microfluidic valve. Much like Liu *et al* [150], a bead was placed behind a thin PDMS layer, held in position by a series of posts. A secondary fluid, separate from the working fluid, was passed across the microsphere to initiate expansion and contraction against the membrane, causing the valve to close and open respectively.

### 2.5.7 Other

A series of papers by Yamahata and Gijs *et al* [37-42] describe a number of microfluidic devices, in part made of PMMA shaped using masked powder blasting. This technique uses gas-flow accelerated micro-scale particles such as alumina to erode bulk material through a laser-cut metal mask. This process can be used to rapid prototype multiple sheets of PMMA, which can then be adhered together to make a multi-level device. However, the blasting powder also erodes the metal mask at a rate of around 0.2  $\mu\text{m/s}$ , decreasing accuracy on masks used multiple times. The surface roughness of the final part is around 1.25  $\mu\text{m}$  [40].

Ultrasonic welding is a technique used commonly in the macro-scale world for the bonding of polymer components made out of materials such as PEEK that cannot be solvent bonded. It is however not commonly used in the fabrication of micropumps and valves. Truckenmüller *et al* [82] used a standard ultrasonic welding machine in the assembly of their piezoelectric micropump, using both PMMA and PEEK. Metal components such as the inlet and outlet tubing were also successfully integrated using the same technique.



### 2.5.8 Stereolithography

Stereolithography is a form of rapid manufacturing technology that is additive in nature – layers of material are deposited in series to build a true 3D model. The materials used include metal powder, which is laser sintered into a solid form, or the repeated layering of cut paper sheets. However, the major form of the technology involves the automated curing of multiple layers of photosensitive resins. A 3D model is created using a computer-aided design (CAD) program. This model is then sliced into multiple layers using specialised software, which then creates a mask for each layer. These masks are then used to pattern sequential layers of the resin. The layer to be patterned is normally defined by the surface of the resin, as in most laser-based SLA (stereolithography apparatus), or as a layer between two glass plates, as seen in the projector-based systems. As such, polymer-based stereolithography it can be seen as a form of automated surface micromachining [11], and also has similarities with multi-layer soft lithography.

The first use of this technology in the fabrication of a micropump was reported by Carozza *et al* in 1995 [161], who produced a piezoelectrically-driven ball-valve micropump with stereolithography fabricated pump body and fluidics, although the exact form of SLA technology employed was not reported. Since then, the field has gone quiet, with the next paper in the literature being Han *et al* in 2005 [115], followed by Hasegawa *et al* in 2008 [162], both of whom created microvalves with an SLA fabricated body. Both papers create only fluidic components using the SLA systems; devices with functional components built using stereolithography are an exciting potential area of future research.

## 2.6 Conclusion

The field of polymer-based micropumps and microvalves has developed quickly over the last 15 years. The original device designs utilising polymeric materials used standard engineering polymers such as PSU and PMMA. As a result, macro-scale fabrication techniques such as machining using drillbits and thermoplastic moulding were common.[74]

However, as new materials were developed for using in microengineering applications, the fabrication techniques evolved as well. Micromachining techniques introduced materials such as PDMS and SU-8, the latter often used to form temporary moulds to shape the former. This technique, known as multi-layer soft lithography, has revolutionised the field of microfluidics, allowing complex 3D structures to be formed from multiple shaped layers of PDMS.

It has been noted that SLA technology, to be reviewed in following chapters, has several features in common with soft lithography, potentially allowing similar device designs to be recreated automatically using 3D printing systems.

## 2.7 References

- [1] S. Shoji and M. Esashi, "Microflow Devices and Systems," *Journal of Micromechanics and Microengineering*, vol. 4, pp. 157-171, Dec 1994.
- [2] P. Gravesen, J. Branebjerg, and O. S. Jensen, "Microfluidics - a review," *Journal of Micromechanics and Microengineering*, vol. 3, pp. 168-182, 1993.
- [3] D. J. Laser and J. G. Santiago, "A review of micropumps," *Journal of Micromechanics and Microengineering*, vol. 14, pp. R35-R64, Jun 2004.
- [4] P. Woias, "Micropumps - past, progress and future prospects," *Sensors and Actuators B-Chemical*, vol. 105, pp. 28-38, Feb 14 2005.
- [5] N.-C. Tsai and C.-Y. Sue, "Review of MEMS-based drug delivery and dosing systems," *Sensors and Actuators A: Physical*, vol. 134, pp. 555-564, 2007.
- [6] D. T. Eddington and D. J. Beebe, "A valved responsive hydrogel microdispensing device with integrated pressure source," *Journal of Microelectromechanical Systems*, vol. 13, pp. 586-593, Aug 2004.
- [7] T. W. Tsuei, R. L. Wood, C. K. Malek, M. M. Donnelly, and R. B. Fair, "Tapered microvalves fabricated by off-axis X-ray exposures," *Microsystem Technologies*, vol. 4, pp. 201-204, Jul 1998.

- [8] J. Fahrenberg, W. Bier, D. Maas, W. Menz, R. Ruprecht, and W. K. Schomburg, "A Microvalve System Fabricated by Thermoplastic Molding," *Journal of Micromechanics and Microengineering*, vol. 5, pp. 169-171, Jun 1995.
- [9] A. Ruzzu, J. Fahrenberg, M. Hecke, and T. Schaller, "Multi-functional Valve components fabricated by combination of LIGA processes and high precision mechanical engineering," *Microsystem Technologies*, vol. 4, pp. 128-131, May 1998.
- [10] S. U. Son, J. H. Seo, Y. H. Choi, and S. S. Lee, "Fabrication of a disposable biochip for measuring percent hemoglobin Alc (%HbAlc)," *Sensors and Actuators a-Physical*, vol. 130, pp. 267-272, Aug 14 2006.
- [11] J. W. Gardner, V. J. Varadan, and O. Awadelkarim, "Microsensors, MEMS and Smart Devices," *John Wiley & Sons Ltd, Chichester*, 2001.
- [12] F. M. Demer, "Ink Jet Printer," *US Patent no. 3,949,410*, 1974.
- [13] L. J. Thomas and S. P. Bessman, "Prototype for an Implantable Micropump Powered by Piezoelectric Disk Benders," *Transactions American Society for Artificial Internal Organs*, vol. 21, pp. 516-522, 1975.
- [14] L. J. Thomas and S. P. Bessman, "Prototype for an Implantable Insulin Delivery Pump," *Proceedings of the Western Pharmacology Society*, vol. 18, pp. 393-398, 1975.
- [15] W. J. Spencer, W. T. Corbett, L. R. Dominguez, and B. D. Shafer, "Electronically Controlled Piezoelectric Insulin Pump and Valves," *Ieee Transactions on Sonics and Ultrasonics*, vol. 25, pp. 153-156, 1978.
- [16] H. T. G. Vanlintel, F. C. M. Vandepol, and S. Bouwstra, "A Piezoelectric Micropump Based on Micromachining of Silicon," *Sensors and Actuators*, vol. 15, pp. 153-167, Oct 1988.
- [17] M. Esashi, S. Shoji, and A. Nakano, "Normally Closed Microvalve and Micropump Fabricated on a Silicon-Wafer," *Sensors and Actuators*, vol. 20, pp. 163-169, Nov 15 1989.
- [18] F. C. M. Vandepol, D. G. J. Wonnink, M. Elwenspoek, and J. H. J. Fluitman, "A Thermo-Pneumatic Actuation Principle for a Microminiature Pump and Other Micromechanical Devices," *Sensors and Actuators*, vol. 17, pp. 139-143, May 3 1989.
- [19] F. C. M. Vandepol, H. T. G. Vanlintel, M. Elwenspoek, and J. H. J. Fluitman, "A Thermopneumatic Micropump Based on Micro-Engineering Techniques," *Sensors and Actuators a-Physical*, vol. 21, pp. 198-202, Feb 1990.
- [20] M. J. Zdeblick and J. B. Angell, "A microminiature electric-to-fluidic valve," *Proc. 4th Int. Conf. on Solid-State Senors and Actuators, Tranducers '87, Tokyo, Japan*, pp. 827-829, June 2-5 1987.
- [21] J. G. Smits, "Piezoelectric Micropump with 3 Valves Working Peristaltically," *Sensors and Actuators a-Physical*, vol. 21, pp. 203-206, Feb 1990.
- [22] B. Bustgens, W. Bacher, W. Menz, and W. K. Schomburg, "Micropump manufactured by thermoplastic molding," *MEMS94 Proc.*, pp. 18-21, 1994.
- [23] S. Sjolander and C. Urbaniczky, "Integrated Fluid Handling System for Biomolecular Interaction Analysis," *Analytical Chemistry*, vol. 63, pp. 2338-2345, 1991.
- [24] S. Shoji, M. Esashi, B. Vanderschoot, and N. Derooij, "A Study of a High-Pressure Micropump for Integrated Chemical Analyzing Systems," *Sensors and Actuators a-Physical*, vol. 32, pp. 335-339, Apr 1992.
- [25] Y. Xia and G. M. Whitesides, "Soft Lithography," *Annual Review of Materials Research*, vol. 28, pp. 153-184, 1998.
- [26] M. A. Unger, H. P. Chou, T. Thorsen, A. Scherer, and S. R. Quake, "Monolithic microfabricated valves and pumps by multilayer soft lithography," *Science*, vol. 288, pp. 113-116, Apr 7 2000.
- [27] J. E. Mark, "Polymer Data Handbook," *Oxford University Press, Inc.*, 1999.
- [28] A. E. Guber, "Potential of microsystems in medicine," *Minimally Invasive Therapy & Allied Technologies*, vol. 4, pp. 267-275, Oct-Dec 1995.
- [29] J. W. Munyan, H. V. Fuentes, M. Draper, R. T. Kelly, and A. T. Woolley, "Electrically actuated, pressure-driven microfluidic pumps," *Lab on a Chip*, vol. 3, pp. 217-220, 2003.
- [30] R. H. W. Lam, K. F. Lei, L. Miao, Z. L. Dong, W. C. Law, Y. K. Suen, W. J. Li, A. H. P. Ho, and S. K. Kong, "Towards automating micro cellular detection process using micro vortex pump arrays," *2005 IEEE/ASME International Conference on Advanced Intelligent Mechatronics, Vols 1 and 2*, pp. 66-71, 2005.
- [31] K. F. Lei and W. J. Li, "Microfluidic mixing by fluidic discretization," *Transducers '05, Digest of Technical Papers, Vols 1 and 2*, pp. 1537-1540, 2005.

- [32] C. Goll, W. Bacher, B. Bustgens, D. Maas, W. Menz, and W. K. Schomburg, "Microvalves with bistable buckled polymer diaphragms," *Journal of Micromechanics and Microengineering*, vol. 6, pp. 77-79, Mar 1996.
- [33] N. T. Nguyen, T. Q. Truong, K. K. Wong, S. S. Ho, and C. L. N. Low, "Micro check valves for integration into polymeric microfluidic devices," *Journal of Micromechanics and Microengineering*, vol. 14, pp. 69-75, Jan 2004.
- [34] A. Sin, C. F. Reardon, and M. L. Shuler, "A self-priming microfluidic diaphragm pump capable of recirculation fabricated by combining soft lithography and traditional machining," *Biotechnology and Bioengineering*, vol. 85, pp. 359-363, Feb 5 2004.
- [35] T. Q. Truong and N. T. Nguyen, "A polymeric piezoelectric micropump based on lamination technology," *Journal of Micromechanics and Microengineering*, vol. 14, pp. 632-638, Apr 2004.
- [36] D. Haefliger, R. Marie, and A. Boisen, "Self-actuated polymeric valve for autonomous sensing and mixing," *Transducers '05, Digest of Technical Papers, Vols 1 and 2*, pp. 1569-1572, 2005.
- [37] C. Yamahata and M. A. M. Gijs, "Plastic micropumps using ferrofluid and magnetic membrane actuation," *Mems 2004: 17th IEEE International Conference on Micro Electro Mechanical Systems, Technical Digest*, pp. 458-461, 2004.
- [38] C. Yamahata, F. Lacharme, J. Matter, S. Schnydrig, Y. Burri, and M. A. M. Gijs, "Electromagnetically actuated ball valve micropumps," *Transducers '05, Digest of Technical Papers, Vols 1 and 2*, pp. 192-196, 2005.
- [39] C. Yamahata, C. Lotto, E. Al-Assaf, and M. A. M. Gijs, "A PMMA valveless micropump using electromagnetic actuation," *Microfluidics and Nanofluidics*, vol. 1, pp. 197-207, Jul 2005.
- [40] C. Yamahata, M. Chastellain, V. K. Parashar, A. Petri, H. Hofmann, and M. A. M. Gijs, "Plastic micropump with ferrofluidic actuation," *Journal of Microelectromechanical Systems*, vol. 14, pp. 96-102, Feb 2005.
- [41] M. Shen, C. Yamahata, and M. A. M. Gijs, "Miniaturized PMMA ball-valve micropump with cylindrical electromagnetic actuator," *Microelectronic Engineering*, vol. 85, pp. 1104-1107, May-Jun 2008.
- [42] M. Shen, C. Yamahata, and M. A. M. Gijs, "A high-performance compact electromagnetic actuator for a PMMA ball-valve micropump," *Journal of Micromechanics and Microengineering*, vol. 18, pp. 1-9, Feb 2008.
- [43] S. Kar, S. McWhorter, S. M. Ford, and S. A. Soper, "Piezoelectric mechanical pump with nanoliter per minute pulse-free flow delivery for pressure pumping in micro-channels," *Analyst*, vol. 123, pp. 1435-1441, Jul 1998.
- [44] N. T. Nguyen and T. Q. Truong, "A fully polymeric micropump with piezoelectric actuator," *Sensors and Actuators B-Chemical*, vol. 97, pp. 137-143, Jan 1 2004.
- [45] T. T. Nguyen, M. Pham, and N. S. Goo, "Development of a peristaltic micropump for bio-medical applications based on mini LIPCA," *Journal of Bionic Engineering*, vol. 5, pp. 135-141, Jun 2008.
- [46] R. Irawan, S. Swaniinathan, P. Aparajita, and S. C. Tjin, "Fabrication and performance testing of disposable micropump suitable for microfluidic chip," *2006 International Conference on Biomedical and Pharmaceutical Engineering, Vols 1 and 2*, pp. 252-255, 2006.
- [47] Y. C. Hsu and T. Y. Chen, "Applying Taguchi methods for solvent-assisted PMMA bonding technique for static and dynamic mu-TAS devices," *Biomedical Microdevices*, vol. 9, pp. 513-522, Aug 2007.
- [48] W. Liu, Z. J. Zhang, and L. Yang, "Chemiluminescence microfluidic chip fabricated in PMMA for determination of benzoyl peroxide in flour," *Food Chemistry*, vol. 95, pp. 693-698, Apr 2006.
- [49] R. Boden, M. Lehto, U. Simu, G. Thornell, K. Hjort, and J. A. Schweitz, "Polymeric paraffin micropump with active valves for high-pressure microfluidics," *Transducers '05, Digest of Technical Papers, Vols 1 and 2*, pp. 201-204, 2005.
- [50] J. Cunneen, Y. C. Lin, S. Caraffini, J. G. Boyd, P. J. Hesketh, S. M. Lunte, and G. S. Wilson, "A positive displacement micropump for microdialysis," *Mechatronics*, vol. 8, pp. 561-583, Aug 1998.
- [51] J. A. Dziuban, J. Mroz, M. Szczygielska, M. Malachowski, A. Gorecka-Drzazga, R. Walczak, W. Bula, D. Zalewski, L. Nieradko, J. Lysko, J. Koszur, and P. Kowalski, "Portable gas chromatograph with integrated components," *Sensors and Actuators a-Physical*, vol. 115, pp. 318-330, Sep 21 2004.
- [52] W. K. Schomburg, R. Ahrens, W. Bacher, S. Engemann, P. Krehl, and J. Martin, "Long-term performance analysis of thermo-pneumatic micropump actuators," *Transducers 97 - 1997 International Conference on Solid-State Sensors and Actuators, Digest of Technical Papers, Vols 1 and 2*, pp. 365-368, 1997.

- [53] C. Goll, W. Bacher, B. Bustgens, D. Maas, R. Ruprecht, and W. K. Schomburg, "An electrostatically actuated polymer microvalve equipped with a movable membrane electrode," *Journal of Micromechanics and Microengineering*, vol. 7, pp. 224-226, Sep 1997.
- [54] A. Furuya, F. Shimokawa, T. Matsuura, and R. Sawada, "Fabrication of fluorinated polyimide microgrids using magnetically controlled reactive ion etching (MC-RIE) and their applications to an ion drag integrated micropump," *Journal of Micromechanics and Microengineering*, vol. 6, pp. 310-319, Sep 1996.
- [55] H. Kawada, H. Yoshida, M. Kamakura, K. Yoshida, M. Saitou, K. Kawahito, and S. Tomonari, "Thermally driven microactuator containing thermal isolation structure with polyimide and its application to microvalve," *Boston Transducers'03: Digest of Technical Papers, Vols 1 and 2*, pp. 1935-1938, 2003.
- [56] P. Krulevitch, W. Bennett, J. Hamilton, M. Maghribi, and K. Rose, "Polymer-based packaging platform for hybrid microfluidic systems," *Biomedical Microdevices*, vol. 4, pp. 301-308, Dec 2002.
- [57] T. E. McKnight, C. T. Culbertson, S. C. Jacobson, and J. M. Ramsey, "Electroosmotically induced hydraulic pumping with integrated electrodes on microfluidic devices," *Analytical Chemistry*, vol. 73, pp. 4045-4049, Aug 15 2001.
- [58] Z. S. Hua, Y. M. Xia, O. Srivannavit, J. M. Rouillard, X. C. Zhou, X. L. Gao, and E. Gulari, "A versatile microreactor platform featuring a chemical-resistant microvalve array for addressable multiplex syntheses and assays," *Journal of Micromechanics and Microengineering*, vol. 16, pp. 1433-1443, Aug 2006.
- [59] G. Thuillier and C. K. Malek, "Development of a low cost hybrid Si/PDMS multi-layered pneumatic microvalve," *Microsystem Technologies-Micro-and Nanosystems-Information Storage and Processing Systems*, vol. 12, pp. 180-185, Dec 2005.
- [60] C. W. Liu, J. Y. Park, Y. G. Xu, and S. Lee, "Arrayed pH-responsive microvalves controlled by multiphase laminar flow," *Journal of Micromechanics and Microengineering*, vol. 17, pp. 1985-1991, Oct 2007.
- [61] M. Lei, A. Salim, R. A. Siegel, and B. Ziaie, "A hydrogel-actuated microvalve for smart flow control," *Proceedings of the 26th Annual International Conference of the IEEE Engineering in Medicine and Biology Society, Vols 1-7*, vol. 26, pp. 2041-2044, 2004.
- [62] M. Khoo and C. Liu, "A novel micromachined magnetic membrane microfluid pump," *Proceedings of the 22nd Annual International Conference of the IEEE Engineering in Medicine and Biology Society, Vols 1-4*, vol. 22, pp. 2394-2397, 2000.
- [63] H. L. Yin, Y. C. Huang, W. L. Fang, and J. W. Hsieh, "A novel electromagnetic elastomer membrane actuator with a semi-embedded coil," *Sensors and Actuators a-Physical*, vol. 139, pp. 194-202, Sep 12 2007.
- [64] J. S. Go and S. Shoji, "A disposable, dead volume-free and leak-free in-plane PDMS microvalve," *Sensors and Actuators a-Physical*, vol. 114, pp. 438-444, Sep 1 2004.
- [65] D. B. Weibel, M. Kruithof, S. Potenta, S. K. Sia, A. Lee, and G. M. Whitesides, "Torque-actuated valves for microfluidics," *Analytical Chemistry*, vol. 77, pp. 4726-4733, Aug 1 2005.
- [66] M. C. Tracey, I. D. Johnston, J. B. Davis, and C. K. L. Tan, "Dual independent displacement-amplified micropumps with a single actuator," *Journal of Micromechanics and Microengineering*, vol. 16, pp. 1444-1452, Aug 2006.
- [67] G. S. Chung and K. B. Han, "Characteristics of a micromachined piezovalve combined with a multilayer ceramic actuator," *Microelectronics Journal*, vol. 38, pp. 690-694, Jun-Jul 2007.
- [68] M. A. Eddings and B. K. Gale, "A PDMS-based gas permeation pump for on-chip fluid handling in microfluidic devices," *Journal of Micromechanics and Microengineering*, vol. 16, pp. 2396-2402, Nov 2006.
- [69] T. S. Hansen, K. West, O. Hassager, and N. B. Larsen, "An all-polymer micropump based on the conductive polymer poly(3,4-ethylenedioxythiophene) and a polyurethane channel system," *Journal of Micromechanics and Microengineering*, vol. 17, pp. 860-866, May 2007.
- [70] L. S. Wang, L. Flanagan, and A. P. Lee, "Side-wall vertical electrodes for lateral field microfluidic applications," *Journal of Microelectromechanical Systems*, vol. 16, pp. 454-461, Apr 2007.
- [71] B. Samel, J. Chretien, R. F. Yue, P. Griss, and G. Stemme, "Wafer-level process for single-use buckling-film microliter-range pumps," *Journal of Microelectromechanical Systems*, vol. 16, pp. 795-801, Aug 2007.

- [72] B. Samel, V. Nock, A. Russom, P. Griss, and G. Stemme, "A disposable lab-on-a-chip platform with embedded fluid actuators for active nanoliter liquid handling," *Biomedical Microdevices*, vol. 9, pp. 61-67, Feb 2007.
- [73] J. Hammacher, A. Fuelle, J. Flaemig, J. Saupe, B. Loechel, and J. Grimm, "Stress engineering and mechanical properties of SU-8-layers for mechanical applications," *Microsystem Technologies*, vol. 14, pp. 1515-1523, 2008.
- [74] B. Li, A. Gueit, and A. Sharon, "Thickness management in three-dimensional laser manufacturing of suspended structures in a single SU-8 layer," *Review of Scientific Instruments*, vol. 77, pp. 1-5, Jun 2006.
- [75] J. Xie, Y. N. Miao, J. Shih, Q. He, J. Liu, Y. C. Tai, and T. D. Lee, "An electrochemical pumping system for on-chip gradient generation," *Analytical Chemistry*, vol. 76, pp. 3756-3763, Jul 1 2004.
- [76] L. J. Yang and K. C. Liu, "SU-8 buckled-type microvalves switched by surface tension forces," *2007 2nd IEEE International Conference on Nano/Micro Engineered and Molecular Systems, Vols 1-3*, pp. 993-996, 2007.
- [77] K. S. Yun, I. J. Cho, J. U. Bu, C. J. Kim, and E. Yoon, "A surface-tension driven micropump for low-voltage and low-power operations," *Journal of Microelectromechanical Systems*, vol. 11, pp. 454-461, Oct 2002.
- [78] K. S. Yun, I. J. Cho, J. U. Bu, G. H. Kim, Y. S. Jeon, C. J. Kim, and E. Yoon, "A micropump driven by continuous electrowetting actuation for low voltage and low power operations," *14th IEEE International Conference on Micro Electro Mechanical Systems, Technical Digest*, pp. 487-490, 2001.
- [79] T. R. Pan, W. Zheng, M. Lei, B. Cavanagh, and B. Ziaie, "A remotely adjustable check-valve array with an electrochemical release mechanism for implantable biomedical microsystems," *Boston Transducers'03: Digest of Technical Papers, Vols 1 and 2*, pp. 115-118, 2003.
- [80] L. J. Yang, J. M. Wang, K. C. Ko, W. P. Shih, and C. L. Dai, "A circular microchannel integrated with embedded spiral electrodes used for fluid transportation," *Sensors and Actuators a-Physical*, vol. 139, pp. 172-177, Sep 12 2007.
- [81] S. Bohm, W. Olthuis, and P. Bergveld, "A plastic micropump constructed with conventional techniques and materials," *Sensors and Actuators a-Physical*, vol. 77, pp. 223-228, Nov 2 1999.
- [82] R. Truckenmuller, Y. Cheng, R. Ahrens, H. Bahrs, G. Fischer, and J. Lehmann, "Micro ultrasonic welding: joining of chemically inert polymer microparts for single material fluidic components and systems," *Microsystem Technologies-Micro-and Nanosystems-Information Storage and Processing Systems*, vol. 12, pp. 1027-1029, Sep 2006.
- [83] J. Y. Shin, J. Y. Park, C. Liu, J. He, and S. C. Kim, "Chemical structure and physical properties of cyclic olefin copolymers (IUPAC Technical Report)," *Pure Appl. Chem.*, vol. 77, pp. 801-814, 2005.
- [84] C. H. Ahn, J. W. Choi, G. Beaucage, J. H. Nevin, J. B. Lee, A. Puntambekar, and J. Y. Lee, "Disposable Smart lab on a chip for point-of-care clinical diagnostics," *Proceedings of the IEEE*, vol. 92, pp. 154-173, Jan 2004.
- [85] C. Das, C. K. Fredrickson, F. T. Tavares, R. Ferguson, Z. Xia, and Z. H. Fan, "Fabricating plastic microfluidic devices with photodefinable microvalves for protein separation," *Micro-Electro-Mechanical Systems - 2005*, vol. 7, pp. 3-7, 2005.
- [86] R. R. Miles and D. L. Schumann, "Thin-walled compliant plastic structures for meso-scale fluidic systems," *Micro- and Nanofabricated Structures and Devices for Biomedical Environmental Applications II*, vol. 3606, pp. 129-136, 1999.
- [87] W. Inman, K. Domansky, J. Serdy, B. Owens, D. Trumper, and L. G. Griffith, "Design, modeling and fabrication of a constant flow pneumatic micropump," *Journal of Micromechanics and Microengineering*, vol. 17, pp. 891-899, May 2007.
- [88] P. K. Yuen, L. J. Kricka, and P. Wilding, "Semi-disposable microvalves for use with microfabricated devices or microchips," *Journal of Micromechanics and Microengineering*, vol. 10, pp. 401-409, Sep 2000.
- [89] Z. Z. Yin and A. Prosperetti, "'Blinking bubble' micropump with microfabricated heaters," *Journal of Micromechanics and Microengineering*, vol. 15, pp. 1683-1691, Sep 2005.
- [90] J. W. Gardner, "Microsensors: Principles and Applications," *John Wiley & Sons Ltd, Chichester*, 1994.
- [91] S. Beeby, G. Ensell, M. Kraft, and N. White, "MEMS Mechanical Sensors," *Artech House, Inc.*, 2004.

- [92] Z. X. Geng, D. F. Cui, H. N. Wang, and X. Chen, "Disposable PDMS diaphragm micropump actuated by PZT," *2006 1st IEEE International Conference on Nano/Micro Engineered and Molecular Systems, Vols 1-3*, pp. 1436-1439, 2006.
- [93] M. Knight and J. House, "Design, fabrication, and test of a peristaltic micropump," *Microsystem Technologies-Micro-and Nanosystems-Information Storage and Processing Systems*, vol. 10, pp. 426-431, Aug 2004.
- [94] S. Bohm, G. J. Burger, M. T. Korthorst, and F. Roseboom, "A micromachined silicon valve driven by a miniature bi-stable electro-magnetic actuator," *Sensors and Actuators a-Physical*, vol. 80, pp. 77-83, Mar 1 2000.
- [95] Y. Su, W. Chen, F. Cui, and W. Zhang, "Analysis and fabrication process of an electromagnetically actuated valveless micropump with two parallel flexible diaphragms," *Proceedings of the Institution of Mechanical Engineers Part C-Journal of Mechanical Engineering Science*, vol. 219, pp. 1007-1014, Sep 2005.
- [96] Y. F. Su, W. Y. Chen, F. Cui, and W. P. Zhang, "Electro-magnetically actuated valveless micropump with two flexible diaphragms," *International Journal of Advanced Manufacturing Technology*, vol. 30, pp. 215-220, Sep 2006.
- [97] C. H. Cheng, C. Chao, Y. N. Cheung, L. D. Xiao, M. Yang, and W. Leung, "A transcutaneous controlled magnetic microvalve based on iron-powder filled PDMS for implantable drug delivery systems," *2008 3rd IEEE International Conference on Nano/Micro Engineered and Molecular Systems, Vols 1-3*, pp. 1115-1118, 2008.
- [98] C. Y. Lee, H. T. Chang, and C. Y. Wen, "A MEMS-based valveless impedance pump utilizing electromagnetic actuation," *Journal of Micromechanics and Microengineering*, vol. 18, pp. -, Mar 2008.
- [99] D. H. Jun, W. Y. Sim, and S. S. Yang, "A novel constant delivery thermopneumatic micropump using surface tensions," *Sensors and Actuators a-Physical*, vol. 139, pp. 210-215, Sep 12 2007.
- [100] J. H. Kim, K. H. Na, C. J. Kang, and Y. S. Kim, "A disposable thermopneumatic-actuated micropump stacked with PDMS layers and ITO-coated glass," *Sensors and Actuators a-Physical*, vol. 120, pp. 365-369, May 17 2005.
- [101] J. C. Yoo, G. S. La, C. J. Kang, and Y. S. Kim, "Microfabricated polydimethylsiloxane microfluidic system including micropump and microvalve for integrated biosensor," *Current Applied Physics*, vol. 8, pp. 692-695, Oct 2008.
- [102] J. C. Yoo, Y. J. Choi, C. J. Kang, and Y. S. Kim, "A novel polydimethylsiloxane microfluidic system including thermopneumatic-actuated micropump and Paraffin-actuated microvalve," *Sensors and Actuators a-Physical*, vol. 139, pp. 216-220, Sep 12 2007.
- [103] O. C. Jeong, S. W. Park, S. S. Yang, and J. J. Pak, "Fabrication of a peristaltic PDMS micropump," *Sensors and Actuators a-Physical*, vol. 123-24, pp. 453-458, Sep 23 2005.
- [104] W. H. Song, J. Kwan, G. V. Kaigala, V. N. Hoang, and C. J. Backhouse, "Readily integrated, electrically controlled microvalves," *Journal of Micromechanics and Microengineering*, vol. 18, pp. -, Apr 2008.
- [105] P. Kumaresan, C. J. Yang, S. A. Cronier, R. G. Blazei, and R. A. Mathies, "High-throughput single copy DNA amplification and cell analysis in engineered nanoliter droplets," *Analytical Chemistry*, vol. 80, pp. 3522-3529, May 15 2008.
- [106] W. H. Grover, A. M. Skelley, C. N. Liu, E. T. Lagally, and R. A. Mathies, "Monolithic membrane valves and diaphragm pumps for practical large-scale integration into glass microfluidic devices," *Sensors and Actuators B-Chemical*, vol. 89, pp. 315-323, Apr 1 2003.
- [107] W. Satoh, H. Hosono, and H. Suzuki, "On-chip microfluidic transport and mixing using electrowetting and incorporation of sensing functions," *Analytical Chemistry*, vol. 77, pp. 6857-6863, Nov 1 2005.
- [108] J. S. Lee and S. Lucyszyn, "Design and pressure analysis for bulk-micromachined electrothermal hydraulic microactuators using a PCM," *Sensors and Actuators a-Physical*, vol. 133, pp. 294-300, Feb 12 2007.
- [109] H. Takao, K. Miyamura, H. Ebi, M. Ashiki, K. Sawada, and M. Ishida, "A MEMS microvalve with PDMS diaphragm and two-chamber configuration of thermo-pneumatic actuator for integrated blood test system on silicon," *Sensors and Actuators a-Physical*, vol. 119, pp. 468-475, Apr 13 2005.
- [110] D. Baechi, J. Dual, and R. Buser, "A high density microchannel network with integrated valves and photodiodes," *14th IEEE International Conference on Micro Electro Mechanical Systems, Technical Digest*, pp. 463-466, 2001.

- [111] W. Y. Sim, H. J. Yoon, O. C. Jeong, and S. S. Yang, "A phase-change type micropump with aluminum flap valves," *Journal of Micromechanics and Microengineering*, vol. 13, pp. 286-294, Mar 2003.
- [112] A. Baldi, Y. D. Gu, P. E. Loftness, R. A. Siegel, and B. Ziaie, "A hydrogel-actuated environmentally sensitive microvalve for active flow control," *Journal of Microelectromechanical Systems*, vol. 12, pp. 613-621, Oct 2003.
- [113] W. L. Benard, H. Kahn, A. H. Heuer, and M. A. Huff, "Thin-film shape-memory alloy actuated micropumps," *Journal of Microelectromechanical Systems*, vol. 7, pp. 245-251, Jun 1998.
- [114] T. Arakawa, T. Sameshima, Y. Sato, T. Ueno, Y. Shirasaki, T. Funatsu, and S. Shoji, "Rapid multi-reagents exchange TIRFM microfluidic system for single biomolecular imaging," *Sensors and Actuators B-Chemical*, vol. 128, pp. 218-225, Dec 12 2007.
- [115] A. Han, M. Graff, O. Wang, and A. B. Frazier, "An approach to multilayer microfluidic systems with integrated electrical, optical, and mechanical functionality," *Ieee Sensors Journal*, vol. 5, pp. 82-89, Feb 2005.
- [116] C. F. Lin, G. B. Lee, C. H. Wang, H. H. Lee, W. Y. Liao, and T. C. Chou, "Microfluidic pH-sensing chips integrated with pneumatic fluid-control devices," *Biosensors & Bioelectronics*, vol. 21, pp. 1468-1475, Feb 15 2006.
- [117] S. Kojima, M. Loughran, and H. Suzuki, "Microanalysis system for pO<sub>2</sub>, pCO<sub>2</sub>, and pH constructed with stacked modules," *Ieee Sensors Journal*, vol. 5, pp. 1120-1126, Oct 2005.
- [118] C. J. Huang, Y. H. Chen, C. H. Wang, T. C. Chou, and G. B. Lee, "Integrated microfluidic systems for automatic glucose sensing and insulin injection," *Sensors and Actuators B-Chemical*, vol. 122, pp. 461-468, Mar 26 2007.
- [119] C. H. Weng, W. M. Yeh, K. C. Ho, and G. B. Lee, "A microfluidic system utilizing molecularly imprinted polymer films for amperometric detection of morphine," *Sensors and Actuators B-Chemical*, vol. 121, pp. 576-582, Feb 20 2007.
- [120] J. H. Kim, C. J. Kang, and Y. S. Kim, "A disposable polydimethylsiloxane-based diffuser micropump actuated by piezoelectric-disc," *Microelectronic Engineering*, vol. 71, pp. 119-124, Feb 2004.
- [121] K. F. Lei, W. C. Law, Y. K. Suen, W. J. Li, Y. Yam, H. P. Ho, and S. K. Kong, "A vortex pump-based optically-transparent microfluidic platform for biotech and medical applications," *Proceedings of the Institution of Mechanical Engineers Part H-Journal of Engineering in Medicine*, vol. 221, pp. 129-141, Feb 2007.
- [122] K. F. Lei, R. H. W. Lam, J. H. M. Lam, and W. J. Li, "Polymer based vortex micropump fabricated by micro molding replication technique," in *Intelligent Robots and Systems, 2004. (IROS 2004). Proceedings. 2004 IEEE/RSJ International Conference on*, 2004, pp. 1740-1745 vol.2.
- [123] W. H. Song and J. Lichtenberg, "Thermo-pneumatic, single-stroke micropump," *Journal of Micromechanics and Microengineering*, vol. 15, pp. 1425-1432, Aug 2005.
- [124] S. Santra, P. Holloway, and C. D. Batich, "Fabrication and testing of a magnetically actuated micropump," *Sensors and Actuators B-Chemical*, vol. 87, pp. 358-364, Dec 10 2002.
- [125] T. R. Pan, S. J. McDonald, E. M. Kai, and B. Ziaie, "A magnetically driven PDMS micropump with ball check-valves," *Journal of Micromechanics and Microengineering*, vol. 15, pp. 1021-1026, May 2005.
- [126] J. S. Go, T. Yamazaki, M. Kanai, H. Sato, S. Kawakami, and S. Shoji, "A disposable, dead volume-free and leak-free monolithic PDMS microvalve," *Boston Transducers'03: Digest of Technical Papers, Vols 1 and 2*, pp. 643-646, 2003.
- [127] T. G. Henares, S. Funano, S. Terabe, F. Mizutani, R. Sekizawa, and H. Hisamoto, "Multiple enzyme linked immunosorbent assay system on a capillary-assembled microchip integrating valving and immuno-reaction functions," *Analytica Chimica Acta*, vol. 589, pp. 173-179, Apr 25 2007.
- [128] P. Dario, N. Croce, M. C. Carrozza, and G. Varallo, "A fluid handling system for a chemical microanalyzer," *Journal of Micromechanics and Microengineering*, vol. 6, pp. 95-98, Mar 1996.
- [129] M. Richter, Y. Congar, J. Nissen, G. Neumayer, K. Heinrich, and M. Wackerle, "Development of a multi-material micropump," *Proceedings of the Institution of Mechanical Engineers Part C-Journal of Mechanical Engineering Science*, vol. 220, pp. 1619-1624, Nov 2006.
- [130] K. Hosokawa and R. Maeda, "A pneumatically-actuated three-way microvalve fabricated with polydimethylsiloxane using the membrane transfer technique," *Journal of Micromechanics and Microengineering*, vol. 10, pp. 415-420, Sep 2000.
- [131] J. M. Berg, R. Anderson, M. Anaya, B. Lahlouh, M. Holtz, and T. Dallas, "A two-stage discrete peristaltic micropump," *Sensors and Actuators a-Physical*, vol. 104, pp. 6-10, Mar 15 2003.
- [132] A. Dodge, E. Brunet, S. L. Chen, J. Goulpeau, V. Labas, J. Vinh, and P. Tabeling, "PDMS-based microfluidics for proteomic analysis," *Analyst*, vol. 131, pp. 1122-1128, 2006.



- [133] C. W. Huang, S. B. Huang, and G. B. Lee, "Pneumatic micropumps with serially connected actuation chambers," *Journal of Micromechanics and Microengineering*, vol. 16, pp. 2265-2272, Nov 2006.
- [134] F. C. Huang, C. S. Liao, and G. B. Lee, "An integrated microfluidic chip for DNA/RNA amplification, electrophoresis separation and on-line optical detection," *Electrophoresis*, vol. 27, pp. 3297-3305, Aug 2006.
- [135] S. J. Lee, J. C. Y. Chan, K. J. Maung, E. Rezler, and N. Sundararajan, "Characterization of laterally deformable elastomer membranes for microfluidics," *Journal of Micromechanics and Microengineering*, vol. 17, pp. 843-851, May 2007.
- [136] H. Y. Tseng, C. H. Wang, W. Y. Lin, and G. B. Lee, "Membrane-activated microfluidic rotary devices for pumping and mixing," *Biomedical Microdevices*, vol. 9, pp. 545-554, Aug 2007.
- [137] C. H. Wang and G. B. Lee, "Pneumatically driven peristaltic micropumps utilizing serpentine-shape channels," *Journal of Micromechanics and Microengineering*, vol. 16, pp. 341-348, Feb 2006.
- [138] J. Wang, Z. Y. Chen, M. Mauk, K. S. Hong, M. Y. Li, S. Yang, and H. H. Bau, "Self-actuated, thermo-responsive hydrogel valves for lab on a chip," *Biomedical Microdevices*, vol. 7, pp. 313-322, Dec 2005.
- [139] J. Y. Baek, J. Y. Park, J. I. Ju, T. S. Lee, and S. H. Lee, "A pneumatically controllable flexible and polymeric microfluidic valve fabricated via in situ development," *Journal of Micromechanics and Microengineering*, vol. 15, pp. 1015-1020, May 2005.
- [140] J. C. Galas, V. Studer, and Y. Chen, "Characterization of pneumatically activated microvalves by measuring electrical conductance," *Microelectronic Engineering*, vol. 78-79, pp. 112-117, Mar 2005.
- [141] S. Lee, W. Jeong, and D. J. Beebe, "Microfluidic valve with cored glass microneedle for microinjection," *Lab on a Chip*, vol. 3, pp. 164-167, 2003.
- [142] J. P. Urbanski, W. Thies, C. Rhodes, S. Amarasinghe, and T. Thorsen, "Digital microfluidics using soft lithography," *Lab on a Chip*, vol. 6, pp. 96-104, 2006.
- [143] J. H. Kim, K. H. Na, C. J. Kang, D. Jeon, and Y. S. Kim, "A disposable thermopneumatic-actuated microvalve stacked with PDMS layers and ITO-coated glass," *Microelectronic Engineering*, vol. 73-74, pp. 864-869, Jun 2004.
- [144] V. Namasivayam, R. H. Liu, B. Towe, and P. Grodzinski, "Design of a self-contained 3D microvalve in PDMS," *Transducers '01: Eurosensors Xv, Digest of Technical Papers, Vols 1 and 2*, pp. 1228-1231, 2001.
- [145] O. C. Jeong, T. Morimoto, Y. Watanabe, and S. Konishi, "Peristaltic PDMS pump with perfect dynamic valves for both gas and liquid," *MEMS 2006: 19th IEEE International Conference on Micro Electro Mechanical Systems, Technical Digest*, pp. 782-785, 2006.
- [146] Y. S. Kim, J. H. Kim, K. H. Na, and K. Rhee, "Experimental and numerical studies on the performance of a polydimethylsiloxane valveless micropump," *Proceedings of the Institution of Mechanical Engineers Part C-Journal of Mechanical Engineering Science*, vol. 219, pp. 1139-1145, Oct 2005.
- [147] J. C. Yoo, M. C. Moon, Y. J. Choi, C. J. Kang, and Y. S. Kim, "A thermopneumatic-actuated polydimethylsiloxane microfluidic system," *2006 1st IEEE International Conference on Nano/Micro Engineered and Molecular Systems, Vols 1-3*, pp. 1379-1383, 2006.
- [148] M. Nakano, S. Katsura, G. Touchard, K. Takashima, and A. Mizuno, "Development of opto-electro static micro-pump using a focused laser in a high-frequency electric field," *Conference Record of the 2005 IEEE Industry Applications Conference, Vols 1-4*, pp. 2189-2193, 2005.
- [149] J. D. Salgado, K. Horiuchi, and P. Dutta, "A conductivity-based interface tracking method for microfluidic application," *Journal of Micromechanics and Microengineering*, vol. 16, pp. 920-928, May 2006.
- [150] R. H. Liu, Q. Yu, and D. J. Beebe, "Fabrication and characterization of hydrogel-based microvalves," *Journal of Microelectromechanical Systems*, vol. 11, pp. 45-53, 2002.
- [151] J. Y. Park, H. J. Oh, D. J. Kim, J. Y. Baek, and S. H. Lee, "A polymeric microfluidic valve employing a pH-responsive hydrogel microsphere as an actuating source," *Journal of Micromechanics and Microengineering*, vol. 16, pp. 656-663, Mar 2006.
- [152] I. D. Johnston, J. B. Davis, R. Richter, G. I. Herbert, and M. C. Tracey, "Elastomer-glass micropump employing active throttles," *Analyst*, vol. 129, pp. 829-834, 2004.
- [153] I. D. Johnston, M. C. Tracey, J. B. Davis, and C. K. L. Tan, "Microfluidic solid phase suspension transport with an elastomer-based, single piezo-actuator, micro throttle pump," *Lab on a Chip*, vol. 5, pp. 318-325, 2005.

- [154] N. B. Justis, D. Y. Zhang, and Y. H. Lo, "Integrated dynamic fluidic lens system for in vivo biological imaging," *Proceedings of the 26th Annual International Conference of the IEEE Engineering in Medicine and Biology Society, Vols 1-7*, vol. 26, pp. 1256-1259, 2004.
- [155] J. Y. Kim, J. Y. Baek, H. J. Chang, and S. H. Lee, "Aligning system for the in-situ microfabrication of multiple microstructures," *2005 3rd IEEE/EMBS Special Topic Conference on Microtechnology in Medicine and Biology*, pp. 315-318, 2005.
- [156] W. Gu, X. Y. Zhu, N. Futai, B. S. Cho, and S. Takayama, "Computerized microfluidic cell culture using elastomeric channels and Braille displays," *Proceedings of the National Academy of Sciences of the United States of America*, vol. 101, pp. 15861-15866, Nov 9 2004.
- [157] A. R. Prakash, S. Adamia, V. Sieben, P. Pilarski, L. M. Pilarski, and C. J. Backhouse, "Small volume PCR in PDMS biochips with integrated fluid control and vapour barrier," *Sensors and Actuators B-Chemical*, vol. 113, pp. 398-409, Jan 17 2006.
- [158] Y. Tanaka, K. Morishima, T. Shimizu, A. Kikuchi, M. Yamato, T. Okano, and T. Kitamori, "An actuated pump on-chip powered by cultured cardiomyocytes," *Lab on a Chip*, vol. 6, pp. 362-368, Mar 2006.
- [159] D. Kim, S. Kim, J. Park, J. Baek, S. Kim, K. Sun, T. Lee, and S. Lee, "Hydrodynamic fabrication and characterization of a pH-responsive microscale spherical actuating element," *Sensors and Actuators a-Physical*, vol. 134, pp. 321-328, Mar 15 2007.
- [160] J. Y. Park, D. J. Kim, S. R. Kim, J. Y. Baek, K. Sun, and S. H. Lee, "Microfluidic valve employing the pH-responsive hydrogel microsphere as an actuating element," *2006 International Conference on Microtechnologies in Medicine and Biology*, pp. 35-38, 2006.
- [161] M. C. Carrozza, N. Croce, B. Magnani, and P. Dario, "A Piezoelectric-Driven Stereolithography-Fabricated Micropump," *Journal of Micromechanics and Microengineering*, vol. 5, pp. 177-179, Jun 1995.
- [162] T. Hasegawa, K. Nakashima, F. Omatsu, and K. Ikuta, "Multi-directional micro-switching valve chip with rotary mechanism," *Sensors and Actuators a-Physical*, vol. 143, pp. 390-398, May 16 2008.

# Chapter 3

---

## 3 Polymeric Micropumps – Design and Actuation

### 3.1 Introduction

In the previous chapter, the polymer materials used for microfabrication and their related fabrication techniques were reviewed. In this section, the working principles of micropumps and valves will be described, as recorded in the literature, with emphasis on those mechanisms that are best suited to polymeric materials. There is also a range of actuation techniques that have been used in the literature. Again, these techniques will be summarised, with a focus on those most suitable for use with polymeric fabrication materials.

### 3.2 Valve Mechanisms

A large number of different polymer-based microvalve designs can be found in the literature. They perform two main functions: rectification and flow control. An overview of the types of valve seen in the literature is presented in *Figure 3.6*. Rectification valves are normally found in pumps, as the majority of pump designs apply force to the working fluid non-directionally. The flow created must therefore be rectified into a single direction to be useful. Rectification of flow is normally carried out by passive mechanisms that do not require extra energy, but instead utilise the energy present in the fluid flow. For this reason, micropumps using passive valves (often referred to as “check valves”) for rectification do not require the pump to be running in order to hold a back pressure. This is however not the case for nozzle/diffuser elements, which are passive but only hold a back pressure when the pump is active.

Active rectification valves are normally only found integrated in discrete micropumps in multi-membrane peristaltic designs, where the outer pump membranes and chambers could be considered as active valves. However, active flow control valves are normally used digitally to

switch flow in a channel on or off, whilst more advanced devices can direct flow from one channel into another. Flow can also be controlled in an analogue fashion, using throttle valves. Finally, “special effect” valves, like the pumps of the same classification, rely on electrical effects to control fluid flow and use no moving parts.

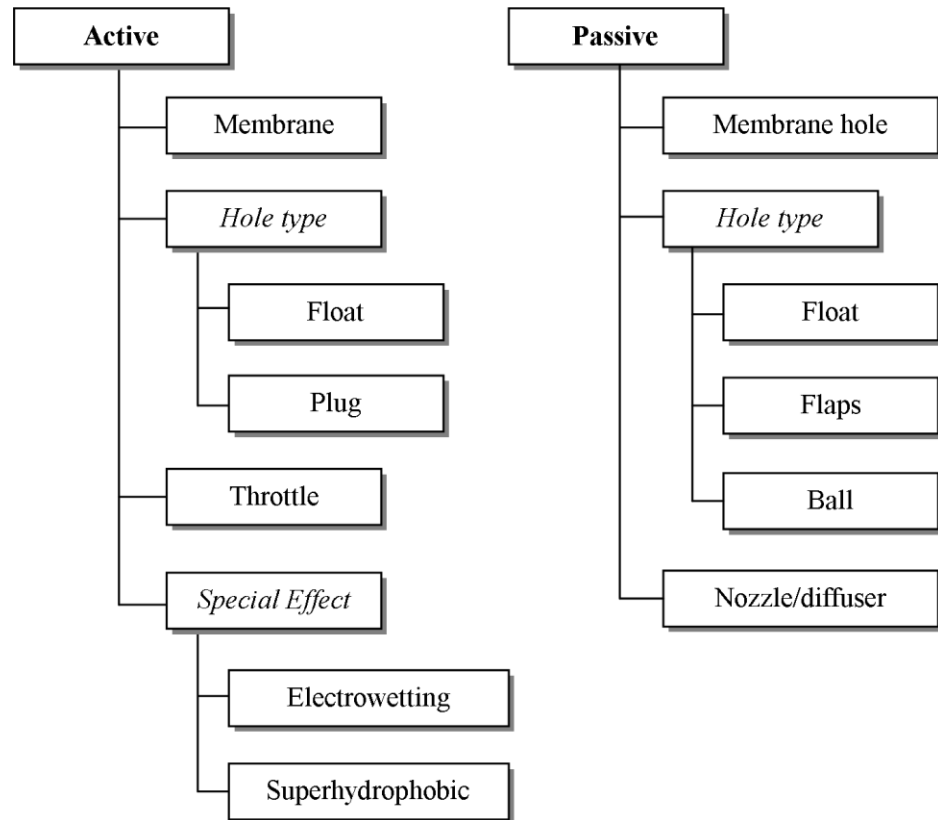


Figure 3.1 – Overview of classification of passive and active microvalves seen in the literature.

### 3.3 Passive Microvalves

#### 3.3.1 Passive Membrane Hole Valves

One of the more simple types of valve is the membrane hole check valve. These devices employ a membrane with a central hole, normally aligned with a small pillar. As shown in *Figure 3.2*, pressure in the working fluid on the pillar side pushes the membrane away from the pillar, and allows flow through the membrane hole; conversely, pressure from the other side pushes the membrane against the pillar, blocking the hole and halting flow. Membrane materials include polyimide [1, 2], silicone rubber [3, 4], polycarbonate [5], polyester [6, 7] and PMMA [8]. In some

designs, such as the aforementioned Büstgens *et al* [1], the valve membrane used is simply a different area of the same pump membrane material, cutting some steps out of fabrication [7]. Membrane hole valves tend to work better at frequencies lower than 50 Hz, and normally produce modest flow rates (<1 ml/min). However, pumping of air is possible if the device is optimised as such, allowing for self-priming devices, which can pump air strongly enough to pull fluid into themselves without having to be primed manually [5].

### 3.3.2 Passive Float Valves

A float valve can be seen as reverse membrane hole valve, where the plug is mobile instead of the membrane. The float is normally suspended over the outlet by multiple arms, which are flexible enough to allow the float structure to be deflected by pressure within the working fluid. The first example of a polymeric passive plug valve can be found in Shoji *et al* in 1992 [9], one of the first polymer microvalves. The overall device was a piezoelectric single-membrane micropump, but was based on silicon technology and is therefore not discussed here. However, the valves consisted of a moulded silicone rubber plug fabricated in a chamfered anisotropically-etched hole in a silicon wafer. The plug arms were fabricated from SU-8 using micromachining techniques, which located the plug in the silicon outlet hole whilst still allowing movement away from the silicon hole if the pressure rose high enough. The plug was 600 by 600  $\mu\text{m}$  at the top and 70 by 70  $\mu\text{m}$  at the bottom. At an applied pressure of 2 kPa, fluid flow through the valve was 170 times higher in the forward direction than when the pressure was applied in the reverse direction.

### 3.3.3 Passive Flaps

A flap valve is a structure connected to only one side of a channel or channel opening. It acts much like a door, opening when pressure is applied from one side, but being pressed shut when pressure is applied from the other. The structure is prevented from opening in the other

direction by stoppers within or on the edge of the channel, or by the fact the flap is bigger than the opening it is sealing. Figure 3.2 gives a simple example of a side-wall flap valve.

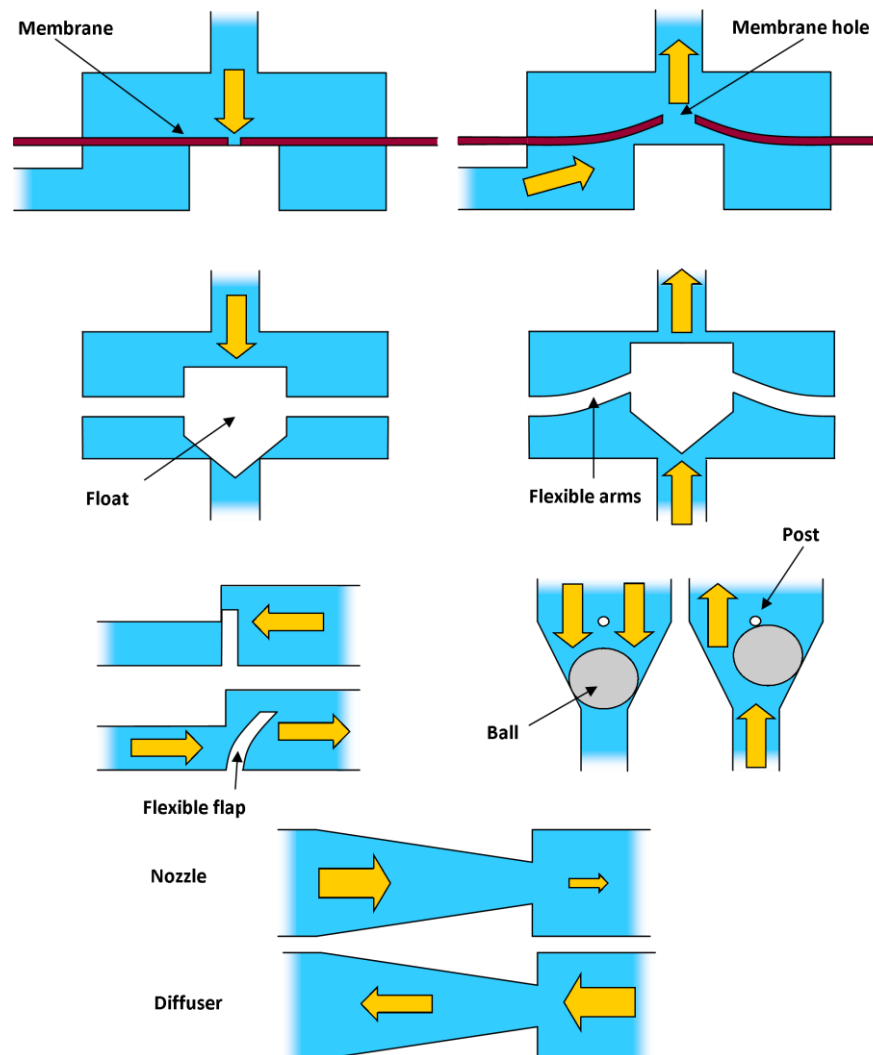


Figure 3.2 - Operational mechanisms of passive microvalves, showing membrane hole, float, flap, ball and nozzle diffuser valves in open and closed states. In the case of nozzle/diffuser valves, there isn't a specific "closed" state; the working fluid is simply more likely to move in one direction than the other when pressure is applied.

Adams *et al* [10] presented a simple flap valve based on PDMS soft lithography fabrication techniques. The flap structure was just 4  $\mu\text{m}$  thick, 24  $\mu\text{m}$  tall and 45  $\mu\text{m}$  wide, obscuring a smaller 11  $\mu\text{m}$  channel when closed. Kim *et al* [11, 12] published a flap valve fabricated by *in-situ* photopolymerisation in 4-hydroxyl butyric acid (4-HBA). Unusually for a hydrogel-fabricated device, the hydrogel is used simply as a mechanical material, rather than as an actuation mechanism, although due to the nature of the hydrogel surface the material had to be lubricated

to prevent it from sticking to the channel walls. Klammer *et al* [13] produced a dual-flap microvalve similar to that found in the human circulatory system, fabricated in PDMS by soft lithography. A number of other passive flap valves fabricated using polymer materials are also found in the literature, all based on similar concepts [14-21].

### 3.3.4 Ball Valves

Ball valves are common in macroscale applications, and use a free ball bearing enclosed within a channel. The ball normally blocks a narrowing in the channel with pressure from one side. Pressure from the other side pushes the ball against a post located across the centre of the channel, as shown in *Figure 3.2*. Ball valves were utilised by Carozza *et al* [22] in their stereolithography fabricated piezoelectrically actuated device. A very high flow rate of 2.7 ml/min was reported, along with a maximum back pressure of 24 kPa, showing that ball valves have promise in high flow rate and back pressure applications. Their major disadvantage however is they limit the device miniaturisation – the balls used in Carozza *et al* were 1.2 mm in diameter, and fabrication of devices incorporating smaller spheres is difficult.

### 3.3.5 Nozzle/Diffuser Elements

Flow rectification does not have to be an active process, and can be achieved by varying the shape of the device microfluidics. *Figure 3.2* shows an example of the geometry employed. The earliest example of nozzle/diffuser implementation in a micropump can be found in Stemme and Stemme, 1993 [23], in which a piezoelectrically actuated silicon-based device is presented. The narrowing of the nozzle and widening of the diffuser, relative to the partially rectified flow, create pressure gradients within the working fluid, which present less flow resistance in one direction – from the nozzle to the diffuser. Using a 19 mm pump membrane, Stemme and Stemme reported flow rates of 16 ml/min and backpressures of around 19 kPa at 100 Hz. Su *et al* [24] presented a magnetically actuated micropump with nozzle/diffuser elements, also fabricated in silicon using anisotropic etching. The pump membrane was micromoulded in PDMS, with

integrated magnetic material, and is discussed further later in this paper. The dual pump membrane design achieved flow rates of around 360  $\mu\text{l}/\text{min}$ .

However, the majority of polymer based micropumps with nozzle/diffuser elements employ planar, 2-dimensional designs, also known as extruded 2D. The first example can be found in Kar *et al* [25], who used a nozzle/diffuser arrangement fabricated in PMMA using X-ray lithography to rectify flow from their piezoelectric piston micropump. A flow rate of 368 nl/min was achieved. Khoo *et al* [26], discussed later in this paper, also used planar nozzle/diffuser elements, fabricated from PDMS using micromachining techniques. The magnetic actuator employed gave a frequency of 2.9 Hz, leading to a flow rate of 1.2  $\mu\text{l}/\text{min}$ .

Kim *et al* described a piezoelectric dual-chamber design [27] along with a single-chamber thermopneumatic device [28]. The piezoelectric device gave a maximum flow rate of 33  $\mu\text{l}/\text{min}$  with a backpressure of 173 Pa and a driving frequency of 300 Hz. In comparison, the thermopneumatic device delivered a flow rate of 78 nl/min at a frequency of 6 Hz and a duty ratio of 10%.

A paper by Justis *et al* [29] demonstrates similar micropump to Kim *et al* [27] with dual chambers with piezoelectric actuation. The pump, fabricated from PDMS using soft lithography, was used to inflate a PDMS lens for use with *in vivo* imaging technology. A much higher pump frequency of 5 kHz was used to drive the piezoelectric disk, resulting in a flow rate of 2.4  $\mu\text{l}/\text{min}$ .

One disadvantage of nozzle/diffuser elements is that they do not produce a back pressure when the pump is not active. This can be solved by adding active valves to the pump design. Yoo *et al* [30] demonstrated a thermopneumatic pump design, similar to Kim's design described above [28], but with a pair of integrated thermopneumatic membrane valves flanking the nozzle/diffuser elements. Due to a low actuator frequency of just 6 Hz, a maximum flow rate of just 80 nl/min



was achieved. A later follow-up paper described a similar system, but with three valves: one on the outlet, and two on the inlet to allow pumping and mixing of two separate working fluids [31].

It is fairly plain from the data published that nozzle diffuser mechanisms are not efficient at low frequencies. This limits their use with lower frequency actuation techniques, specifically thermopneumatic. However, at high frequencies both high back pressures and flow rates are achievable, making nozzle/diffuser mechanisms ideal for piezoelectric actuation.

### **3.4 Active Valves**

#### **3.4.1 Active Membrane Valves**

Perhaps the most numerous and simple active polymer microvalve in the literature is the membrane type. These valves utilise a thin membrane or diaphragm, deflected by a variety of actuators, to block a microfluidic channel. There are a number of ways the membrane can block the channel. The simplest devices simply employ a membrane above the channel, which the membrane deflects into to block [32-34]. These devices may include a raised weir in the channels so the membrane deflection required is minimised [35-37]. In other designs, the membrane moves down to block a hole at the bottom of a chamber under the membrane [38, 39], which may have a collar [40-47], again to minimise the deflection required. Membrane deflection can also be minimised by thickening the centre of the valve membrane [48-53].

The first active membrane microvalve utilising a polymer material is found in Sjolander *et al* 1991 [36]. The valve is part of a  $\mu$ TAS system, and is fabricated using multiple stacked moulded polystyrene plates. The 0.5 mm diameter valve membrane is made of silicone rubber, fabricated using a moulding process, and is sandwiched between two of the plates. Actuation is provided by a pneumatic port above the membrane, deflecting the membrane down onto a weir formation.

### 3.4.2 Active plug valves

Kim *et al* [11] presented a hydrogel-actuated plug microvalve, fabricated using a combination of PDMS soft lithography for the valve body and *in-situ* photopolymerisation for the hydrogel actuation element. The hydrogel element sits around a fixed post and is in contact with the PDMS mobile plug. A secondary fluid, separate from the working fluid, is passed over the hydrogel actuator. pH variations in the secondary fluid cause the hydrogel to expand or contract, closing and opening the plug valve.

### 3.4.3 Throttle Valves

For the purpose of this review, a throttle valve is a fluidic device in which the cross-sectional area of the fluidic channel is made larger or smaller to respectively encourage and slow the movement of fluid through the channel. To a certain extent, most active valves behave in this manner, in that whilst a certain actuation power is required to fully close the device, any power input below this threshold only partially closes the fluidic channel. Throttle valves may be used for rectification, but can also be used to control flow rates through microfluidic systems.

There are a number of polymeric throttle valves reported in the literature. The first is found in Johnson *et al* [54]. The device is a reciprocating displacement micropump, which consists of a single pump membrane flanked by a pair of novel throttle valves. The pump itself is composed of a multi-layer soft lithography fabricated fluidics layer sandwiched between glass base layers. The actuation system is composed of three separate piezoelectric discs, which deflect and distort the pump membrane and the throttle structures in turn, much like a peristaltic micropump. The throttles are composed of a number of PDMS posts, separated by only 20  $\mu\text{m}$ , as shown in *Figure 3.8*. As the piezoelectric elements are activated and deactivated, this gap is reduced and increased by the deflection of the piezoelectric disc. The activation of the two flanking throttle valves is timed with that of the pump membrane, allowing rectification and

therefore directional flow in either direction. With a driving frequency of 50 Hz a maximum flow rate of around 300  $\mu\text{l}/\text{min}$  was measured with a backpressure of 5.5 kPa.

A follow up paper by the same group [55] outlined a device of similar design, which instead had only a single offset piezoelectric actuator, rather than the original three separate discs. This offset created a wave in the device, contracting the inlet throttles whilst opening the outlet throttles, and *vice versa*. A flow rate of 132  $\mu\text{l}/\text{min}$  with a back pressure of 6.0 kPa was achieved with a pump frequency of 800 Hz. However, due to the offset required, the device was only capable of flow in one direction.

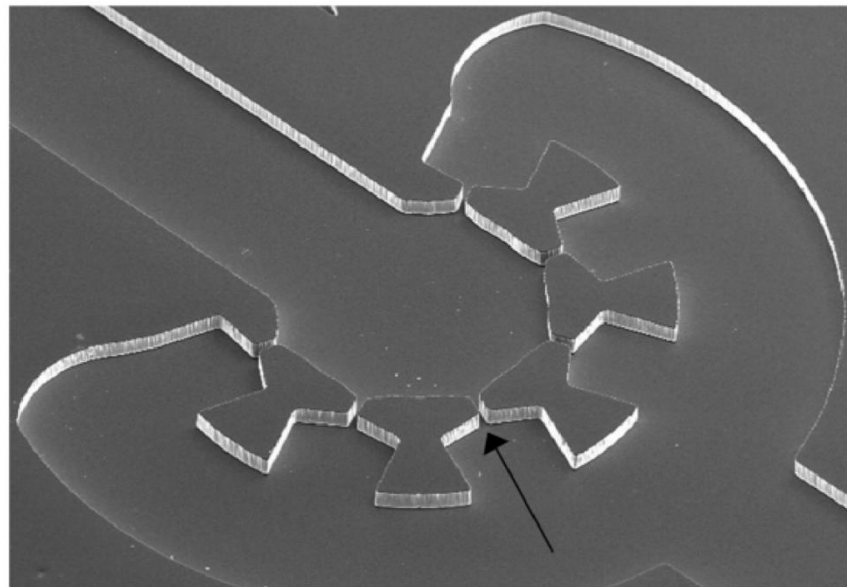
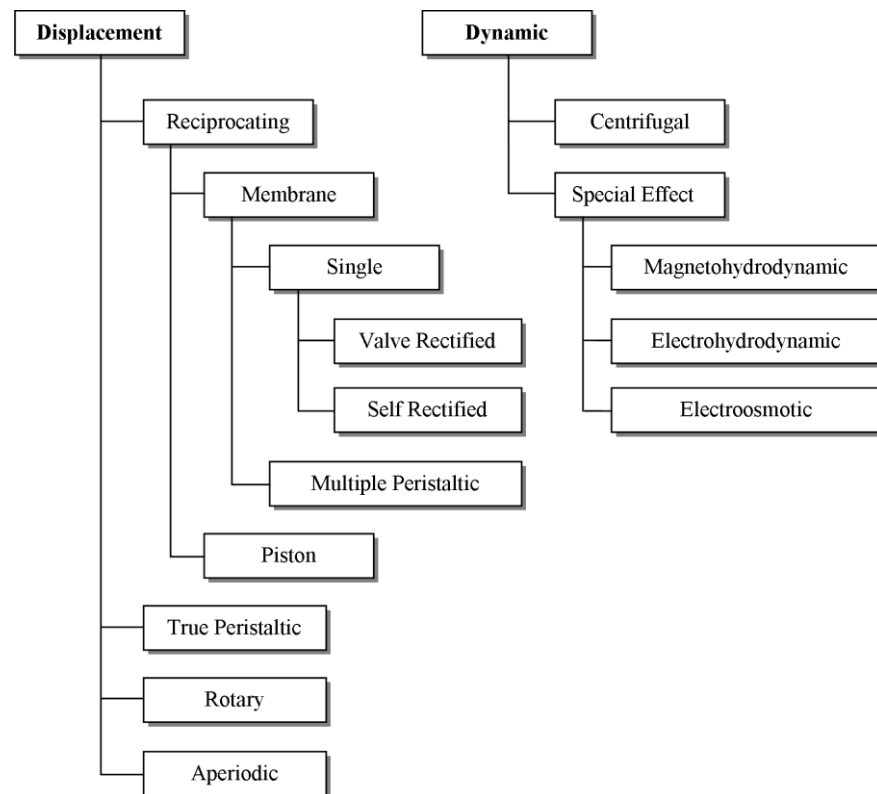


Figure 3.3 – PDMS microstructures employed as active throttle valves by Johnson et al [54]. The arrow points to one of the gaps in the structure, just 20  $\mu\text{m}$  across. These gaps are closed by the action of a piezoelectric disc placed over the throttle structure.

### 3.5 Pump Mechanisms

A pump, regardless of the working fluid, can be defined as a device that exerts a force in order to move a fluid. To the end-user, how the pump achieves this movement is normally irrelevant. However, different applications may require mechanisms that are tolerant of specific conditions, such as bubble formation, or the presence of solid particles in the working fluid. Other requirements may include a specific flow rate, smooth flow or good backpressures even when the pump is not running.

Krutzch and Cooper [56] put forward a system of macroscale pump classification based on the mechanism employed by the device to exert force on the working fluid. This system has been previously adapted for use with micropumps by Laser and Santiago [57]. The system divides pumps broadly into two categories, displacement and dynamic, an overview of which can be seen in *Figure 3.4*. Displacement-type micropumps are by far the most prevalent, and use moving boundaries within the device to change the volume of a pump chamber. On the other hand, dynamic micropumps exert a continuous force via either mechanical momentum or electrical effects. Wherever possible in this chapter, flow rate and backpressure data will be provided.



*Figure 3.4 – Classification system for micropumps put forward by Laser and Santiago [57].*

It should be noted that when it comes to flow rates, bigger is not always better. For many microscale fluidics applications such as micro total analysis systems ( $\mu$ TAS), slow flow rates are favourable due to the small volumes of sample and reagents being handled. In such systems, the volume precision and flow rate resolution of the pump device is often more important, along with

the reaction time of any valves present. Additionally, compromises must sometime be made in portable systems between outright performance and energy consumption.

### **3.6 Reciprocating Displacement Micropumps**

#### **3.6.1 Membrane Micropumps**

The vast majority of reciprocating displacement micropumps, and in fact of micropumps in general, are membrane-based. In these pumps, a force provided by an actuator deflects a thin membrane or diaphragm into and out of the working fluid. Even before the rise of all-polymer designs, polymeric materials were often used in the fabrication of the diaphragm, as they are more flexible than the alternative silicon, glass or metal membranes available using traditional micromachining processes. The use of polymer materials can lead to greater efficiency when combined with some actuation techniques, as less energy is required to deflect the membrane a given distance, and the potential deflection is greater. The deflection achieved is usually positive i.e. into the working fluid, although it may also be negative or bidirectional. The area underneath the membrane on the working fluid side can be referred to as the “pump chamber”. The movement of the membrane relative to this chamber varies the volume of the working fluid contained within it, and this force upon the fluid is turned into a rise or fall in pressure in the working fluid via friction between the working fluid and pump body. The pressure created is normally non-directional, although some membrane-based devices exist that do not require rectification, normally by offset of the membrane or actuator relative to some design feature such as a weir. However, flow rectification is normally achieved using some form of microvalve.

A large number of polymer micropumps reported in the literature utilise a single pump membrane, with rectification carried out by separate microvalves. As the membrane movement in membrane-based reciprocating displacement devices is both into and out of the working fluid, it is necessary to have some mechanism whereby this dual-direction flow is converted into a single direction for the flow to be useful. This can be achieved in a large number of ways, and the

process is known as rectification. *Figure 3.5* gives a generalised example of how such valved devices work. These designs are too numerous to list here, and many are similar in concept to the aforementioned Büstgens *et al* [1], the first all-polymer micropump. This design incorporated a 4 mm diameter 100  $\mu\text{m}$  deep pump chamber, fabricated using thermoplastic moulding from polysulphone. The pump membrane is thermopneumatically actuated, and is flanked by a pair of 750  $\mu\text{m}$  diameter passive membrane hole valves. A maximum flow rate of 44  $\mu\text{l}/\text{min}$  was reported, along with a backpressure of 3.8 kPa. Many more examples of single-membrane reciprocating displacement micropumps are listed in this chapter, but most are more noteworthy due to their valve design, actuation mechanism or fabrication technique. These devices will therefore be discussed in more detail in latter sections of the chapter.

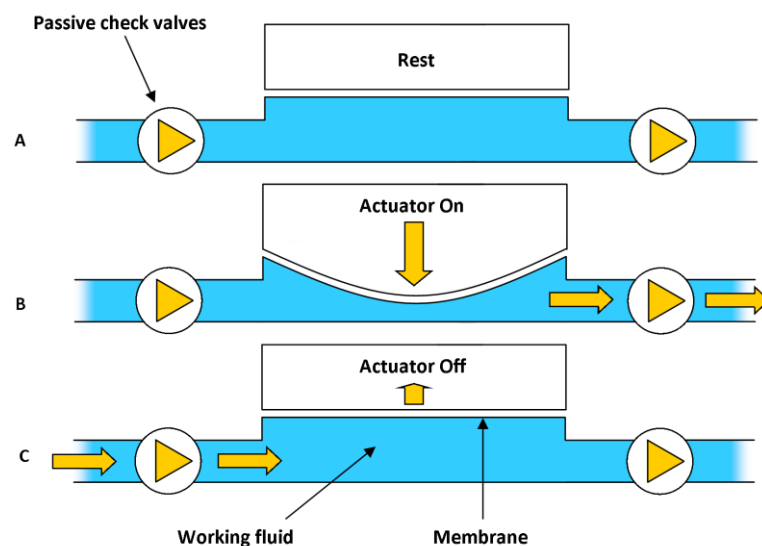


*Figure 3.5 – Basic operational principles employed by single-membrane reciprocating displacement micropump designs.*

As mentioned above, rectification can also be carried out by adaptations of the pump membrane or chamber, such as weirs in the pump chamber and/or an offset of the actuation force on the membrane, allowing a micropump that is composed of just a single membrane and chamber. For example, Tracey *et al* [58] presented a micropump with a single elongated pump chamber, made from PDMS using soft lithography, where the glass pump diaphragm had an offset piezoelectric actuator. Due to the offset, the actuator caused a wave to form in the diaphragm,

passing over a pair of weirs in the chamber that trapped the moving working fluid as the wave passed over them. The working principle is shown in *Figure 3.6*. The final device actually has two pump chambers, actuated by the same piezoelectric disc but pumping independent working fluids. Each pump could produce a flow rate of around 750  $\mu\text{l}/\text{min}$ , rising to 1400  $\mu\text{l}/\text{min}$  if the pump chambers were used in parallel on the same working fluid.

Perhaps the simplest types of membrane micropumps are peristaltic in action. These devices blur the definition of pump and valve – each membrane used is identical, and operates in series along a microfluidic channel. These designs bear a resemblance to linear-type macroscale peristaltic pumps. The initially activated membrane creates a seal or flow resistance, which is usually imperfect but enough to influence the flow direction. The subsequent sequential activation of the remaining pump membranes creates a directional flow. An advantage of this design is the dual-role of the membranes as both valves and pumps, which is useful in  $\mu\text{TAS}$  systems where space is at a premium. Another useful characteristic of these devices is they are not restricted by the direction of the rectification valves of single membrane pumps, and can create flow in either direction.

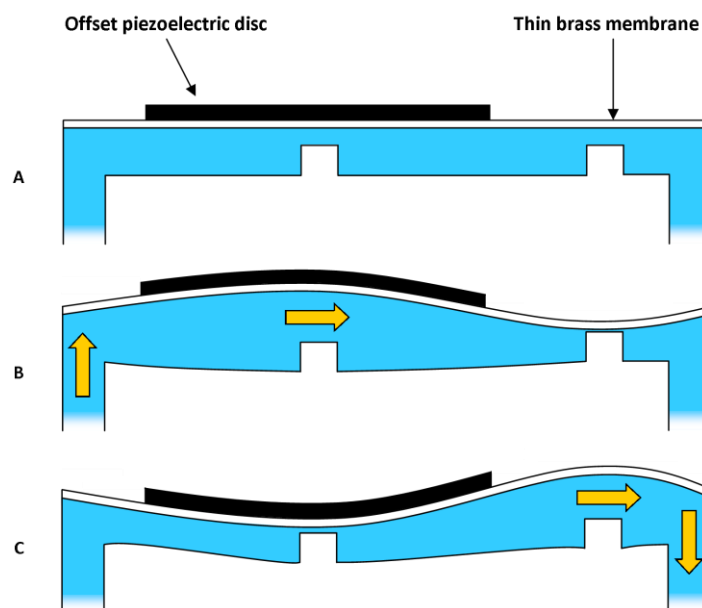


*Figure 3.6 – Working principal employed by device published by Tracey et al [58].*

Multi-membrane peristaltic polymer pumps are normally found with 3 active membranes, with thermopneumatic [59, 60], pneumatic [61-71], electromagnetic [72] and Braille display [73] actuation methods all reported. The earliest polymer multi-membrane peristaltic micropump in the literature is Unger *et al* in 2000 [70], who presented the first soft-lithography based microfluidics device. Since this paper there have been a relatively large number of such designs reported, perhaps due to the explosion in devices built using PDMS and soft lithography.

A good example of a polymer peristaltic membrane micropump can be found in Jeong *et al* [60], where a simple 3-membrane thermopneumatic device is reported. The device body and fluidics were fabricated by a mixture of PDMS multilayer soft lithography and machining techniques, whilst the microheaters required for the thermopneumatic operation were fabricated onto a glass base layer using micromachining. A diagram showing the operation of the pump can be seen in *Figure 3.7*. A maximum flow rate of 0.37  $\mu\text{l}/\text{min}$  was found at a frequency of 2 Hz. Interestingly, the same authors have also produced a very similar design actuated by pneumatic mechanisms [61], which could pump both air and water. Only the flow rate for air is reported, at 86  $\mu\text{l}/\text{min}$  at 3 Hz.

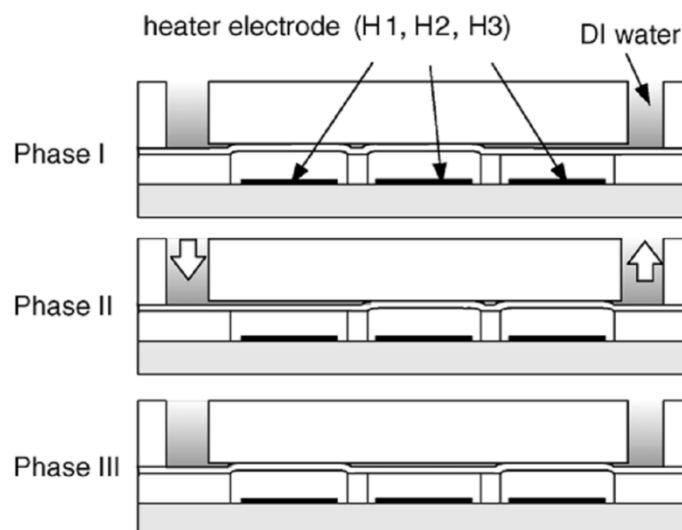


*Figure 3.7 - The working principle of a thermopneumatic 3-membrane peristaltic micropump, taken from Jeong et al [60].*



### 3.6.2 Reciprocating Piston

Although there are a large number of reciprocating piston macroscale pumps, there are very few micropumps utilising this design. This is because the ratio of the strength of a solid piston microstructure compared to the force required counteracting friction between the piston and the micropump body is not favourable at such small scales.

However, a pair of papers by Yamahata *et al* [3, 74] overcame this problem by using a ferrofluidic plug that can be moved externally using a rare earth magnet. The working principle can be seen in *Figure 3.8*.

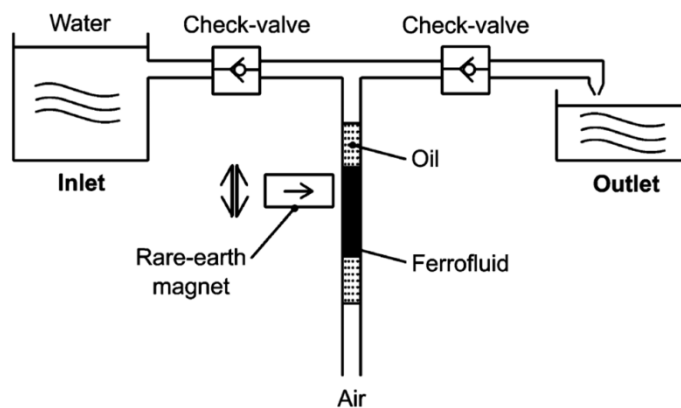


*Figure 3.8 – Working principle of a reciprocating displacement piston-based micropump, utilising a ferrofluidic plug. A mobile rare earth magnet is used to move the ferrofluid. Taken from Yamahata et al [3].*

### 3.6.3 Rotary

Rotary devices utilise a pair of gear structures intermeshing across a microfluidic channel. They are similar at first glance to dynamic centrifugal micropumps, but utilise a completely different mechanism to impart energy to the working fluid. The rotation of the gears traps pockets of the working fluid between the gear teeth, pushing it along the channel. An example of this design can be found in Dewa *et al* [75]. This rotary device is reported as the first microfabricated micropump not to use a membrane as part of its mechanism with all components of the micropump are fabricated by a sacrificial LIGA process. The gears were 200  $\mu\text{m}$  thick, with a pitch diameter of 1.392 mm, one with an embedded permalloy magnet used for actuation via an

external servo with its own magnetic bar. A flow rate of 350  $\mu\text{l}/\text{min}$  with a back pressure of around 13.7 kPa was reported at 5000 RPM. The device was self-priming and could also hold a 282 Pa vacuum on the inlet side.

#### 3.6.4 Air Detonators

The interesting concept of “air detonators” was outlined in Ahn *et al* [76] as part of their  $\mu\text{TAS}$  system. The detonators consist of a small pocket of trapped compressed air, separated from the device fluidics by a membrane, in this case fabricated from cyclic olefin copolymer (COC) using micromoulding techniques. A microhotplate is etched onto the membrane, and upon activation melts the membrane, releasing the compressed air and moving the working fluid. This by definition is a one-shot process. However, a series of detonators positioned correctly within the  $\mu\text{TAS}$  system can deliver a small sample from the insertion point to a reaction area with minimal power output – the energy required to melt the COC membranes was found to be only 100 mW for 350 ms.

### 3.7 Dynamic Micropumps

Some micropump designs do not rely on reciprocating movement, and instead apply pressure continuously to the working fluid. Dynamic micropumps do not require rectification or valves to produce directional flow, although rotary displacement pumps also share this characteristic.

#### 3.7.1 Centrifugal Micropumps

In the field of macro-scale pumps, by far the most common dynamic pump is the centrifugal, or vortex pump, used in applications such as air conditioning vents and high-throughput liquid pumps. However, their miniaturisation is limited by poor performance as the Reynolds number of the working fluid decreases, leading to bubble formation and loss of efficiency [57].

### 3.7.2 Special Effect Devices

There are a wide range of micropumps that have no moving parts, and instead use electrical effects to apply force to a working fluid. Krutzch and Cooper [56] grouped these pumps into a single category known as “special effect” pumps, as these mechanisms are less utilised in larger scale devices. The exact details of how these pumps operate will not be covered here, as they are not relevant to the theme of this review. However papers such as Laser and Santiago [57] explain in detail how these fluidic interactions are achieved and modelled.

Electrohydrodynamic (EHD) pumps operate by creating interactions with ions isolated in a dielectric (non-conducting) working fluid using electrodes in contact with the working fluid. There are several variations of mechanism used by these devices. Conducting EHD micropumps create flow by applying a voltage between a pair of electrodes suspended in the working fluid [77].

Electroosmotic devices do not require an ionic solution, and instead operate by working on the charged bilayer that forms when a liquid encounters a solid surface. Movement created in the boundary layer drags the rest of the working fluid along, creating an unusual looking flow that is faster at the boundaries than in the centre of the tube – the reverse profile of normal flow in a capillary. These designs often require high voltages and produce lower flow rates than electrodynamic pumps, albeit without the requirement of an ionic working fluid [78].

Magnetohydrodynamic devices operate by applying a magnetic field to a current-carrying working fluid, therefore creating movement by imparting a Lorentz force on the ions. Wang *et al* [79] fabricated a device from SU-8 and PDMS that used this principle.

## 3.8 Actuation Techniques

A wide range of actuation techniques are available to power micropumps and microvalves, ranging from the high-frequency, low deflection piezoelectric actuators to high deflection, low frequency techniques such as thermopneumatic devices. As the vast majority of

micropumps and microvalves are membrane-based, this section will concentrate on those actuation techniques used in this field. Although most all-polymer devices employ the low frequency, high deflection actuators, in some situations the high-frequency piezoelectric actuators are beneficial, and otherwise polymer devices can have the metal or silicon-based membrane integrated during fabrication. Other, more exotic actuation techniques such as cardiomyocyte-based devices are also discussed.

### 3.8.1 Piezoelectric

A piezoelectric material is a crystalline substance that has an asymmetrical crystal structure, and is polar i.e. it contains separated charges. *Figure 3.9* compares crystalline structures that exhibit no piezoelectric effect with those that do. When the material is at rest, the charge within the crystal is spread evenly, and the free charge exists as a series of dipoles within the material. However, when a pressure is applied to the crystal structure, the charge is forced into a dipole. This charge can be collected by a pair of electrodes across the piezoelectric crystal, should the electrodes be in the direction of the dipole created. This effect can also be reversed – if a DC voltage is applied across the electrodes, the material will deflect in a direction dependant on the polarisation plane of the crystal lattice [80].

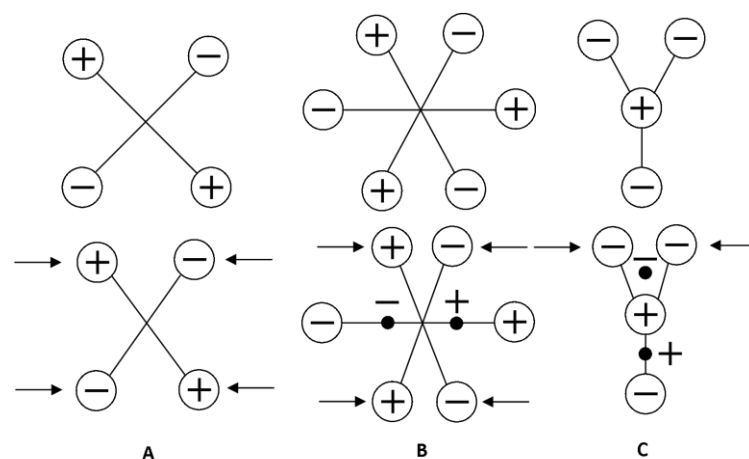


*Figure 3.9 - Effect of stress on different molecules: A—Centrosymmetric, stress produces no polarisation; B—Polarisation parallel to stress; C—Polarisation perpendicular to stress. Taken from Pointon et al.*

These principles have been used in the creation of microsensors and microelectrical mechanical systems (MEMS), either directly in strain gauges or as part of surface acoustic wave (SAW) devices [81]. Piezoelectric actuation was a common technique among early traditionally machined [82-84] and silicon-based micropump designs [85, 86]. There are two ways a piezoelectric disc can be used in micropump designs. Lateral drivers expand in a lateral direction compared to the membrane, causing the membrane to distort and deflect as it is stretched and contracted. Alternatively, the deflection can be set up perpendicular to the membrane, forcing it directly up and down. However, the rising use of elastomeric polymers for pump and valve membranes has relegated piezoelectric actuation to the sidelines in polymer micropump actuation, especially as designs increasingly become entirely polymeric in nature. As said above, thin polymer membranes are much more flexible than glass and silicon layers and require far less force applied to deflect a given distance, making them more suitable to lower-frequency drivers such as thermopneumatic and pneumatic actuators. However, when it comes to devices with glass or silicon membranes, piezoelectric actuation is the only driver that can produce enough force to deflect the material.

There are a number of polymer-based micropumps and microvalves that utilise a glass or silicon membrane deflected by a piezoelectric driver. The mechanism of the throttle valves reported in Johnson *et al* 2004 [54, 55] are described earlier in this review, and both the pump and throttle membranes are piezoelectrically actuated. Another notable paper is the previously mentioned stereolithography-based Carozza *et al* [22], which has a 10 mm piezoelectric disk on top of an 18 mm diameter, 0.1 mm thick brass membrane.

### 3.8.2 Magnetic

Magnetic actuation has been widely used to drive both micropumps and microvalves. Actuation normally involves some form of electromagnet interacting either with a rare earth magnet or a secondary electromagnet. However, devices have also been produced using movable magnets, or by using ferrofluids as the secondary magnetic material.

Dario *et al* [47] described the first polymer-based magnetically actuated micropump and microvalve. Their membrane microvalve actuation design consisted of a rare earth magnet connected on one side to a mobile core and on the other side to the valve membrane. The mobile core was located inside a stationary wire coil. Current was applied to the coil, causing the magnet and membrane to be deflected downwards, closing the valve. The micropump design was similar, but had a magnet on both sides of the mobile core, allowing a reciprocating movement to be produced by driving the coil with a square wave.

Bohm *et al* [6] produced a self-priming reciprocating displacement single membrane pump, with passive membrane hole valves. They actuated the pump membrane using both piezoelectric (discussed above) and electromagnetic methods. The magnetic actuation design consisted of an NdFeB magnet partially inserted into a wire coil, with spacers used to prevent the magnet moving too far into the coil. The pump was tested at a constant current of 100 mA, with the optimum pumping frequency for water being 50 Hz. Flow rates were similar to the piezoelectric version, at around 2 ml/min, but back pressures were lower at around 10 kPa with water. However, pump rates were found to be up to 40 ml/min with gas at a frequency of 400 Hz. This higher frequency and flow rate is possible due to the lower viscosity of gas compared to water, giving a system where the damping effect of the working fluid is far lower. Further work by the same lead author [87] gave a bi-stable magnetically actuated membrane microvalve. This employed an electromagnetic actuation system similar to that used in bi-stable relays and mechanical latches for hard drive read/write heads.

The magnetic material used for actuation can also be incorporated into the device membrane. As discussed earlier in the micromachining section, Khoo *et al* [26] produced a single-membrane reciprocating displacement pump with passive nozzle/diffuser valves. The final device has strips of a permalloy material (Ni80Fe20) located within the pump membrane, which allows deflection of the membrane via an external magnetic field.

Another design involves placing a small amount of magnetic material onto the actuated membrane. Santra *et al* [4] mixed Sm-Co powder with 10 wt.% Silastic T2 silicone, which was moulded into shape and glued onto the pump diaphragm. This resulted in a single membrane reciprocating displacement micropump with passive membrane hole valves, with a maximum flow rate with air of 257  $\mu\text{l}/\text{min}$  when driven by a 190 mA square-wave current at 3.0-4.5 Hz. The maximum pump pressure generated was calculated at around 1 MPa. The pump system could draw water along a channel whilst pumping air, but could not drive water directly due to damping effects and poor bubble tolerance.

### 3.8.3 Electrostatic

As magnetic actuation has become popular in polymer-based micropumps and microfluidic devices, it is perhaps surprising that there is only one electrostatically-actuated device in the literature. It was presented by Goll *et al* [88], and has been previously discussed as an active float microvalve. Electrostatic actuation has the advantage of being relatively simple, relying on the attraction of two opposite-pole electrodes, and it is thus easy to integrate into microscale systems. Unfortunately the voltage required is normally relatively high (around 150 V in Goll *et al*), and the deflection fairly small in comparison to other actuation mechanisms such as thermopneumatic. It is possible the niche for small-deflection devices, where the requirements for such high voltages are not problematic, has already been filled in this field by piezoelectric devices.

### 3.8.4 Pneumatic

Whereas most other actuators require only some form of electronics and a power source in addition to the device, pneumatic actuators rely on pneumatic pressure being provided from a separate source. This may be an air line, or in the case of portable devices a small macroscale air pump, along with high-speed pneumatic valves. This can make it difficult to directly compare pneumatically-actuated micropumps and valves with other devices that include integrated actuation. However, in situations where the pneumatic power is available, they can be effective devices, more so where the important characteristic of the device is small volume handling rather than portability. Perhaps unsurprisingly, nearly all pneumatic devices are membrane-based, and the membrane is normally a form of elastic polymer such as PDMS or other silicone rubber compounds.

An early example of a pneumatic device can be found in the previously mentioned Sjolander *et al* [36]. The microvalve presented is a good example of a general pneumatic device. A chamber containing the working fluid is separated from a secondary chamber by a thin membrane. The secondary chamber is pressurised and released to atmosphere sequentially, inflating and deflating the membrane into and out of the working fluid.

A wide variety of other pneumatic devices have been presented in the literature. Kim *et al* [89] presented a PDMS soft lithography fabricated  $\mu$ TAS system for cell culturing, featuring a pneumatic single membrane pump and a active membrane microvalves. The pump was rectified using hydrogel flap check valves. A number of other single-membrane pneumatic micropumps are also reported using polymer membranes, most utilising PDMS membranes [12, 90, 91], although polyimide [2], polypropylene [92] and acrylic [93] materials are also reported.

A large number of multiple membrane peristaltic pneumatic micropumps can be found in the literature, all after Unger *et al* [70]. All have also been fabricated from PDMS using soft lithography [62-64, 67-69]. Uniquely to pneumatically actuated devices of this type, actuation can



be carried out by a single actuator element. A series of papers by Huang *et al* [94, 95] and Wang *et al* [96] utilise a “serpentine pneumatic” actuation approach, where each pneumatic chamber is connected by a winding microchannel. A micrograph of the device in action can be seen in *Figure 3.10*. A pneumatic pulse is fed into the first chamber, which then passes to the second and third chamber in turn, deflecting each membrane in turn and creating a peristaltic action. The length of the serpentine channels between the chambers can be tuned to make the device more efficient. A maximum flow rate of 7.43  $\mu\text{l}/\text{min}$  was achieved with a pump rate of 9 Hz and a pneumatic pressure of 20 PSI (137.9 kPa).

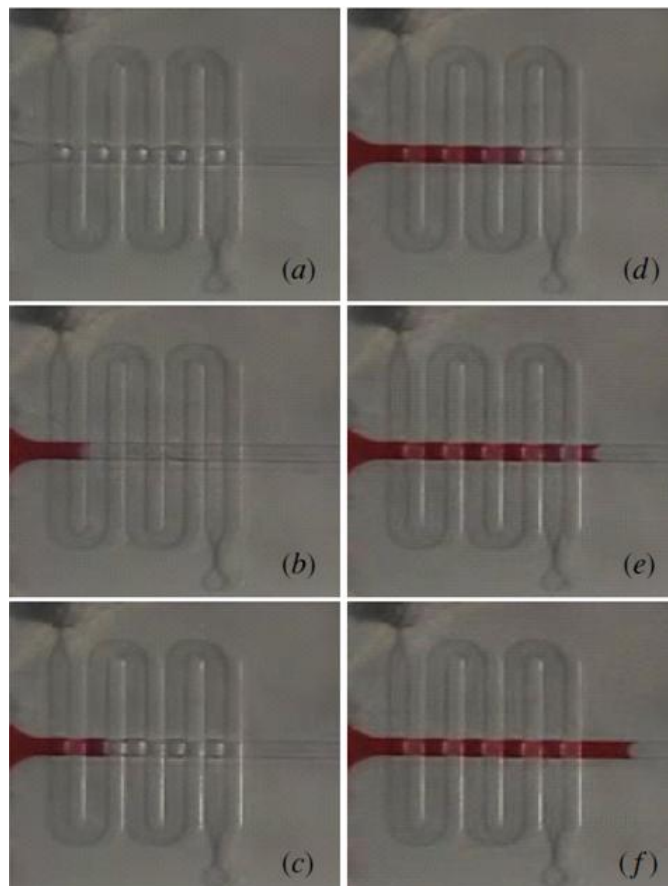


*Figure 3.10 – Multiple micrographs showing the sequential peristaltic action of the novel pneumatic micropump presented by Wang *et al* [96]. The serpentine-shape pneumatic microchannel is visible over the working fluid channel, separated by a thin PDMS membrane. A pulse of pneumatic pressure is fed into the device via the input port (upper) through to the outlet port (lower), deflecting each membrane created as the pneumatic channel passes over the working fluid channel. This causes a peristaltic movement in the working fluid, as shown in the movement of the red-coloured liquid in (a)-(f).*

### 3.8.5 Thermopneumatic

One of the most prevalent actuation methods for micropumps and microvalves utilises the pressure difference created by material expanding and contracting due to changes in its temperature. The majority are membrane-based, and use microhotplates to heat small volumes of air in a chamber separated from the working fluid by the pump membrane. An early example is Büstgens *et al* [1], a single-membrane micropump, the mechanism of which is discussed earlier in this chapter. The polyimide membrane is sandwiched between a pair of thermoplastically-moulded layers, with a titanium microhotplate sputtered and patterned directly onto the membrane. An interesting effect is observed due to the shape of the heater and tensional stress deliberately induced in the titanium during fabrication, where the membrane takes on a corrugated shape. This allows the membrane to deflect further for a given pressure.

Other devices integrate the microhotplate as part of the chamber rather than the membrane. Kim *et al* [28] present a single-membrane pump rectified by a pair of nozzle-diffuser elements, while Yoo *et al* [97] note a device similar in design but with a 3-membrane peristaltic mechanism. Both devices fabricated in PDMS using multilayer soft lithography on a glass substrate.

Wego *et al* [7] fabricated a device using purchased 70  $\mu\text{m}$  wire suspended across a chamber fabricated from a PCB board. The Kapton/Mylar membrane showed a deflection of 350  $\mu\text{m}$  for a peak input power of 10 W (mean power 1 W), giving a maximum reported flow rate and back pressure of 0.37 mL/min and 70 mbar respectively with passive membrane hole valves.

A number of devices use the expansion caused by the thermally-linked phase change of a solid or liquid substrate. Sim *et al* [98] produced a single-membrane micropump micromachined in glass with a thin silicone rubber membrane and passive flap valves. The actuation method used water heated to boiling point in a chamber under the membrane. The water vapour created expands, before contracting and condensing as the hotplate is turned off. The microhotplate used

was coated in silicon nitride to prevent electrolysis occurring. A maximum flow rate of 6  $\mu\text{l}/\text{min}$  and a backpressure of 10 PSI (68.9 kPa) were obtained.

A large number of thermopneumatic valves are reported in the literature. The majority use air as the expanding medium, with a few exceptions using paraffin wax. All are membrane-type valves. Papers by Henares *et al* [99] and Namasivayam *et al* [38] use peltier elements rather than microhotplates to provide the heat required by the system. Due to the high power requirements of peltier elements for heating/cooling compared to microhotplates, both devices employ non-air substrates to allow low-temperature valve control. Henares *et al* use a thermo-responsive polymer coating on the valving capillary that shrinks during heating to around 40°C. Namasivayam *et al* on the other hand used a hydrocarbon known as Vertrel, which has a low boiling point of 55°C.

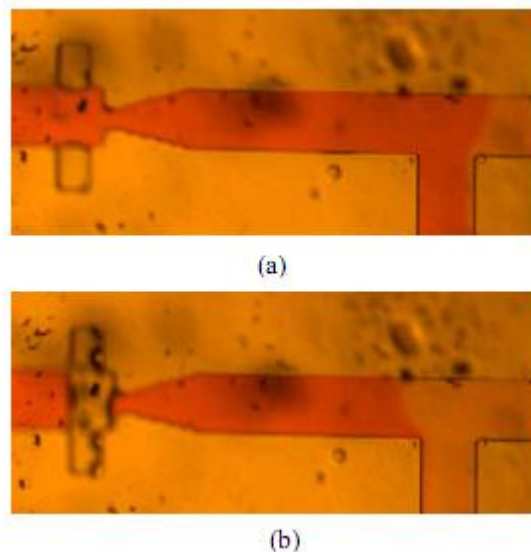
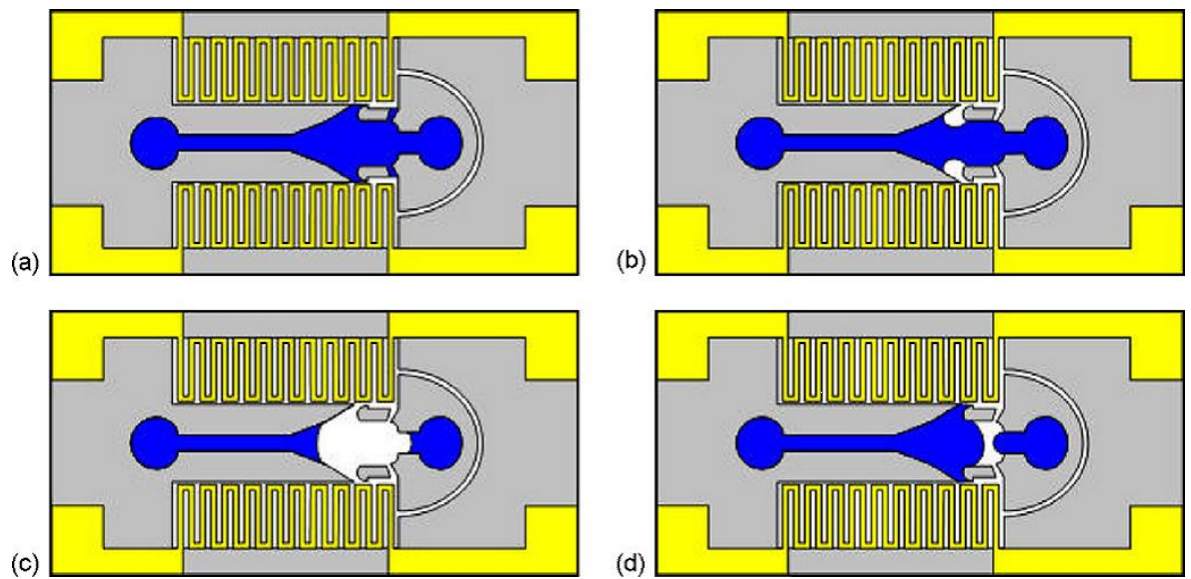


Figure 3.11 – Microvalve device presented by Xu *et al* [100]. (a) A pair of air pockets are trapped in microfluidic structures either side of a fluidic channel, just before a narrowing in the channel. (b) Localised heating by an upstream (left) microhotplate causes the expansion of the air, until the bubbles block the channel.

Another device using controlled bubble formation is found in Xu *et al* [100]. As shown in Figure 3.11, the microvalve detailed uses a pair of flanking air pockets, either side of, and just before the narrowing of a channel. A coil heater upstream of the valve was used to heat the air in both pockets, causing the air to expand and cross the channel, blocking flow. A relatively slow

reaction time of 25 s was recorded at a heater input of 0.31 W. Jun *et al* [101] presented a micropump based on a bubble caught within the working fluid. The principle of its actuation is shown in *Figure 3.12*. This interesting design uses surface tension effects to draw droplets of working fluid forward. Flow rates were very low, with a discharge/refill time of around 20 s and a stroke volume of around 110 nl. However, the maximum deviation in stroke volume was only around 3%, making it ideal for transdermal drug delivery where accuracy is paramount.



*Figure 3.12 – Working principle of thermopneumatic “trapped bubble” micropump presented by Jun et al [102]. The working fluid chamber is specifically shaped to take advantage of the surface tension effects present at small scales – the chamber, shown full of the blue working fluid in (a), is around 5 mm long, including the inlet and outlet nodes. In (b) the microheaters, seen on both sides of the working fluid chamber, are activated, expanding the air trapped within them. Ultimately this leads to the discharge stroke as the expanding bubbles meet across the chamber (c). Finally, the hotplates are deactivated, cooling the air which returns to its normal volume. Due to the shape of the chamber, the returning movement during the suction stroke (d) is mainly in the forward direction.*

### 3.8.6 Hydrogel

The precise definition of a gel is an evolving one, but is generally agreed to be a substance composed of a network of molecules that are linked via both chemical crosslinks and physical interactions within a solvent [103]. A hydrogel is simply a gel whose solvent is water. Hydrogels have a range of useful properties, such as the slow-release of drug molecules, and can in some cases absorb large amounts of water and subsequently expand. This expansion can be caused by exposure to fluid of a certain pH, or simply by exposure to water.

Hydrogels are normally used as an actuation material, however designs are limited by the slow response times associated with the material. The only polymer-based device in the literature that could claim to be a pump is found in Eddington *et al* [104]. This device consisted of a hydrogel actuated active membrane valve and a large chamber topped with a membrane, itself also actuated by a hydrogel. The main chamber would contain some form of drug for delivery once conditions were reached for the activation of the hydrogel. The valve was integrated to build up pressure within the main chamber after the activation of the hydrogel, allowing more efficient emptying of the chamber once the valve was opened. The device was one-shot, and intended for implantation into patients requiring drug dosage dependant on specific conditions within the body.

Most of the other designs found in the literature are active membrane type [49, 53, 105-109], which are more suited to hydrogel actuation in applications where response time is not critical and where the functioning of the device is designed to be dependent on external factors. Kim *et al* [11] reported an active plug valve actuated by a hydrogel post isolated from the working fluid. Also reported in the same paper was a pneumatically-actuated micropump with hydrogel passive flap valves fabricated by *in-situ* photopolymerisation, an example of how hydrogels can also be used as structural materials. The technique of *in-situ* photopolymerisation, discussed in more detail in the previous chapter, allows hydrogels to be injected into previously fabricated structures and cured precisely into complex planar shapes.

### 3.8.7 Cardiomyocytes

A small number of papers have reported devices actuated using biological methods, specifically using cardiomyocytes – muscle cells found in the heart. These cells have a natural rhythmic contraction, which can be used to deflect membranes and other actuator components. In all reported cases, these cells have been taken from neonatal rats. Tanaka *et al* [15] presented a reciprocating displacement membrane micropump with passive polyimide flap valves. The pump

was fabricated using soft lithography in PDMS, with the 10  $\mu\text{m}$  thick membrane made using membrane techniques. A layer of the cultured cells was placed over a push-bar, itself connected to the membrane, with the cell layer attached to the pump body. Contractions in the cell layer caused the membrane to deflect via force applied to the push bar. It was found that the pump frequency could be controlled by varying the temperature of the cell media, and a maximum flow rate of 2 nl/min was achieved.

Although these techniques are interesting in a technical sense, the potential applications are limited. The cells do not require an external power source, but do require to be immersed in media contain both nutrition and antimicrobial agents, which must be changed frequently. Ironically, the change of media in theory could be carried out by a separate micropump, or possibly by the movement of a secondary working fluid by the same pump. Cell survival is reasonable, with still functioning cells reported after a week by Park *et al* [110]. The flow rates reported however are quite low, and fabrication of the pumps requires access to biological facilities and skilled staff.

### 3.9 Conclusion

In this chapter, the mechanisms and actuation methods utilised by polymer-based micropumps and microvalves were discussed. A number of key themes can be drawn from this discussion. In the initial research into microfluidic devices, the materials utilised in the machining and micromachining fabrication steps normally utilised were limited to stiff and brittle substances such as glass, silicon and bulk metals. In these designs, piezoelectric actuation was most prevalent, as stiff-membrane based devices required high frequency, low deflection actuation to compensate for the brittle nature and lack of flexibility of the material.

However, the advent of polymer-based materials in the field allowed for the rise of actuation techniques such as pneumatic, thermopneumatic, magnetic and hydrogel-based, which give larger membrane deflections at the expense of the deflection force. Membrane materials

such as polyimide and PDMS are both flexible and strong, and can take advantage of the larger stroke volumes provided by these actuation techniques. Researchers can often be seen publishing microfluidic devices as test devices for new materials or fabrication techniques, and it could be said that the innovation is primarily in the fabrication and materials area, rather than in the design of the devices themselves.

It could be said that a large number of polymer-based micropump designs are not unique to polymer based devices, and could be achieved using conventional micromachining techniques and materials. This is most obvious in designs such as the special effect micropumps, and in design elements such as nozzle/diffusers, which are commonly used in both polymer and more conventionally micromachined devices. In these cases, the use of polymer materials is advantageous due to greater ease of fabrication offered by polymer techniques, as discussed in the previous chapter. However, there are some concepts such as gas permeation pumps and air detonators that hold promise in the field of lab-on-a-chip systems that are unique to polymer based designs. Polymer devices are ideal in applications such as medical devices, where the disposable nature of polymer materials means they can be incinerated after use, preventing infections by contaminated multi-use devices.

Through these chapters, micropump mechanisms utilising fabrication techniques such as micromachining have been referred to as “conventional”. However, as the materials and fabrication processes involving polymers have continued to advance over the last 15 years, the use of polymeric materials in microfluidic devices has become nearly ubiquitous. As a result, polymer devices have moved out of the shadow of their micromachined forefathers and can now be considered the convention rather than the exception.

### 3.10 References

- [1] B. Bustgens, W. Bacher, W. Menz, and W. K. Schomburg, "Micropump manufactured by thermoplastic molding," *MEMS94 Proc.*, pp. 18-21, 1994.
- [2] J. Cunneen, Y. C. Lin, S. Caraffini, J. G. Boyd, P. J. Hesketh, S. M. Lunte, and G. S. Wilson, "A positive displacement micropump for microdialysis," *Mechatronics*, vol. 8, pp. 561-583, Aug 1998.
- [3] C. Yamahata and M. A. M. Gijs, "Plastic micropumps using ferrofluid and magnetic membrane actuation," *Mems 2004: 17th IEEE International Conference on Micro Electro Mechanical Systems, Technical Digest*, pp. 458-461, 2004.
- [4] S. Santra, P. Holloway, and C. D. Batich, "Fabrication and testing of a magnetically actuated micropump," *Sensors and Actuators B-Chemical*, vol. 87, pp. 358-364, Dec 10 2002.
- [5] K.-P. Kamper, Dopfer, J., Ehrfeld, W. and Oberbeck, S., "A self-filling low-cost membrane micropump," *Proc. 11th Annual Int. Workshop on Micro Electro Mechanical Systems* pp. 432-437, 1998.
- [6] S. Bohm, W. Olthuis, and P. Bergveld, "A plastic micropump constructed with conventional techniques and materials," *Sensors and Actuators a-Physical*, vol. 77, pp. 223-228, Nov 2 1999.
- [7] A. Wego and L. Pagel, "A self-filling micropump based on PCB technology," *Sensors and Actuators a-Physical*, vol. 88, pp. 220-226, Mar 5 2001.
- [8] R. Truckenmuller, Y. Cheng, R. Ahrens, H. Bahrs, G. Fischer, and J. Lehmann, "Micro ultrasonic welding: joining of chemically inert polymer microparts for single material fluidic components and systems," *Microsystem Technologies-Micro-and Nanosystems-Information Storage and Processing Systems*, vol. 12, pp. 1027-1029, Sep 2006.
- [9] S. Shoji, M. Esashi, B. Vanderschoot, and N. Derooij, "A Study of a High-Pressure Micropump for Integrated Chemical Analyzing Systems," *Sensors and Actuators a-Physical*, vol. 32, pp. 335-339, Apr 1992.
- [10] M. L. Adams, M. L. Johnston, A. Scherer, and S. R. Quake, "Polydimethylsiloxane based microfluidic diode," *Journal of Micromechanics and Microengineering*, vol. 15, pp. 1517-1521, Aug 2005.
- [11] J. Y. Kim, J. Y. Baek, H. J. Chang, and S. H. Lee, "Aligning system for the in-situ microfabrication of multiple microstructures," *2005 3rd IEEE/EMBS Special Topic Conference on Microtechnology in Medicine and Biology*, pp. 315-318, 2005.
- [12] J. Kim, J. Baek, K. Lee, Y. Park, K. Sun, T. Lee, and S. Lee, "Photopolymerized check valve and its integration into a pneumatic pumping system for biocompatible sample delivery," *Lab on a Chip*, vol. 6, pp. 1091-1094, 2006.
- [13] I. Klammer, A. Buchenauer, G. Dura, W. Mokwa, and U. Schnakenberg, "Novel valve for microfluidic PDMS-based systems," *Mems 2008: 21st IEEE International Conference on Micro Electro Mechanical Systems, Technical Digest*, pp. 626-629, 2008.
- [14] T. T. Nguyen, V. K. Nguyen, Y. Yoo, and N. S. Goo, "A novel polymeric micropump based on a multilayered ionic polymer-metal composite," *IECON 2006 - 32nd Annual Conference on IEEE Industrial Electronics, Vols 1-11*, pp. 1652-1657, 2006.
- [15] Y. Tanaka, K. Morishima, T. Shimizu, A. Kikuchi, M. Yamato, T. Okano, and T. Kitamori, "An actuated pump on-chip powered by cultured cardiomyocytes," *Lab on a Chip*, vol. 6, pp. 362-368, Mar 2006.
- [16] T. R. Pan, W. Zheng, M. Lei, B. Cavanagh, and B. Ziaie, "A remotely adjustable check-valve array with an electrochemical release mechanism for implantable biomedical microsystems," *Boston Transducers'03: Digest of Technical Papers, Vols 1 and 2*, pp. 115-118, 2003.
- [17] H. Liu, A. A. O. Tay, S. Y. M. Wan, and G. C. Lim, "A low cost polymer based piezo-actuated micropump for drug delivery system," *Nsti Nanotech 2004, Vol 1, Technical Proceedings*, pp. 251-254, 2004.
- [18] A. Mercanzini, M. Bachmann, A. Jordan, Y. Amstutz, N. De Rooij, and N. Stergiopoulos, "A low power, polyimide valved micropump for precision drug delivery," *2005 3rd IEEE/EMBS Special Topic Conference on Microtechnology in Medicine and Biology*, pp. 146-149, 2005.
- [19] T. T. Nguyen, N. S. Goo, V. K. Nguyen, Y. Yoo, and S. Park, "Design, fabrication, and experimental characterization of a flap valve IPMC micropump with a flexibly supported diaphragm," *Sensors and Actuators a-Physical*, vol. 141, pp. 640-648, Feb 15 2008.
- [20] J. Loverich, I. Kanno, and H. Kotera, "Single-step replicable microfluidic check valve for rectifying and sensing low Reynolds number flow," *Microfluidics and Nanofluidics*, vol. 3, pp. 427-435, Aug 2007.



- [21] T. T. Nguyen, M. Pham, and N. S. Goo, "Development of a peristaltic micropump for bio-medical applications based on mini LIPCA," *Journal of Bionic Engineering*, vol. 5, pp. 135-141, Jun 2008.
- [22] M. C. Carrozza, N. Croce, B. Magnani, and P. Dario, "A Piezoelectric-Driven Stereolithography-Fabricated Micropump," *Journal of Micromechanics and Microengineering*, vol. 5, pp. 177-179, Jun 1995.
- [23] E. Stemme and G. Stemme, "A Valveless Diffuser/Nozzle-Based Fluid Pump," *Sensors and Actuators a-Physical*, vol. 39, pp. 159-167, Nov 1993.
- [24] Y. F. Su, W. Y. Chen, F. Cui, and W. P. Zhang, "Electro-magnetically actuated valveless micropump with two flexible diaphragms," *International Journal of Advanced Manufacturing Technology*, vol. 30, pp. 215-220, Sep 2006.
- [25] S. Kar, S. McWhorter, S. M. Ford, and S. A. Soper, "Piezoelectric mechanical pump with nanoliter per minute pulse-free flow delivery for pressure pumping in micro-channels," *Analyst*, vol. 123, pp. 1435-1441, Jul 1998.
- [26] M. Khoo and C. Liu, "A novel micromachined magnetic membrane microfluid pump," *Proceedings of the 22nd Annual International Conference of the IEEE Engineering in Medicine and Biology Society, Vols 1-4*, vol. 22, pp. 2394-2397, 2000.
- [27] J. H. Kim, C. J. Kang, and Y. S. Kim, "A disposable polydimethylsiloxane-based diffuser micropump actuated by piezoelectric-disc," *Microelectronic Engineering*, vol. 71, pp. 119-124, Feb 2004.
- [28] J. H. Kim, K. H. Na, C. J. Kang, and Y. S. Kim, "A disposable thermopneumatic-actuated micropump stacked with PDMS layers and ITO-coated glass," *Sensors and Actuators a-Physical*, vol. 120, pp. 365-369, May 17 2005.
- [29] N. B. Justis, D. Y. Zhang, and Y. H. Lo, "Integrated dynamic fluidic lens system for in vivo biological imaging," *Proceedings of the 26th Annual International Conference of the IEEE Engineering in Medicine and Biology Society, Vols 1-7*, vol. 26, pp. 1256-1259, 2004.
- [30] J. C. Yoo, M. C. Moon, Y. J. Choi, C. J. Kang, and Y. S. Kim, "A thermopneumatic-actuated polydimethylsiloxane microfluidic system," *2006 1st IEEE International Conference on Nano/Micro Engineered and Molecular Systems, Vols 1-3*, pp. 1379-1383, 2006.
- [31] J. C. Yoo, M. C. Moon, Y. J. Choi, C. J. Kang, and Y. S. Kim, "A high performance microfluidic system integrated with the micropump and microvalve on the same substrate," *Microelectronic Engineering*, vol. 83, pp. 1684-1687, Apr-Sep 2006.
- [32] J. C. Galas, V. Studer, and Y. Chen, "Characterization of pneumatically activated microvalves by measuring electrical conductance," *Microelectronic Engineering*, vol. 78-79, pp. 112-117, Mar 2005.
- [33] J. S. Go and S. Shoji, "A disposable, dead volume-free and leak-free in-plane PDMS microvalve," *Sensors and Actuators a-Physical*, vol. 114, pp. 438-444, Sep 1 2004.
- [34] J. S. Go, T. Yamazaki, M. Kanai, H. Sato, S. Kawakami, and S. Shoji, "A disposable, dead volume-free and leak-free monolithic PDMS microvalve," *Boston Transducers'03: Digest of Technical Papers, Vols 1 and 2*, pp. 643-646, 2003.
- [35] E. C. Jensen, W. H. Grover, and R. A. Mathies, "Micropneumatic digital logic structures for integrated microdevice computation and control," *Journal of Microelectromechanical Systems*, vol. 16, pp. 1378-1385, Dec 2007.
- [36] S. Sjolander and C. Urbaniczky, "Integrated Fluid Handling System for Biomolecular Interaction Analysis," *Analytical Chemistry*, vol. 63, pp. 2338-2345, 1991.
- [37] A. E. Guber, "Potential of microsystems in medicine," *Minimally Invasive Therapy & Allied Technologies*, vol. 4, pp. 267-275, Oct-Dec 1995.
- [38] V. Namasivayam, R. H. Liu, B. Towe, and P. Grodzinski, "Design of a self-contained 3D microvalve in PDMS," *Transducers '01: Eurosensors Xv, Digest of Technical Papers, Vols 1 and 2*, pp. 1228-1231, 2001.
- [39] M. Richter, Y. Congar, J. Nissen, G. Neumayer, K. Heinrich, and M. Wackerle, "Development of a multi-material micropump," *Proceedings of the Institution of Mechanical Engineers Part C-Journal of Mechanical Engineering Science*, vol. 220, pp. 1619-1624, Nov 2006.
- [40] S. Haeberle, N. Schmitt, R. Zengerle, and J. Ducree, "A centrifugo-magnetically actuated gas micropump," *MEMS 2006: 19th IEEE International Conference on Micro Electro Mechanical Systems, Technical Digest*, pp. 166-169, 2006.
- [41] S. Haeberle, N. Schmitt, R. Zengerle, and J. Ducree, "Centrifugo-magnetic pump for gas-to-liquid sampling," *Sensors and Actuators a-Physical*, vol. 135, pp. 28-33, Mar 30 2007.

- [42] R. Boden, M. Lehto, U. Simu, G. Thornell, K. Hjort, and J. A. Schweitz, "Polymeric paraffin micropump with active valves for high-pressure microfluidics," *Transducers '05, Digest of Technical Papers, Vols 1 and 2*, pp. 201-204, 2005.
- [43] G. S. Chung and K. B. Han, "Characteristics of a micromachined piezovalue combined with a multilayer ceramic actuator," *Microelectronics Journal*, vol. 38, pp. 690-694, Jun-Jul 2007.
- [44] T. Rogge, Z. Rummeler, and W. K. Schomburg, "Polymer micro valve with a hydraulic piezo-drive fabricated by the AMANDA process," *Sensors and Actuators a-Physical*, vol. 110, pp. 206-212, Feb 1 2004.
- [45] C. K. L. Tan, M. C. Tracey, J. B. Davis, and I. D. Johnston, "Continuously variable mixing-ratio micromixer with elastomer valves," *Journal of Micromechanics and Microengineering*, vol. 15, pp. 1885-1893, Oct 2005.
- [46] J. Fahrenberg, W. Bier, D. Maas, W. Menz, R. Ruprecht, and W. K. Schomburg, "A Microvalve System Fabricated by Thermoplastic Molding," *Journal of Micromechanics and Microengineering*, vol. 5, pp. 169-171, Jun 1995.
- [47] P. Dario, N. Croce, M. C. Carrozza, and G. Varallo, "A fluid handling system for a chemical microanalyzer," *Journal of Micromechanics and Microengineering*, vol. 6, pp. 95-98, Mar 1996.
- [48] J. Y. Baek, J. Y. Park, J. I. Ju, T. S. Lee, and S. H. Lee, "A pneumatically controllable flexible and polymeric microfluidic valve fabricated via in situ development," *Journal of Micromechanics and Microengineering*, vol. 15, pp. 1015-1020, May 2005.
- [49] J. Y. Park, D. J. Kim, S. R. Kim, J. Y. Baek, K. Sun, and S. H. Lee, "Microfluidic valve employing the pH-responsive hydrogel microsphere as an actuating element," *2006 International Conference on Microtechnologies in Medicine and Biology*, pp. 35-38, 2006.
- [50] J. Y. Park, S. H. Lee, and C. W. Liu, "Control of plural number of arrayed microvalves using pH-responsive hydrogel," *2007 IEEE Sensors, Vols 1-3*, pp. 1388-1391, 2007.
- [51] J. Y. Park, H. J. Oh, D. J. Kim, J. Y. Baek, and S. H. Lee, "A polymeric microfluidic valve employing a pH-responsive hydrogel microsphere as an actuating source," *Journal of Micromechanics and Microengineering*, vol. 16, pp. 656-663, Mar 2006.
- [52] C. Goll, W. Bacher, B. Bustgens, D. Maas, W. Menz, and W. K. Schomburg, "Microvalves with bistable buckled polymer diaphragms," *Journal of Micromechanics and Microengineering*, vol. 6, pp. 77-79, Mar 1996.
- [53] D. Kim, S. Kim, J. Park, J. Baek, S. Kim, K. Sun, T. Lee, and S. Lee, "Hydrodynamic fabrication and characterization of a pH-responsive microscale spherical actuating element," *Sensors and Actuators a-Physical*, vol. 134, pp. 321-328, Mar 15 2007.
- [54] I. D. Johnston, J. B. Davis, R. Richter, G. I. Herbert, and M. C. Tracey, "Elastomer-glass micropump employing active throttles," *Analyst*, vol. 129, pp. 829-834, 2004.
- [55] I. D. Johnston, M. C. Tracey, J. B. Davis, and C. K. L. Tan, "Microfluidic solid phase suspension transport with an elastomer-based, single piezo-actuator, micro throttle pump," *Lab on a Chip*, vol. 5, pp. 318-325, 2005.
- [56] W. C. Krutzch, Cooper, P., "Introduction: Classification and Selection of Pumps," (*New York: McGraw-Hill*), 2001.
- [57] D. J. Laser and J. G. Santiago, "A review of micropumps," *Journal of Micromechanics and Microengineering*, vol. 14, pp. R35-R64, Jun 2004.
- [58] M. C. Tracey, I. D. Johnston, J. B. Davis, and C. K. L. Tan, "Dual independent displacement-amplified micropumps with a single actuator," *Journal of Micromechanics and Microengineering*, vol. 16, pp. 1444-1452, Aug 2006.
- [59] M. Knight and J. House, "Design, fabrication, and test of a peristaltic micropump," *Microsystem Technologies-Micro-and Nanosystems-Information Storage and Processing Systems*, vol. 10, pp. 426-431, Aug 2004.
- [60] O. C. Jeong, S. W. Park, S. S. Yang, and J. J. Pak, "Fabrication of a peristaltic PDMS micropump," *Sensors and Actuators a-Physical*, vol. 123-24, pp. 453-458, Sep 23 2005.
- [61] O. C. Jeong, T. Morimoto, Y. Watanabe, and S. Konishi, "Peristaltic PDMS pump with perfect dynamic valves for both gas and liquid," *MEMS 2006: 19th IEEE International Conference on Micro Electro Mechanical Systems, Technical Digest*, pp. 782-785, 2006.
- [62] J. M. Berg, R. Anderson, M. Anaya, B. Lahlouh, M. Holtz, and T. Dallas, "A two-stage discrete peristaltic micropump," *Sensors and Actuators a-Physical*, vol. 104, pp. 6-10, Mar 15 2003.
- [63] C. H. Wang and G. B. Lee, "Automatic bio-sampling chips integrated with micro-pumps and micro-valves for disease detection," *Biosensors & Bioelectronics*, vol. 21, pp. 419-425, Sep 15 2005.

- [64] A. Dodge, E. Brunet, S. L. Chen, J. Goulpeau, V. Labas, J. Vinh, and P. Tabeling, "PDMS-based microfluidics for proteomic analysis," *Analyst*, vol. 131, pp. 1122-1128, 2006.
- [65] C. W. Huang, S. B. Huang, and G. B. Lee, "Pneumatic micropumps with serially connected actuation chambers," *Journal of Micromechanics and Microengineering*, vol. 16, pp. 2265-2272, Nov 2006.
- [66] F. C. Huang, C. S. Liao, and G. B. Lee, "An integrated microfluidic chip for DNA/RNA amplification, electrophoresis separation and on-line optical detection," *Electrophoresis*, vol. 27, pp. 3297-3305, Aug 2006.
- [67] C. F. Lin, G. B. Lee, C. H. Wang, H. H. Lee, W. Y. Liao, and T. C. Chou, "Microfluidic pH-sensing chips integrated with pneumatic fluid-control devices," *Biosensors & Bioelectronics*, vol. 21, pp. 1468-1475, Feb 15 2006.
- [68] H. Y. Tseng, C. H. Wang, W. Y. Lin, and G. B. Lee, "Membrane-activated microfluidic rotary devices for pumping and mixing," *Biomedical Microdevices*, vol. 9, pp. 545-554, Aug 2007.
- [69] C. H. Weng, W. M. Yeh, K. C. Ho, and G. B. Lee, "A microfluidic system utilizing molecularly imprinted polymer films for amperometric detection of morphine," *Sensors and Actuators B-Chemical*, vol. 121, pp. 576-582, Feb 20 2007.
- [70] M. A. Unger, H. P. Chou, T. Thorsen, A. Scherer, and S. R. Quake, "Monolithic microfabricated valves and pumps by multilayer soft lithography," *Science*, vol. 288, pp. 113-116, Apr 7 2000.
- [71] S. J. Lee, J. C. Y. Chan, K. J. Maung, E. Rezler, and N. Sundararajan, "Characterization of laterally deformable elastomer membranes for microfluidics," *Journal of Micromechanics and Microengineering*, vol. 17, pp. 843-851, May 2007.
- [72] T. R. Pan, E. Kai, M. Stay, V. Barocas, and B. Ziaie, "A magnetically driven PDMS peristaltic micropump," *Proceedings of the 26th Annual International Conference of the IEEE Engineering in Medicine and Biology Society, Vols 1-7*, vol. 26, pp. 2639-2642, 2004.
- [73] W. Gu, X. Y. Zhu, N. Futai, B. S. Cho, and S. Takayama, "Computerized microfluidic cell culture using elastomeric channels and Braille displays," *Proceedings of the National Academy of Sciences of the United States of America*, vol. 101, pp. 15861-15866, Nov 9 2004.
- [74] C. Yamahata, M. Chastellain, V. K. Parashar, A. Petri, H. Hofmann, and M. A. M. Gijs, "Plastic micropump with ferrofluidic actuation," *Journal of Microelectromechanical Systems*, vol. 14, pp. 96-102, Feb 2005.
- [75] A. S. Dewa, K. Deng, D. C. Ritter, C. Bonham, H. Guckel, and S. Massood-Ansari, "Development of LIGA-Fabricated, Self-Priming, In-Line Gear Pumps," *Transducers '97, 1997 International Conference on Solid-State Sensors and Actuators*, pp. 757-760, June 1997 1997.
- [76] C. H. Ahn, J. W. Choi, G. Beaucage, J. H. Nevin, J. B. Lee, A. Puntambekar, and J. Y. Lee, "Disposable Smart lab on a chip for point-of-care clinical diagnostics," *Proceedings of the IEEE*, vol. 92, pp. 154-173, Jan 2004.
- [77] T. Hasegawa, S. Toga, M. Morita, T. Narumi, and N. Uesaka, "Micro-flow control and micropump by applying electric fields through a porous membrane," *Jsme International Journal Series B-Fluids and Thermal Engineering*, vol. 47, pp. 557-563, Aug 2004.
- [78] Y. Takemori, S. Horiike, T. Nishimoto, H. Nakanishi, and T. Yoshida, "High pressure electroosmotic pump packed with uniform silica nanospheres," *Transducers '05, Digest of Technical Papers, Vols 1 and 2*, pp. 1573-1576, 2005.
- [79] L. S. Wang, L. Flanagan, and A. P. Lee, "Side-wall vertical electrodes for lateral field microfluidic applications," *Journal of Microelectromechanical Systems*, vol. 16, pp. 454-461, Apr 2007.
- [80] A. J. Pointon, "Piezoelectric Devices," *IEEE Proceedings-a-Science Measurement and Technology*, vol. 129, pp. 285-307, 1982.
- [81] J. W. Gardner, V. J. Varadan, and O. Awadelkarim, "Microsensors, MEMS and Smart Devices," *John Wiley & Sons Ltd, Chichester*, 2001.
- [82] L. J. Thomas and S. P. Bessman, "Prototype for an Implantable Micropump Powered by Piezoelectric Disk Benders," *Transactions American Society for Artificial Internal Organs*, vol. 21, pp. 516-522, 1975.
- [83] L. J. Thomas and S. P. Bessman, "Prototype for an Implantable Insulin Delivery Pump," *Proceedings of the Western Pharmacology Society*, vol. 18, pp. 393-398, 1975.
- [84] W. J. Spencer, W. T. Corbett, L. R. Dominguez, and B. D. Shafer, "Electronically Controlled Piezoelectric Insulin Pump and Valves," *IEEE Transactions on Sonics and Ultrasonics*, vol. 25, pp. 153-156, 1978.
- [85] H. T. G. Vanlintel, F. C. M. Vandepol, and S. Bouwstra, "A Piezoelectric Micropump Based on Micromachining of Silicon," *Sensors and Actuators*, vol. 15, pp. 153-167, Oct 1988.

- [86] J. G. Smits, "Piezoelectric Micropump with 3 Valves Working Peristaltically," *Sensors and Actuators a-Physical*, vol. 21, pp. 203-206, Feb 1990.
- [87] S. Bohm, G. J. Burger, M. T. Korthorst, and F. Roseboom, "A micromachined silicon valve driven by a miniature bi-stable electro-magnetic actuator," *Sensors and Actuators a-Physical*, vol. 80, pp. 77-83, Mar 1 2000.
- [88] C. Goll, W. Bacher, B. Bustgens, D. Maas, R. Ruprecht, and W. K. Schomburg, "An electrostatically actuated polymer microvalve equipped with a movable membrane electrode," *Journal of Micromechanics and Microengineering*, vol. 7, pp. 224-226, Sep 1997.
- [89] J. Y. Kim, H. Park, K. H. Kwon, J. Y. Park, J. Y. Baek, T. S. Lee, H. R. Song, Y. D. Park, and S. H. Lee, "A cell culturing system that integrates the cell loading function on a single platform and evaluation of the pulsatile pumping effect on cells," *Biomedical Microdevices*, vol. 10, pp. 11-20, Feb 2008.
- [90] W. H. Grover, A. M. Skelley, C. N. Liu, E. T. Lagally, and R. A. Mathies, "Monolithic membrane valves and diaphragm pumps for practical large-scale integration into glass microfluidic devices," *Sensors and Actuators B-Chemical*, vol. 89, pp. 315-323, Apr 1 2003.
- [91] A. Sin, C. F. Reardon, and M. L. Shuler, "A self-priming microfluidic diaphragm pump capable of recirculation fabricated by combining soft lithography and traditional machining," *Biotechnology and Bioengineering*, vol. 85, pp. 359-363, Feb 5 2004.
- [92] R. R. Miles and D. L. Schumann, "Thin-walled compliant plastic structures for meso-scale fluidic systems," *Micro- and Nanofabricated Structures and Devices for Biomedical Environmental Applications II*, vol. 3606, pp. 129-136, 1999.
- [93] W. Inman, K. Domansky, J. Serdy, B. Owens, D. Trumper, and L. G. Griffith, "Design, modeling and fabrication of a constant flow pneumatic micropump," *Journal of Micromechanics and Microengineering*, vol. 17, pp. 891-899, May 2007.
- [94] C. J. Huang, Y. H. Chen, C. H. Wang, T. C. Chou, and G. B. Lee, "Integrated microfluidic systems for automatic glucose sensing and insulin injection," *Sensors and Actuators B-Chemical*, vol. 122, pp. 461-468, Mar 26 2007.
- [95] S. B. Huang, M. H. Wu, Z. F. Cui, Z. Cui, and G. B. Lee, "A membrane-based serpentine-shape pneumatic micropump with pumping performance modulated by fluidic resistance," *Journal of Micromechanics and Microengineering*, vol. 18, pp. 1-12, Apr 2008.
- [96] C. H. Wang and G. B. Lee, "Pneumatically driven peristaltic micropumps utilizing serpentine-shape channels," *Journal of Micromechanics and Microengineering*, vol. 16, pp. 341-348, Feb 2006.
- [97] J. C. Yoo, M. C. Moon, C. J. Kang, and Y. S. Kim, "Thermopneumatic-actuated PDMS microvalve and micropump integrated with the same fabrication process," *Transducers '05, Digest of Technical Papers, Vols 1 and 2*, pp. 664-667, 2005.
- [98] W. Y. Sim, H. J. Yoon, O. C. Jeong, and S. S. Yang, "A phase-change type micropump with aluminum flap valves," *Journal of Micromechanics and Microengineering*, vol. 13, pp. 286-294, Mar 2003.
- [99] T. G. Henares, S. Funano, S. Terabe, F. Mizutani, R. Sekizawa, and H. Hisamoto, "Multiple enzyme linked immunosorbent assay system on a capillary-assembled microchip integrating valving and immuno-reaction functions," *Analytica Chimica Acta*, vol. 589, pp. 173-179, Apr 25 2007.
- [100] W. Xu, H. Xue, M. Bachman, and G. P. Li, "Virtual walls in microchannels," *2006 28th Annual International Conference of the IEEE Engineering in Medicine and Biology Society, Vols 1-15*, pp. 4245-4248, 2006.
- [101] D. H. Jun and S. S. Yang, "The influence of the pump chamber geometry on the characteristics of the micropump operated by surface tension," *2008 3rd IEEE International Conference on Nano/Micro Engineered and Molecular Systems, Vols 1-3*, pp. 665-668, 2008.
- [102] D. H. Jun, W. Y. Sim, and S. S. Yang, "A novel constant delivery thermopneumatic micropump using surface tensions," *Sensors and Actuators a-Physical*, vol. 139, pp. 210-215, Sep 12 2007.
- [103] J. P. A. Fairclough and A. I. Norman, "Structure and rheology of aqueous gels," *Annual Reports Section "C" (Physical Chemistry)*, vol. 99, pp. 243-276, 2003.
- [104] D. T. Eddington and D. J. Beebe, "A valved responsive hydrogel microdispensing device with integrated pressure source," *Journal of Microelectromechanical Systems*, vol. 13, pp. 586-593, Aug 2004.
- [105] Y. D. Gu, A. Baldi, B. Ziaie, and R. A. Siegel, "Modulation of drug delivery rate by hydrogel-incorporating MEMS devices," *2nd Annual International IEEE-Embs Special Topic Conference on Microtechnologies in Medicine & Biology, Proceedings*, pp. 406-409, 2002.

- [106] M. Lei, A. Salim, R. A. Siegel, and B. Ziaie, "A hydrogel-actuated microvalve for smart flow control," *Proceedings of the 26th Annual International Conference of the IEEE Engineering in Medicine and Biology Society, Vols 1-7*, vol. 26, pp. 2041-2044, 2004.
- [107] R. H. Liu, Q. Yu, and D. J. Beebe, "Fabrication and characterization of hydrogel-based microvalves," *Journal of Microelectromechanical Systems*, vol. 11, pp. 45-53, 2002.
- [108] C. W. Liu, J. Y. Park, Y. G. Xu, and S. Lee, "Arrayed pH-responsive microvalves controlled by multiphase laminar flow," *Journal of Micromechanics and Microengineering*, vol. 17, pp. 1985-1991, Oct 2007.
- [109] A. Baldi, Y. D. Gu, P. E. Loftness, R. A. Siegel, and B. Ziaie, "A hydrogel-actuated smart microvalve with a porous diffusion barrier back-plate for active flow control," *Fifteenth IEEE International Conference on Micro Electro Mechanical Systems, Technical Digest*, pp. 105-108, 2002.
- [110] J. Y. Park, I. C. Kim, J. G. Baek, M. S. Cha, J. S. Kim, S. H. Park, J. H. Lee, and B. K. Kim, "Micro pumping with cardiomyocyte-polymer hybrid," *Lab on a Chip*, vol. 7, pp. 1367-1370, 2007.

# Chapter 4

---

## 4 Additive Layer Manufacture

### 4.1 Introduction

Traditional engineering manufacturing methods are based on the removal of material from bulk to form a final component. In recent years however, another type of system has started to appear. These machines can be classified under a number of blanket terms, including “rapid prototyping” (RP), “rapid manufacturing” and “additive layer manufacture” (ALM) systems. The common characteristic these technologies share is they are additive in nature, and do not require human intervention during component fabrication [1].

Early machines using these technologies were generally regarded as rapid prototyping systems, and normally applications were not in the fabrication of end-user components. They were used purely in prototyping roles, for aesthetic demonstration of consumer devices under development and for “form-fit-and-function” testing, where novel components fabricated quickly purely to check they fit within an existing mechanism, before being fabricated “for real” using a traditional reductive technique. Another early application was in the production of sacrificial wax moulds for metal casting. Companies using rapid prototyping systems in such applications reported reductions in product production cycle time of between 30% and 90%. The car company Ford reported a 30% to 50% reduction in vendor quotes when using models produced using rapid prototyping; vendors felt more confident in their ability to produce a part when they have a solid representation of the component to assess [2].

However, the initial systems had a number of drawbacks over conventional reductive techniques, principally in the mechanical properties of the additive materials and in resolution. The move from rapid prototyping to rapid machining required these hurdles to be overcome, and

subsequent development of more engineering-grade additive materials has started to make rapid machining a reality.

There are a wide range of different ALM technologies available, ranging from laminated object manufacture systems that use thin sheets of material to build up large models, to stereolithography machines that use selective curing of photosensitive polymer resins. There is a similarly wide range of companies developing and marketing such systems, each with a number of customised additive materials. In this chapter, the field of commercial ALM systems will be reviewed within the context of their operating principles. Each technology will be assessed with a view to applications in micro electrical mechanical systems (MEMS) and microfluidics.

## 4.2 Classification of Additive Layer Manufacture

As mentioned above, all ALM systems share the same key characteristics: the final component is produced in an additive process, which is itself automatic, and requires no intervention during the fabrication steps. A large number of ALM systems have since been developed, all with their own strengths and weaknesses.

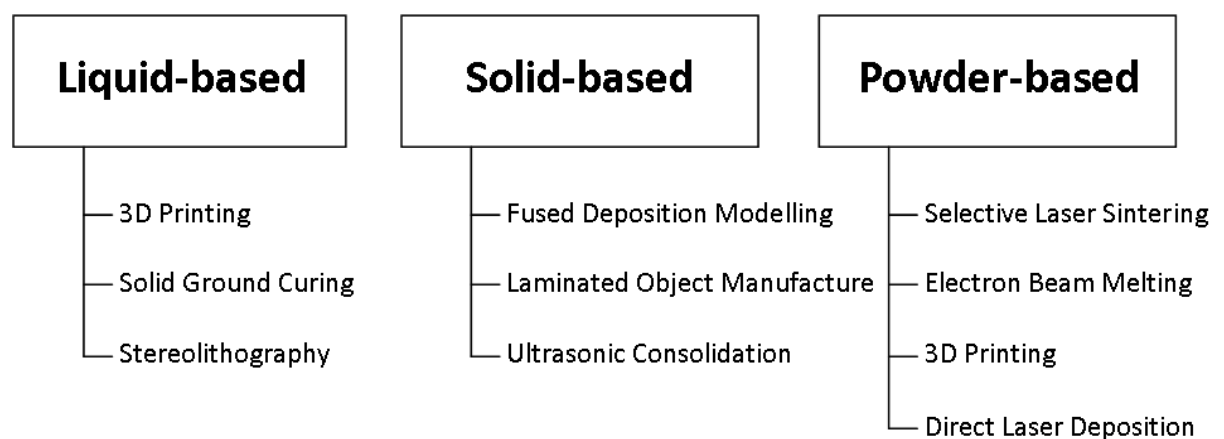


Figure 4.1 – Classification of additive layer manufacture (ALM) systems, as found in Liou 2008 [2].

However, all these systems can be described according to the pre-process material they work with: liquid-based, solid-based and powder-based [2]. Liquid-based ALM systems, such as stereolithography (SLA) and inkjet technologies, utilise a liquid pre-polymer mix, that is cured

using light, normally ultra-violet (UV). On the other hand, solid-based systems manipulate thin polymer or metal films to form 3D objects. Finally, powder-based ALM involves the fusing of sequential layers of metal or polymer powder using a laser. This classification is shown in *Figure 4.1*, and will be expanded upon in this section.

### 4.3 ALM System Selection

When choosing a rapid manufacturing system, there are a number of factors to take into consideration and a wide variety of manufacturers and machines available commercially. When looking towards microengineering, we are perhaps swimming against the tide, as the majority of systems are being tailored towards larger build envelopes, in order that larger or multiple components may be fabricated in a single build. Our applications however require a high resolution, which may be achieved by compromising the build volume. Material strength is key in some large-scale applications. However, most microengineering components are not subjected to a large amount of stress in use, and their scale means the material is proportionally stronger in any case. Of course, price is also a consideration.

Powder-based systems such as SLS apparatus possess reasonably high resolutions, but are unsuitable due to the excess material being nearly impossible to remove from internal microfluidic channels. Similarly, solid-based technologies such as LOM systems are unsuited to applications with internal features. FDM apparatus are popular in macroscale industrial roles, in part due to their use of proven engineering polymers. However, their resolution is not sufficient for microengineering applications, and small overhangs require solid supports.

This left the liquid-based SLA (stereolithography) and 3DP (3D printing) technologies. 3DP in theory has an excellent price/resolution point, but its mechanism requires supports for any given type of overhang, again precluding any use for internal structures. This leaves SLA technology. Although laser-based machines are capable of good resolutions and have large build volumes, their higher price makes them unattractive for use in research, as shown in *Table 4.1*.



Company	EnvisionTEC	3D Systems	3D Systems	3D Systems
System	Perfactory Mini Multi-Lens	Viper	iPro 8000	iPro 9000 XL
Price (£)	80,000	145,000	360,000	825,000
Mechanism	Projector	Nd:YVO <sub>2</sub> Laser	Nd:YVO <sub>2</sub> Laser	Nd:YVO <sub>2</sub> Laser
Resolution (µm)	20 x 20 x 25	75 x 75 x 20	130 x 130 x 50	130 x 130 x 50
Build Area (mm)	28 x 21 x 150	125 x 125 x 250	650 x 750 x 50	1500 x 750 x 550
Min Resin Fill(£)	~ 75	4,576	13,585	~ 110,000

*Table 4.1 – Costs of ownership for EnvisionTEC Perfactory Mini Multi-Lens projector-based MSL system, and a range of competing laser-based systems produced by 3D Systems. 3D Systems Viper and iPro 8000 “Min Resin Fill” cost based on lowest cost resin available and the quoted fill; iPro 9000XL resin capacity is not quoted directly and is therefore estimated in comparison to the iPro 8000 build envelope. Perfactory “Min Resin Fill” cost based on a full resin tray of 500 ml, and a cost of £225 per 1.5 litres. All costs listed without value added tax (V.A.T.) and were correct as of Q1 2010.*

The author believes that a good compromise can be found in the EnvisionTEC Perfactory range of systems. These SLA systems, described above, give resolutions of around 20-25 µm. Although laser-based SLA systems are capable of similar resolutions, they are also several orders more expensive. This is due to the much larger build volume afforded by the technique, which is not as critical in microengineering applications. Another major cost consideration is the fact that laser-based systems build down into a large resin vat. This means that the volume of resin required for operation is far higher, up to £200,000 for the iPro 9000 XL (price correct as of Q1 2010, excluding V.A.T.).

The materials used for stereolithography are polymer-based, making them suitable for disposable medical and biological applications, and the acrylate resins are generally biocompatible. Another vital aspect of the EnvisionTEC range is the ability to produce complex internal geometries easily, without a filler material. The solid support materials used by 3D printing, and the excess powder used to create internal cavities in powder-based techniques precludes both these devices from selection. Liquid based SLA systems require the removal of liquid resin from internal cavities post fabrication, which is much more practical at small scales. A closer look at the EnvisionTEC range of SLA systems follows in the following sections.

#### 4.4 Stereolithography

The original ALM systems were based on the process of stereolithography, which uses ultraviolet (UV) light to selectively cure photosensitive liquid into solid models. There are a number of ways this can be achieved, but the most common way is by using a laser to cure the top region of a vat of resin, a method also known as single-photon stereolithography. The basic principles of this system are shown in *Figure 4.2*. A Z-mobile build platform is immersed in a resin vat, and is positioned a short distance below the surface of the resin. The layer of resin between the top of the resin vat and the build platform is cured by rastering the laser across the area of resin to be cured, and this cured region sticks to the build platform. The Z-platform moves down a defined distance, and a sweeper bar moves across the layer. The process then repeats, with overlapping sections of each layer adhered together by chemical crosslinking.

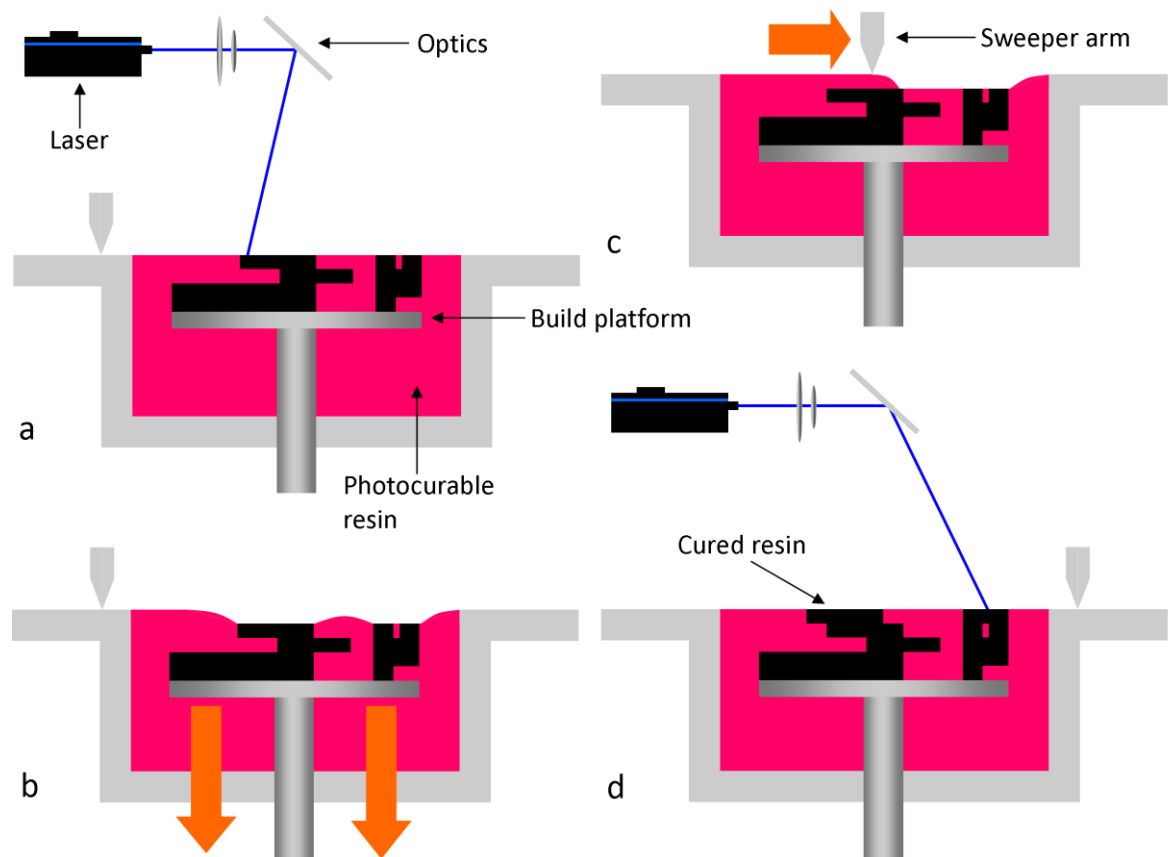


*Figure 4.2 - Steps used in laser-based stereolithography. In (a), a laser cures a thin layer of resin between previously cured resin and the top of the resin vat. The build platform subsequently lowers by a layer thickness (b), and a sweeper blade then moves across the surface of the resin and freshly cured polymer (c). The process then repeats, as the laser cures the next layer of resin (d).*

The first commercially available stereolithography system was produced by 3D Systems [3] in 1987; it was also the first commercial ALM system. As a result, 3D Systems hold the registered trademark for the acronym “SLA” (Stereolithography Apparatus). The company now offers a range of “solid imagine systems”, including SLA, fused deposition modelling and selective laser sintering devices. The SLA system range includes both the Viper™ and iPro™ devices, both of which use the method described above, sporting resolutions in the sub-200µm range.

This process is known as single-photon SLA as the photons emitted by the laser are used directly in the curing process, and are of the specific wavelength required by the photoinitiator to start the curing sequence. This limits this mechanism to curing only exposed resin at the top of the vat of resin, and therefore requires the sweeper mechanism to form a fresh layer of resin between the sequential laser exposures.

Another type of SLA, known as dual-photon, avoids this problem by exposing the resin selectively to photons of a secondary wavelength. The laser optical system is set up to allow focussing in 3D within the entire resin vat. Although the primary photon beam emitted by the laser is not of the correct wavelength to cure the resin, it is specifically set to excite a fluorescent component of the resin. When excited above a certain energy level, the fluorescent component releases a secondary photon which is specific to the resin photoinitiator. By carefully controlling the laser focus to only deliver sufficient primary photon (or energy) density in a small defined area, localised curing within the resin can be achieved. The process is outlined in *Figure 4.3*.

This technique has not yet been used in a commercial system. However, it has most famously been used by Kawata *et al* [3] in their brief communication in *Nature* journal in 2001. The paper presented a series of microstructures fabricated in a urethane-acrylate resin, cured using a primary infrared laser. One of the microstructures is shown in *Figure 4.4*.

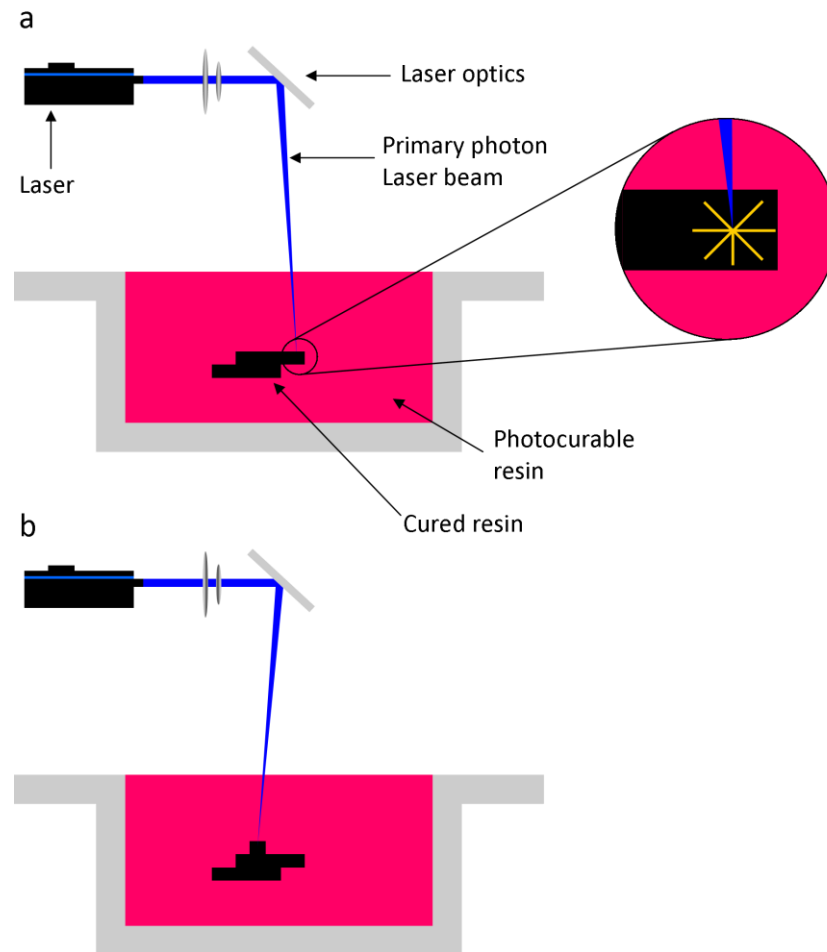


Figure 4.3 – Mechanism employed by dual-photon SLA systems. Main process details in text. Cut-out shows the secondary photon release (yellow) causing the initiation of curing within the resin.

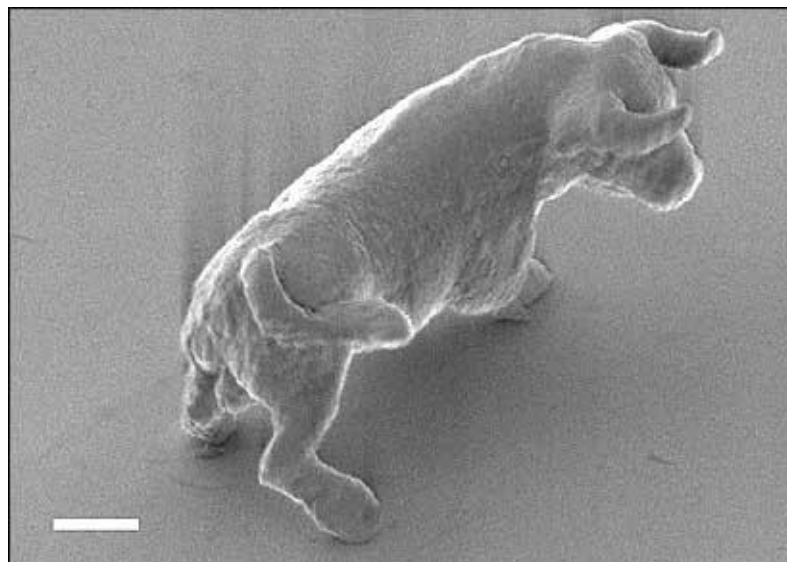


Figure 4.4 – “Micro-bull” presented by Kawata et al [3] in 2001. The structure is just  $10\ \mu\text{m}$  long and  $7\ \mu\text{m}$  tall (length scale bar =  $1\ \mu\text{m}$ ), and was fabricated using a urethane-acrylate resin exposed to a primary infra-red laser beam focussed in 3 dimensions. The resolution of the proprietary system was  $150\ \text{nm}$ , and the structure was fabricated over a period of 3 hours.

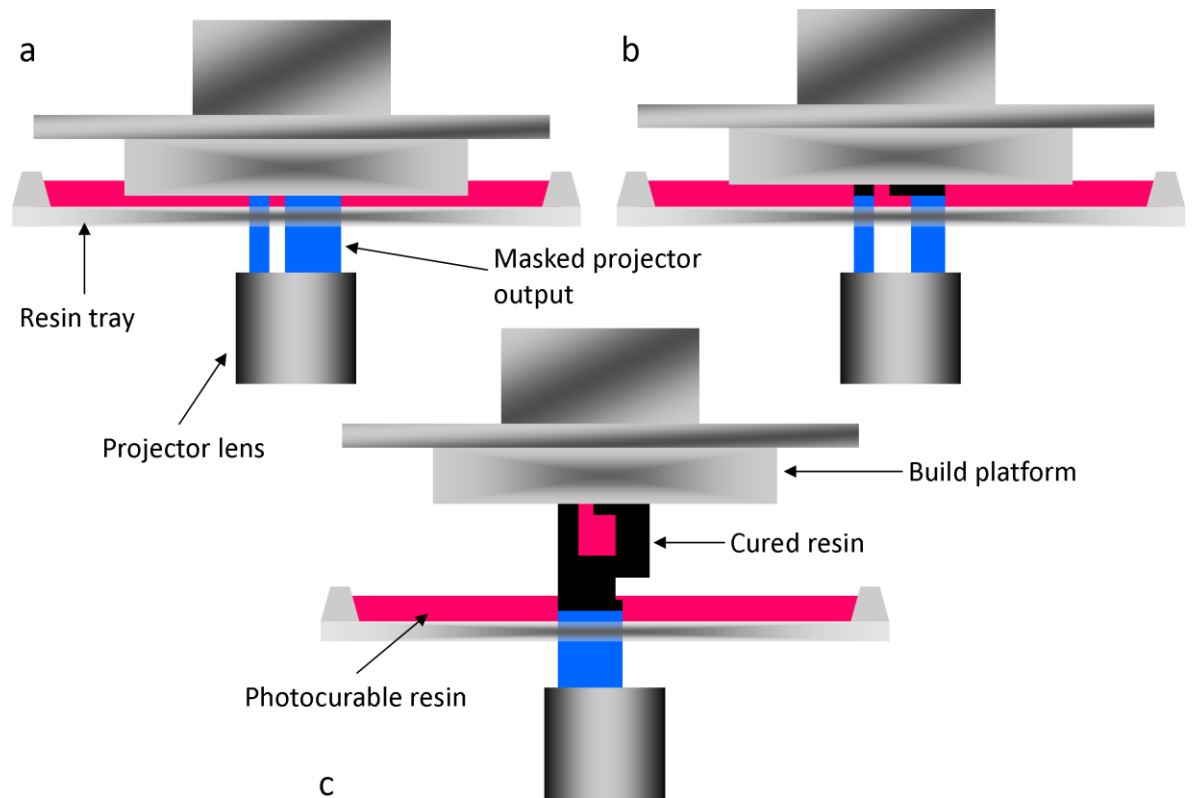


Figure 4.5 - Steps used in projector-based stereolithography. The Z-axis mobile build platform (a) moves down into the resin tray, creating a layer of resin which is subsequently cured by the masked output of a projector mounted below the tray (a). The build platform moves up one layer thickness, and the process is repeated (b). This sequence is repeated until the final build rises out of the resin tray (c).

A different single-photon mechanism is used by EnvisionTEC's series of Perfactory® SLA systems [4]. The Perfactory® range uses the output of Digital Light Processing (DLP) projectors, rather than lasers, to cure photosensitive resins. The technology behind the DLP projectors is discussed later in this chapter. At a basic level the mechanism can be seen as an inverse of the normal SLA process, and is shown in Figure 4.5. Instead of the resin layer for curing being formed between the top of a large vat of resin and a build platform, it is formed between the build platform and the bottom of a shallow transparent resin tray. The projector is fixed below the resin tray, and is focussed onto the gap between the build platform and the resin tray. The projector outputs sequential masked bitmaps for each fabricated layer, with the build platform moving up one layer thickness between each exposure, carrying the previously cured resin. This design has the dual cost advantages of not requiring expensive laser devices and optics, along with requiring far less resin in the build tray, reducing material costs. The EnvisionTEC range of SLA systems is

also summarised in *Table 4.2*. Although a number of other systems are advertised on the company's website, these are derivative of those systems listed in the table, targeted at specific applications such as dentistry and sacrificial casting.

One disadvantage of single-photon SLA systems is the handling of overhangs. Every fabricated layer must have some form of connection to the build platform; it will otherwise not travel with the rest of the fabricated component when the build platform moves. In order to allow the fabrication of overhangs, separate support structures can be generated by specialised CAD software such as Materialise Magics [5], which analyses the 3D model for unsuitable overhang features that require support, and creates the support structures.

Support structures in SLA systems are designed to be mechanically weak, but are strong enough to allow the overhang fabrication. This weakness is useful in post processing, as the support structures are easy to remove from the build. However, support structures may also be required for internal overhangs in monolithic builds, but cannot be removed after fabrication. As a result, certain internal structures may have fabrication faults, and consideration may be needed towards the splitting of the part into multiple builds to avoid this problem. Further discussion of support structures used in other ALM systems can be found later in this section, with detailed discussion of those structures used in the EnvisionTEC range of machines in the relevant section towards the end of this chapter.

A subset of more recently developed SLA systems are known as microstereolithography (MSL) devices. These systems are defined by their higher pixel resolution, normally below 100 micron. However, it could be said that this definition is no longer required, as nearly all commercially available SLA systems from 3D Systems and EnvisionTEC could be classed as MSL apparatus. The next major boundary is therefore nanostereolithography (NSL), with sub-micron resolutions.

Although these systems differ only in resolution to standard SLA machines, in practice their use and applications differ [6]. Often high resolutions come at the price of job throughput and build area; for example, several of the 3D Systems devices offer a “high definition” mode that sacrifices build area to achieve smaller feature sizes. In the projector-based EnvisionTEC systems, the output of the projector is simply focused onto a smaller area to achieve the same effect. It has also been noted that although support structures are still required for undercutting structures, it is needed less for MSL systems as small horizontal structures being produced are able to self-support. The relative viscosity of the resin at such small scales also helps hold fabricated microstructures in place.

One major disadvantage of stereolithography is in the material properties of the cured resins. As materials have to be blended in such a way that they are photocurable, and the monomers used must be liquid when uncured. As a result, the material properties of the cured material are often not ideal. Material costs also tend to be quite high compared to other systems. Furthermore, freshly fabricated material removed from SLA machines is normally only around 80% cured, and thus post-curing is required in a UV lightbox. Finally, machine calibration and initial setup can be time consuming.

Despite these drawbacks, it is clear that no other ALM mechanism outside of liquid-based 3D printing offers the potential resolution of SLA systems. The resolution is limited only by the focus ability of the optics utilised, and the material strength issues are less of a problem at the scales required in micro- and nanostereolithography applications.

## **4.5 EnvisionTEC**

### **4.5.1 Company Profile**

EnvisionTEC [4] was formed in 2002 in Marl, Germany, and have since developed and marketed a range of unique Digital Light Processing™ (DLP) projector-based SLA systems. They have also developed a range of acrylate, wax and epoxy based rapid manufacture materials. EnvisionTEC has focused its research into 2 main markets: medical applications, such as hearing aid earpieces and dental crowns, and the rapid production of sacrificial wax-based components for the jewellery industry. According to its own literature, the company enjoys a 60% market share in the hearing aid earpiece market, along with a 50% share of the jewellery industry's market for rapid manufactured wax moulds [7]. However, it also produces machines targeted at general industrial rapid prototyping and machining, toys, animation and tissue engineering.

### **4.5.2 ALM System Range**

The EnvisionTEC range of SLA systems can be divided into 3 categories. The first is the only EnvisionTEC developed system not to use a projector – the Perfactory® 3D-Bioplotter. This system instead uses fused deposition modelling (FDM) techniques, as used by a large number of EnvisionTEC's competitors. The system has been developed for use with biocompatible materials, such as biodegradable polyesters, for use in tissue engineering applications.

The PerfactoryXtreme® and PrefactoryXede® systems are very similar in mechanism to laser-based SLA devices. Developed comparatively recently, they employ the large resin vat used in the SLA devices produced by 3D Systems. However, instead of using a laser to cure the resin, a projector is positioned above the resin, focused down onto a Z-mobile build platform. These systems have advantages in acquisition costs over laser-based systems, and are able to produce much larger parts than the other projector-based EnvisionTEC systems. However, this comes at a price premium over the other machines in EnvisionTEC's range.



	Projector resolution (Pixels, X/Y)	Native resolution ( $\mu\text{m}$ , X/Y/Z)	Build area (mm, X/Y/Z)	ERM
Perfactory® Standard Zoom	1400 × 1050	86 × 86 × 25	120 × 90 × 230	✓
Perfactory® Mini Multi-Lens	2800 × 2100	42 × 42 × 15	84 × 63 × 230	✓
Perfactory® Mini Multi-Lens (2007)	1400 × 1050	20 × 20 × 25	28 × 21 × 230	✓
Perfactory® Desktop	1024 × 768	40 × 40 × 35	40 × 30 × 100	
PerfactoryXede®	2100 × 1400	128 × 128 × 25	457 × 304 × 508	✓
Ultra	1600 × 1200	158 × 158 × 20	254 × 190 × 203	✓
Perfactory® 3D Bio-Plotter™	-	50 × 50 × 50	300 × 300 × 300	

*Table 4.2 – Summary of the range of EnvisionTEC rapid manufacture SLA systems. In the case of systems with multiple resolution options, the highest resolution system specification is shown. Additional derived options listed on the company website are simply application-targeted versions of the machines above – see text for further information. The specification of the 2007 Perfactory® Mini Multi-Lens used in the Sensors Research Laboratory. ERM = Enhanced Resolution Module; DSP = Digital Shell Printer (hearing aid industry specification).*

The final group contains the Standard, Mini Multi-Lens, Desktop and Ultra systems, in where the projector sits below a transparent tray containing the photosensitive resin. The mechanism used by these systems has been described previously, and is outlined in *Figure 4.5*.

A summary of the EnvisionTEC range of SLA systems is shown in *Table 4.2*. There is a variety of variations on each system, with derived machines either having different options in terms of build area and resolution, or are set option packs aimed at specific applications such as dental or the jewellery industry. Both the Desktop and Standard Zoom Perfactory® systems have “Digital Dental Printer” (DDP) and “Digital Shell Printer” (DSP) variations, target at the rapid manufacture of dental moulds and hearing aid components respectively. The EnvisionTEC Aureus is a Perfactory® Desktop unit with a higher resolution projector aimed at the jewellery industry, whilst the Perfactory® Standard UV option is fitted with optics capable of outputting higher frequency ultraviolet light, allowing the curing of the specific UV materials discussed in more detail later in this section. Finally, the PerfactoryXede® has a lower-resolution sibling known as the PerfactoryXtreme®.

#### 4.5.3 Digital Light Processing Technology and the DMD Chip

All EnvisionTEC SLA systems are based on high-resolution DLP black and white projectors. DLP technology was developed in 1987 by Texas Instruments, and employs a digital mirror device (DMD) [8]. This chip consists of up to 2 million individual microscopic mirrors in a grid, each of which is mounted on a microhinge. These microhinges allow the angle of the mirrors relative to an incident light source to be varied into either an “on” or “off” position via an electrostatic actuation system. Mirrors in the “on” position reflect the incident light towards the output optics, generating a white pixel; mirrors in the “off” position reflect the incident light away from the optics, resulting in a black pixel. The mirrors can however be switched between the two states at around 2 kHz, allowing a 1024-colour greyscale to be produced, with a mirror switching at 50% duty cycle outputting a grey in brightness half way between white and black.

DLP chips are available in either 1- or 3-chip devices. In a single chip device, the input white light, produced by a high-performance bulb, is filtered through a filter wheel that uses a series of both primary and secondary colours in sequence. The filter wheel is synchronised with the DLP chip, and the activity of each mirror on each filter pass is dependent on the levels of each filter colour in the final output pixel. Due to the high speed switching, the output image appears as a moving colour image by the human eye. Devices using this DLP mechanism are generally found in consumer devices such as high definition projection televisions, business projectors and home theatre systems, and are capable of creating up to 16.7 million separate colours (“high colour”). An additional filter is used by all DLP projection devices to prevent any non-visible radiation in the input beam reaching and damaging the chip. The EnvisionTEC SLA systems use single-chip DLP projectors without the colour filters, as only a black and white image is required. This does not mean that the mirrors are used in only “off” and “on” states continuously, as the mirror modulation is used in the flux calibration of the focused light output.

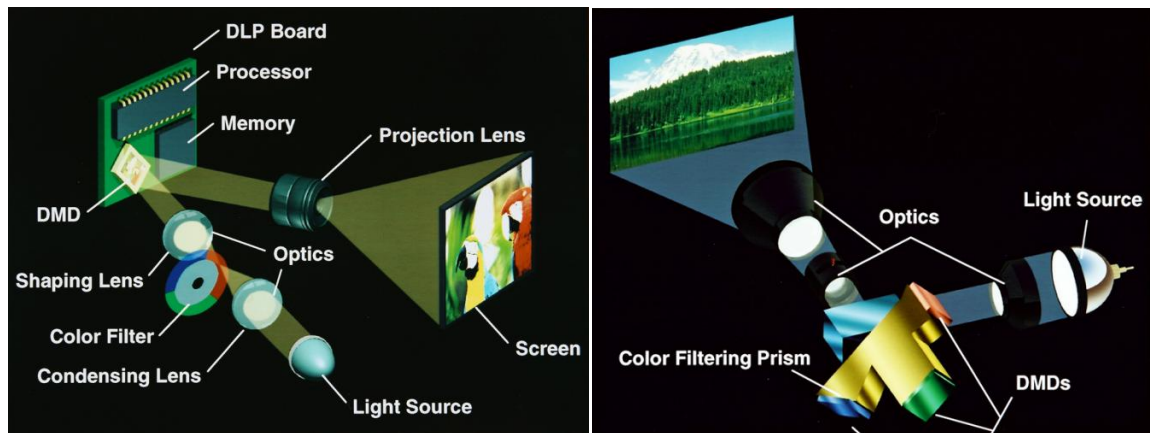


Figure 4.6 – Comparison of (a) single chip and (b) 3-chip DLP projection systems. Taken from DLP.com [9].

Higher-end DLP projection devices, such as cinema projectors, use a 3-chip approach. White light from the input source is split into the primary colours using a prism. Each of the 3 primary colour beams is focused onto its own DLP chip. The output from the chips is then recombined to form the final full colour image. This mechanism produces a brighter, higher quality image, and produced an enhanced colour gamut of 35 trillion colours (“deep colour”). The differences between single- and 3-chip DLP systems are shown in *Figure 4.6*.

#### 4.5.4 Enhanced Resolution Module (ERM)

All EnvisionTEC systems employing a projector system, with the exception of the Desktop series, have an optional component called an enhanced resolution module (ERM). This system allows two masks to be generated for each layer to be fabricated, the second with the pixel grid shifted half a pixel width across and down in the X- and Y-axes respectively.

The ERM mode does not change the resolution of the projector; the smallest theoretically feature size achievable is still one pixel. However, the pixel placement accuracy is doubled, allowing smoother component edges where such edges are not parallel to the pixel matrix, and allowing non-exposed areas theoretically half the diameter of the original system. The advantages and limitations of this system are shown in *Figure 4.7*.

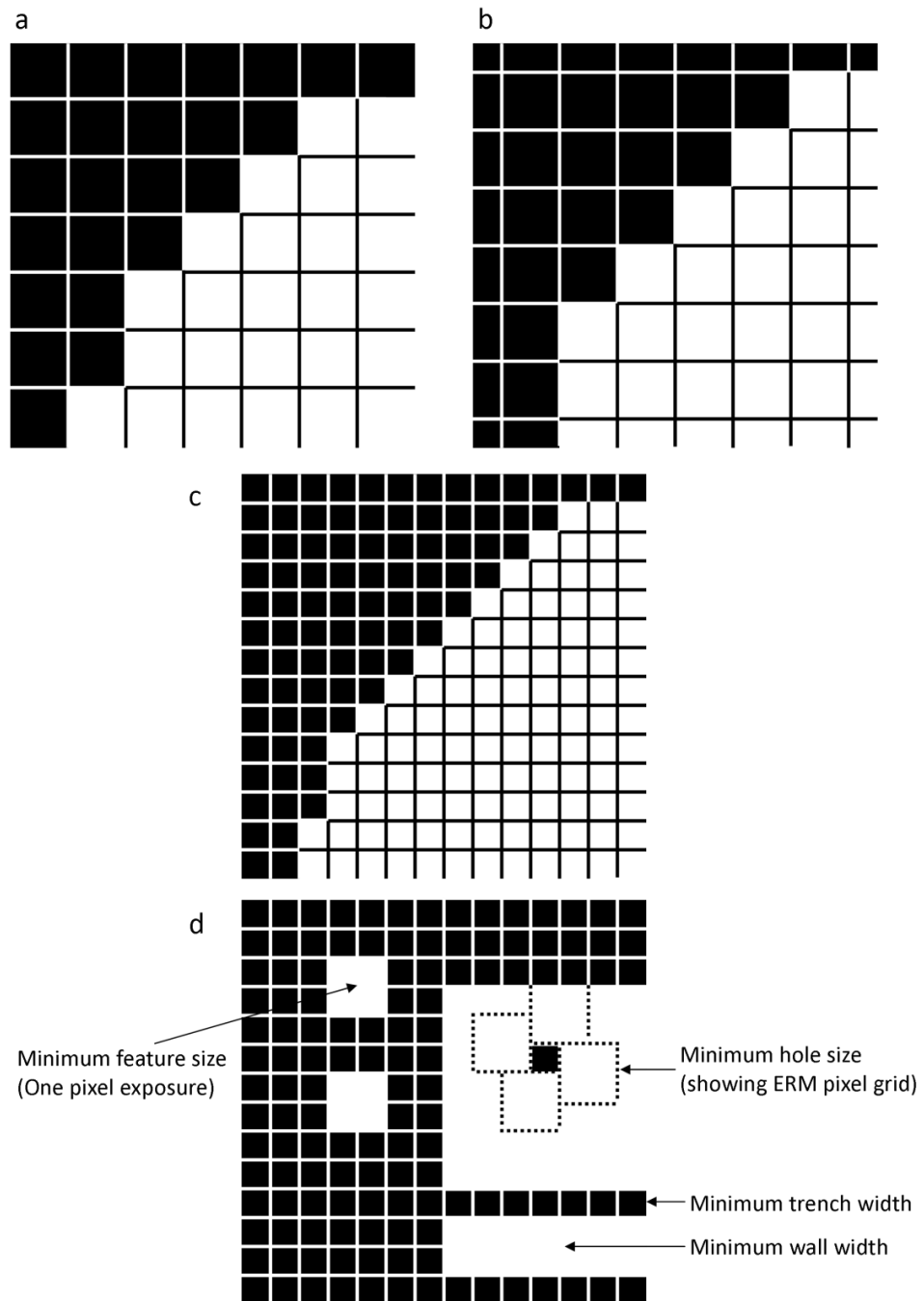


Figure 4.7 – Demonstration of the effect of the enhanced resolution module (ERM) fitted as an option on a number of EnvisionTEC Perfactory ALM systems. (a) shows the image mask generated for a layer in a build processed by the EnvisionTEC Perfactory RP software. (b) shows the complementary mask produced for the ERM mode, with the pixel mesh offset diagonally by half a pixel diagonal width. (c) shown the composite image of (a) and (b), giving a smoother edge. (d) shows the limitations of the system, with the minimum solid feature size still being one pixel (white squares, top left), whilst the theoretical hole size is  $\frac{1}{4}$  the area (black squares, middle right), which can be extended to decrease the minimum trench width and minimum wall width (lower right).

## 4.6 Additive Layer Materials

EnvisionTEC have developed a range of photocurable materials, aimed at applications including general prototyping, dentistry and sacrificial casting. The materials tested by the Sensors Research Laboratory are outlined in *Table 4.3*. The system was purchased in order to produce high precision, low-head space customisable sensor covers, the vast majority of which are produced in R11, as it is a general purpose prototyping material. In reasonably large bulk, over around 1 mm<sup>2</sup>, it is a relatively stiff, non-brittle material. However, in smaller features it can become weak, although it retains enough strength to retain some elastic properties.

<b>Material Name</b>	<b>Tensile Strength (MPa)</b>	<b>Young's Modulus (MPa)</b>	<b>Hardness (Shore)</b>	<b>Application</b>
<i>R11</i>	<i>49.7</i>	<i>-</i>	<i>86</i>	<i>General prototyping</i>
<i>PIC100</i>	<i>16.8</i>	<i>-</i>	<i>69</i>	<i>Sacrificial casting</i>
<i>eShell 200</i>	<i>57.8</i>	<i>2,400</i>	<i>83</i>	<i>Hearing aids</i>
<i>RCP25 Nanocure</i>	<i>46</i>	<i>4,890</i>	<i>93.1</i>	<i>General prototyping</i>

*Table 4.3 – Summary of materials evaluated by the Sensors Research Laboratory using the EnvisionTEC Perfactory Mini Multi-Lens rapid manufacturing system. Data taken from EnvisionTEC data sheets [10].*

eShell 200 and RCP25 Nanocure are both stronger bulk materials, but are too brittle to use in situations where flexibility is advantageous. Both are also significantly more viscous in their uncured form, with Nanocure in theory requiring a heated resin tray in order for the resin to keep a useable consistency. PIC100 was deemed as a too soft material for microengineering applications, which is not surprising as it is a wax-based material that it targeted at sacrificial casting applications. As a result of both the material properties and practical experience of producing parts with the materials, R11 was deemed the most promising resin for microengineering applications.

## 4.7 SLA System Operations

The Sensors Research Laboratory has owned a number of EnvisionTEC Perfactory Mini Multi-Lens systems, each with a higher specification and resolution than the previous. The microneedle research in later chapters was carried out using a machine with a  $30 \times 30 \times 25 \mu\text{m}$  X/Y/Z resolution. However, in 2007, a new model was purchased, with a higher  $20 \times 20 \times 25 \mu\text{m}$  specification. This machine is shown in *Figure 4.8*, and was used in the development of MSL micropumps, also discussed in later chapters.



*Figure 4.8 – Photograph of the EnvisionTEC Perfactory Mini Multi-Lens rapid manufacturing system purchased by the Sensors Research Laboratory in 2007. It has a  $20 \times 20 \times 25 \mu\text{m}$  X/Y/Z resolution.*

In this section, the physical and software operations required to fabricate components using the SLA system are outlined, followed in the next chapter by a showcasing the capabilities of the machine via a series of functional components fabricated during the course of this project, along with specific test builds.

#### 4.7.1 Machine Build Operations

Although the concepts behind fabricating components using the Mini Multi-Lens system are shown in *Figure 4.5*, this does not explain the workflow used in practice. Before fabrication can start, the machine must be turned on, and allowed to go through its start-up procedure. Once this is complete, the projector must be initialised, and allowed to warm up. It has been found a warm-up period of around 20-30 minutes is sufficient for the bulb to reach peak light output. The projector output is then briefly calibrated, a process that will be discussed in a later section. Once these steps are completed, the system is ready to receive data and begin fabrication.

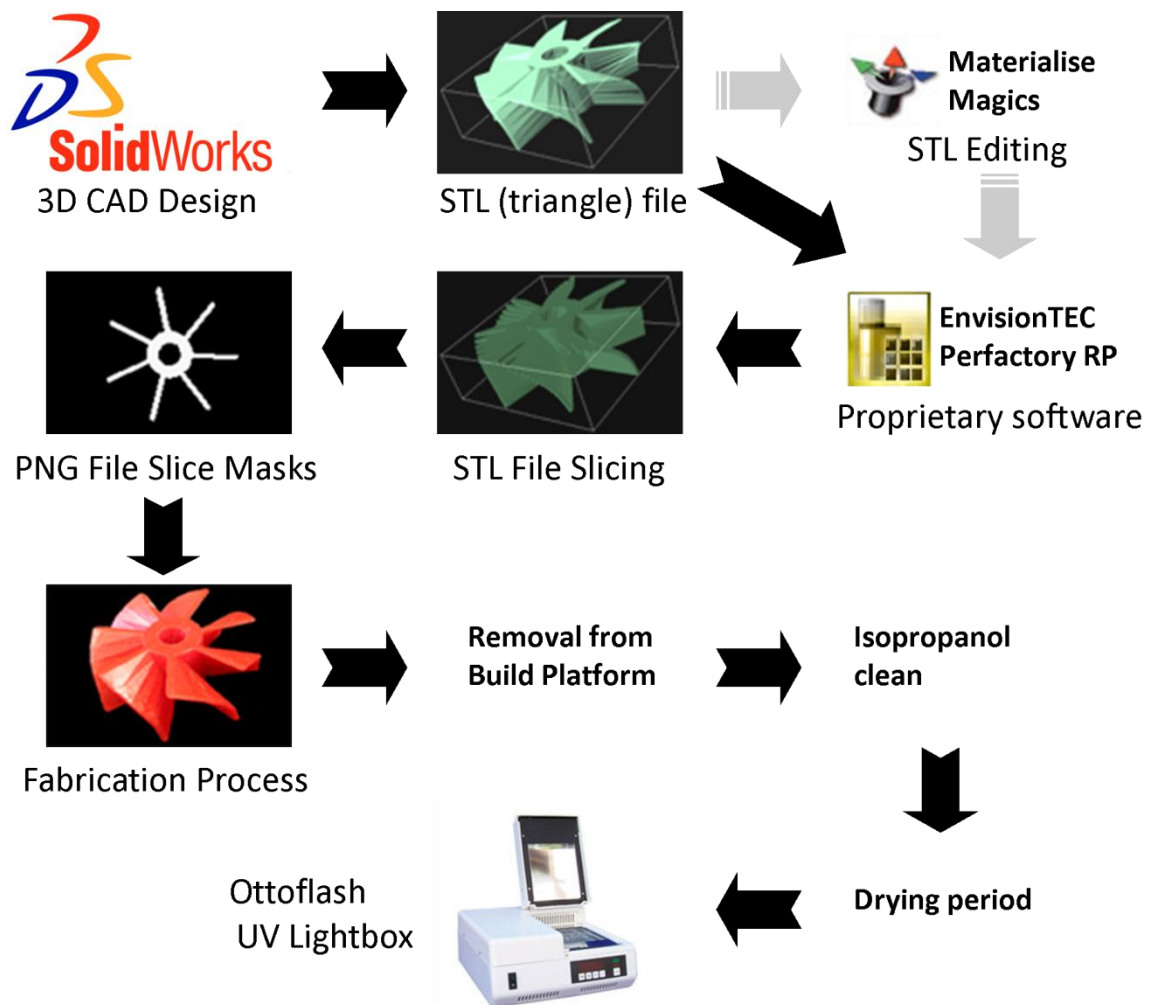


*Figure 4.9 – Workflow for fabrication of components using the EnvisionTEC Perfactory Mini Multi-Lens system. Explanation in text.*

The workflow from this point onwards is shown in *Figure 4.9*. The part to be fabricated is produced using the SolidWorks CAD package, although any software with an STL (standard stereolithography CAD file type) export option can be used. Once the design is complete, the data is saved in STL format. Depending on the geometries required, this file can either be edited using Materialise Magics software, or loaded directly into the EnvisionTEC Perfactory RP package. Details of the software used can be found in later sections, but in simplest terms the RP software slices the CAD model into a series of 2D slices, each of which is represented by a PNG file. Each PNG is projected in series, with the build platform rising one layer thickness each time, to form the complete part.

#### **4.7.2 Post Processing Operations**

Once the build has completed, the build platform rises above the resin, carrying the fabricated component to a position where both can be removed from the system. A simple screw-thread locking system allows the platform to be locked or released from the machine. The component is removed from the build platform using a hobby-knife, which is used to break the surface tension between the platform and component.

At this point, the component is still covered in liquid resin, the amount dependant on the amount of time the build has been able to “drip dry” into the resin tray after fabrication has finished. The excess resin is removed by washing in isopropanol, which emulsifies the resin. This process can be sped up using an ultrasonic bath, although it has been found that prolonged periods of cleaning can damage delicate parts. This is partially due to over-cleaning, as the isopropanol will start to attack the hardened resin once the liquid excess has been removed, but also due to the force of the ultrasound creating stress in the component.

Once cleaned, the part is allowed to air dry to remove any solvent. This may be accelerated by the use of syringes or compressed air in parts with internal fluidics or structures. Finally, the part is fully cured using the Otofash (pictured in *Figure 4.9*) or Metalight QX1



lightboxes. In order to save build time, the Perfactory range of machines do not 100% cure the resin layer by layer, but instead cure to a level of around 60-70%. This allows the cured resin to become solid, but post-curing is required to fully solidify the structure.

The Otofash unit uses strobe lights to produce the required light wavelength, and dosing is controlled by setting the number of flashes, at a rate of 10 per second. The Metalight is theoretically less powerful, but produces a more consistent light level via always-on fluorescent tubes, with the dosing controlled in minutes of exposure. It has been found that the Otofash is usable for builds with large bulk, but can heat up smaller components, causing surface cracking. However, this can be avoided using multiple short bursts of curing, rather than a single long one, with cooling periods in between. Unless otherwise stated, the post-curing process used for components listed in this thesis is either 3000 flashes (5 minutes) in the Otofash, in 1000-flash bursts, or 15 minutes in the Metalight QX1.

#### **4.7.3 Calibration**

In order to maintain build quality, it is necessary for regular calibration to take place. These can be divided into 2 categories, initial setup procedures and regular procedures. During initial setup, the Z-axis platform must be calibrated so the system knows where the resin tray is in relation to its upper stop point, which is found accurately using an integrated pressure sensor. At the same time, the resin tray support mechanism must be made parallel to the build platform. Failure to complete this can result in damage to the machine, as the platform may crash into the tray, or failure of builds, as the platform will not get close enough to the tray for the cured resin to stick to the platform.

The Z-axis initial calibration uses a “calibration tray”, which has the same thickness (2 mm) as a standard resin tray, but lacks the sidewalls that would interfere with the calibration process. The tray is shown *in situ* in *Figure 4.10*. The Z-axis platform, with build platform installed, is manually lowered until it is a short distance from the calibration tray, which has been covered

with a piece of clean A4 paper. The paper is used to protect the calibration plate, as a 100  $\mu\text{m}$  thick steel feeler gauge is pushed underneath the 4 corners of the build platform. If one or more corners are felt to be “stiffer” in gauge insertion than the others, the calibration tray holding mechanism can be altered in its orientation using the spring-loaded screws on each corner.

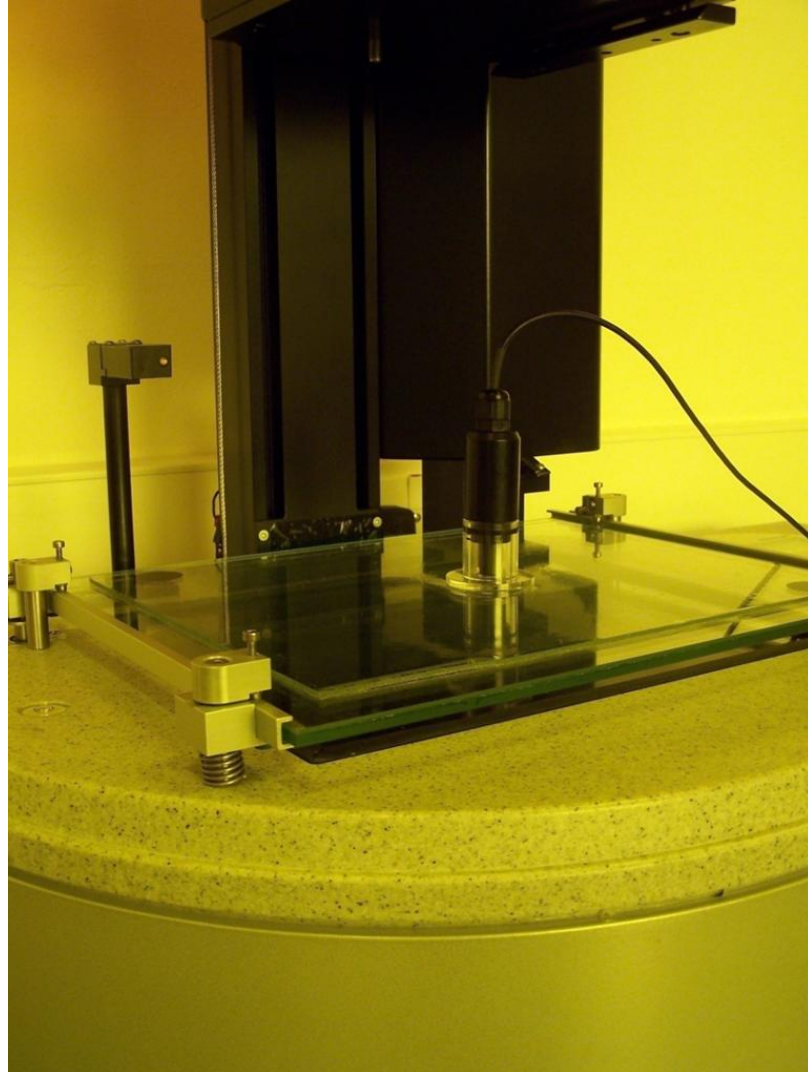


*Figure 4.10 – EnvisionTEC Perfactory Mini Multi-Lens system with calibration plate inserted in place of the resin tray. Also pictured is the integrated light sensor.*

This process carries on, normally with multiple adjustments, until the operator is reasonably certain that each corner is as close to the calibration tray as possible, and that therefore the tray and build platform are parallel. The paper is then removed, and the Z-axis platform is moved down 300  $\mu\text{m}$  – 100  $\mu\text{m}$  for the paper, 100  $\mu\text{m}$  for the feeler gauge, and 100  $\mu\text{m}$  to allow for operator error. The build platform is then flush against the calibration plate, and

this value is taken as the “zero” point for the Z-axis. A further menu allows for the system “pre-pressure” to be set. At the start of the build, the platform lowers to the zero position, and then moves a set distance further, normally around 50  $\mu\text{m}$ . This extra pressure, against the silicon-coated tray, creates an extra-thin layer of resin to be cured, which enhances the adhesion of subsequent layers to the build platform.

Once the position and orientation of the resin tray has been fixed, the projector must be focused. Due to the short distance between the projector lens and the resin tray (around 150 mm) and the high resolutions involved, even small changes in the position of the resin tray can cause the projector not to be focussed exactly onto the top of the resin tray, where each layer is cured. The calibration process however is somewhat crude. One operator must reach into the machine, and take hold of the focussing ring of the projector lens. A second operator loads the calibration plate, and places smoked paper across it. In the focussing calibration mode, a fine detail mask is projected, which the second operator views through an eye piece through the smoked paper. The first operator then moves the focussing ring back and forth, until the second finds the point at which the image is in focus, and the procedure finishes. As mentioned above, this system is rather crude, and could do with automation. However, it is possible for a skilled operator to reach a good level of accuracy.

Another initial setup calibration is the size of the build area. This can vary with the exact position of the resin tray and the projector focus post calibration. Again, this measurement is taken in a slightly haphazard method, using the smoked paper and a pair of callipers. The projector emits across its whole projection area, which shows as a rectangle on the smoked paper. This can then be measured using the callipers in the X/Y axes. The measurements are entered into both the machine via its keypad, and into the Perfactory Configuration Center (see below), through which the further calibration option of the “cube job” is available. This job file builds cubes of a predetermined size in the corners of the build area, which can be measured in

turn to check that both the size of the parts is accurate and the build area is rectangular. Defects in the shape of the build area can be caused by the projector not being parallel to the resin tray, which can be set up using a spirit level on both the calibration plate and the projector itself. The projector frame can then be altered using integrated screw threads until it is parallel with the resin tray.

There are two types of calibration that must take place every time the machine is switched on. Due to variations in the light output of the projector bulb over time, it is necessary to calibrate the projector brightness. This is carried out with the calibration plate inserted. The Perfactory Mini Multi-Lens system has a built-in light sensor, pictured in *Figure 4.10*, which is used to measure the light output of the projector. In the projector brightness calibration procedure, a round masked output is projected through the calibration plate, with the diameter of the light beam being slightly larger than that of the light sensor. The operator places the light sensor over the output beam, and the light level is read off the integrated liquid crystal display of the system. The light level can then be increased or decreased by the operator, in steps of around 5-10 mW/dm<sup>2</sup>. For R11, the recommended light level is around 600 to 620 mW/dm<sup>2</sup>, but tests found that a lower level of 580 mW/dm<sup>2</sup> produced less “over-cure”, where the curing process in overhanging areas was too high. This thickened the overhanging structure, resulting in geometry defects.

Once the projector brightness has been set, the “grey mask” must be calibrated. As mentioned earlier, the DLP chips employed in the Perfactory Mini Multi-Lens projector have many micro-scale mirrors, which can be switched between “on” and “off” positions. This is a digital process, but the mirrors can be driven by pulse width modulation to produce shades of grey. It is found that different areas of the DLP chip can be more reflective than others, requiring a calibration step to ensure that the light level is consistent across the whole build area allowed by the projector.

Much as with the projector brightness calibration procedure, a round masked beam is projected up through the calibration plate, which the operator once again places the light sensor over. The light level is measured, and the operator confirms a stable reading has been reached by pressing the machine's "Enter" button of the machine. The next beam is then projected onto the build area, working from top left to bottom right, moving in rows left to right across the build area. A total of 48 individual readings are taken, which overlap to allow better calculation of the average light level. Once the procedure has been completed, the lowest and highest light levels are displayed, along with the percentage difference between them, which can be used to diagnose problems with the DLP chip. On average, a non-calibrated system will have a max/min difference of around 10-15%. The projector then outputs across the whole of the build area, allowing the operator to check the grey mask settings with the light sensor. An observable difference of 10% across the range is acceptable, although in practice a value of less than 5% is easily achievable.

### **4.8 Software**

#### **4.8.1 SolidWorks**

SolidWorks is a 3D CAD package designed for applications such as automotive design. At a basic level, it works on the principle of "solids", where 2D geometric shapes are extruded to form simple structures. Multiple planes can be created for the creation of more complex compound shapes, along with extruded cuts. Extruded cuts and bosses can be defined either simply by a 1D direction, or in shapes that are more complex by using a path drawn on a perpendicular plane. Shapes can be mirrored, or patterned across a surface, with the patterns either being defined linearly or over curved paths, defined either by edges on the component already created or using lines in separate drawings. There are built-in text tools, which allow embossed labelling, along with other finishing tools such as chamfer options. Importantly, the program allows the export of high-resolution STL files for use in the rapid manufacturing systems.

The package also includes a number of more advanced features, such as the ability to build large working assemblies from multiple CAD structures. Relations, or “mates”, can be added between each part to define their interactions, and complex systems such as car engines can be linked together as they would be in real life. This allows an extra layer of prototyping and testing for large-scale applications, but is less useful in microengineering applications where most of the parts built are monolithic. SolidWorks also has the option for direct output of CAD data in a technical drawing format. These drawings can also be exported as DXF and DWG files (AutoCAD etc). Finally, the built in mechanical testing software, COSMOSWorks can be used in a number of configurations, including calculation of mechanical stress, fluid dynamics calculations and in areas such as heat transfer through a structure.

#### **4.8.2 EnvisionTEC Perfactory Start Centre**

Every rapid manufacturing system on the market has its own dedicated software package, and the Perfactory Mini Multi-Lens is no exception. EnvisionTEC bundle the Perfactory Start Centre with the system, which acts as a gateway to 5 main programs. The Perfactory Buildstyle Editor is used to create configuration files for custom materials on the Perfactory Desktop series, and is not used with the Mini Multi-Lens (this function is instead carried out by the Perfactory RP software). The Perfactory Configuration Center assists in machine setup, with administrative and calibration options, such as the ability to compensate for component shrinkage during post-processing (not found to be a problem with the small-scale builds used during this project).

The Perfactory RP software has two main areas, the first of which is shown in *Figure 4.11*. The front-end of the program is a simple 3D viewer, which allows the user to load CAD data in STL format, and then rotate and translate the components either individually or as a group. Once rotated into the correct plane, the software can also automatically place the multiple parts, in some cases rotating them in order that more complex geometries may fit in the build area. Support structures created using Materialise Magics (see below) can be imported along with their

part. Usefully, the supports are locked in position with their component, allowing easy manipulation of their parent part without having to worry about the positioning of the supports as well.

The second part of the Perfactory RP software allows the setting of the build parameters and JOB file creation. The first window, “Parameter for data processing”, allows the layer thickness, support structure parameters and diagnostic and repair functions to be changed. The layer thickness is normally set during part import procedures, and the program loads the default parameters for the resin selection and thickness, with greater thicknesses requiring longer layer exposure times. The thickness selection option in this section of the program allows fine tuning of the thickness, in steps smaller than the normal 25  $\mu\text{m}$ .

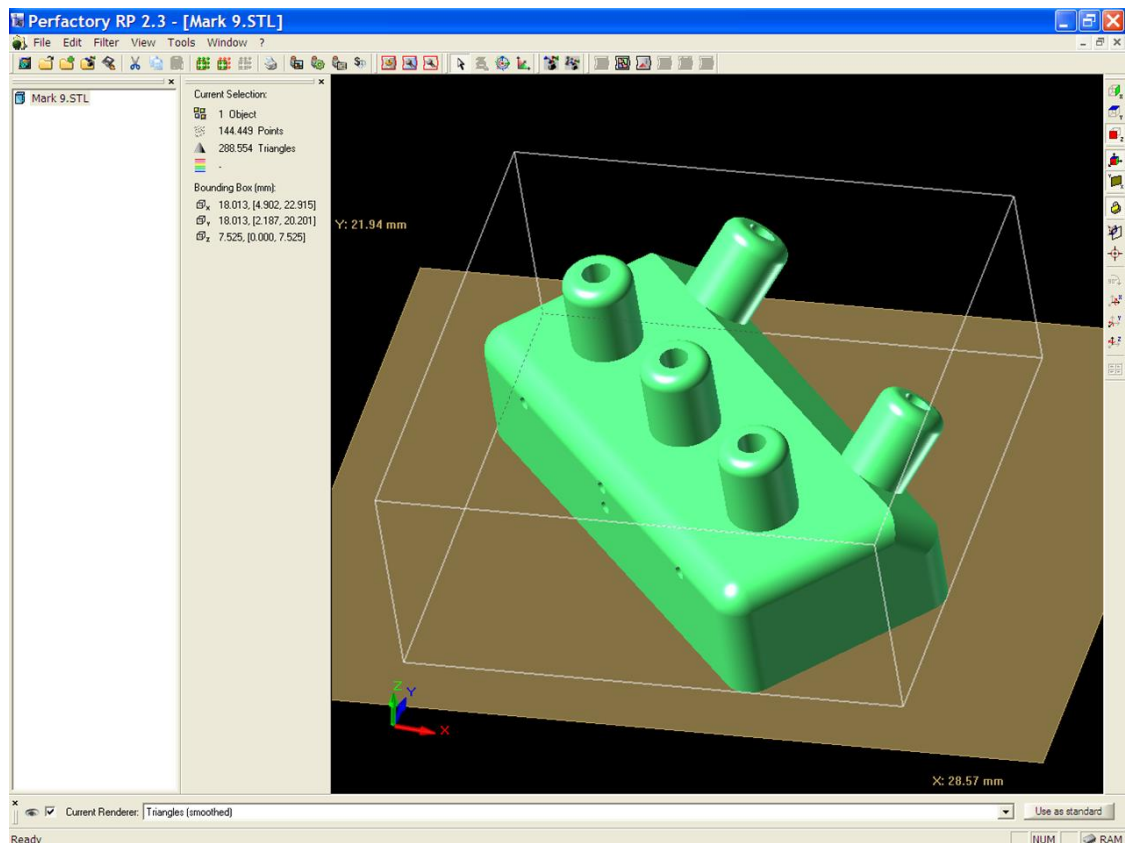


Figure 4.11 – Screenshot of the front end of the Perfactory RP software, provided by EnvisionTEC for use with the Perfactory Mini Multi-Lens system. Part shown is Mk9 self-priming micropump. The brown area represents the build area of the system.

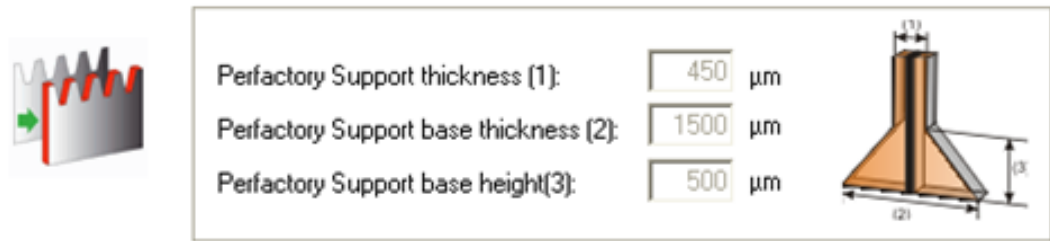


Figure 4.12 – Support settings available via the Perfactory RP program, with defaults shown for R11.

As shown in Figure 4.12, the support structure settings are also customisable. The process for creating supports using Materialise Magics is discussed below. The output from Magics is processed by the Perfactory RP software, allowing the support thickness, base thickness and base height to be altered dependant on the size of the build, with larger parts in theory requiring stronger, thicker supports. It has been found however that the defaults for R11 are sufficient for most small-scale components.

The second window is the “Placement” screen, which groups all the parts placed onto the build area into a single bounding box. This box can then be moved around the build area, with the default being a central position. The bounding box can also be repeated multiple times if space allows, permitting multiple parts to be fabricated without having to import multiple copies.

The third and most important window is the “Building Parameter” screen. This allows the customisation of nearly all the fabrication parameters. These parameters are shown in Table 4.4. As shown in the table, parameters can be set for both “standard” and “burn-in” layers. Layers of the component fabricated early during the build process are treated differently to those later layers, due to complications in the build sequence. The layers are fully cured using longer exposure times, enhancing layer adhesion to the glass build platform. Using default factory values, the burn-in layers receive nearly 3 times the exposure of the standard layers. The reduction in exposure in standard layers also allows quicker builds, and prevents excessive over-cure, where unsupported structures such as membranes end up much thicker than designed due to the depth of curing increasing with exposure time.



	<b>Burn-in</b>	<b>Standard</b>	<b>Min</b>	<b>Max</b>
Exposure time (s)	9.5	3.5	0.5	20.0
Separation distance (mm)	7.0	4.5	2.0	7.5
Levelling velocity (mm/s)	0.8	1.05	0.8	1.05
Peeling velocity (mm/s)	0.8	1.05	0.3	1.2
Waiting time (Peeling) (s)	30.0	1.0	60.0	0.5*
Waiting time (Levelling) (s)	2.0	0.5	60.0	0

*Table 4.4 – Parameters configurable using the Perfactory RP software. Explanation in text. \* Minimum value for burn-in layers is 20 s.*

Another set of parameters altered during the burn-in process are those associated with the peeling and levelling mechanisms used to separate the freshly fabricated layers from the resin tray, whilst still attached to the build platform. *Figure 4.13* shows the process of peeling and levelling used during the layer fabrication. There are 4 main stages in the fabrication of a single layer: curing, peeling, build platform positioning, and levelling. The separation distance defines the distance the resin tray moves at the two back corners during peeling, defining the angle at which the tray stops moving. The peeling and levelling speeds tell the mechanism how quickly they should move the tray to this maximum angle. Finally, the waiting times define a short period after both peeling and levelling where the mechanism halts to allow resin to flow in the tray to fill the voids left behind by the cured resin that has in effect been removed from the resin tray.

In burn in layers, the waiting times are increased 30 times compared to the standard layer, especially after peeling. This is because the build platform is fully submerged into the resin tray, and it takes longer for fresh resin to flow back into the void left behind after peeling. In the later standard layers, the majority of the void becomes the part under fabrication, as the build platform moves out of the resin. The part is much smaller, and therefore the resin takes less time to flow back. The separation distance is also increased during burn-in layers for the same reason, increasing the angle of the resin tray and increasing the rate of resin back-flow into the large void left by the build platform. The peeling speed is also reduced during burn-in layers, again to allow the resin more time to back-flow, but also to reduce the chance of early build failure due to stress

during the peeling process. The slower initial peel speed also reduces the stress on the overall build mechanism, caused by overcoming the large suction forces exerted by the resin on the build platform as it is pulled from the resin.

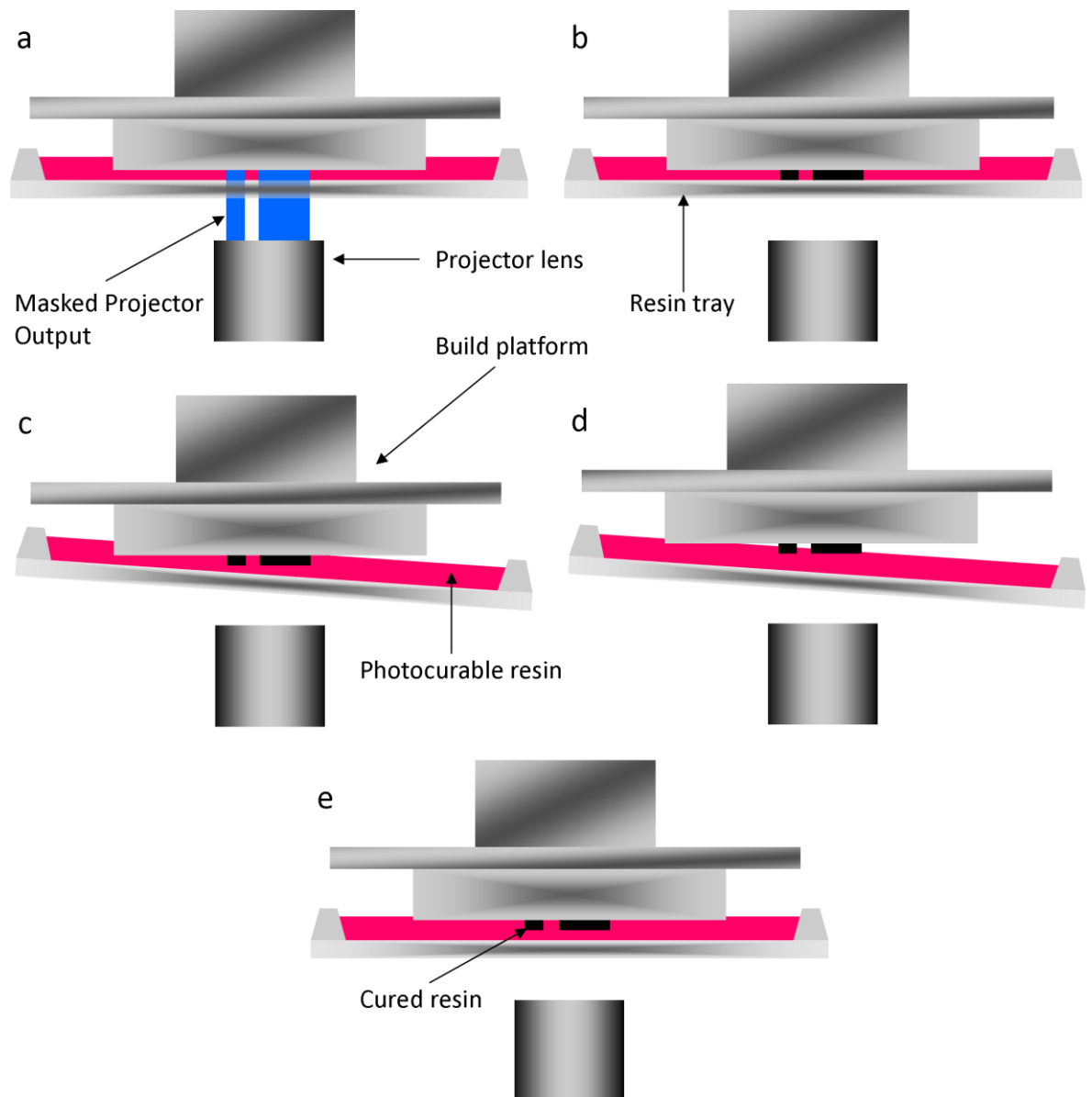


*Figure 4.13 – Processes used during peeling and levelling steps of the fabrication mechanism employed by the EnvionTEC Perfactory Mini Multi-Lens system. (a) shows the first layer being cured by a masked output from the projector, resulting in a cured layer of resin trapped between the resin tray and build platform (b), along with unexposed liquid resin. (c) shows the peeling process, where the resin tray tilts (shown from the side for clarity; is from the back of the tray in reality), peeling the fabricated layer from the resin tray. (d) the build platform moves up one layer thickness. (e) the resin tray levels to its original position, and the mechanism is ready for the projector to cure the next layer.*

The number of layers fabricated using the burn-in parameters is defined on one of the Perfactory RP menus; it is normally set at 400  $\mu\text{m}$ , or 16 times 25  $\mu\text{m}$  fabrication layers. It should be noted that in laterally-thin parts, a large burn-in zone compared to the overall thickness of the part (30-50%) can cause warping during post-curing. Acrylate resins naturally shrink during curing, and as the burn-in layers are already fully cured, the standard layers shrink and bow the structure.

Often in large builds, especially those using supports (see below) or in parts with multiple, small contact points with the build platform, it is advisable to set up a “base plate”. This is a flat structure, defined by the bounding box of the part under fabrication, which is built before the layers of the component. It is normally set at 400 micron thick, and therefore normally contains the entire burn-in zone. The component, including any supports, is then built on top of this structure as if it were the bottom of the build platform.

The majority of the components presented in this thesis were designed not to require a base plate, and could be built directly off the build platform. However, it has been found that a base plate is advisable in any builds where the total area of any given layer in the component exceeds around 150% of that of the first layer fabricated. The vast majority of builds in this category performed without a base plate will fall off whilst the larger area layers are being fabricated, as the suction force of the new layer against the resin tray overcomes the adhesion of the component to the build platform. However, any components with open features that terminate in the first layers of a build should not be used with a base plate, as the plate will naturally block these features.

The fourth and final window in the Perfactory RP software allows the user to customise how the JOB file is created. A JOB file contains the masks for each layer of the build, in PNG image format, along with a pair of configuration files that contain the build settings decided on by the operator. This file can either be simply saved to disk, or transferred to the Perfactory Mini Multi-Lens system directly, either with or without saving to disk. Once all the options have been

selected, the Perfactory RP software can be instructed to process the component(s) into a JOB file.

Once the data has been transferred to the Perfactory Mini system, control is handed over to the Perfactory Direct program. This is a simple window that shows the status of the machine, including what JOB file it is currently building, along with the time passed and remaining in that fabrication process. It also allows the uploading of pre-prepared JOB files to the machine, which can be queued and ordered, as well as cancelled remotely. However, it is not possible to begin the build process from the software; this must be done directly by an operator.

The final piece of software offered by the Perfactory Start Centre is the Perfactory Job Modifier. This package allows the viewing of pre-prepared JOB files, showing the parameters they were processed for (e.g. peeling speed etc.), and allows these parameters to be changed and saved without having to re-process the file from scratch. It also allows the individual mask files to be viewed, either in a multi-mask grid view or in a closer-zoom individual view. This can be useful, as it has been known on occasion for mistakes to occur during the STL file processing steps, which can lead to aberrations in the masks created by the Perfactory RP software. One such bug can occur if the SolidWorks CAD software is set to export STL files with an angle accuracy of less than 2 degrees, as this can cause swept cut shapes to be missed out of the STL, blocking complex internal fluidics.

A separate bug in the Perfactory RP software can sometimes occur when the “Close holes automatically” option is checked, under the diagnostic options of the first window of the Perfactory RP JOB file processing options. This mode closes what are assumed aberrations in the STL file, which can occur in larger CAD files. However, small-scale internal structures such as those found in microengineering components can be mistaken for aberrations and closed up, again blocking internal fluidic channels. As a result, in the majority of the builds shown in this thesis, this mode has been turned off.

### 4.8.3 Materialise Magics

As mentioned above, a number of build geometries may require support structures in order that they may be fabricated properly. Magics, unlike SolidWorks, can be used to directly edit STL files, in theory allowing components to be created directly in Magics. However, the design tools are less sophisticated than those found in SolidWorks, and often design in Magics requires the direct manipulation of the model triangles, which is somewhat cumbersome after long-term use of the simple interface of the SolidWorks software.

However, the major use for the Magics package in practice is in the production of support structures. As shown in *Figure 4.14*, it is not possible for the Perfactory Mini Multi-Lens system to fabricate overhangs that double-back on the main component structure. In order for these geometries to be copied from the CAD data, support structures can be created. The Materialise Magics software package has a number of advanced functions for the identification of impossible overhang geometries and for the design of suitable supports.

Support structures are needed due to the requirement for every feature of the component being fabricated to have some kind of contact directly down to the build platform. Features without this required contact do not resolve properly during fabrication, and are left behind on the resin tray. Support structures are created to bridge the gaps between the build platform and the overhang, and consist of a number of flat vertical walls, topped by a number of teeth structures that connect the walls to the build geometry. The teeth are thin enough on contact with the component structure that they can be easily snapped off by hand during postprocessing, normally after the isopropanol wash step, but before postcuring in the lightbox. It is often necessary to subject the component itself to a second isopropanol wash after support removal, to remove any excess resin that may have been trapped between the often-complex support structures and the component.

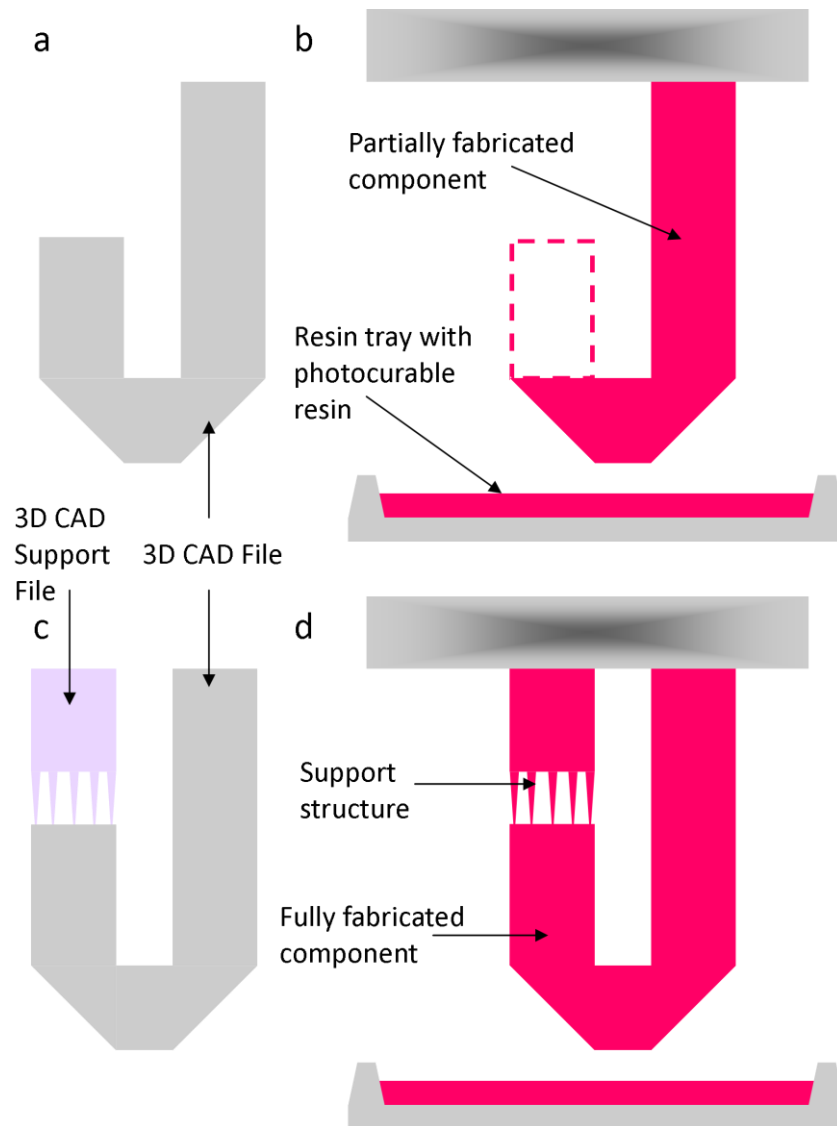


*Figure 4.14 – Geometry conditions where support structures are required. (a) shows a CAD geometry that is impossible if built from the bottom up, with the resultant build (b) missing the double-back overhanging structure. (c) shows the CAD geometry with the required supports (purple structure), resulting in a complete structure shown in (d). The support structures can be snapped off once the build has been removed from the glass build platform.*

The support structures themselves are designed by the Magics software, with in theory no user input beyond part import and initial setup required. The software analyses the part for horizontal surfaces, and then decides if they require support structures. It then selects from a range of support styles, dependant on the shape of the horizontal area required. The styles range from single-point supports, which are a single tooth on top of a pair of crossed walls, to more complex patterns with wall cross-hatching, boundary features and many tens of support teeth.

However, more often than not with smaller structures, user intervention is required. This is especially important with parts with internal structures, as the program often determines that horizontal ceilings of internal chambers and fluidic channels are in need of supports. A horizontal surface is deemed to require a support if any part of it is over 3 mm away from a supporting wall. In theory, overhangs and ceilings further away from walls are at risk of sagging during fabrication, but in practice, it is often possible to create internal structures without supports, possibly due to the supporting pressure of the trapped excess resin left in the fluidics. However, the software does not make the distinction between vulnerable external horizontal areas and internal ceilings. The building of support structures to internal planes is disastrous in any case, as the supports will normally completely block the internal void, causing loss of function for these features. The user must therefore cycle through the software-chosen areas in need of support, and remove internal features from the list. There is also a vast array of options available for customisation of support structures, including tooth length, width and spacing and wall crosshatch spacing. Each style of support is individually customisable, although it has been found that the factory defaults are reasonably reliable.

Once the structure of the supports has been finalised, they are exported as an STL file. The file name is the same as the component name, with an “s\_” prefix. The Perfactory RP software recognises this on import, and as described previously matches the support to the component in relative space, treating the two STL files as a single component. The support STL file does not define the exact dimensions of the supports to be fabricated, only their position and the position of the teeth. The wall width and base width/height are customisable in the Perfactory RP software, as shown previously in *Figure 4.12*. Another customisation option available in the Perfactory software suite from version 2.3 onwards is the ability to double-expose support structures, allowing them to be fully cured and thus stronger, without over-curing the component layers. This option creates a second mask only containing the support structures, which is exposed over the original masks that contain both the component and support structures.

When working with small-scale components, it is often not advantageous to use support structures. Although often successful when used with macroscale components, the burr left behind by the supports often overwhelms the component structures in parts made for microengineering applications. It is therefore often easier to design parts in such a way that supports are not required, building them directly from a flat surface on the component. This can sometimes be made more difficult by the inclusion of structures such as membranes that can only be built in the horizontal plane. However, it has been found that the majority of microengineering components investigated in this thesis can be built without the use of supports with minimal design compromises.

## **4.9 Conclusion**

The field of rapid manufacturing is nascent but expanding quickly. In some respects it is a solution without a problem, and has yet to find a “killer app” to drive sales of systems or bring machines into the home market. However, a number of niches have been found in industry, including in the production of sacrificial moulds for metal casting, or in the production of prototype components for wind tunnel testing in motorsport.

However, as the technologies develop and evolve, rapid manufacturing systems are beginning to blur the definition between design and manufacture. An engineer can design a component, and be holding a physical version within the same day, depending on its complexity and size. Although the applications of form, fit and function are prototype-based, advances in the materials, especially those engineering plastics used in fused deposition modelling systems, are allowing functional components to be produced much more quickly than those fabricated using more traditional machining techniques.

Rapid manufacturing technologies have the potential to revolutionise the field of intellectual property. If the operator possesses the CAD data for a component, he or she can theoretically reproduce it anytime, anywhere, and on any given machine. This is assisted by the



ubiquity of the STL CAD file format, along with support industries such as 3D scanners for reverse engineering of competitor's components.

The range of commercially available ALM systems has been reviewed for suitability for use in microengineering applications. The only systems available that could successfully build internal structures were those employing a liquid-based SLA approach. The EnvisionTEC range of DLC-projector SLA systems represents the best resolution/price point of the available systems. The EnvisionTEC Perfactory Mini Multi-Lens system was chosen, as it was at the time the flagship EnvisionTEC product, with an X/Y/Z resolution of  $20 \times 20 \times 25 \mu\text{m}$ . In the next chapter, the fabrication abilities of the system will be showcased through a variety of components built during this project.

#### 4.10 References

- [1] L. Wood, "Rapid Automated Prototyping: An Introduction," *Industrial Press Inc.*, 1993.
- [2] F. W. Liou, "Rapid prototyping and engineering applications: a toolbox for prototype development," *CRC Press*, 2008.
- [3] S. Kawata, H. B. Sun, T. Tanaka, and K. Takada, "Finer features for functional microdevices," *Nature*, vol. 412, pp. 697-698, 2001.
- [4] EnvisionTEC, "EnvisionTEC Computer Aided Modelling Devices," *[online]*, vol. Available: <http://www.envisiontec.de> [accessed 16th July 2009], 2009.
- [5] M. Magics, "Materialised Magics: Driving Your Innovations," *[online]*, vol. Available: <http://www.materialise.com/materialise/view/en/92074-Magics.html> [Accessed 19th July 2009], 2009.
- [6] V. K. Varadan, X. Jiang, and V. V. Varadan, "Microstereolithography and other Fabrication Techniques for 3D MEMS," *John Wiley & Sons, Ltd*, 2001.
- [7] EnvisionTEC, "About Us," *[online]*, vol. Available: <http://www.envisiontec.de/index.php?id=27&L=%23%23%23LANGID%23%23> [Accessed 27th July 2009], 2009.
- [8] T. Instruments, "DLP Projectors," *[online]*, vol. Available: <http://www.dlp.com/> [Accessed 27th July 2009], 2009.
- [9] T. Instruments, "How DLP Technology Works," *[online]*, vol. Available: <http://www.dlp.com/tech/what.aspx> [Accessed 27th July 2009], 2009.
- [10] EnvisionTEC, "EnvisionTEC Computer Aided Modelling Devices," *[online]*, vol. Available: <http://www.envisiontec.de/> [accessed 16th July 2009], 2009.

# Chapter 5

---

## 5 SLA Capabilities

### 5.1 Introduction

In the following chapter, example components fabricated with the EnvisionTEC Perfactory Mini Multi-Lens system will be presented, to show the capabilities and limitations of the system, the purpose of which is to inform future designs of components produced through this thesis. Some of the components were built specifically to push the capabilities of the system; others were related to this project. A number of other builds were fabricated for other members of the Sensors Research Laboratory, or beyond for academic applications in the Departments of Biological Sciences and Chemistry at the University of Warwick. Finally, some components were fabricated for collaborators at other academic institutions, in order to take advantage of the high-performance SLA system we have at our disposal.

### 5.2 Macroscale Components

As discussed in the previous chapter, the vast majority of ALM systems are aimed at macroscale industrial applications. These machines can often have build volumes measured in cubic meters, and are capable of fabricating large scale prototypes of components normally produced using traditional ablative techniques. However, the EnvisionTEC Perfactory Mini Multi-Lens system used by the Sensors Research Laboratory is set up with a build volume of  $28 \times 21 \times 250$  mm. Parts that can be termed “macro” in scale are therefore somewhat different to those produced by other systems. However, when using the terminology for MEMS devices, the prefix “micro” is used for those structures with a functional parameter of less than  $100 \mu\text{m}$ . There are therefore components that have been built that do not conform to this definition, but are still interesting from a technical viewpoint.

It can be assumed that for all the components built with delicate or microscale features, the build parameters used were as per the standards, except with the peel speed set at 500  $\mu\text{m}/\text{sec}$  (around 50% normal speed), to reduce the force on the build by the peeling mechanism. It can also be assumed that all the parts presented were fabricated from R11 resin. Average build times are around 4 mm in the Z-axis per hour.

### 5.2.1 Demonstration Parts

In order to show potential collaborators or the public what SLA systems are capable of, it is often beneficial to produce less technical components that the person might recognise. For this reason a series of demonstration parts were created, and are shown in *Figures 5.1 and 5.2*. *Figure 5.1* shows a relatively simple structure, that of the football World Cup, built at both 100 mm and 1,500  $\mu\text{m}$  tall.

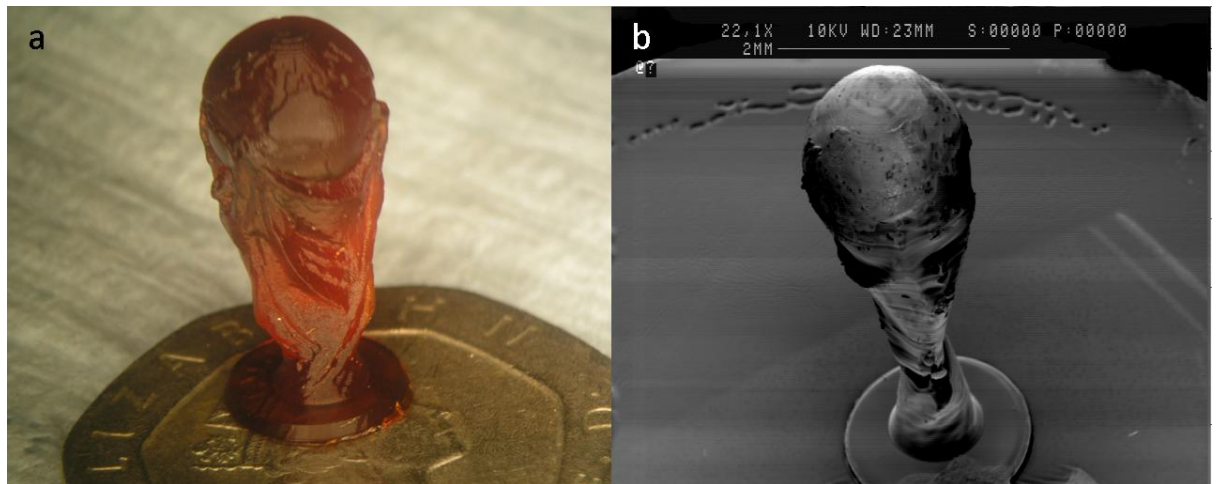


*Figure 5.1 – (a) Photograph of a 100 mm tall “World Cup” structure; (b) SEM electron micrograph of the same model built just 1.5 mm tall. Both structures were produced using the Perfactory Mini Multi-Lens microstereolithography system.*

The characters in *Figures 5.2a and b* should be recognisable to anyone in the Western World. The Homer Simpson model has a hollow can and donut, although the overhanging shirt collar structure was too small to support and therefore has not resolved. The rook model shown in *Figures 5.2c and d* is a popular test part in the ALM industry, as it displays complex internal

geometries that are nearly impossible to replicate using ablative techniques. However, in the majority of cases the model produced is somewhat larger than displayed here.

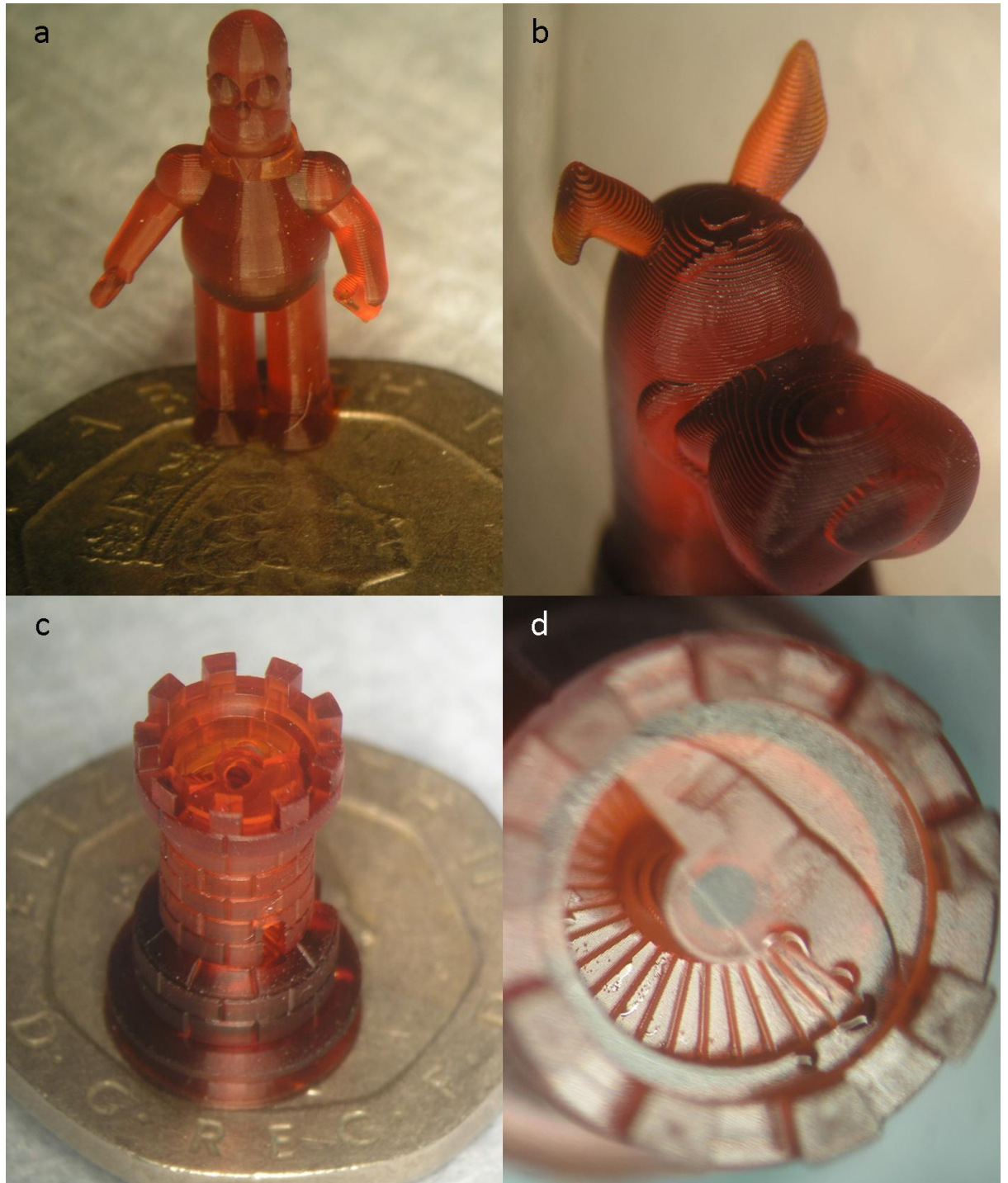


*Figure 5.2 – Demonstration parts fabricated using the Perfactory Mini Multi-Lens SLA system. (a) 1,200  $\mu\text{m}$  tall Homer Simpson figure, with hollow donut and drinks can. (b) Head of Scooby Doo character, fabricated in 50  $\mu\text{m}$  layer thickness, with layers clearly visible. (c) Rook chess piece build, with UK 20 p piece for scale. (d) Top-down view of rook, showing internal spiral staircase.*

### 5.2.2 Microchannel Arrays

In collaboration with Mr. Fauzan Che Harun of the Sensors Research Laboratory, a series of microchannel arrays were designed and fabricated by the author, an example of which can be seen in *Figure 5.3*. The arrays were to be used as gas chromatography channels for use in an electronic nose, and needed to be both compact and long in order to achieve odour separation. The array length reached up to around 3 metres, spanning back and forth across a  $27 \times 20 \times 40$  mm structure. The component shown in *Figure 5.3* also has integrated pipe connectors, and later components were designed with built-in, low headspace sensor covers [1].

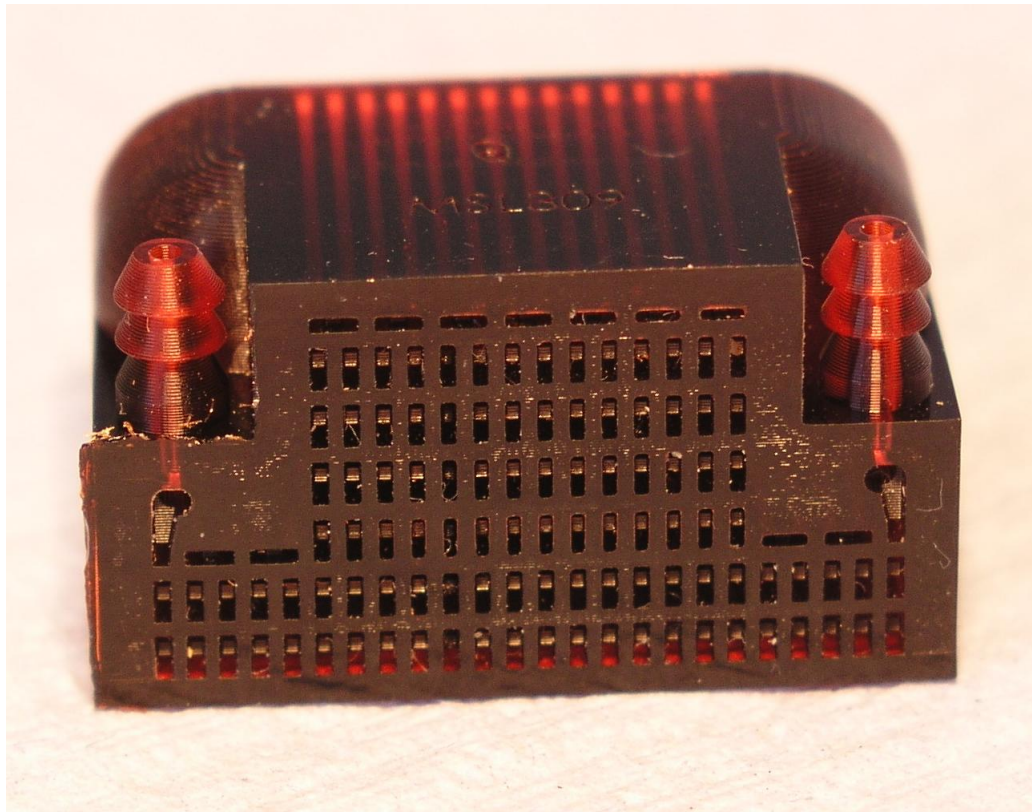


*Figure 5.3 – Microchannel array fabricated using the Perfactory Mini Multi-Lens SLA system. The structure measures 27 mm across and 20 mm deep/tall, and features a pair of integrated pipe fittings. The total channel length was in the order of 3 metres, with the channel width being 500  $\mu\text{m}$ .*

As has been discussed previously, one problem with ALM systems is the removal of excess material from inside internal cavities. Due to the length of the channels being created, it was not possible to fabricate the channel in a single long bore. Each loop of the channel is therefore open to the outside of the structure, to allow the excess resin to escape during post-processing. The

channels were sealed by spin coating UV-sensitive adhesive onto a glass slide, which was then pressed against the open ends of the channel structure. The resultant channel was found to be leak-free.

Smaller channels, down to just 100  $\mu\text{m}$  in width were attempted during the prototyping stages, but were found to not release the excess resin easily, presumably due to surface tension effects. Decreasing the structure depth, and therefore the individual channel depth, helped but reduced the yield in terms of overall channel length – channels below 200  $\mu\text{m}$  in width do not resolve well over distances of more than around 10 mm. It was therefore decided that 500  $\mu\text{m}$  was a reasonable compromise. This structure is a good example of a component that would be extremely time consuming to fabricate using normal ablative technologies. In comparison, using standard build parameters, this structure would take no more than 3 hours to build unattended, followed by around 30 minutes of post-processing time.

### 5.2.3 Overhanging structures

One of the problems to be overcome when fabricating components using an SLA system is in the avoidance of overhangs. Although support structures can be built, sometimes they can cause further problems. *Figure 5.4* shows a pair of test membrane components, used in the long-term testing of the membranes fabricated in the system (see following chapters). The components had integrated pneumatic fittings, which were easiest to integrate horizontally. However, these overhangs are too big to fabricate successfully without supports, as shown by the right hand component in *Figure 5.4*. The left hand component had supports built for it, but the support structures left behind a burr that was difficult to remove, although in practice it didn't affect the functionality of the part.

A test build was set up to determine if angling the overhangs would allow support-less overhangs to be built. The test build can be seen, along with screenshots from the original SolidWorks CAD file, in *Figure 5.5*.



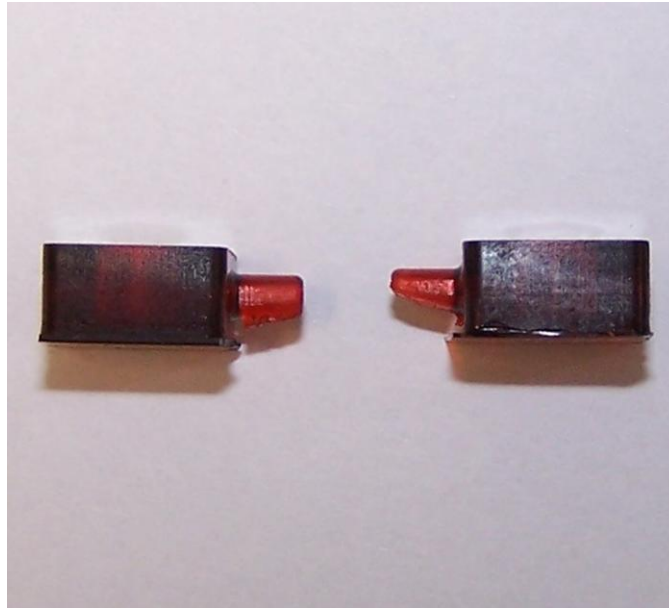


Figure 5.4 – A pair of test membranes fabricated using the Perfactory Mini Multi-Lens system. Both components were built from the bottom of the figure upwards, thus requiring supports for the overhanging pneumatic ports. The left-hand component had supports constructed, and a layer of burr can be seen beneath the cylindrical overhang. The right-hand component had no supports, and therefore the lower edge of the cylinder has been pulled up by the repeated peeling forces. Both parts were functional.

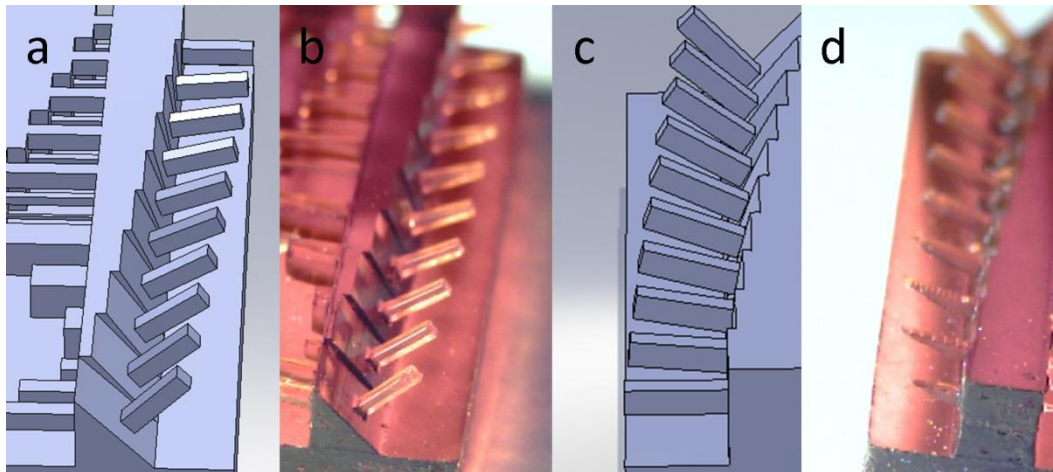


Figure 5.5 – Angled overhang tests. Features  $500\ \mu\text{m}$  in width were projected  $2\ \text{mm}$  out from a series of angled bases, from  $0^\circ$  (horizontal) to  $45^\circ$ , in  $5^\circ$  steps. (a) and (c) are the 3D CAD designs used, whilst (b) and (d) are the corresponding micrographs of the completed part, taken from each side due to the low focal length of the microscope making taking images of the whole structure impossible.

The micrographs in Figure 5.5 show that angles from around  $25^\circ$  and above are suitable for building reasonably small-scale overhangs without supports. As a result of this test, future devices were built with angled pipe fittings, as can be seen in Figure 5.6.



*Figure 5.6 – Angled pipe fittings integrated into a micropump design (see following chapter). The fittings are angled in order to avoid the use of supports, and are angled at 45° from horizontal.*

### 5.3 Microscale Components and Features

Although the parts produced at macroscale are impressive, the Perfactory Mini Multi-Lens system does not have the build volume to produce parts of a useful size. It has been specifically set up in order to maximise resolution at the cost of build area, and in this section a number of microscale components will be discussed.

#### 5.3.1 Meshes

An early test component fabricated using the Perfactory Mini Multi-Lens SLA system was a fine horizontal mesh, supported by a circular frame. The part was fabricated using the standard build parameters, and shown in *Figure 5.7*. As can be seen, the fine detail afforded by the SLA system can be used to create structures that are both complex and robust. The meshes required a series of prototype builds, of differing hole and mesh sizes, until the composite 50 and 100  $\mu\text{m}$  mesh shown was found to give good fabrication yields. The mesh was flexible, and could be bent with the end of a finger before returning to its original shape.



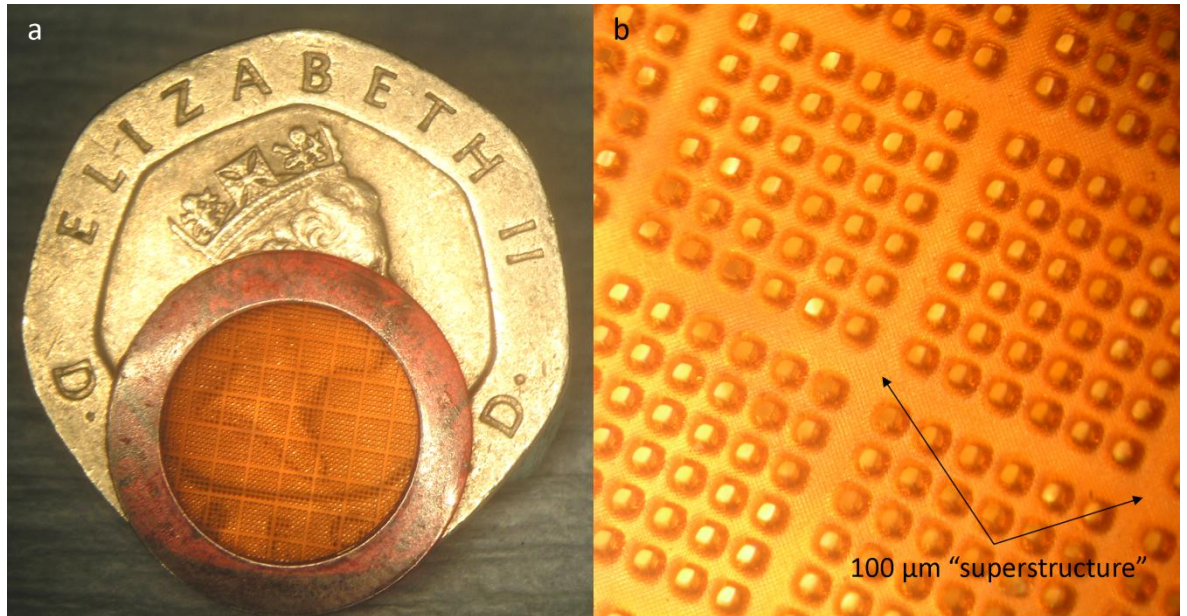


Figure 5.7 – Photographs of a circular mesh test piece fabricated using the Perfactory Mini Multi-Lens SLA system. (a) Mesh with UK 20p piece for scale. (b) Close-up of the mesh, which is 100  $\mu\text{m}$  thick, built in 25  $\mu\text{m}$  layers, with 100  $\mu\text{m}$  wide holes in a 50  $\mu\text{m}$  wide mesh. It was found that a 100  $\mu\text{m}$  wide “superstructure” mesh increased the mesh yields to close to 100%, resisting the fabrication forces.

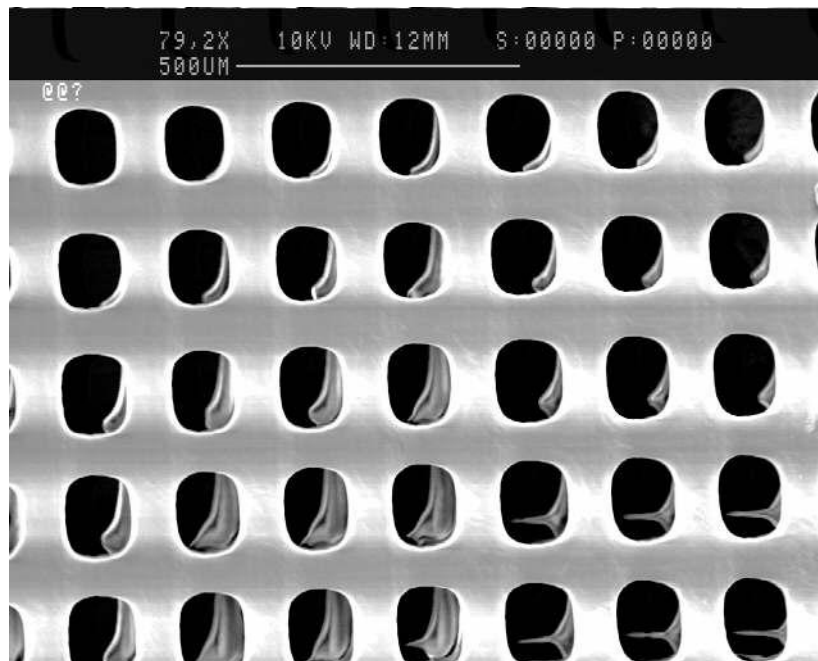
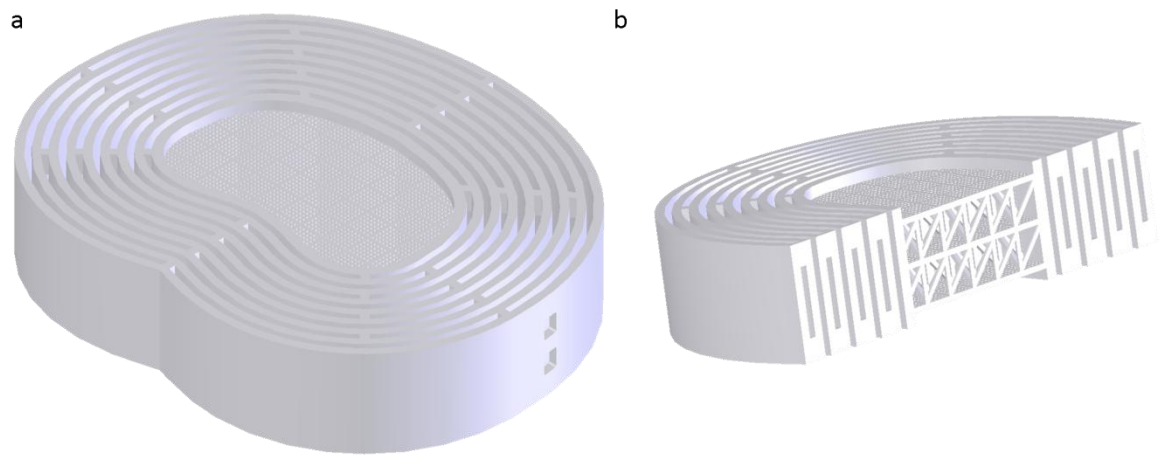


Figure 5.8 – SEM electron micrographs of a 100  $\mu\text{m}$  mesh with 100  $\mu\text{m}$  holes. Although the structure itself was reasonably regular, the mesh can be seen to have delaminated.

Further structural details can be seen in *Figure 5.8*. This mesh was a 100  $\mu\text{m}$  wide structure surrounding 100  $\mu\text{m}$  square holes. As can be seen, the holes are not square at high magnification, and take the appearance of a micro-sized plastic fencing. Although the front layer is uniform, the back layers have delaminated. This was found to be a particular problem with uniform meshes, whilst those with an overarching superstructure, as shown in *Figure 5.7* did not suffer from this problem. The holes size did not seem to have a bearing, although if the hole size to mesh size ratio got too high then often the mesh would be weak due to the resultant lack of material in the mesh itself.

The mesh structures were seen to have potential as scaffolds for tissue engineering applications. In collaboration with Dr. Judith Hoyland of Manchester University, the structure seen in *Figure 5.9a* was designed using SolidWorks. The structure was created as a scaffold for replacement back disks, and was separated into two concentric structures: a central mesh, surrounded by a number of linked concentric rings. The inner mesh structure was actually composed of 3 parallel mesh elements, identical to those seen in *Figure 5.7*, joined by a series of interconnected struts, as shown in the cut-away view in *Figure 5.9b*. The struts were designed to aid the migration of cells between the meshes, and were 200  $\mu\text{m}$  wide square structures.

The part was fabricated horizontally on the build platform, using standard fabrication parameters. The resulting component can be seen in *Figure 5.10*. The structure was surprisingly strong and flexible, with pressure applied laterally to the concentric rings causing elastic deformation of the structure, but no breakages or cracks in the surface. Opening up the structure (not shown) allowed confirmation that the internal cross-beam structure had indeed fabricated, although a few struts were not fully in contact with the upper meshes.



*Figure 5.9 – Structure designed in SolidWorks as a potential scaffold for tissue engineering, in collaboration with Dr. Judith Hoyland of the School of Medicine at Manchester University.*

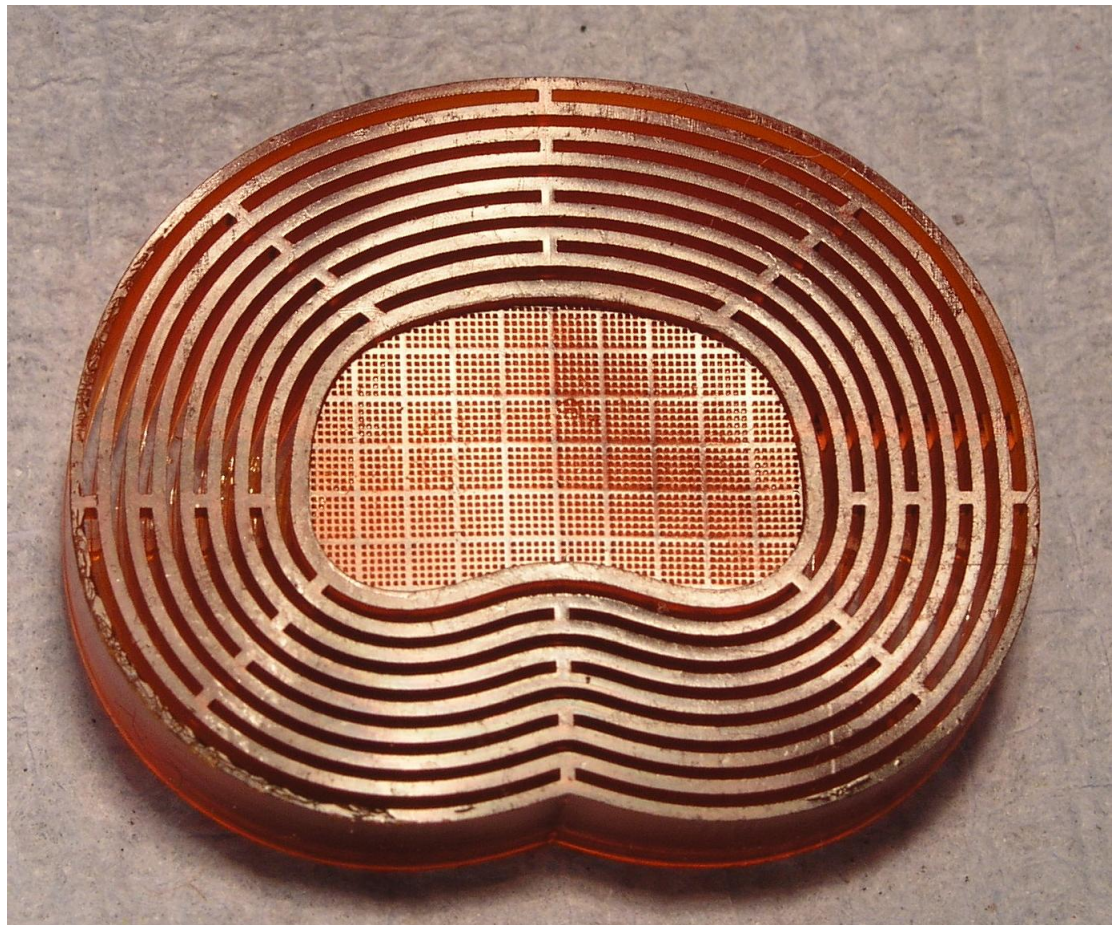


*Figure 5.10 – Resultant structure fabricated using the Perfactory Mini Multi-Lens SLA system, from the CAD data shown in Figure 5.10. The structure is 30 mm across its widest point.*



The structures shown are a good example of geometries that would simply have been impossible using traditional machining techniques. This is taken further by the mesh sphere shown in *Figure 5.11*. This delicate looking, yet surprisingly robust component measures 600  $\mu\text{m}$  across, and is composed of a hexagonal lattice of 70  $\mu\text{m}$  thick struts. The ball is not entirely perfect, as there is a small break in the structure that corresponds to where it was built off the platform, it maintains its shape, and can even be bounced off hard surfaces without damage.

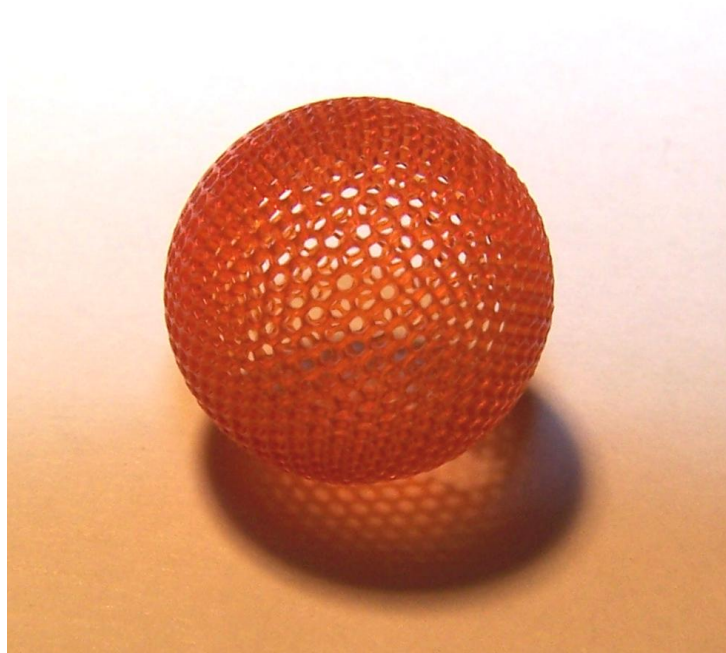


*Figure 5.11 – Mesh sphere fabricated using the Perfactory Mini Multi-Lens SLA system. It is composed of a hexagonal lattice of 70  $\mu\text{m}$ -thick struts.*

Although *Figure 5.8* shows that complex vertical structures are possible, it was found that thin vertical features such as meshes and membranes did not build well. This can be seen in *Figure 5.12*. Although these meshes shown did resolve, these were two of only a few of these 100  $\mu\text{m}$  thick structures that did build to completion. Many others ripped during fabrication, seemingly independently of the hole size. Therefore builds containing thin features such as meshes or membranes are generally constrained in their positioning on the build platform, to avoid such aberrations.

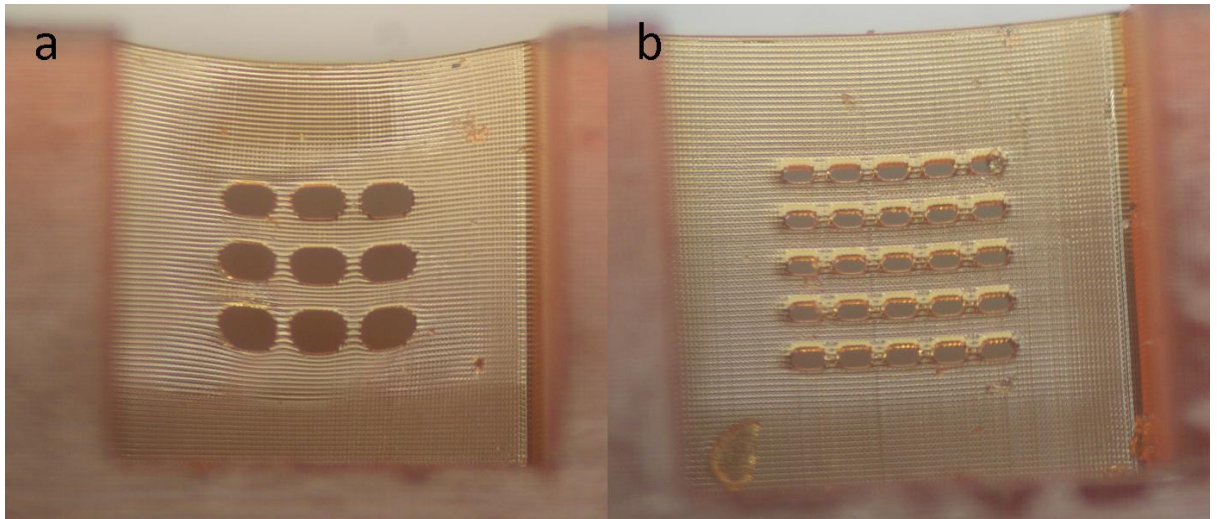


Figure 5.12 – 100  $\mu\text{m}$  thin mesh structures built on a vertical plane, with (a) 200  $\mu\text{m}$  and (b) 100  $\mu\text{m}$  diameter holes. It is noticeable that the horizontal struts of the mesh are wider than the vertical features. The struts in the CAD file were of the same size.

### 5.3.2 Microscale Test Build

In order to push the envelope of the SLA system, a test build was designed to probe the minimum feature sizes and the ability of the system to produce complex micro-scale structures. The fabricated components can be seen in *Figure 5.13*. The microstructure shown in *Figure 5.13a* was reproduced well from the CAD drawing, with only a slight enlargement of the base of the structure legs visible. The bridge structure in *Figure 5.13b* also fabricated well, although damage is visible on the upper edge where some material has peeled away during fabrication. Perhaps the most impressive feature is the wall structure in *Figure 5.13c*, which at 20  $\mu\text{m}$  wide is constructed from the exposure from only a single pixel in the projector. However, less successful was the tree-like structure shown in *Figure 5.13d*. This was designed with 3 offset branches, 100  $\mu\text{m}$  wide with 20  $\mu\text{m}$  sidewalls. As can be seen, these have nearly entirely failed to build. It is assumed that although extremely thin features, such as those seen in *Figure 5.13c* are possible when built from a large bulk of cured material, the relatively small amount of material present in the “trunk” of the structure in *Figure 5.10d* means that the whole structure will move around during fabrication. This may cause misalignments of the pixel grid, with each layer not being directly on top of the last, causing structural weakness and the resultant build failure.

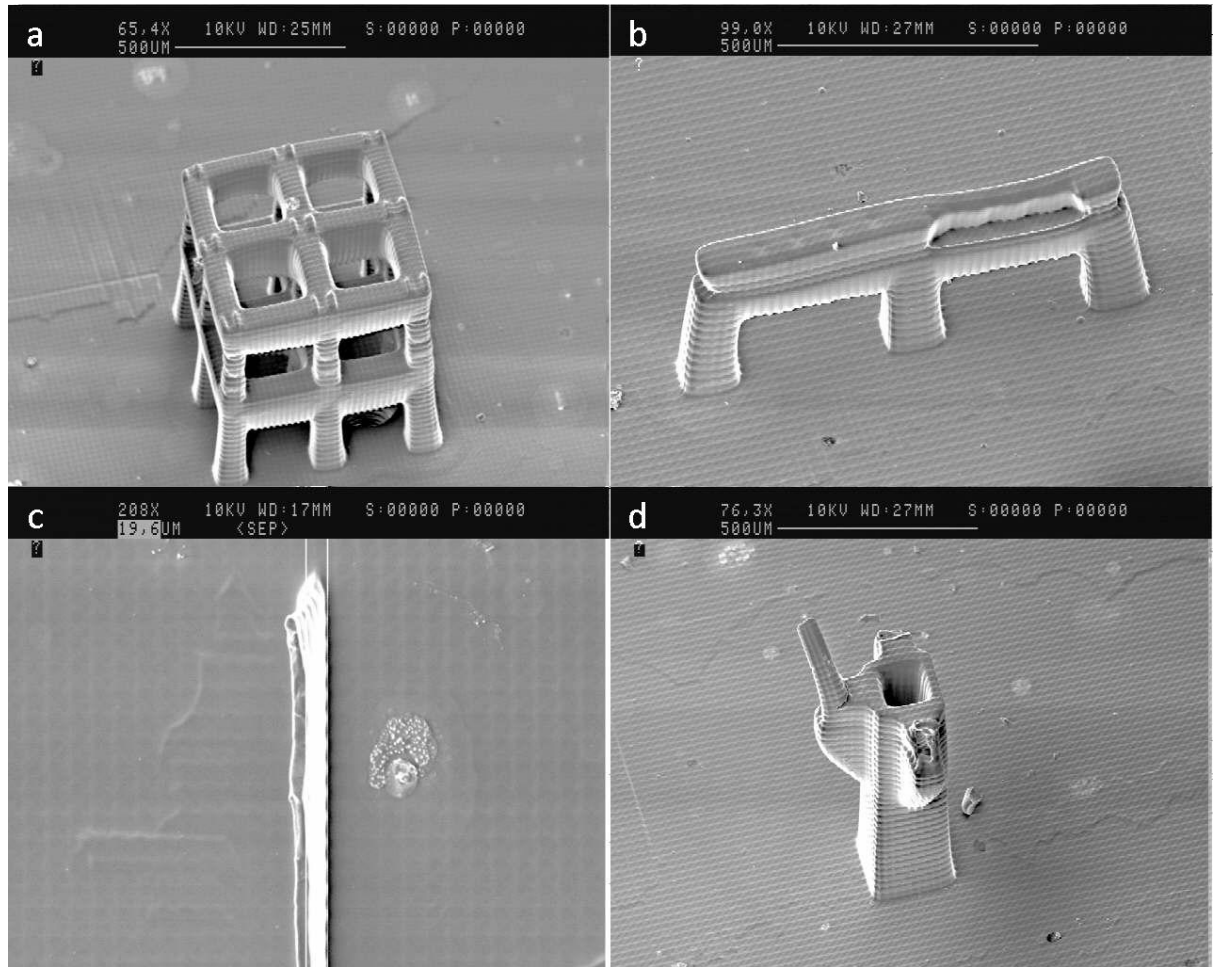


Figure 5.13 – SEM electron micrographs of test build designed to probe the minimum feature sizes of the Perfactory Mini Multi-Lens system. (a) A microstructure, with 100  $\mu\text{m}$  wide beams meshed together. The structure stands 645  $\mu\text{m}$  tall, and is 700  $\mu\text{m}$  wide. (b) A bridge structure, once again with 100  $\mu\text{m}$  wide struts. The structure is 300  $\mu\text{m}$  tall and 900  $\mu\text{m}$  long. (c) 20  $\mu\text{m}$  wide, 200  $\mu\text{m}$  tall wall structure, a single pixel width wide. (d) Failed tree-like structure, standing around 700  $\mu\text{m}$  tall (was designed as 900  $\mu\text{m}$ ). The central post was designed to have 3 offset “branches”, which were hollow with 20  $\mu\text{m}$  wide outer walls.

### 5.3.3 Single Pixel Structures

It was decided to try and produce a microstructure using the Perfactory Mini Multi-Lens consisting of just the exposure of the resin by a single pixel. Pillars 20  $\mu\text{m}$  wide were attempted as part of the build shown in Figure 5.13, but no features were found on the component. Later experiments relating to MSL-produced microneedles (see following chapters) did however produce a result. A pyramidal microstructure was designed as part of a larger array of microneedle shapes. The structure in question was just 125  $\mu\text{m}$  tall, and 100  $\mu\text{m}$  wide, and is shown in Figure 5.14. At the tip of the structure, which can be seen to be composed of just 5

times 25  $\mu\text{m}$  thick layers, was a single 20  $\times$  20  $\mu\text{m}$  blob of cured resin, representing the light output from a single pixel.

It is assumed that the previous columns had failed as they were built at 20  $\mu\text{m}$  width directly from a flat bulk base. This may have caused extra stress during the peeling process, as the breaking surface tension between the resin tray and the bulk part may have ripped off the microstructures. However, the pyramid being built in steps increases the distance from the single pixel to the bulk material, and may have reduced this stress, allowing the fabrication to complete successfully.

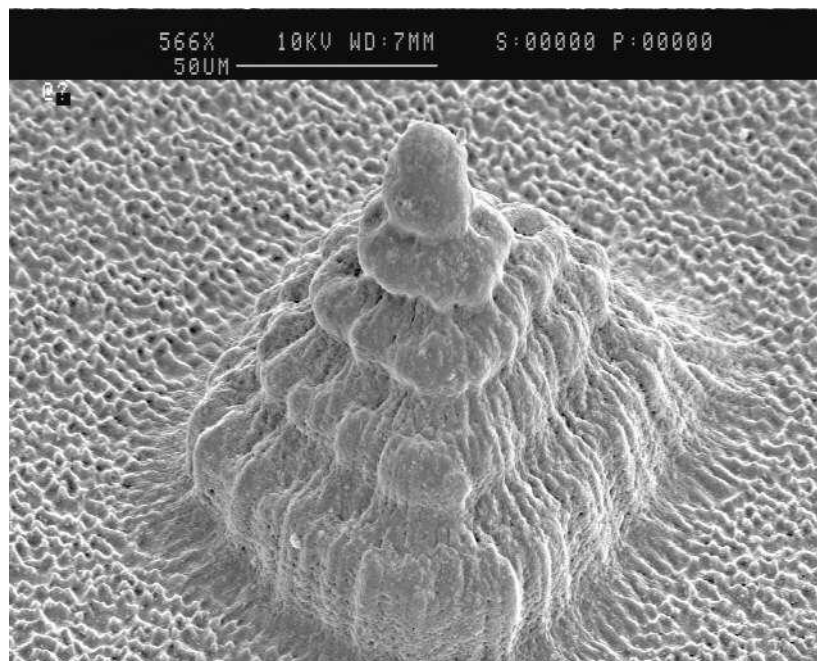


*Figure 5.14 – Pyramidal microstructure fabricated using the Perfactory Mini Multi-Lens system. The structure is 100  $\mu\text{m}$  wide and 125  $\mu\text{m}$  tall, and has a point of 20  $\times$  20  $\mu\text{m}$  area that is the output curing of a single projector pixel.*

#### 5.4 Surface Patterning

As can be seen in *Figure 5.14*, the surface of the bulk cured resin is often rough on a micron scale. It is assumed this roughness is caused by the curing processes of the resin. What is interesting however is that the roughness when viewed from above via an electron microscope (the surface appears smooth under light microscopy) takes on a visible grid-like pattern, as shown in *Figure 5.15*. This grid is formed of 20  $\times$  20  $\mu\text{m}$  squares, again corresponding to a single projector

pixel output. It is currently unknown why this occurs, although presumably it is due to the gaps between the mirrors in the DLP chip. Although DLP chip projectors are meant to be superior to similar LCD devices due to having no “dead space” between pixels, it is apparent that on a very small scale, this dead space is still visible.

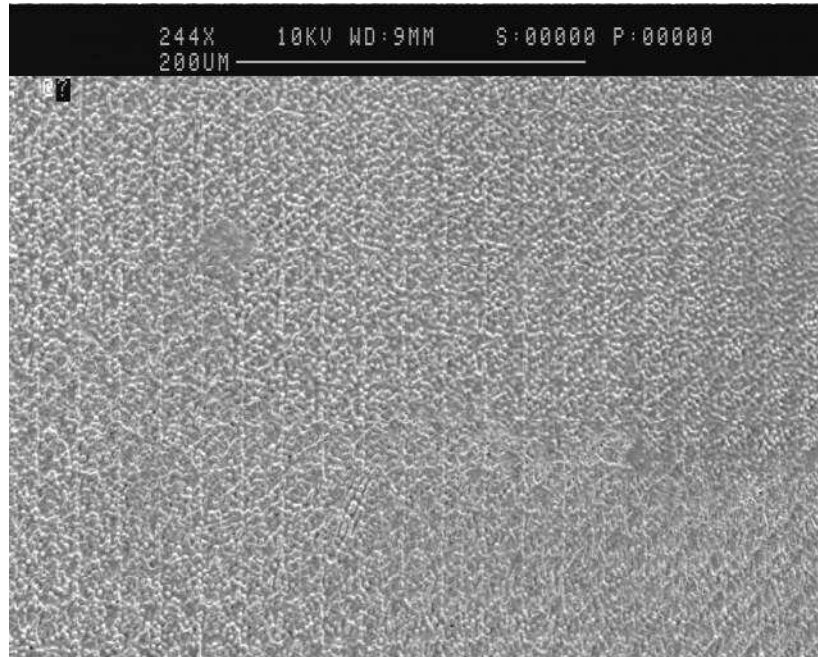


*Figure 5.15 – SEM electron micrograph of bulk cured resin surface, as fabricated by the Perfactory Mini Multi-Lens system. A  $20 \times 20 \mu\text{m}$  grid-like pattern in the surface roughness is clearly visible.*

## 5.5 Fabrication Time

As outlined in section 4.8.2 of the previous chapter, there are a number of machine fabrication parameters that can be altered pre-build. These include the exposure time for each layer, the peeling speed and the waiting time between process steps. For example, in the majority of components presented in this thesis with fine detail (i.e. sub  $500 \mu\text{m}$  features) were fabricated with the peeling speed turned down from  $1 \text{ mm/s}$  to  $0.5 \text{ mm/s}$  in order to reduce the force imparted onto the freshly fabricated features during the peeling process. This however reduces the speed of fabrication. For less complex, “bulk-material” builds, this setting can be left in its default state, as the system defaults have been factory calibrated for use on bigger components for rapid prototyping and form-and-fit applications. *Figure 5.16* compares the fabrication time of a simple cube shape to that of a more complex, membrane-containing design.



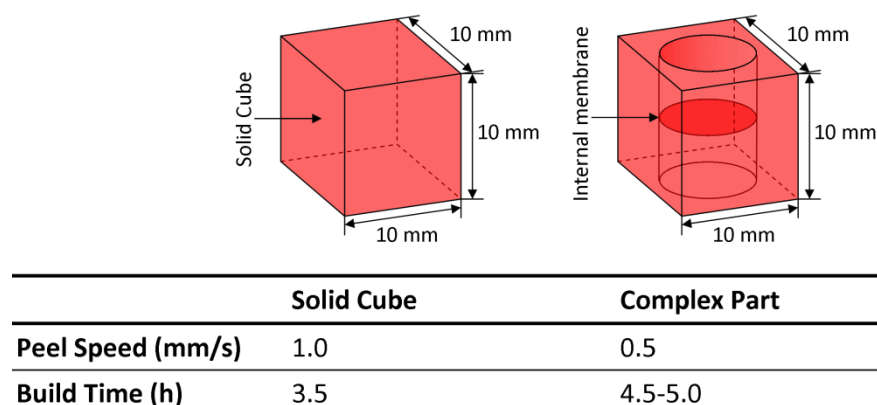


Figure 5.16 – Build time comparison for a simple 10 mm “bulk material” cube fabricated using standard factory settings for peel speed vs. a more complex part, of the same size, containing a thin membrane that requires a half peel speed setting for maximum fabrication yield.

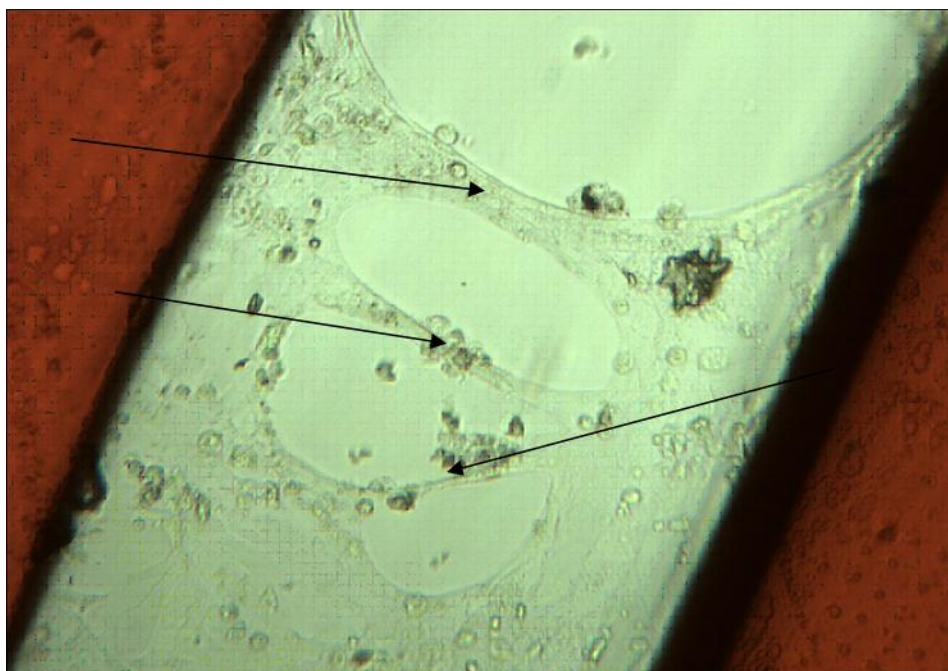


Figure 5.16 – Stem cells growing on a tissue scaffold fabricated from R11 using the Perfactory Mini Multi-Lens System. Clumps of cells are marked. Courtesy of Dr. J. Hoyland of Manchester University School of Medicine.

## 5.6 Biocompatibility Testing

As mentioned previously, collaborative work was carried out using the Perfactory Mini Multi-Lens with Dr. Judith Hoyland of the School of Medicine at Manchester University on potential scaffolds for tissue engineering, specifically for replacement back disks. Samples of the structures were sent to the University of Manchester, where they were treated with stem cells. After 48 hours, it was found that the cells had adhered to the disks, and had started to grow. The

cells adhered to the structure can be seen in *Figure 5.16*. Although this is a significant step towards the production of cell scaffolds by SLA techniques, further research will be needed into the bioabsorbable photocurable materials required for such a process.

## 5.7 Projector Output

The EnvisionTEC Perfactory Mini Multi-Lens SLA system is projector-based, outputting a wide range of light wavelengths across the visible spectrum. In order to investigate the curing mechanism used by the system, an output spectrum was taken using an Ocean Optics HR2000+ High-Resolution spectrometer [2]. The data collected can be seen in *Figure 5.17*. The data shows that the output varies by around 50%, from minima at between 800 and 900 nm (low-end infra red), and peaks at around 720 nm (red) and between 400 and 550 nm (blue/cyan/green).

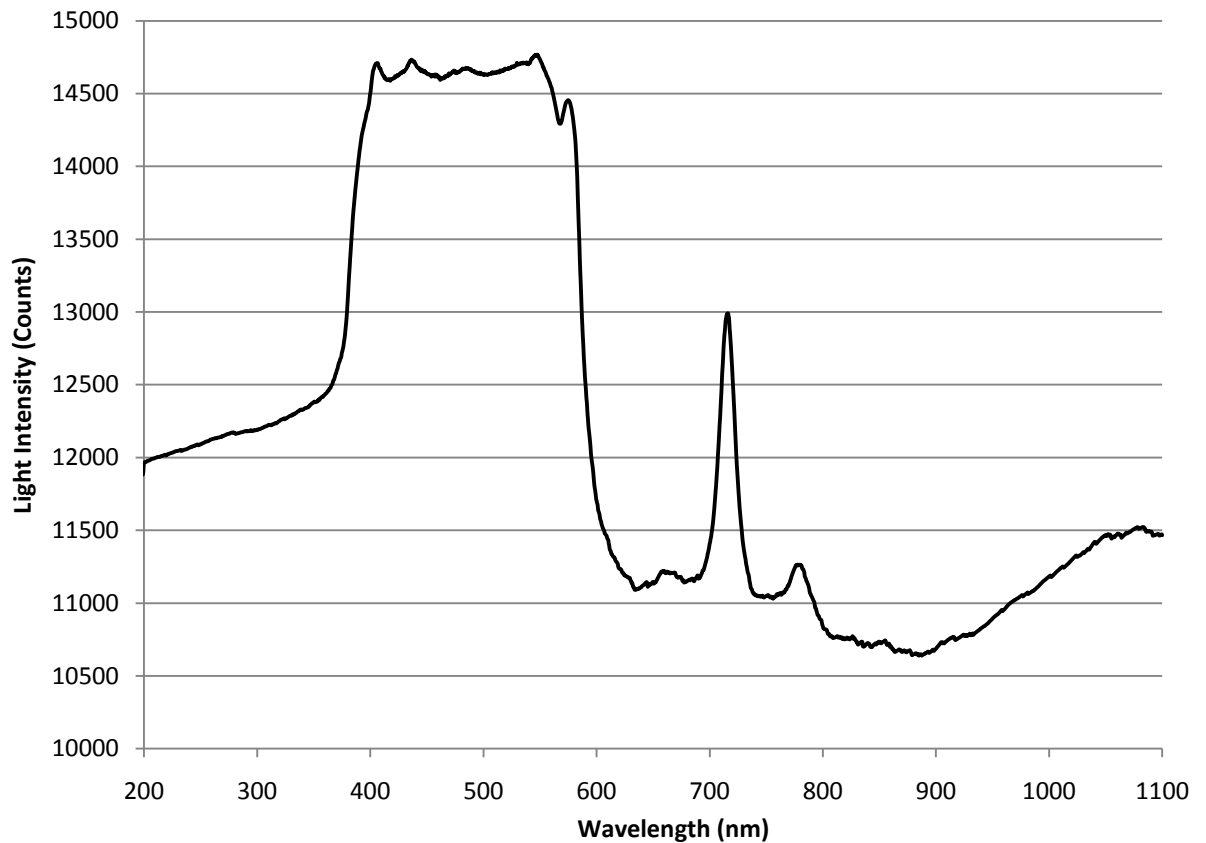


*Figure 5.17 – Spectra obtained from EnvisionTEC Perfactory Mini Multi-Lens system.*

This plot can be compared to the absorption data of the photoinitiator in the EnvisionTEC R11 resin, Ciba® Irgacure® 369. *Figure 5.18* shows the absorption plot, along with the chemical structure of this compound. As can be seen, the majority of the energy absorbed by the initiator is in the UV to high-blue range, with a peak at around 320 nm. Although it is clear therefore that the output of the Perfactory system is not tuned to the input of the initiator used in R11, that the bulb used produces enough light intensity to allow curing. Although this is inefficient, it does allow the system to use a wide variety of initiators to cure an equally wide range of photosensitive resins, unlike laser-based systems where the range of materials is limited by the wavelength of the laser employed.

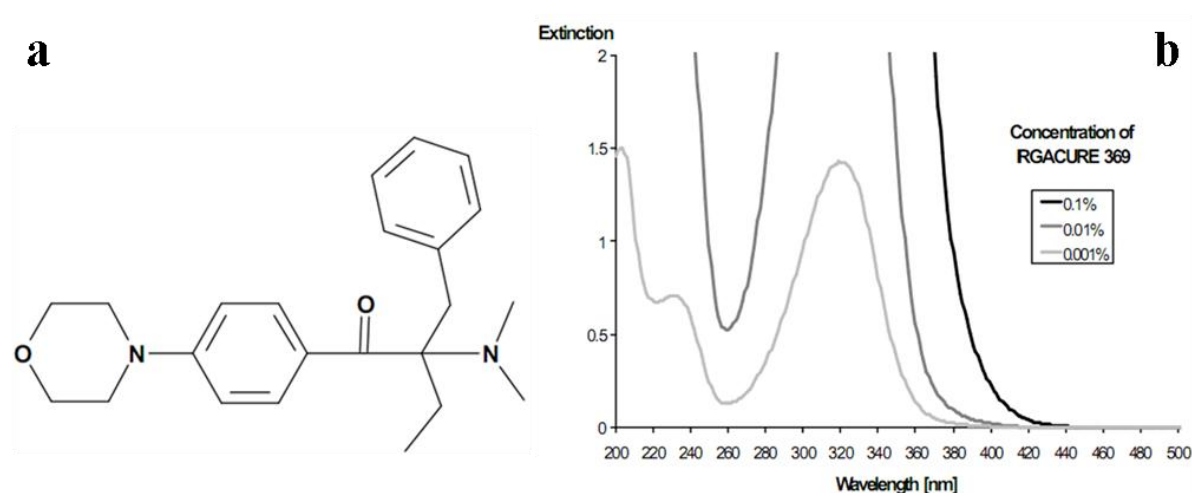


Figure 5.18 – Chemical structure (a) and absorption profile (b) of Ciba® Irgacure® 369 photoinitiator found in EnvisionTEC R11 photosensitive resin. Taken from chemical datasheet [3].

## 5.8 Conclusion

The EnvisionTEC range of SLA systems is unique in the field of SLA systems in its use of projectors rather than lasers. The mechanism used by the EnvisionTEC systems, specifically the Perfactory Mini Multi-Lens, has been discussed in detail. The software used during the system workflow allows great customisation of the fabrication processes, with certain key parameters such as the peeling time having a great effect on the quality of the components produced, and the features achievable. The calibration process also has a bearing on the quality of the components,

although several stages of the procedures such as the projector focussing are somewhat low-tech in their implementation.

A series of test geometries were fabricated using standard build parameters, except with a 500  $\mu\text{m}/\text{sec}$  peeling speed (about 50% of the default). It was found that the major problem of overhangs in component geometries could be solved either via altering the angle of the overhang, by keeping the overhang sufficiently small or by supporting it at both ends with a wall. Part orientation is the major factor when trying to avoid the use of extra support structures, although this can lead to compromises in the design, especially during the fabrication of membrane structures, which must be built horizontally. Other horizontal thin structures such as meshes are another capability. Although vertical thin structures are possible, their use is limited in the Z-axis due to the peeling forces created by the build mechanism.

It has also been shown that complex microfluidic structures are possible using this SLA system. The EnvisionTEC Perfactory machine has an advantage over systems using similar techniques, in that it uses an “upside down” approach, where the new cured resin is added to the bottom of the structure being built. This allows the ceiling of microfluidic channels to be fabricated without the use of supports, provided the channels are small enough; it has been found that square cross-section fluidics in the range of 500-1000  $\mu\text{m}$  in diameter are possible. However, uncured resin is trapped within the internal structures created during the process, which must be removed during cleaning, limiting the length of the internal channels. This limitation can be overcome by exposing the channels to the outside of the structure at regular intervals, or by including “cleaning holes” that can be blocked using other materials after the build is complete.

Tests were carried out into the biocompatibility of the cured R11 resin. Although stem cells were found to adhere and grow on R11 scaffolds, it is not thought that it is a suitable material for implantation, as it does not biodegrade. Further research in this area is required, as

currently there are no commercially-available materials that are suited for this role. The development of new materials for the EnvisionTEC Perfactory range is helped by the use of a wide-spectrum projector, which can potentially activate a wide range of photoinitiators.

Overall, it has been shown in this and the previous chapter that the EnvisionTEC Perfactory Mini Multi-Lens system is able to produce structures for microengineering applications both accurately and quickly. For future reference when building microstructures, the design parameters shown in *Table 5.1* were collated from the test builds outlined in this chapter.

Feature	Theoretical	Expert User	Novice User
Horizontal channel cross-section	10 × 25	100 × 100 (length <5 mm)	500
Vertical hole cross-section	10 × 10	100 × 100 (if drafted out)	500
Wall width	20	20	200
Pillar cross-section	20 × 20	100 × 100	400 × 400
Overhang	-	1.5 mm	1.0 mm
Trench width	20	50—60	100

*Table 5.1 – Design parameters taken from test builds fabricated using the EnvisionTEC Perfactory Mini Multi-Lens SLA system. All values in micron unless otherwise indicated. The “theoretical” values represent the highest resolution obtainable by the machine. “Expert User” values are those that can be in practice achieved under ideal conditions by an experienced system operator, whereas “Novice User” values are those that will nearly always resolve if included in a device design without advanced optimisation or changing of build parameters.*

## 5.9 References

- [1] F. K. Che Harun, P. H. King, J. A. Covington, and J. W. Gardner, "Novel gas chromatographic microsystem with very large sensor arrays for advanced odour discrimination," *IEEE SENSORS 2007*, pp. 1361-1363, 2007.
- [2] O. Optics, "HR2000+ High Resolution Spectrometer," <http://www.oceanoptics.com/products/hr2000+.asp>.
- [3] Ciba, "Irgacure 369," [www.ciba.com/tds\\_369-2.pdf](http://www.ciba.com/tds_369-2.pdf).

# Chapter 6

---

## 6 Microneedles

### 6.1 Introduction

Drugs are a major tool in the treatment of disease. There are a variety of different compounds available for use in medical areas including pain relief, the treatment of microbial infection, vaccines and various anaesthetics. Drugs are also available as lifestyle aids, such as contraceptives and vitamins [1]. In order to be effective, a drug must be absorbed into the bloodstream and be carried until it reaches the area where treatment is required, which may be localised or systemic in nature.

There are 3 main routes for pharmacological agents into the body: oral, topical and intravenous. A given drug can often be administered via multiple routes, to be chosen by the medical professional overseeing the patient's care. The routes available for a drug molecule can be affected by the size of the drug molecule, the position of the malaise to be treated within the body, the chemical properties of the drug e.g. hydrophobicity, the status of the patient and the urgency of the treatment required [2]. Care must also be taken to allow for pharmacokinetic effects, such as the compartmentalisation of drug molecules within certain areas of the body, the agent's half-life within the blood system and the rate of excretion. All of these factors can vary by patient, and are generally dependent on dosing and the period between multiple doses [3].

#### 6.1.1 The Oral Route

The oral route allows the patient to swallow solid pills, or a liquid suspension containing the medication. Although this is probably the most common route taken by over-the-counter medications such as painkillers, it can also be fraught with difficulties. The pill or suspension must survive through the acid environment of the stomach and into the small intestine, where it can be

absorbed into the bloodstream. Once in the blood, the drug must then survive the passage through the liver [1].

### **6.1.2 The Topical Route**

Topical treatments are applied to the skin in cream form, and are absorbed through the epidermis and into the blood capillaries in the superficial arteriovenous plexus. The topical use of drugs is limited to those compounds that are able to cross the stratum corneum, the outer layer of dead cells that provides the main barrier to external damage to the body. The usable compounds are therefore restricted to low molecular-weight lipophilic drugs, and topical treatments are normally restricted to application directly onto a diseased area, such as in the treatment of eczema using hydrocortisone cream. However, some exceptions exist, such as in nicotine and contraceptive patches [1].

### **6.1.3 The Intravenous Route**

For those drugs where neither oral nor topical administration is possible, for example for large molecular weight proteins, intravenous delivery via a hypodermic needle is often the only option. Although in the Western World oral administration is more prevalent, this is sometimes seen as more of a matter of culture than medical importance, and the delivery of more simple drugs via injection is more common in other parts of the world [2].

The first use of a hollow needle in medicine can be found in the writings of the Iraqi ophthalmologist Ammar bin Ali in around 1000 AD. He used the device to suck cataracts from the lenses of effected eyes with some success [4]. It wasn't until the 19<sup>th</sup> Century that the use of hollow needles designed to break the skin was developed independently by both Dr. Alexander Wood of the Royal College of Physicians of Edinburgh [5], and Charles Gabriel Pravaz of Lyon [6]. Wood's needle was developed for the direct injection of opiates for the combat of pain, whereas Pravaz's device was designed to administer precise volumes of ferric chloride for the treatment of aneurysms.

The intravenous route avoids the problems associated with absorption through the gastrointestinal tract and skin, and is often used where the speed of treatment is key. However, the use of hypodermic needles is limited due to a number of factors. Many patients have needle phobias (trypanophobia), and scar tissue can form in areas repeatedly used for injection, limiting intravenous use in patients requiring long-term treatment. There can also be side effects realised due to the high localised concentration of the drug at the insertion point, which can be avoided by using other routes [1]. Intravenous drug delivery does not avoid the problems associated with liver metabolism, kidney excretion and drug compartmentalisation. It does however avoid the initial pass through the liver after absorption via the gastrointestinal tract.

Finally, there are considerable problems with cross-infection of needle users during the sharing of needles, although this is primarily a problem localised to unregulated recreational drug use. However, it is also a problem in developing countries, where the facilities may not exist to properly process used needles, and the finances may not be available to allow the use of disposable equipment. A more serious problem in developed countries is needle-stick injury, where a healthcare professional or patient is accidentally injured by a needle. This injury can occur before or after the needle is used, and there is a high risk of infection following a needle-stick injury by a dirty needle, from serious diseases such as HIV (AIDS) and hepatitis B. The healthcare union UNISON estimated in 2000 that there were around 100,000 needle-stick injuries in the UK each year, whilst the US Centre for Disease Control (CDC) reported that in 1999 between 600,000 and 800,000 healthcare workers suffered needle-stick injuries [7].

However, despite these drawbacks, there are a variety of drugs that require intravenous injection to be effective. An additional factor is the need for controlled bloodletting, either for use in medical tests or in blood transfusions. It can therefore be said that intravenous needles, despite their problems, are here to stay. Researchers are now focussing their attention on working around the major problems associated with hypodermic needles: those of patient pain



and associated phobias, tissue damage, and the risk of needle stick injury and cross-contamination. The former problems can be resolved by design changes, whereas the latter can be solved by a combination of design and financial factors. However, research is not limited to improvements in current therapies, and has also centred on novel approaches such as direct gene therapy and DNA vaccination [8].

## 6.2 Human Skin

### 6.2.1 Structure

The human skin is perhaps the most under-appreciated organ of the body, to the point that the majority of the population would not regard it as an organ at all. It is the barrier between the regulated environment of the body and the unpredictable world beyond, weighing in at an adult average of 4 kg and covering an area of 2 square meters [9]. The major functions of the skin are summarised in *Table 6.1*.

An overview of the histological (cellular) structure of human skin can be seen in *Figure 6.1*. The structure of skin is defined by three main layers. The subcutis hypodermis is the underlying layer, connecting the skin to the underlying tissue, containing the deep arteriovenous plexus (blood vessels) and subcutaneous fat. On top of this lies the dermis, which contains a large number of small blood capillaries, linking from the lower blood vessels to the superficial arteriovenous plexus, a dense layer of arterial and venous capillaries just below the boundary between the dermis and the epidermis. Also contained in the dermis are the dermal nerve fibres and other functional components such as sebaceous and eccrine (sweat) glands and hair follicles.

Finally, the epidermis forms the surface layer of the skin. In terms of drug absorption, this is the most important layer, and is composed of an upper “horny” layer called the stratum corneum, and a lower growing layer known as the basal layer. Although they are seen as separate in histograms, as shown in *Figure 6.2*, they are in fact composed of the same line of cells.

The basal cells divide, pushing the previous generation of cells outwards towards the surface. As they move closer to the edge of the skin, they undergo cellular changes, shutting down all cellular processes and breaking down their nucleus. By the time they arrive at the skin surface, some 60 days after their initial differentiation, they are simply a dead shell, a cellular brick held in regimented layers by a lipid cement [9].

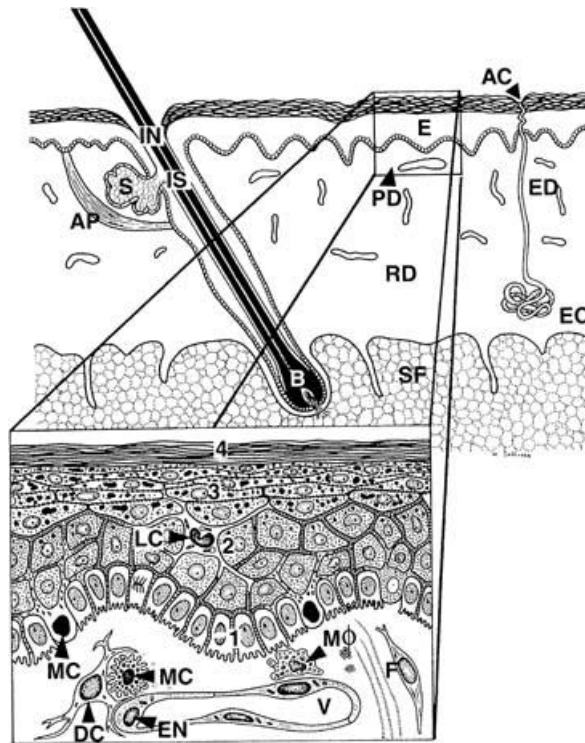


Figure 6.1 - Schematic overview of the architecture and cytologic constituents of normal human skin. This projection demonstrates the cellular components of the epidermis and superficial dermis in greater detail, with epidermal strata denoted numerically. 1, stratum basalis (subcutis hypodermis); 2, stratum spinosum (dermis); 3, stratum granulosum (epidermis, basal layer); 4, stratum corneum (epidermis, horny layer). AC, eccrine acrosyringium; AP, arrector pili muscle; B, follicular bulb; DC, perivascular dendritic cell; E, epidermis; EC, coil of eccrine gland; ED, dermal eccrine duct; EN, endothelial cell; F, fibroblast; IN, follicular infundibulum; IS, follicular isthmus; LC, Langerhans cell; MC, mast cell; Mφ, macrophage; PD, papillary dermis; RD, reticular dermis; S, sebaceous gland; SF, subcutaneous fat; V, vessel. Taken from Velazquez and Murphy, 2004 [10].

An important aspect of skin physiology regarding its penetration by drugs is its thickness, and specifically the thickness of the epidermis. This however can vary from 0.1 mm on the eyelids to nearly 1 mm on the soles of the feet. In general, the thickness tends to vary in proportion to the amount of hair carried by that area of the skin, with regions like the scalp being relatively thin, and hairless areas like the hands and feet being particularly thick [9]. The stratum corneum is the

biggest barrier to high molecular weight, hydrophilic drugs entering the blood, and is generally held to be around 10-20  $\mu\text{m}$  thick [11]. With the dense superficial arteriovenous plexus just below the epidermis, it is obvious that penetration through the skin for drug dispensing or bloodletting need not be further than a few hundred microns. With this in mind, researchers have turned their attention to smaller needle structures, also known as microneedles.

<b>Function</b>	<b>Structure/cell involved</b>
<i>Protection against damage from sources:</i>	
Physical & chemical	Horny layer
UV radiation	Melanocytes
Microbial	Langerhans cells
Preservation of internal environment	Horny layer
Retention of internal fluids and compounds	Horny layer
Shock absorption	Dermis and subcutaneous fat
Temperature regulation	Blood vessels, eccrine sweat glands
Insulation	Subcutaneous fat
Sensation	Specialized nerve endings
Lubrication	Sebaceous gland
Protection and manipulation	Nails
Calorie reserve	Subcutaneous fat
Vitamin D synthesis	Keratinocytes
Body odour/pheromones	Apocrine sweat glands
Psychosocial, display/aesthetic	Skin, lips, hair and nails.

Table 6.1 – Functions of the skin. Adapted from Hunter et al 2002 [9].

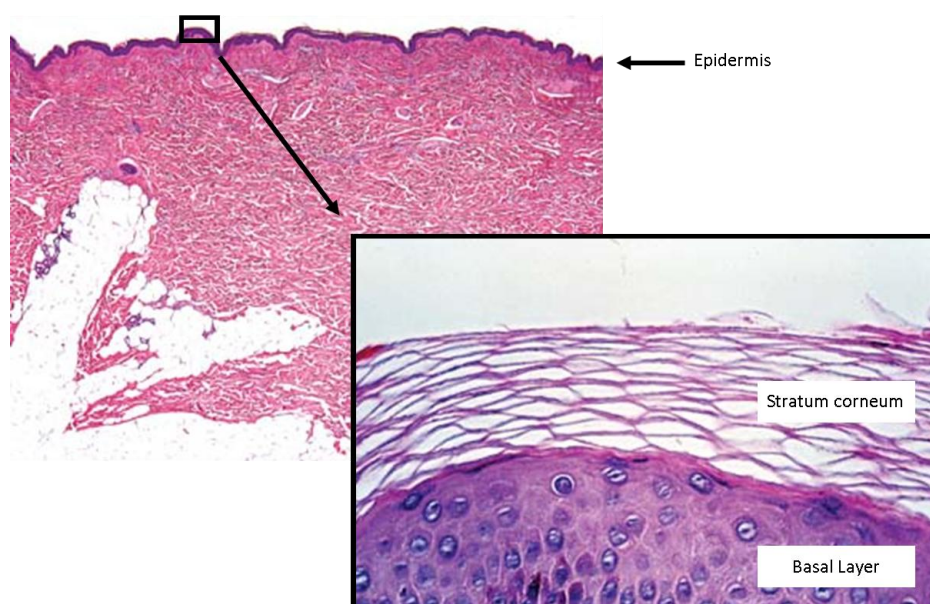


Figure 6.2 – Histograms of the skin, showing the dermis and epidermis (boxout), which itself is composed of the basal layer and the stratum corneum. Adapted from Velazquez and Murphy, 2004 [10].

## 6.2.2 Mechanical Properties of Skin

As said previously, the thickness of human skin varies with its location on the body. There have been a number of publications where the mechanical strength of skin has been tested, summarised in *Table 6.2*.

<i>Authors</i>	<i>Sites</i>	<i>Order of Magnitude</i>	<i>Device</i>
<i>Grahame [12, 13]</i>	<i>Forearm</i>	<i>18 to 57 MPa</i>	<i>Suction</i>
<i>Sanders [14]</i>	<i>Dorsal side forearm</i>	<i>0.1 to 0.02 MPa</i>	<i>Tortion</i>
<i>Alexander [15]</i>	<i>Forearm, upper back</i>	<i>350 to 270 N/m</i>	<i>Suction</i>
	<i>Forearm, anterior back</i>	<i>270 to 800 N/m</i>	
<i>Agache [16]</i>	<i>Dorsal side of the forearm</i>	<i>0.42-0.85 MPa</i>	<i>Tortion</i>
<i>Leveque [17]</i>	<i>Forearm, anterior part</i>	<i>1.1 to 1.32 MPa</i>	<i>Tortion</i>
<i>and Escoffier [18]</i>			
<i>Barel [19]</i>	<i>Forearm</i>	<i>0.13 to 0.17 MPa</i>	<i>Suction</i>
	<i>Forehead</i>	<i>0.20 to 0.32 MPa</i>	
<i>Pannisset [20] and Agache [21]</i>	<i>Forearm, anterior part</i>	<i>0.25 MPa</i>	<i>Suction</i>

*Table 6.2 – Mechanical properties of human skin. Taken from Diridollou et al [22].*

Mathematical models have also been created to model human skin deformation and interactions, either treating skin as a simple isotropic elastic membrane [22], or using a more complex non-homogenous, anisotropic, non-linear approach [23]. However, mathematical models are only accurate to within a certain range, and as can be inferred from *Table 6.2*, initial conditions must be carefully selected to give reasonable output for the site on the body being modelled. Other complications arise due to variability between individuals, and in individuals as they age [13, 18]

## 6.3 Current Microneedle Research

### 6.3.1 Classification

The field of microneedle research is new and rapidly changing in its focus. The idea that a needle needs only penetrate the epidermis in order to deliver therapeutic agents is generally thought to be first found in a patent by Gerstel and Place in 1976 [24]. The principles used by the device are summarised in *Figure 6.3*. Like the majority of microneedles reported in the literature since [25], the device is not a single needle, but an array of identical microstructures, defined as

around 5 to 100  $\mu\text{m}$  tall in the patent. The needles are hollow (not visible in *Figure 6.3*), and connect to a shared reservoir containing the drug to be injected. However, it is not apparent if the patent ever led to any viable devices, and further research was delayed for decades due to the limitations of the microfabrication techniques of the time.

The development of the field can be tracked by review papers found in the literature. McAllister *et al* [8] in 2000 categorised microneedles by the scale of the treatment provided by the microneedle structures, with sections on cellular, localised and systemic drug delivery within the body. The majority of the devices reviewed were based on the micromachining of silicon. Advances in this area had allowed Lin *et al* [26] to produce what are possibly the first microneedles from silicon in their conference paper of 1993, with a later full journal follow-up in 1999 [27]. These devices, 1 to 3 mm in length, were produced laterally upon a silicon substrate using surface micromachining, and included an integrated “blinking bubble” thermopneumatic micropump. The silicon processing steps used in the fabrication of the devices, along with micrographs of the finished structure, can be seen in *Figure 6.4*.

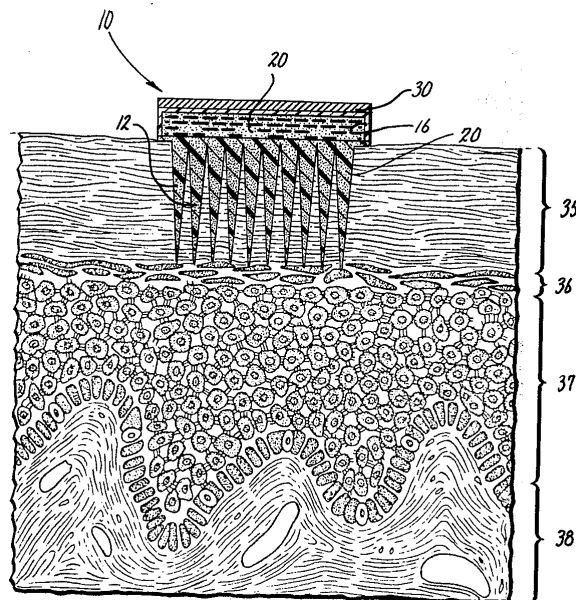


*Figure 6.3 – Drawing showing the principles used by microneedle devices. An array of microstructures 5 to 100  $\mu\text{m}$  tall pierces the skin through the stratum corneum and into the basal layer of the epidermis. The microneedles are hollow (not shown in figure) and connect to a shared reservoir containing the drug. Taken from Gerstel and Place, 1976 [24].*

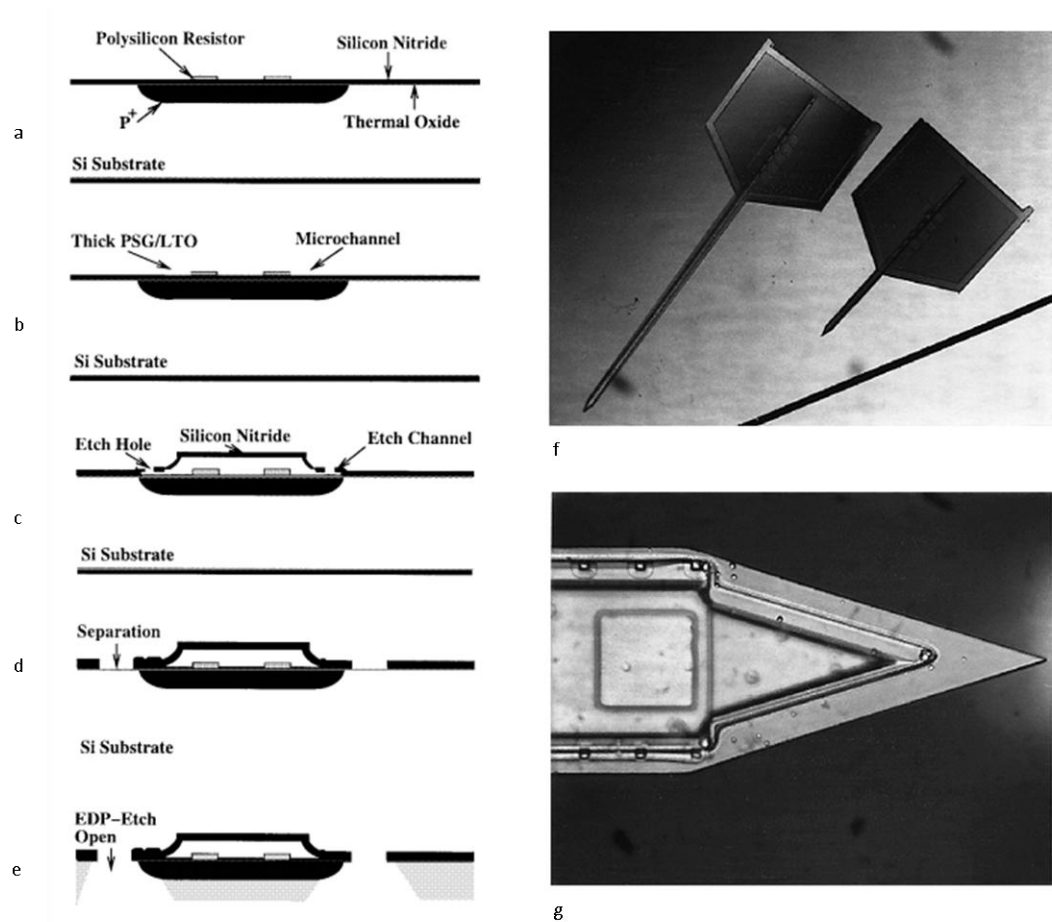


Figure 6.4 – In-plane microneedles developed by Lin *et al* [27].

A later review in 2004 by Reed and Lye [11] grouped the devices by their plane relative to their substrate. This silicon-micromachining-based approach to categorisation was viable at the time, as the majority of devices were still silicon based. The change in characterisation reflected the movement away from single-needle “in-plane” structures, such as those presented by Lin *et al* [26, 27], Brazzle *et al* [28, 29], Papautsky *et al* [30], Talbot and Pisano [31] and Chen *et al* [32]. These structures were complex, both in design and fabrication. Although this meant that additional design features could be integrated, such as MEMS actuators and microsensors, it also made them expensive to manufacture. As a result, most have been used only in neuroscience as probes for sensing and influencing cellular processes.

However, the designs shown earlier in the patent of Gerstel and Place [24] were “out of plane”, and arranged in multi-structure arrays, and the high aspect-ratio fabrication techniques required for their realisation were being developed. In 1998, Henry *et al* [33] produced arrays of

out-of-plane microneedles using reactive ion etching (RIE), which has been a popular fabrication technique since for such silicon-based devices. The structures fabricated can be seen in *Figure 6.5*.

As can be seen, these structures are similar to those postulated by Gerstel and Place's [24] 1976 patent. However, they lack the inner hole or "lumen" found in macroscale hypodermic needles. These types of structures are still useful in therapeutic situations, and are classified in the 2008 review paper by Arora *et al* [25] as "solid" microneedles. The review reflected the evolving field of microneedle research by classifying microneedles under 4 categories: the aforementioned "solid" structures, "hollow" devices, "dissolving" microneedles and "coated" microneedles. All these groups are out-of-plane microneedle arrays, which has now become the prevalent design in therapeutic use, with the area of in-plane devices being dropped entirely. These categories are outlined in *Figure 6.6*.

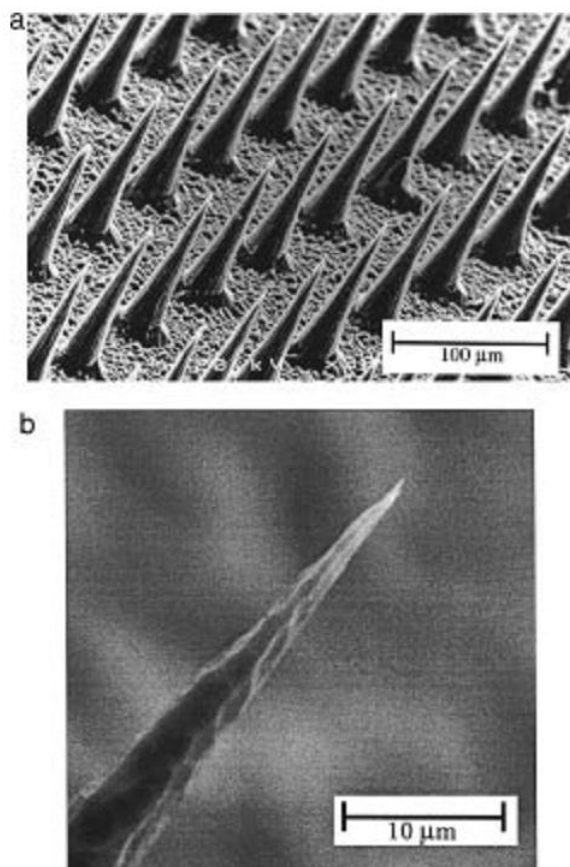


*Figure 6.5 – Scanning electron micrographs of microneedles made by the reactive ion etching technique. Taken from Henry et al [33].*

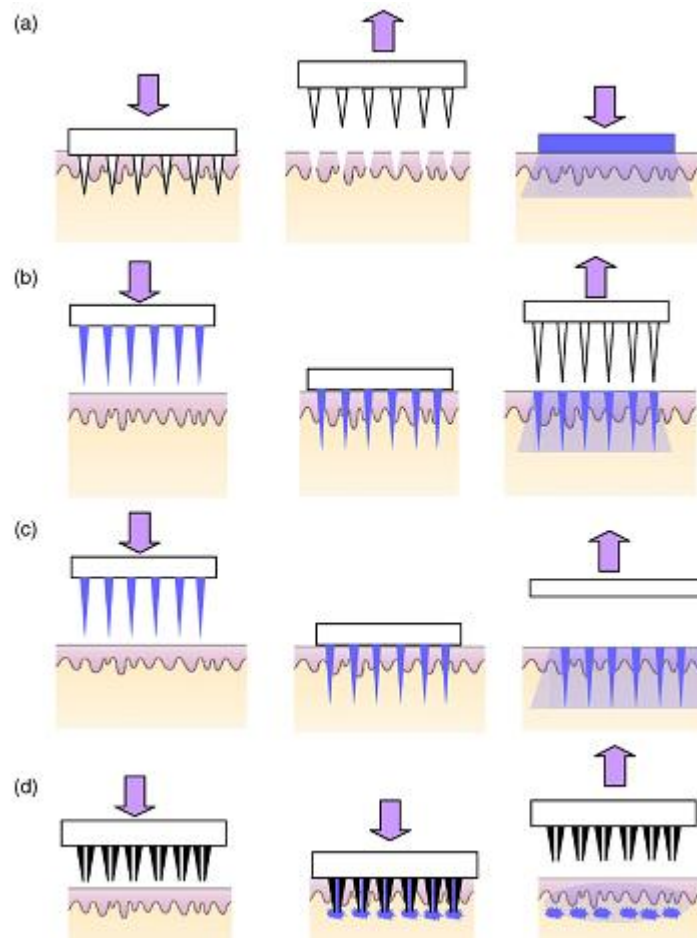


Figure 6.6 - Schematic of drug delivery using different designs of microneedles: (a) solid microneedles for permeabilizing skin via formation of micron-sized holes across stratum corneum. The needle patch is withdrawn followed by application of drug-containing patch, (b) solid microneedles coated with dry drugs or vaccine for rapid dissolution in the skin, (c) polymeric microneedles with encapsulated drug or vaccine for rapid or controlled release in the skin, (d) hollow microneedles for injection of drug solution. Taken from Arora et al [25].

There are a number of reasons out-of-plane microneedles have become more prevalent in the literature. They are less complex in fabrication than their in-plane forefathers, reducing costs and allowing the structures to head towards the \$0.10-1.00 per-device barrier that would need to be crossed to allow commercialisation [25]. Fabrication is also simplified by the fact that the dimensions of the needle structure and/or lumen is controlled lithographically via masks, rather than via film or dope layers that can rarely increase beyond a few tens of micron. They are also in general stronger, as they are part of an array rather than a single fragile structure [11].



### 6.3.2 Solid Microneedles

The simplest subset of out-of-plane microneedle arrays are solid-type, and are simply sharp microstructures capable of breaking through the stratum corneum. Unlike hypodermic needles, they lack the internal bore required for direct injection of drugs, and cannot be used for bloodletting. Instead, drugs can be applied in a topical form, as either a cream or a patch, with the microneedle array creating micro-sized pores in the epidermis through which the drug can be absorbed. This process can increase the skin permeability by several orders of magnitude [33-35].

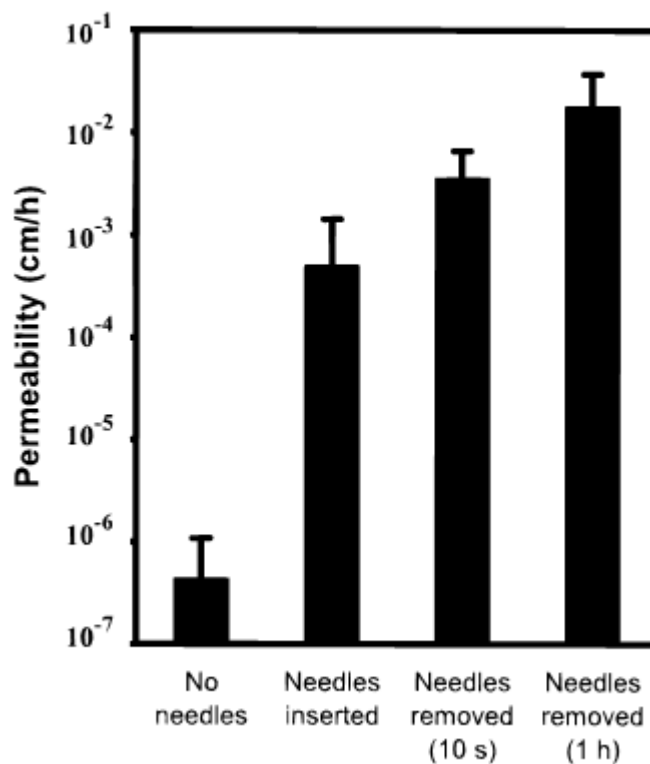
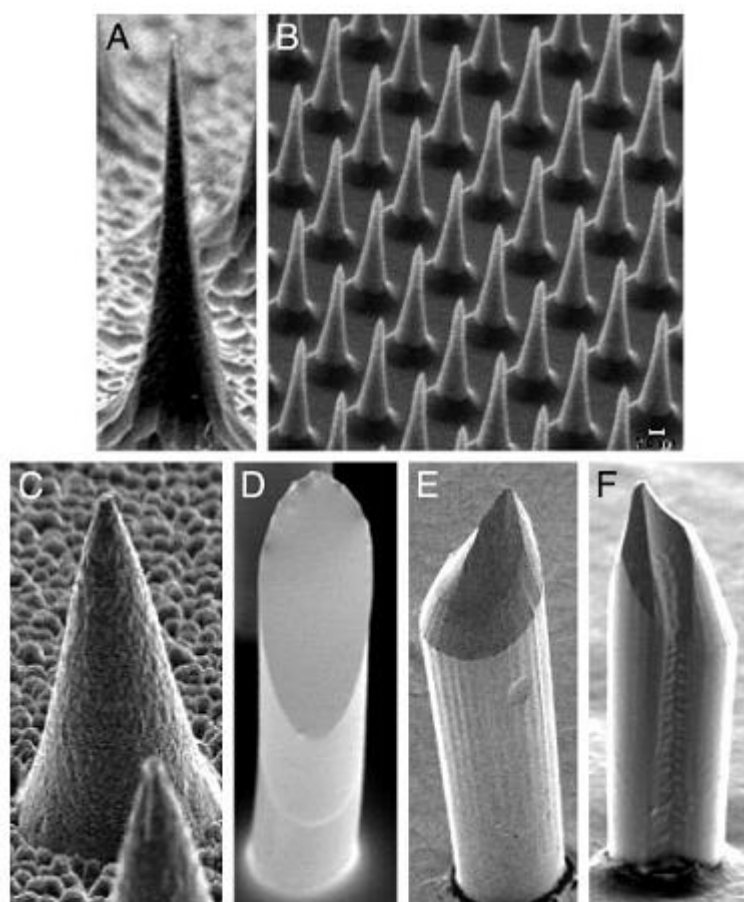


Figure 6.7 – Permeability of human skin treated with different microneedle protocols *in vitro*. Increases of 3 to 4 orders of magnitude were observed for microneedles (1) inserted and left in skin, (2) inserted for 10 s and then removed, and (3) inserted for 1 h and then removed. Such large increases in skin permeability have the potential to significantly increase the number and types of drugs which can be delivered across the skin. Each data point represents the average of 7 to 9 experiments. Standard deviation bars are shown. Taken from Henry et al [33].

As mentioned previously, the first example of solid microneedles can be found in Henry *et al* [33], the first study to demonstrate microneedles for transdermal drug delivery. The structures (seen in Figure 5 above) were designed to be pressed into the skin, either with the topical cream already applied, or inserted and removed before the cream was applied. Permeability data,

collected *in vitro* using human cadaver skin as the membrane in a Franz diffuser chamber, can be seen in *Figure 6.7*. Similar devices were later produced, along with a number of other microneedle structures, by McAllister *et al* [34] of the same group at the Georgia Institute of Technology. The structures can be seen in *Figure 6.8*, and were fabricated from silicon, metal and polymer materials by a combination of RIE and micromachining, electrodeposition and micromoulding respectively. Similar diffusion tests were carried out as in Henry *et al* [33], showing a major increase in skin permeability of a range of high molecular weight molecules including insulin, calcein and bovine serum albumin (BSA).



*Figure 6.8 – Solid microneedles fabricated out of silicon, polymer, and metal imaged by scanning electron microscopy. (A) Silicon microneedle 150  $\mu\text{m}$  tall from a 400-needle array etched out of a silicon substrate. (B) Section of an array containing 160,000 silicon microneedles (25  $\mu\text{m}$  tall). (C) Metal microneedle (120  $\mu\text{m}$  tall) from a 400-needle array made by electrodepositing onto a polymeric mould. (D–F) Biodegradable polymer microneedles with bevelled tips from 100-needle arrays made by filling polymeric moulds. (D) Flat-bevel tip made of polylactic acid (400  $\mu\text{m}$  tall). (E) Curved-bevel tip made of polyglycolic acid (600  $\mu\text{m}$  tall). (F) Curved-bevel tip with a groove etched along the full length of the needle made of polyglycolic acid (400  $\mu\text{m}$  tall). Taken from McAllister *et al* 2003 [34].*

Mikszta *et al* [35-37] produced arrays of what they termed “microenhancer arrays”, or MEAs. These structures were scraped across, rather than pressed into, the upper layers of the skin, disrupting the cellular organisation and allowing the passage of DNA vaccine into the basal epithelium and the supporting layers. Gene expression reported after topically-applied gene transfer was found to be 1,000-2,800-fold higher after MEA treatment in a mouse model, when compared to purely topical treatment. Where 12 passes of the MEAs were applied, gene expression actually outstripped that found when using intravenous and intramuscular macroscale injection [35].

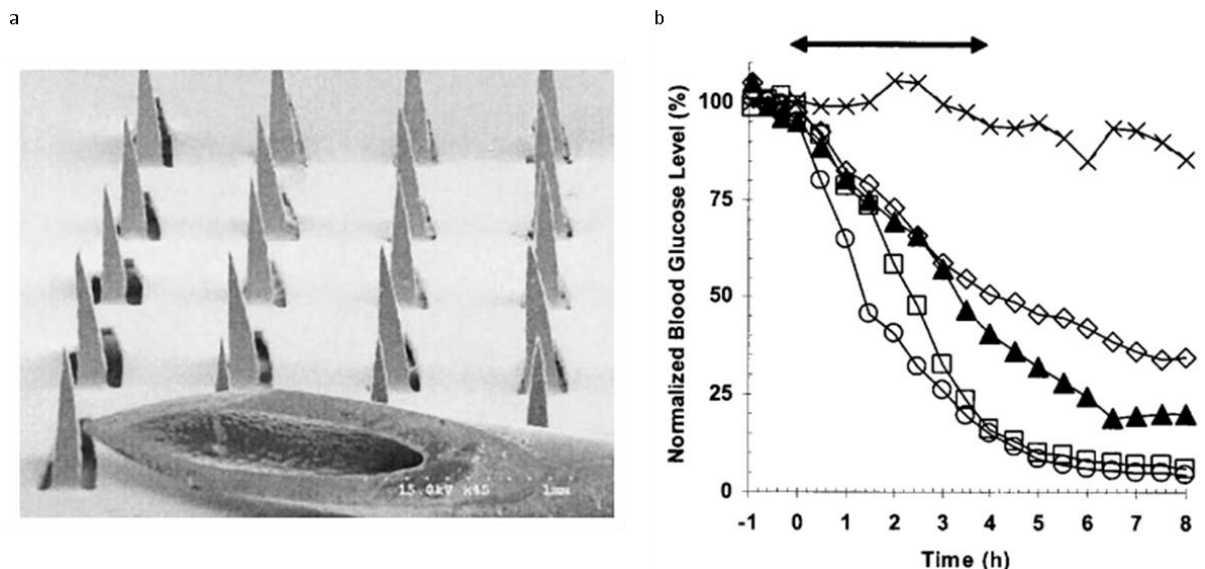


Figure 6.9 – (a) Scanning electron micrograph of solid metal microneedles shown next to the tip of a 27-gauge hypodermic needle. The complete microneedle array contains 105 needles, each measuring 1000  $\mu\text{m}$  in length, 50  $\mu\text{m}$  by 200  $\mu\text{m}$  in cross section at the base, and tapering to a sharp tip with an angle of 20°. (b) Changes in blood glucose level in diabetic, hairless rats after insulin delivery using microneedles (▲), subcutaneous hypodermic injection of 0.05 U (◇), 0.5 U (□), or 1.5 U (○) of insulin, or passive delivery across untreated skin (x). Microneedles were inserted into skin for 10 min and then removed. Insulin solution was applied to the skin immediately after microneedle insertion and left on the skin for 4 h (as shown by arrow). Subcutaneous injections took a few seconds to perform. The pharmacodynamic effect of insulin delivery by microneedles was bounded by that of 0.05-0.5 U injected subcutaneously. Data are expressed as mean values ( $n \geq 3$ ) with average standard deviation associated with each data point of 14%. Blood glucose levels have been normalised relative to average pretreatment levels. From Martanto *et al* [38].

Another paper, again from Georgia Tech, demonstrated laser cut metal microneedles [38]. As shown in Figure 6.9a, the structures produced were simply triangle-cut sections of the 50  $\mu\text{m}$ -thick stainless steel sheet, bend upwards to create the needle array. In Figure 6.9b, the results of *in vivo* tests in a hairless rat model are shown. Hairless rats were given type 1 diabetes,

using an injection of streptozotocin, which is toxic to the pancreatic cells, which normally produce insulin. A topical insulin solution was applied to skin treated with the microneedles, and the fall in glucose levels were compared with injected insulin of varying concentration. The microneedle delivery route was found to reduce the concentration of glucose in the rat's bloodstream by around 80%, 6.5 hours after the treatment. This was around 4 times the drop seen in the control, and comparable to the effect seen in the intravenous route. However, it should be noted that the microneedles were left in place for around 10 minutes, and the topical solution was left in place for around 4 hours. Although this may sound excessive, it is possible in treatment that a patch containing the insulin could be used instead of a loose solution.

### 6.3.3 Hollow Microneedles

A number of out-of-plane microneedle structures have been produced that do have a central lumen. In theory, these structures allow the controlled injection of therapeutic agents in solution, rather than simply relying on increased diffusion as with solid microneedles. Assuming the microneedles are long enough to get through the basal layer of the epithelium, they can reach the superficial arteriovenous plexus, allowing systemic delivery of drugs and bloodletting. This is however at the expense of mechanical strength, as hollow structures of similar dimension to their solid counterparts must by definition be fabricated from less material. The lumen must be kept clear of tissue during needle insertion in order for the devices to function.

The first hollow out-of-plane microneedle arrays were fabricated by Chun *et al* [39]. They were fabricated using silicon micromachining, with the 5  $\mu\text{m}$  wide, 30  $\mu\text{m}$  long structures were designed for transfecting individual cells with DNA. The fabrication process, along with electron micrographs of the finished structures, is shown in *Figure 6.10*. Although the structures presented are both elegant and ideally suited for cellular delivery, they are not suitable for general medical use. Although their 30  $\mu\text{m}$  length seems about the perfect length to pierce the 15 to 25  $\mu\text{m}$  thick stratum corneum, in practice the required length is closer to 100 to 150  $\mu\text{m}$ , due to

skin features such as wrinkles and hair. The fact that the microneedles are in arrays also has a bearing, as the skin is distorted by the surrounding microneedle structures.

Another out-of-plane hollow microneedle array fabricated using silicon micromachining techniques, in conjunction with RIE, can be seen in Gardiniers *et al* [40] in 2003. As shown in *Figure 6.11*, an initial horseshoe-shaped structure was fabricated with an internal elliptical post via wet etching and silicon nitride deposition techniques. This then formed an etch-resistant mask, that allowed an off-plane slow etch across an Si(111) plane, forming the microneedle structure.

An interesting way to avoid blockage of the needle lumen is outlined in Griss and Stemme [41]. Again, silicon microstructures were fabricated using micromachining techniques and RIE, with RIE used to define the high aspect-ratio features. The structures realised are shown in *Figure 6.12*.

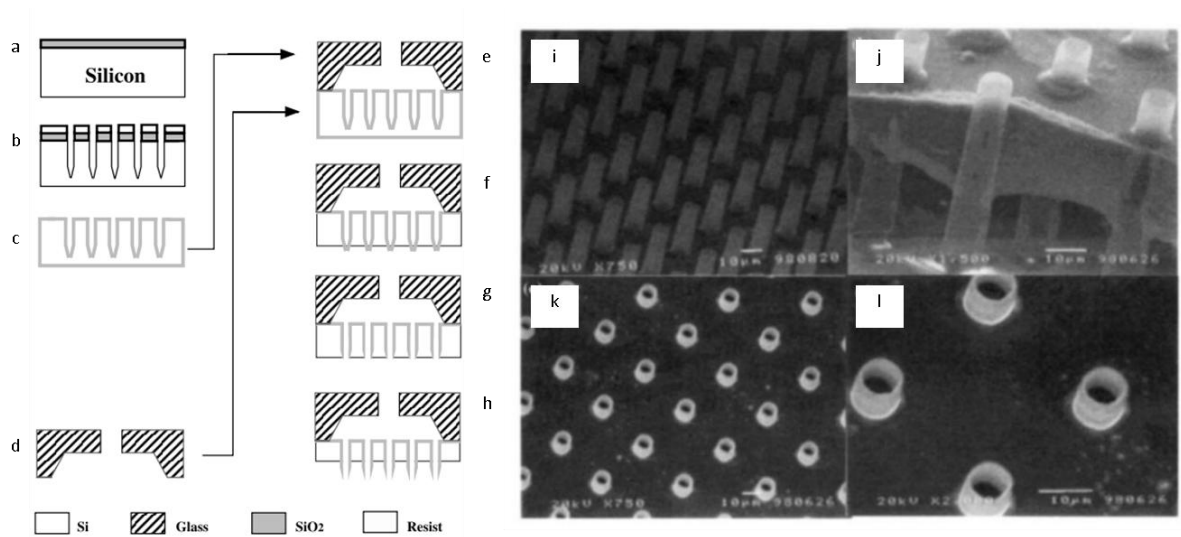


*Figure 6.10 – Process flow for hollow microneedles presented in Chun et al [39]. (a) Silicon wafer is patterned. (b) Silicon is etched as deep as 100  $\mu\text{m}$ . (c) The entire wafer is reoxidised 1 to 2  $\mu\text{m}$ . (d) A Pyrex glass substrate is drilled and etched in BHF. (e) The silicon part is bonded anodically with a processed Pyrex glass. (f) Back-side silicon etching in TMAH solution. (g) Tip oxide etching in buffered HF. (h) Silicon etching in TMAH. (i) Hollow microcapillaries, 30  $\mu\text{m}$  long, approximately 5  $\mu\text{m}$  in diameter, and 1  $\mu\text{m}$  in thickness. (j) Cross-sectional view of hollow microcapillaries. (k) Top view. (l) Close-up view of (j).*

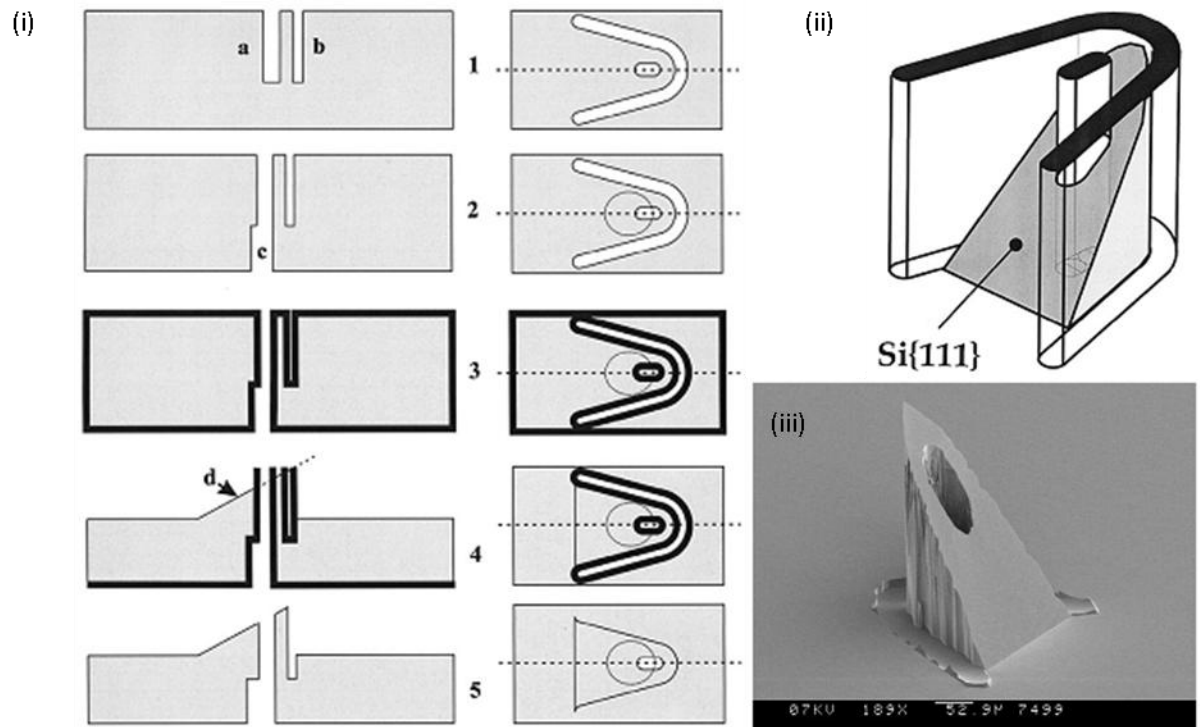


Figure 6.11 – Microneedles fabricated by Gardiniers et al [40]. (i) Microneedle fabrication sequence. The drawings on the left give a cross section of the structure after each processing step, along the dotted line in the top view drawings that are shown on the right. The thick black line represents a silicon nitride coating that is used as a protection layer during KOH etching. (ii) The slot and flow channel, bound by silicon nitride walls that are resistant against KOH etching, after step 4 of the process sequence in (i). (iii) SEM picture of a 350  $\mu\text{m}$  high microneedle, with a base of 250  $\mu\text{m}$  (measured in widest direction). The elliptical flow channel is 70  $\mu\text{m}$  in its widest direction.

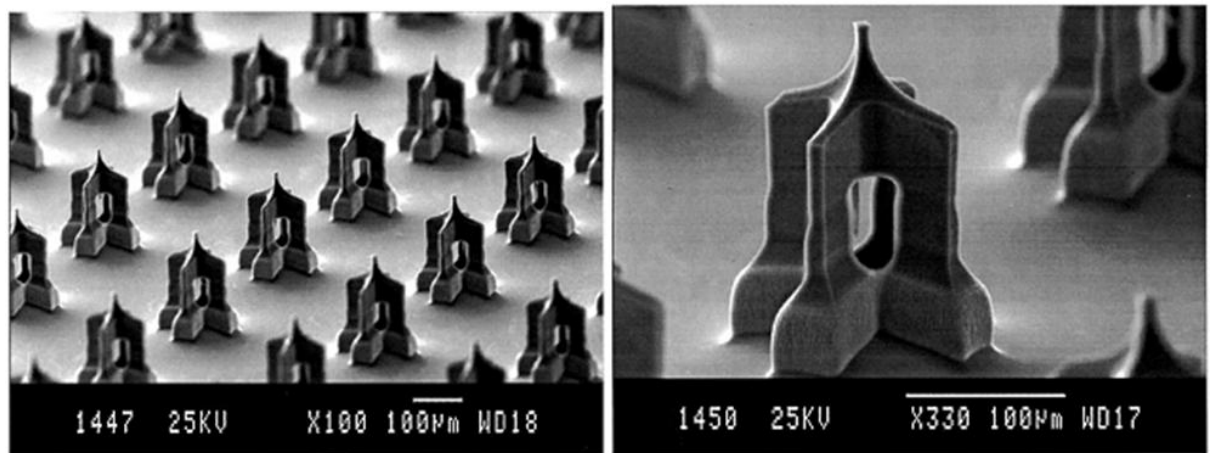


Figure 6.12 –SEM images of side-opened microneedles, the hole beginning approximately 50  $\mu\text{m}$  above the base of the needle. The length of the structure is 210  $\mu\text{m}$ . Taken from Griss and Stemme [41].

Moon *et al* [42] used LIGA, or X-ray lithography to shape PMMA hollow microneedle structures. The technique has been discussed in previous chapters, but basically involves the use of a collimated X-ray beam to expose and break down PMMA resist layers. Moon *et al* used a masked beam perpendicular to the array plane to define the triangular structures, along with their central lumen, followed by an angled beam to taper the structures to a tip. Although high aspect-ratio structures are possible using LIGA, the expense of obtaining time on the synchrotron X-ray sources required is prohibitive and limits LIGA use in practice.

#### 6.3.4 Safety and Pain Response

As the use of microneedles of any kind is in its infancy, it is perhaps too early to comment fully on the safety of microneedles. It is apparent though that they could offer advantages over traditional hypodermic needles. Hypodermic needles are long, and must be inserted manually due to their size. Microneedles require less accurate targeting to be effective, so long as they are used on skin thin enough for the structures to pierce. This could allow for automated systems, where the needle arrays are retracted into a protective casing before and after action, reducing the risk of infection by needlestick injury. So far, there have been no infections reported as a result of microneedle action, irritation is reported in a variety of publications as being mild and very little bleeding is normally found during *in vivo* testing [25].

Another key design point is to minimise the amount of pain experienced by the patient. A number of *in vivo* studies have reported subjects reporting very little or no pain, with needles up to a couple of hundred micron reports no pain [35, 41, 43]. A more in-depth analysis was carried out by Gill *et al* [44], who used double-blind tests with analogue scale pain response measurement. The microneedles were fabricated using the laser cutting process described previously [45], in a range of heights and widths. In all cases, the pain experienced by the subjects was significantly less than that found when hypodermic needles were used. It was found a 3-fold increase in microneedle height lead to a 7-fold increase in pain, whilst a 10-fold increase in the

number of microneedles doubled the pain experienced. It was concluded that microneedles not only reduced pain due to their physical size, but also greatly reduced the anxiety associated with hypodermic needles.

## 6.4 Conclusion

The human skin is a potent barrier to large, hydrophilic drug molecules, and topical administration is limited as a result. Due to the inherent limitations of the oral route, with difficulties in both internal absorption and degradation in the gastrointestinal tract, a large number of drug molecules such as insulin must be administered via the intravenous route. A number of problems are associated with intravenous administration, including needle stick injury, damage to tissue due to repeated insertion and patient phobias. Microneedles offer a potential route around these problems, along with offering many unique treatment types not available using traditional hypodermic needles.

Much like the development of micropump research, initial microneedle fabrication techniques were confined to silicon micromachining. Early papers reported in-plane needles, which tended to be relatively long, and complex in both fabrication and structure. This limited their appeal for mass production due to fabrication costs, although the ability to integrate features such as micropumps and electrodes directly into the needle structures means that they have still found use in fields such as neurology and biological research.

More recently, the focus has turned to out-of-plane arrays of microneedle structures, aided by the development of high aspect-ratio silicon etching techniques such as RIE. These much smaller geometries, normally between 100 and 1000  $\mu\text{m}$  tall are in general much simpler to fabricate due to their structure. Four main areas of research have developed. Simple micro-scale sharp structures can be used as solid microneedles, which open pores in the upper layers of the skin. This treatment of the skin allows much greater transit through the skin via subsequent topical application of drug molecules than if the microneedles had not been used.



Hollow microneedles attempt to replicate hypodermic needles on a micro-scale, and have been fabricated in glass using traditional glass-pulling techniques, PMMA using LIGA and metals using electrodeposition into polymer moulds. Micromoulding in polymer or silicon masters has become a popular fabrication technique for the shaping of polymer microneedle arrays. It can be noted that rapid manufacture techniques such as stereolithography have never been used in the literature for the creation of microneedle arrays, and this is potential area of future research.

It is likely that the full commercialisation of microneedle devices is less than a decade away. Their arrival will need to be preceded in a reduction in production costs and detailed clinical trials investigating their safety and efficacy. However, it is obvious that they have the potential to revolutionise the field of drug delivery and the collection of blood samples for analysis.

## 6.5 References

- [1] B. Greenstein and A. Greenstein, "Concise Clinical Pharmacology," 2007.
- [2] R. G. Finch, "15. General principles of the treatment of infection," In Greenwood, D. ed. Antimicrobial Chemotherapy, vol. 3rd Edition, 1995.
- [3] S. S. Jambhekar and P. J. Breen, "Basic Pharmacokinetics," 2009.
- [4] I. B. Syed, "Islamic Medicine: 1000 Years Ahead of its Times," JISHIM, vol. 2, pp. 2-9, 2002.
- [5] A. Wood, "A new method of treating neuralgia by the direct application of opiates to the painful points," Edin Med Surg J, pp. 265-281, 1855.
- [6] J. Rosenhek, "Needle trade," Doctor's Review, vol. [online], 2009.
- [7] "Sharp end," Hazards, pp. 4-5, 2000.
- [8] D. V. McAllister, M. G. Allen, and M. R. Prausnitz, "Microfabricated microneedles for gene therapy and drug delivery," Annual Review of Biomedical Engineering, vol. 2, pp. 289-313, 2000.
- [9] J. Hunter, J. Savin, and M. Dahl, "Clinical Dermatology," vol. 3rd Edition, 2002.
- [10] E. F. Velazquez and G. F. Murphy, "Chapter 3 - Histology of the Skin," In Elder, D. E. Ed, LEVER'S Histopathology of the Skin, vol. 9th Edition, 2004.
- [11] M. L. Reed and W. K. Lye, "Microsystems for drug and gene delivery," Proceedings of the IEEE, vol. 92, pp. 56-75, Jan 2004.
- [12] R. Grahame, "Elasticity of human skin in vivo," Ann Phys Med, vol. 10, pp. 130-134, 1969.
- [13] R. Grahame and P. J. L. Holt, "The influence of ageing on the in vivo elasticity of human skin," Gerontologia, vol. 15, pp. 121-139, 1969.
- [14] R. Sanders, "Torsional elasticity of human skin in vivo," Pflugers Arch, vol. 342, pp. 255-260, 1973.
- [15] H. Alexander and T. H. Cook, "The mechanical characterization of human skin in vivo," PhD Thesis, Stevens Institute of Technology, New Jersey, USA, 1975.
- [16] P. G. Agache, C. Monnear, J. L. Leveque, and J. Rigal, "Mechanical properties and Young's modulus of human skin in vivo," Archives of Dermatological Research, vol. 269, pp. 221-232, 1980.
- [17] J. L. Leveque, J. De Rigal, P. G. Agache, and C. Monneur, "Influence of ageing on the in vivo extensibility of human skin at low stress," Arch Dermatol Res, vol. 269, pp. 127-135, 1980.

- [18] C. Escoffier, J. Derigal, A. Rochefort, R. Vasselet, J. L. Leveque, and P. G. Agache, "Age-Related Mechanical-Properties of Human-Skin - an Invivo Study," *Journal of Investigative Dermatology*, vol. 93, pp. 353-357, Sep 1989.
- [19] A. O. Barel, R. Lambrecht, and P. Clarys, "Mechanical function of the skin: state of the art," In Elsner, P., Barel, A. O., Berardesca, E., Gabard, B., Serup, eds. *Skin bioengineering techniques and applications in dermatology and cosmetology*. Curr Probl Dermatol., vol. Basel: Karger, pp. 69-83, 1998.
- [20] F. Panisset, "Le stratum corneum: sa place dans la fonction mecanique de la peau humaine in vivo," MD thesis, Franche-Comte University, Besancon, France, 1992.
- [21] P. G. Agache, "Noninvasive assessment of a biaxial Young's modulus of human skin in vivo," 9th Int Sym Bioeng Skin, vol. Sendai, 1992.
- [22] S. Diridollou, F. Patat, F. Gens, L. Vaillant, D. Black, J. M. Lagarde, Y. Gall, and M. Berson, "In vivo model of the mechanical properties of the human skin under suction," *Skin Research and Technology*, vol. 6, pp. 214-221, Nov 2000.
- [23] F. M. Hendriks, D. Brokken, C. W. J. Oomens, F. P. T. Baaijens, and J. B. A. M. Horsten, "Mechanical properties of different layers of human skin," MATE internal presentation, vol. Available online: <http://www.mate.tue.nl/mate/pdfs/249.pdf> [Accessed 10th August 2009], 2000.
- [24] M. S. Gerstel and V. A. Place, "Drug Delivery Device," U.S. Patent No. 3,964,482, 1976.
- [25] A. Arora, M. R. Prausnitz, and S. Mitragotri, "Micro-scale devices for transdermal drug delivery," *International Journal of Pharmaceutics*, vol. 364, pp. 227-236, 2008.
- [26] L. Lin, A. P. Pisano, and R. S. Muller, "Silicon Processed Microneedles," *Dig. Transducers '93, Int. Conf. Solid-State Sensors and Actuators*, pp. 237-240, 1993.
- [27] L. W. Lin and A. P. Pisano, "Silicon-processed microneedles," *Journal of Microelectromechanical Systems*, vol. 8, pp. 78-84, Mar 1999.
- [28] J. Brazzle, S. Mohanty, and A. B. Frazier, "Hollow metallic micromachined needles with multiple output ports," *Proc. SPIE, Microfluidic Devices and Systems II*, vol. 3877, pp. 257-266, 1998.
- [29] J. D. Brazzle, I. Papautsky, and A. B. Frazier, "Micromachined needle arrays for drug delivery or fluid extraction," *Ieee Engineering in Medicine and Biology Magazine*, vol. 18, pp. 53-58, 1999.
- [30] I. Papautsky, J. Brazzle, H. Swerdlow, R. Weiss, and A. B. Frazier, "Micromachined pipette arrays," *Ieee Transactions on Biomedical Engineering*, vol. 58, pp. 812-819, June 2000 2000.
- [31] N. H. Talbot and A. P. Pisano, "Polymolding: two wafer polysilicon micromolding of closer-flow passages for microneedles and microfluidic devices," *Tech. Dig. Solid-State Sensor and Actuator Workshop*, pp. 265-268, 1998.
- [32] J. Chen, K. D. Wise, J. F. Hetke, and S. C. Bledsoe Jr., "A multi-channel nural probe for selective chemical delivery at the cellular level," *Ieee Transactions on Biomedical Engineering*, vol. 44, pp. 760-769, 1997.
- [33] S. Henry, D. V. McAllister, M. G. Allen, and M. R. Prausnitz, "Microfabricated microneedles: A novel approach to transdermal drug delivery," *Journal of Pharmaceutical Sciences*, vol. 87, pp. 922-925, Aug 1998.
- [34] D. V. McAllister, P. M. Wang, S. P. Davis, J. H. Park, P. J. Canatella, M. G. Allen, and M. R. Prausnitz, "Microfabricated needles for transdermal delivery of macromolecules and nanoparticles: Fabrication methods and transport studies," *Proceedings of the National Academy of Sciences of the United States of America*, vol. 100, pp. 13755-13760, Nov 25 2003.
- [35] J. A. Mikszta, J. B. Alarcon, J. M. Brittingham, D. E. Sutter, R. J. Pettis, and N. G. Harvey, "Improved genetic immunization via micromechanical disruption of skin-barrier function and targeted epidermal delivery," *Nature Medicine*, vol. 8, pp. 415-419, Apr 2002.
- [36] J. A. Mikszta, V. J. Sullivan, C. Dean, A. M. Waterston, J. B. Alarcon, J. P. Dekker, J. M. Brittingham, J. Huang, C. R. Hwang, M. Ferriter, G. Jiang, K. Mar, K. U. Saikh, B. G. Stiles, C. J. Roy, R. G. Ulrich, and N. G. Harvey, "Protective immunization against inhalational anthrax: A comparison of minimally invasive delivery platforms," *Journal of Infectious Diseases*, vol. 191, pp. 278-288, Jan 15 2005.
- [37] J. A. Mikszta, J. P. Dekker, N. G. Harvey, C. H. Dean, J. M. Brittingham, J. Huang, V. J. Sullivan, B. Dyas, C. J. Roy, and R. G. Ulrich, "Microneedle-based intradermal delivery of the anthrax recombinant protective antigen vaccine," *Infection and Immunity*, vol. 74, pp. 6806-6810, Dec 2006.
- [38] W. Martanto, S. P. Davis, N. R. Holiday, J. Wang, H. S. Gill, and M. R. Prausnitz, "Transdermal delivery of insulin using microneedles in vivo," *Pharmaceutical Research*, vol. 21, pp. 947-952, Jun 2004.

- [39] K. Chun, G. Hashiguchi, H. Toshiyoshi, and H. Fujita, "Fabrication of array of hollow microcapillaries used for injection of genetic materials into animal/plant cells," *Japanese Journal of Applied Physics Part 2-Letters*, vol. 38, pp. L279-L281, Mar 1 1999.
- [40] H. J. G. E. Gardeniers, R. Luttge, E. J. W. Berenschot, M. J. de Boer, S. Y. Yeshurun, M. Hefetz, R. van't Oever, and A. van den Berg, "Silicon micromachined hollow microneedles for transdermal liquid transport," *Journal of Microelectromechanical Systems*, vol. 12, pp. 855-862, Dec 2003.
- [41] P. Griss and G. Stemme, "Side-opened out-of-plane microneedles for microfluidic transdermal liquid transfer," *Journal of Microelectromechanical Systems*, vol. 12, pp. 296-301, Jun 2003.
- [42] S. J. Moon and S. S. Lee, "A novel fabrication method of a microneedle array using inclined deep x-ray exposure," *Journal of Micromechanics and Microengineering*, vol. 15, pp. 903-911, May 2005.
- [43] S. Kaushik, A. H. Hord, D. D. Denson, D. V. McAllister, S. Smitra, M. G. Allen, and M. R. Prausnitz, "Lack of pain associated with microfabricated microneedles," *Anesthesia and Analgesia*, vol. 92, pp. 502-504, Feb 2001.
- [44] H. S. Gill, D. D. Denson, B. A. Burris, and M. R. Prausnitz, "Effect of microneedle design on pain in human volunteers," *Clinical Journal of Pain*, vol. 24, pp. 585-594, Sep 2008.
- [45] H. S. Gill and M. R. Prausnitz, "Coated microneedles for transdermal delivery," *Journal of Controlled Release*, vol. 117, pp. 227-237, Feb 12 2007.

# Chapter 7

## 7 Microneedle Design and Optimisation

### 7.1 Introduction

In the previous chapter, the field of microneedles was reviewed. In the following sections, the development of a range of arrays of SLA-fabricated microneedles will be documented, from the CAD design, through the finite element analysis and ending with the mechanical testing of the optimised designs.

### 7.2 Microneedle Design

A range of 5 microneedle geometries were designed using the SolidWorks computer aided design (CAD) package. The designs are shown in *Figure 7.1*. The designs shown were chosen to reflect a selection of the structures found in the literature, allowing the optimum design to be chosen using finite element analysis (FEA) modelling techniques.

Each design has a number of key variables, which can be altered during FEA modelling to produce the optimum combination for each of the geometries shown in *Figure 7.1*. These key variables are shown in *Figure 7.2*. The range of variables used in this study are shown in *Table 7.1*, along with a number of variables taken from the literature for comparison.

<i>Reference</i>	<i>Tip Radius (<math>\mu\text{m}</math>)</i>	<i>Needle Height (<math>\mu\text{m}</math>)</i>	<i>Bore Radius (<math>\mu\text{m}</math>)</i>	<i>Base Width (deg)</i>	<i>Array Spacing (<math>\mu\text{m}</math>)</i>
<i>This Study</i>	<i>15 - 60</i>	<i>200 - 1200</i>	<i>15 - 45</i>	<i>150 – 600</i>	<i>200 – 800</i>
<i>McAllister et al [1]</i>	<i>75</i>	<i>500</i>	<i>22.5</i>	<i>300</i>	<i>~ 400</i>
<i>Stoeber and Liepmann [2]</i>	<i>50</i>	<i>200</i>	<i>20</i>	<i>425</i>	<i>~ 500</i>
<i>Griss and Stemme [3]</i>	<i>10</i>	<i>200</i>	<i>30</i>	<i>160</i>	<i>~ 300</i>

*Table 7.1 – Range of variables considered in this study, compared to previous work in the literature.*

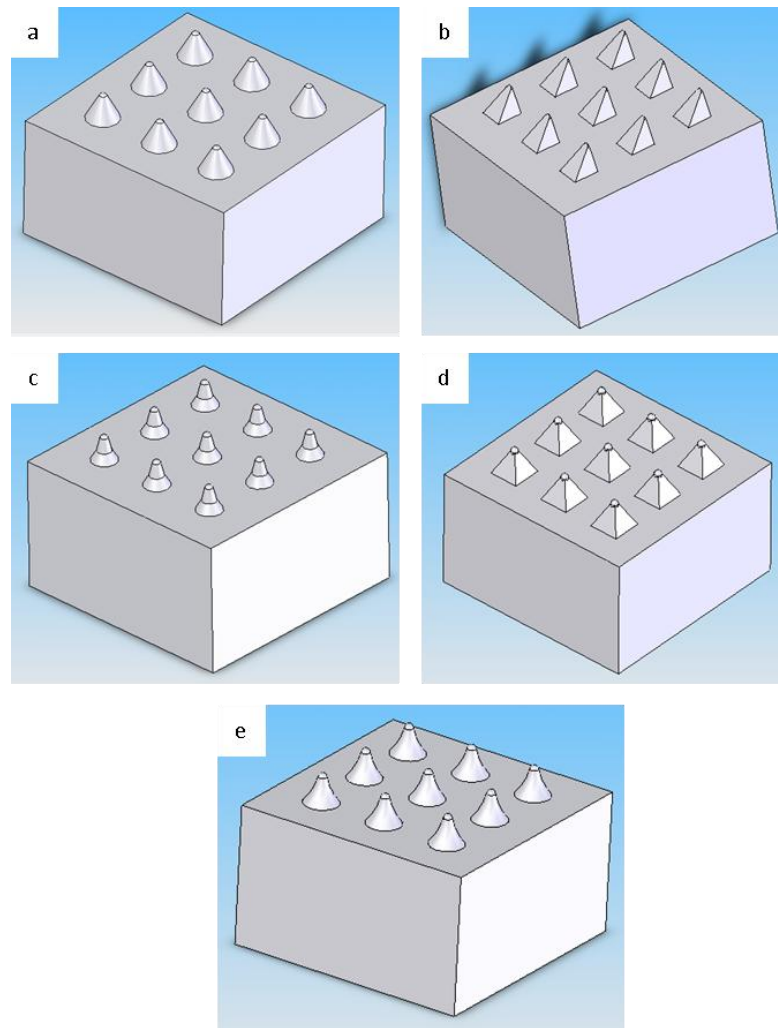


Figure 7.1 – Microneedle array structures, designed using SolidWorks CAD package. (a) Conical, (b) asymmetric pyramid, (c) stepped cone, (d) symmetric pyramid and (e) inverted trumpet.

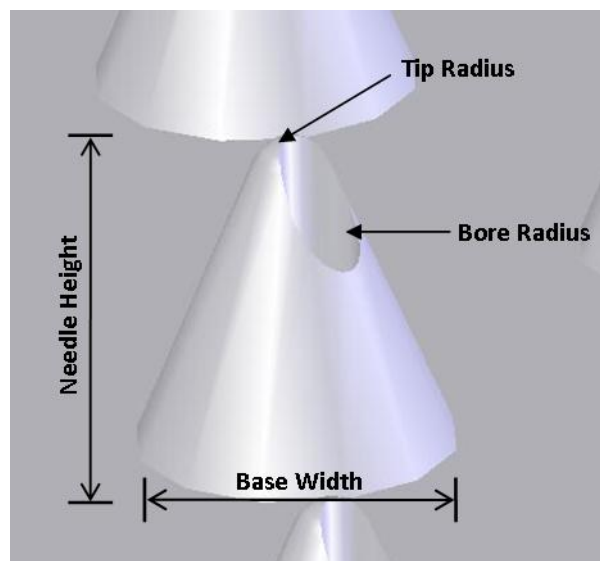


Figure 7.2 – Key variables for microneedle geometries tested. Another available variable is the spacing of the array, between microneedle structures.

Although modelling ranges of all of the variables listed in *Table 7.1* would be ideal, it would require too many iterations to be practical. However, the number of design iterations required can be greatly reduced by limiting the parameters varied during the analysis. Davis *et al* [4] in 2004 found the major factors governing the force required to fracture their hollow nickel microneedles, fabricated using LIGA techniques, were the wall thickness, the wall angle and the needle tip radius. As a result, the parameters varied in this study were the bore diameter (analogous to the wall thickness) and tip radius. Bore variation includes no bore, in effect testing a solid microneedle design. The needle height was set at an arbitrary 400  $\mu\text{m}$ , as it was felt this was long enough for skin penetration, and was a height easily fabricated using the EnvisionTEC Perfactory Mini Multi-Lens system, which has a Z-axis resolution of 25  $\mu\text{m}$ . Finally, the microneedle base width was set at and again arbitrary 300  $\mu\text{m}$ .

Individual CAD files were produced for each geometric variation, and tested using SolidWorks' built-in FEA modelling suite, COSMOSWorks. The array models were subjected to incremental force on the needle tip, perpendicular to the array plane. The needle is assumed to have failed once the sum of the stress within the structures reaches the tensile strength of a model photopolymer material, in this case the EnvisionTEC Perfactory resin e-Shell 100 (tensile strength 47.8 MPa). Although this method of analysis, known as the Von Mises method, can underestimate the actual strength of the structures *in vivo*, i.e. when inserted into the skin, this underestimation can be incorporated into the require safety margin required for such devices. The raw data collected is shown in *Table 7.2*, and shown graphically in *Figure 7.3*.

There are a number of observations that can be made from the data shown in *Table 7.2* and *Figure 7.3*. The weakest geometry by far is the asymmetric pyramid, with a failure force of less than one tenth of the other symmetric designs. The addition of a central bore to the design, which was offset from the needle tip, exacerbates this weakness far more than in the other symmetric designs, a result which is in line with previous studies [4]. Several examples of

asymmetric microneedle arrays can be found in the literature, including Gardiniers *et al* [5] and Moon *et al* [6], in silicon via micromachining techniques and PMMA via LIGA processes. In both cases, the asymmetric design was used more because of the limitations of the fabrication process, rather than due to any optimisation steps. It is likely that the design is inefficient when handling load due to the force being offset through the structure, and the success of these designs can perhaps be attributed to the higher tensile strengths of the materials used: 6.9 GPa and 76 MPa for silicon [7] and PMMA [8] respectively, compared to the 47.8 MPa of EnvisionTEC e-Shell 100. It is clear that a more efficient design is required for use with weaker photocurable polymers, and therefore the design of the asymmetric pyramid was discarded.

	<b>Bore Radius (<math>\mu\text{m}</math>)</b>	<b>Tip Radius (<math>\mu\text{m}</math>)</b>			
		<b>15</b>	<b>30</b>	<b>45</b>	<b>60</b>
<b>Conical</b>	0	0.021	0.110	0.267	0.464
	15	0.024	0.104	0.229	0.415
	30	0.020	0.102	0.241	0.428
	45	0.021	0.104	0.254	0.390
<b>Inverted Trumpet</b>	0	0.024	0.102	0.244	0.419
	15	0.025	0.111	0.227	0.419
	30	0.024	0.116	0.224	0.464
	45	0.024	0.115	0.249	0.416
<b>Symmetric Pyramid</b>	0	0.021	0.091	0.212	0.352
	15	0.021	0.089	0.213	0.365
	30	0.019	0.091	0.213	0.375
	45	0.017	0.091	0.217	0.375
<b>Asymmetric Pyramid</b>	0	0.003	0.014	0.026	0.038
	15	0.003	0.013	0.023	0.029
	30	0.003	0.013	0.023	0.030
	45	0.003	0.011	0.021	0.028
<b>Stepped-Cone</b>	0	0.030	0.118	0.256	0.423
	15	0.028	0.101	0.252	0.416
	30	0.028	0.104	0.250	0.423
	45	0.028	0.104	0.256	0.416

Table 7.2 – Simulated failure forces for six microneedle geometries in arrays of  $3 \times 3$  needles. Forces are expressed in Newtons and are per needle.

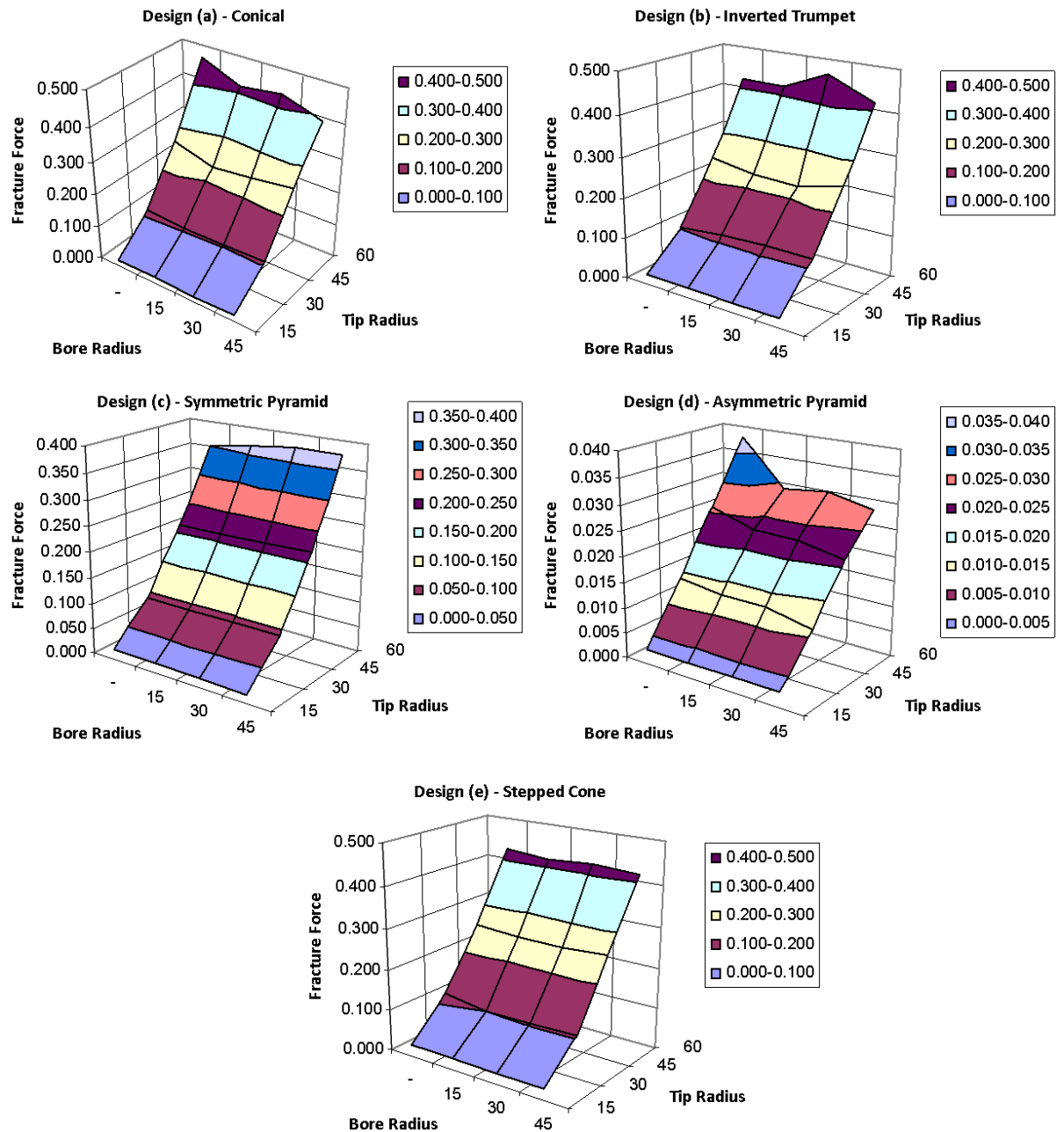


Figure 7.3 – Graphical representations of needle failure force, with respect to microneedle tip and bored radius. All forces in Newtons and are per needle. All radii in micron. Simulated microneedle material is EnvisionTEC e-Shell 100, with a tensile strength of 47.8 MPa.

The data collected shows that, in all the geometries tested, the major variable was the size of the tip, with the bore radius making relatively little difference. This is perhaps not surprising, as a large needle tip will distribute the force more efficiently when in contact with a flat, hard surface, which is applicable in these models. However, although the overall strength of the microneedle structure is important, it is not the only factor governing their efficiency. A sharper needle point will concentrate the force exerted through the needle over a smaller area,



causing less stress to be placed upon the overall structure. The non-isotropic nature of skin enhances this effect. The relatively low strengths suggested at small tip radius cannot therefore be seen as directly indicative of their performance *in vivo*. However, as noted earlier, this underestimation can be factored in as part of any safety margins required for microneedle devices, and therefore the data is still meaningful.

In practice however, the needle tip radius is limited by the resolution of the EnvisionTEC Perfactory Mini Multi-Lens system to be used in their fabrication. At the time of this study, the smallest feature size achievable was 30  $\mu\text{m}$ , with the Enhanced Resolution Module (ERM) allowing a pixel accuracy of 15  $\mu\text{m}$ . Therefore, a tip radius of 45  $\mu\text{m}$  was seen as achievable for fabrication and mechanical testing. Of the remaining geometries, the inverted trumpet and stepped cone were chosen over the symmetrical pyramid and conical designs. The symmetrical pyramid was discounted due to its inferior calculated breakage strength. The conical design in theory offers better performance with a 45  $\mu\text{m}$  tip radius. However, the inverted trumpet and stepped cone structures offered better performance at lower tip radii, and therefore were chosen due to the assumption that lower tip radii would be attempted later in the study.

### 7.3 Modelling Skin/Microneedle Interaction

As well as modelling the failure forces of the microneedle geometries, a model was created that simulated the effect of the microneedles on the surface of the skin. As mentioned above, the previous stress failure simulations assume the needles are being pressed into a hard flat surface. When being inserted into skin *in vivo*, the skin will distort around the microneedle structures before failure, and this new simulation was designed to model this behaviour. In order to model skin penetration, a non-linear skin model was produced, expressing Mooney-Rivlin behaviour, a model commonly used in the simulation of elastic, rubber-like materials.

The model was set up by inputting selected human skin properties into the COSMOSWorks material database, based on Hendriks *et al* [9]. Using SolidWorks, a small 3 × 3

array of inverted-trumpet type microneedles, as described above, was placed parallel to a separate cube defined as the skin material. A non-linear FEA was performed, with the skin block stationary in space. A contact set was defined, modelling the interaction between the microneedle tips and the skin surface, allowing the stress to be calculated. The displacement between the skin block and the microneedle array was auto-stepped in 10 ms intervals, and the level of stress was monitored. The test finished once the skin stress was measured at above 3.183 MPa, a previously published maximum skin strength found in the literature [10].

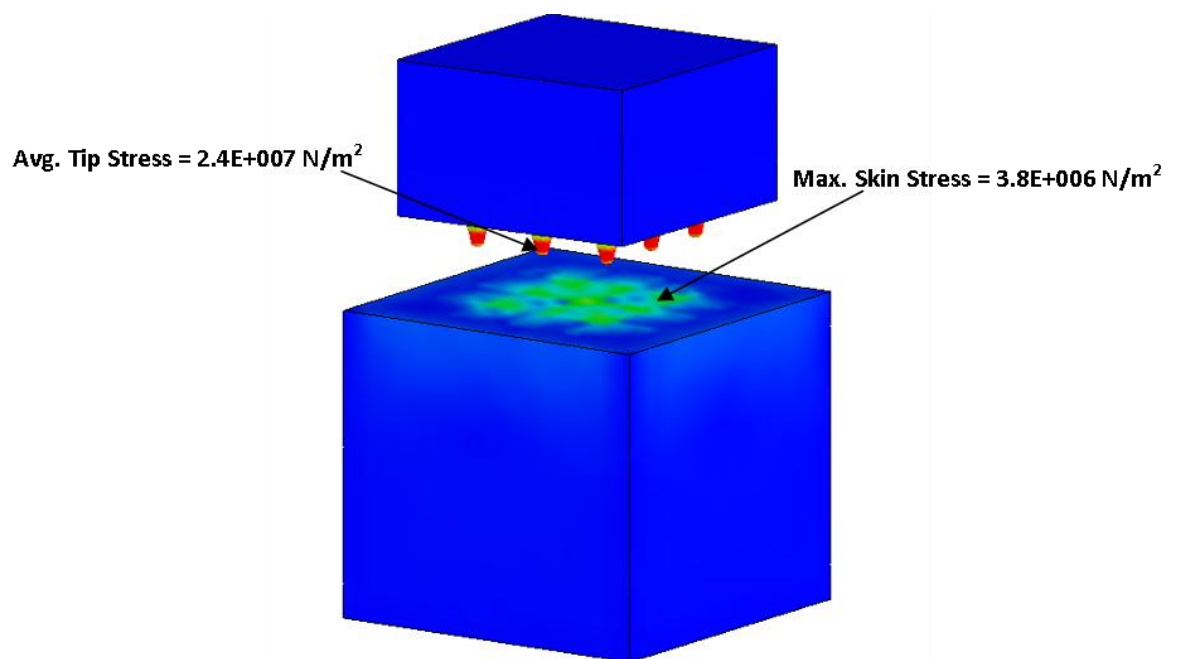


*Figure 7.4 – Microneedle array and skin model assembly, after simulation. The microneedle array and skin model are shown separately for clarity.*

The results of this model can be found in *Figure 7.4*. The data shows that at a skin stress of 3.8 MPa, the needle tip stress reaches a maximum of around 24 MPa. As the maximum skin stress is above that required to puncture the skin, and the needle stress is well below that of the tensile strength of the photocurable material (47.8 MPa), it can be assumed that the needle array has punctured the skin without breaking. However, due to the non-linear behaviour of skin, a definitive conclusion cannot be made without testing the device on actual skin.

## 7.4 MSL Fabrication of Microneedles

The microneedle arrays were fabricated using a microstereolithography-based rapid additive manufacture process. The processes used by the EnvisionTEC Perfactory Mini Multi-Lens have been discussed in detail in previous chapters. A number of photocurable resins were available for this system at the time the study was carried out. These materials, along with their physical properties, are shown in *Table 7.3*.

	<i>Perfactory R5/R11</i>	<i>Perfactory Y8</i>	<i>Perfactory E-Shell 100</i>	<i>PMMA</i>
<b>Modulus of Elasticity (MPa)</b>	1245 – 1510	282 – 707	2360	3230
<b>Elongation at Break (%)</b>	11 – 25	27	5.9	4
<b>Tensile Strength (MPa)</b>	31 – 39	5.9	47.8	65.7
<b>Flexural Strength (MPa)</b>	40 – 45	25	66.7	98

*Table 7.3 – Typical material properties for a number of EnvisionTEC Perfactory resins available at the time of this study. Data for PMMA, a common microengineering polymer, are also displayed for comparative purposes.*

Both e-Shell 100 and R11 were chosen for the production of prototype microneedle arrays, although in practice it was R11 that was nearly exclusively utilised. R11 is a more useable material in practice, and is less viscous than e-Shell 100, which can help with the fabrication of the tiny microstructures, inhibiting the formation of bubbles during fabrication.

The initial prototype needle arrays were designed using SolidWorks, and consisted of arrays of microneedle structures ranging in height from 200 to 1200  $\mu\text{m}$ . The initial parameters were set at the factory defaults, with a layer thickness of 50  $\mu\text{m}$ . The resulting builds were gold coated and visualised using a scanning electron microscope (SEM). The micrographs obtained from this first test build can be seen in *Figure 7.5*. This initial build was not successful, it was assumed due to a lack of Z-axis resolution and a fast peeling speed. To test these assumptions, a secondary build was completed using a 25  $\mu\text{m}$  layer thickness. Micrographs of these structures

can be seen in *Figure 7.6*. Once again, the needle structures were not successfully completed, although structure retention on top of the base was better than in the 50  $\mu\text{m}$  test.

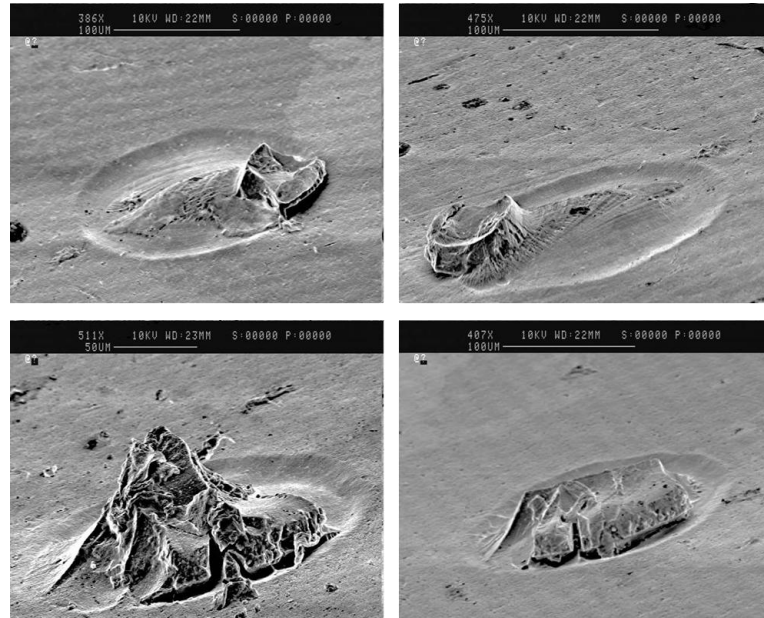


*Figure 7.5 – Initial unsuccessful prototype microneedle array. The material used was R11, with machine parameters set at factory defaults (1000  $\mu\text{m/s}$  peeling speed) with a 50  $\mu\text{m}$  layer thickness.*

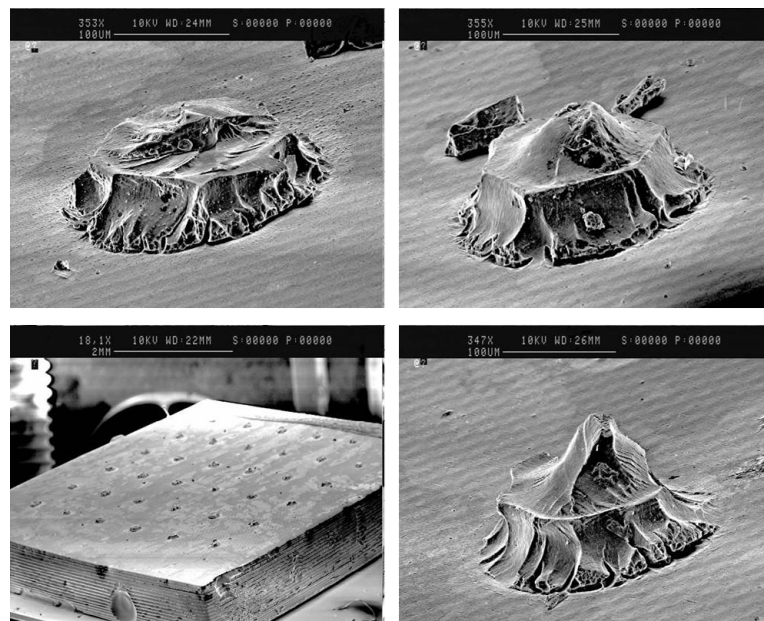


*Figure 7.6 – Second unsuccessful fabrication attempt, using a Z-axis resolution of 25  $\mu\text{m}$ .*

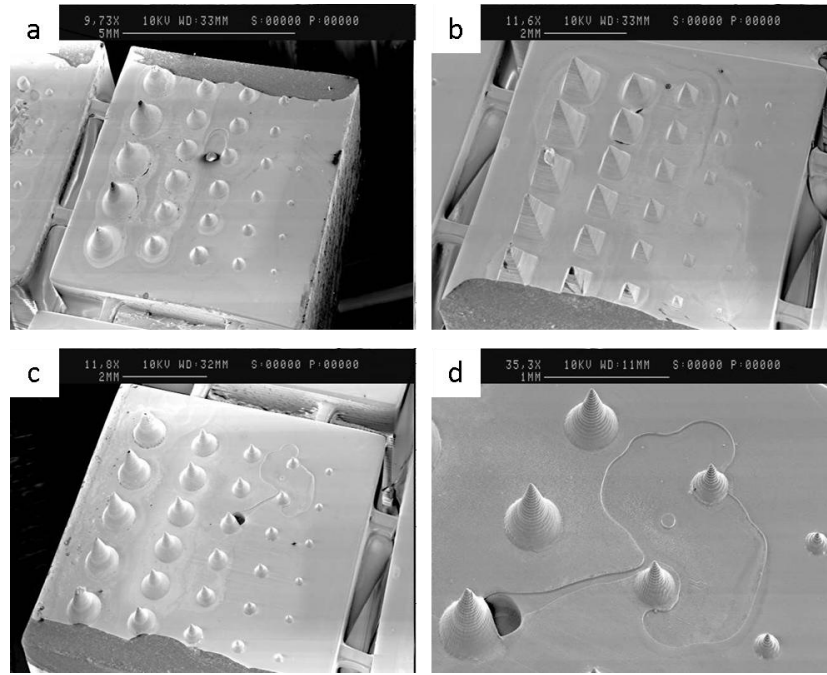


Figure 7.7 – Successful prototype build of MSL microneedles, showing (a) inverted trumpet, (b) symmetric pyramid and (c) stepped cone geometries. (d) is a close up of the damage caused by a bubble formed in the resin during fabrication.

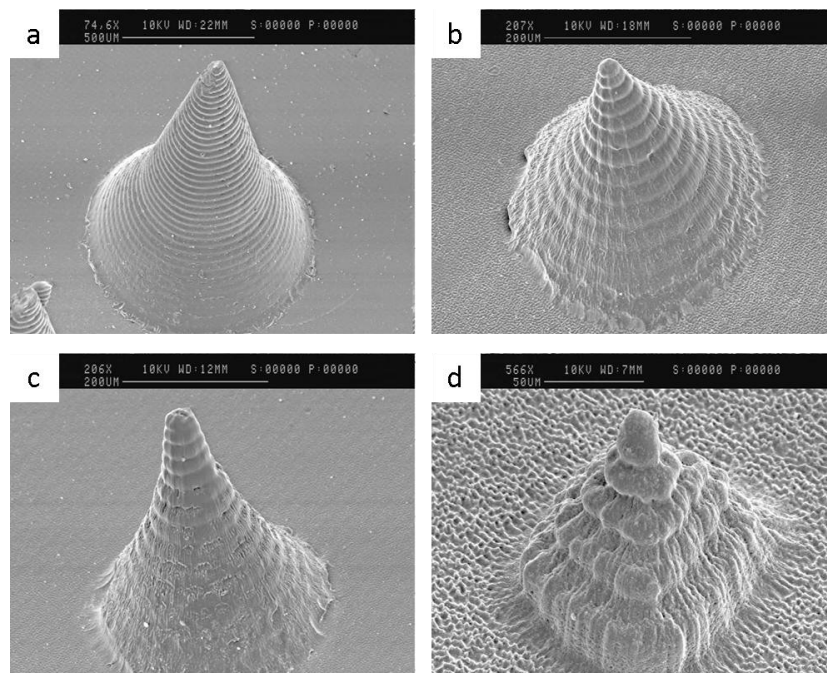


Figure 7.8 – SEM close-ups of microneedles fabricated using MSL. (a) is a 400 μm tall stepped cone geometry, (b) is a 400 μm tall inverted trumpet geometry, (c) is a 200 μm tall inverted trumpet, and (d) is a 125 μm tall symmetric pyramid. Fabrication layers can be clearly seen, each being an average of 25 μm thick.

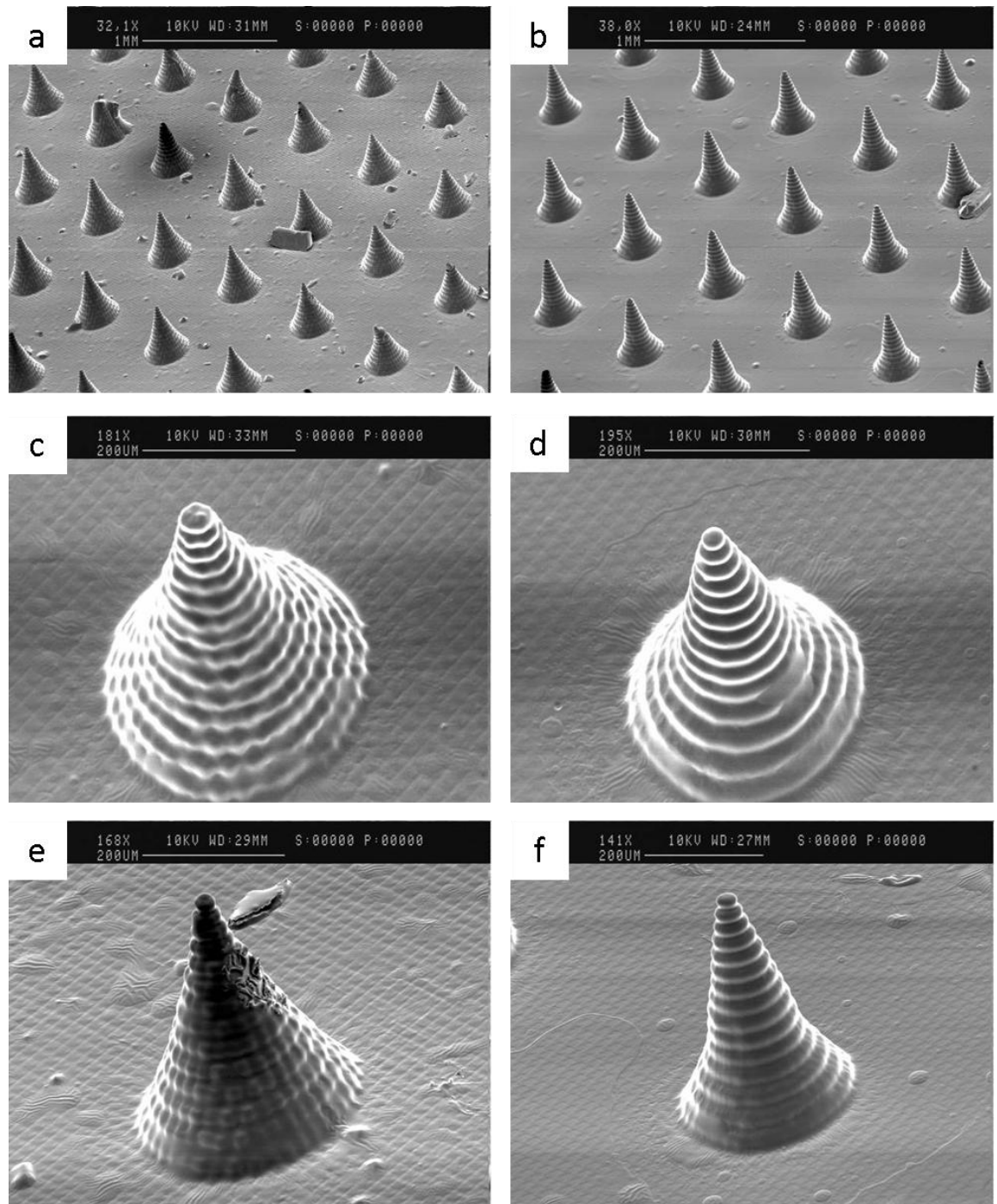


Figure 7.9 – Microneedle arrays produced for mechanical testing. (a) shows an array of inverted trumpet geometries, (b) an array of stepped cone geometries, (c) and (e) show inverted trumpet designs from two angles, (d) and (f) show the same for the stepped cone designs. Significant debris and needle damage can be seen in (a), although it is unclear if this was caused by factors during or after fabrication. The arrays were arranged in straight  $9 \times 9$  grids, and each structure was  $400 \mu\text{m}$  tall. The array separation was  $750 \mu\text{m}$ .

With the Z-axis resolution ruled out as the sole cause of the fabrication problems, a third test build was run. For this third run, a new CAD model was produced with thicker bases, as it was noticed that the thinner bases used in the first two runs warped during the post-build processing

and curing steps. The peeling speed of the system was also reduced to 500  $\mu\text{m/s}$  to try and reduce stress on the microstructures during fabrication.

The changes to both the base thickness and the peeling speed led to the structures seen in *Figure 7.7*, seen in close-up in *Figure 7.8*. The electron micrographs show that the 25  $\mu\text{m}$  Z-axis resolution is sufficient for microneedles of between 200 and 400  $\mu\text{m}$ , in order for the geometries to be copied well from the CAD data. Heights below this level start to show excessive “stepping” i.e. the Z-resolution was too low to produce a smooth structure. It was therefore decided that the microneedle arrays to be produced for testing should be 400  $\mu\text{m}$  tall. Both the inverted trumpet and stepped cone designs showed excellent reproducibility and build accuracy across a range of heights. A number of uniform arrays were produced, for use in mechanical testing. Both inverted trumpet and stepped cone geometries were used, on separate bases, with an array separation of 750  $\mu\text{m}$ . The arrays, shown in *Figure 7.9*, were arranged in straight rows in a  $9 \times 9$  grid.

## **7.5 Testing of MSL Microneedle Arrays**

### **7.5.1 FEM Analysis**

In order to validate the modelling used in this study, further analysis was carried out on the maximum stress experienced by a full  $9 \times 9$  array of 400  $\mu\text{m}$  microneedles before mechanical testing was carried out. The geometries used were those selected by the initial modelling: the stepped cone and inverted trumpet. Results from these tests could then be compared with mechanical testing data produced from arrays produced using the same CAD data used in the FEM analysis.

A model was produced in COSMOS similar to that used previously, with each needle in the array subjected to a force on its tip perpendicular to the array plane. This force would increase until the maximum stress in the structure reached that of the tensile strength of the fabrication material. For the mechanical tests, the selected material was EnvisionTEC Perfactory R11, chosen

as it was a proven reliable material that could be depended on when producing multiple identical arrays for testing. The mechanical properties of R11 (see *Table 7.3*) were used to create a custom material in COSMOS for the FEM analysis.

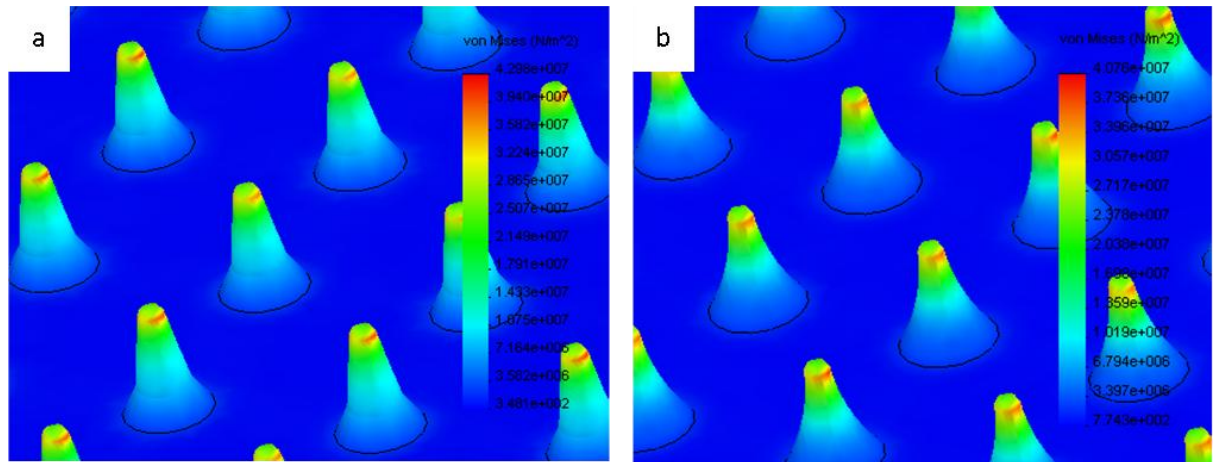


Figure 7.10 – Microneedle arrays after simulation. The colour spectrum indicates the stress distribution throughout the needle structures. (a) is an array of stepped cone geometry microneedles, (b) shows an array of inverted trumpet structures.

The results of this analysis are shown in *Figure 7.10* and *Table 7.4*. They show the stress distribution for both geometries are similar, although the stepped cone shows a slight higher failure force per needle. It is likely that the identical tip diameter causes the similar result, and the stepped cone has more material further towards the tip, resulting in the larger break force result.

	<i>Inverted Trumpet</i>	<i>Stepped Cone</i>
<b>Material Strength (R11)</b>	39 MPa	39 MPa
<b>Force Level at Max. Stress</b>	16.61 N	17.17 N
<b>Failure Force Per Needle</b>	0.205 N	0.212 N

Table 7.4 – Tabulated failure values for each microneedle design, as calculated in FEM analysis.

By increasing the applied force beyond that of maximum of the material, the normal failure mode can be visualised, as shown in *Figure 7.11*. As could be expected, with the load being applied axially, the failure mode in both geometries is one of the crushing of the material.



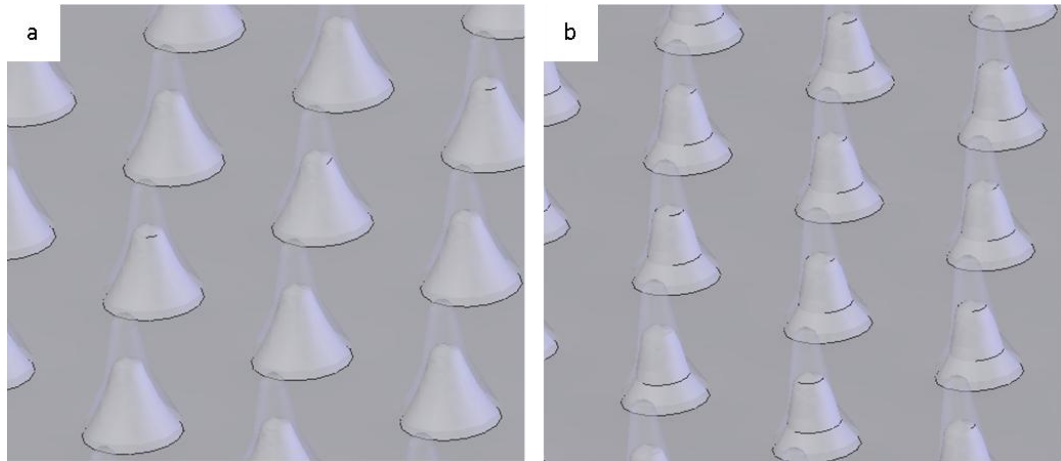


Figure 7.11 – Representation of simulated failure mode of microneedles under axial load. (a) is an array of stepped cone geometry microneedles, (b) shows an array of inverted trumpet structures.

### 7.5.2 Mechanical Testing

A test rig was constructed to measure the axial failure force of arrays of our MSL-fabricated microneedle arrays. An overview of the apparatus can be seen in *Figure 7.12*. Each microneedle array was placed into the sample site, held in position by the pressure generated by a loaded spring. The spring was calibrated as giving a force of 2.27 N/mm, and was mounted on a Schneeberger frictionless table. The position of the table was controlled by the displacement control screw thread, and the displacement was measured using a TESA Displacement probe connected to a readout display. As pressure was applied to the microneedle array, the structures were visualised under an optical microscope mounted above the sample site. A failure force was deemed to have occurred once the needles had deformed significantly. Although this is a subjective measure, the testing of 7 separate but identically fabricated arrays of each geometry keeps error to a minimum. Both arrays consisted of 400  $\mu\text{m}$  tall needle structures, with a 45  $\mu\text{m}$  radius tip, spaced at 700  $\mu\text{m}$ , fabricated from EnvisionTEC Perfactory R11.

The results of the mechanical testing can be seen in *Table 7.5* and *Figure 7.13*. As with the FEM analysis, both geometries produced similar results. However, unlike the FEM data, the mechanical data suggests the inverted trumpet is the strongest shape under axial load. Also

notable is the expected underestimation in the simulation results compared to those produced via mechanical testing.

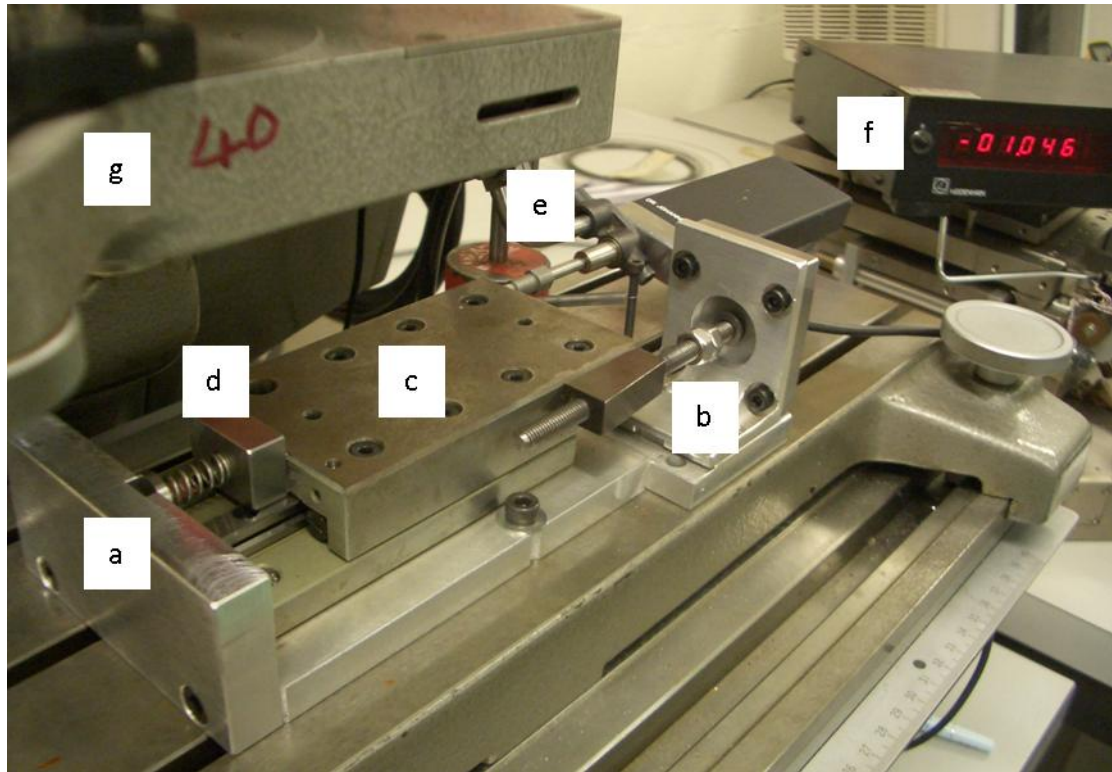


Figure 7.12 – Apparatus for mechanical testing of MSL fabricated microneedle arrays. (a) Microneedle sample site, (b) displacement control, (c) Schneeberger Frictionless Table, (d) spring load, (e) TESA Displacement Sensor, (f) TESA Numerical Display, (g) top mounted optical microscope.

<i>Failure Force Per Needle (N)</i>		
<i>Sample No.</i>	<i>Inverted Trumpet</i>	<i>Stepped Cone</i>
1	0.278	0.237
2	0.29	0.282
3	0.292	0.248
4	0.287	0.22
5	0.237	0.255
6	0.251	0.206
7	0.205	0.256
<b>Average Failure Force</b>	<b>0.263</b>	<b>0.243</b>

Table 7.5 – Data collected from MSL microneedle arrays via mechanical testing, via the test rig shown in Figure 11.

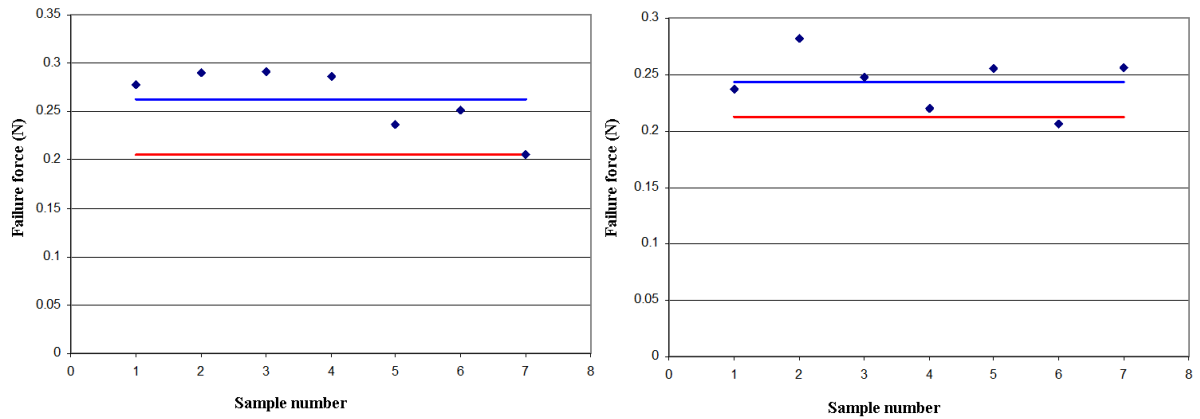


Figure 7.13 – Graphical representation of results gathered from mechanical test rig. The figure compares simulated failure forces (red) to measured failure forces (blue, line indicates average) for (a) inverted trumpet and (b) stepped cone geometries.

A reasonable range of data is present, probably due to deficiencies in the testing procedure. The microscope was only able to focus upon the top row of needles in the array, meaning it was their failure force that was truly being measured, not that of the array as a whole. Post test observation of the arrays showed uneven wear on some samples, suggesting that the force was not evenly spread across the whole array. However, it was observed that the majority of needles underwent a crushing failure mode, indicating that for the most part the force was relatively even. A low number of the structures did however undergo a bowing failure mode, indicating imperfect axial load in some cases. This could go some way to explain the stepped cone geometry being stronger than the inverted trumpet in testing, although simulation results suggested otherwise. The stepped cone design has more material toward the needle tip, which in theory would make it less susceptible to non-axial loads. This weakness would not be found in simulations, which assume perfect axial load.

However, although the testing was not as accurate as could have been achieved, it was perhaps overkill in any case. Assuming an axial load, the 90  $\mu\text{m}$ -diameter needle tips would have been experiencing pressures of around 30 to 32 MPa at the measured point of failure – nearly ten times required pressure in order for a needle structure to pierce the skin [10]. It is therefore

reasonable to assume that these structures are capable of creating the micropores required for the diffusion of large macromolecules such as insulin across the skin.

## 7.6 Hollow Microneedles by MSL

Further fabrication tests were carried out with microneedle structures containing a central bore for the direct administration of drugs or the taking of blood samples. The structures were essentially the same basic geometries as described above, but with an 80  $\mu\text{m}$  hole parallel to the needle axis, either through the centre of the needle or offset down the side of the geometry. The fabrication settings used were also the same as those used for the solid structures above.

The central-bore microneedles can be seen in *Figure 7.14*. Both the stepped cone and inverted trumpet geometries exhibited the results shown, with the upper half of the structure missing. It is likely that although the MSL system had enough resolution to complete the needle walls further up the needle structure than shown, in practice it is likely the cured photopolymer did not have enough strength at such low feature sizes to resist the stresses of the peeling process during fabrication.

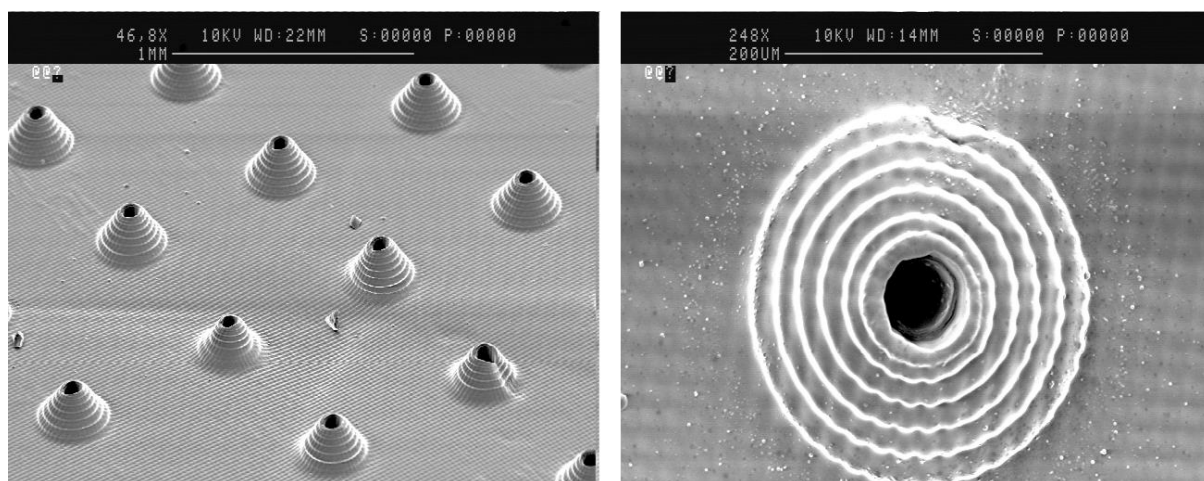


*Figure 7.14 – Hollow microneedles with a central 80  $\mu\text{m}$  bore, showing build failure in the upper part of the microneedle structure.*

More promising results were shown in those structures fabricated with an offset lumen, as shown in *Figure 7.15*. Using these designs, the upper portion of the shape is retained. It is not

known how the bore affects the mechanical strength of the structures, compared to the same geometries in solid configuration, and it can be assumed that due to the offset, asymmetric geometry, that the failure mode is more likely to be bowing in nature.

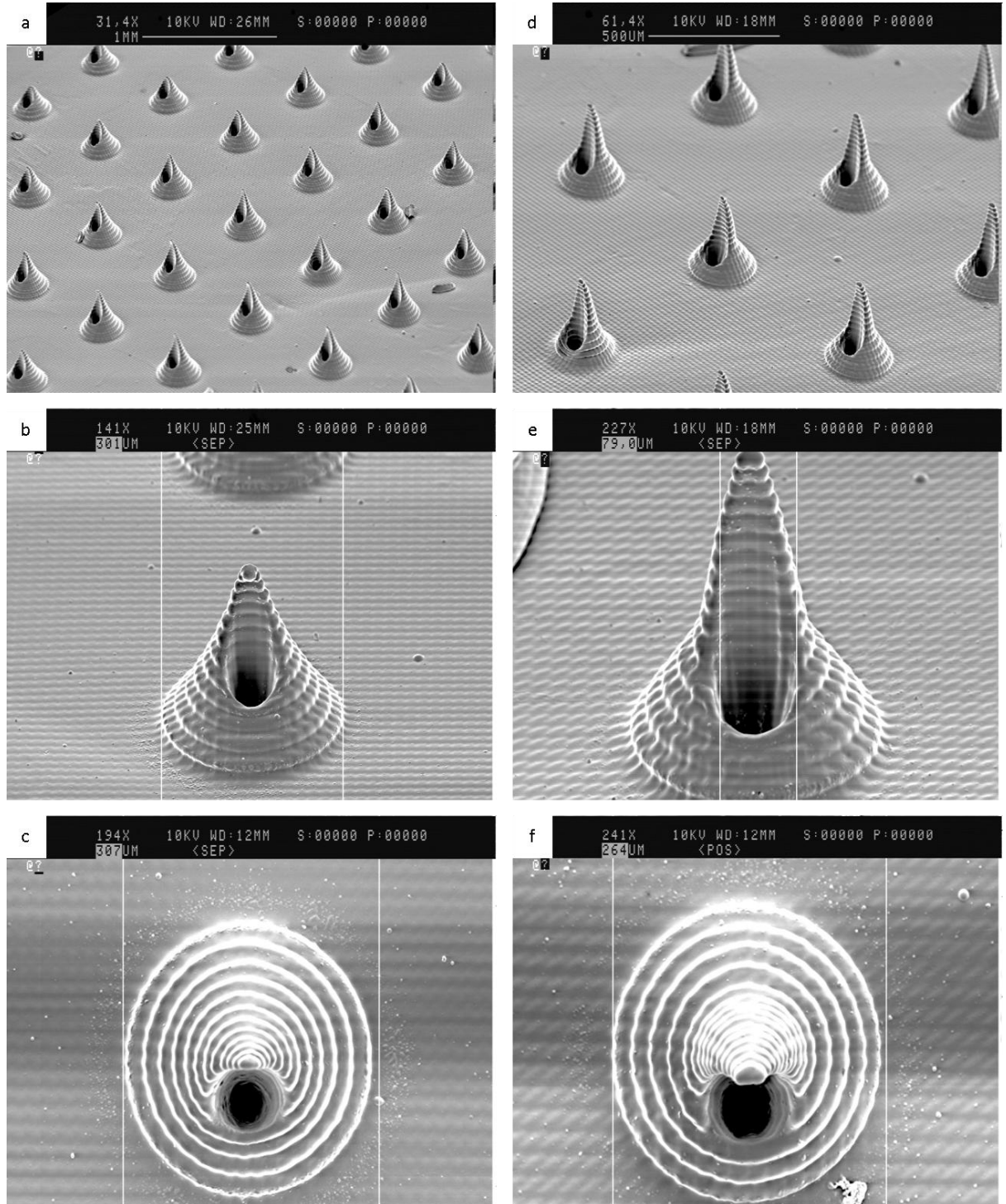


Figure 7.15 – SEM images of MSL fabricated hollow microneedle structures with offset 80  $\mu\text{m}$  diameter internal bore. (a), (b), and (c) – inverted trumpet geometry in array, single needle and aerial view; (d), (e), (f) – same for stepped cone geometry.

The main problem that is found with these hollow microneedles is not in the fabrication of the needle geometry itself, but in resolving the bore beyond the depth of the needle shape. As has been shown in Chapter 4, the EnvisionTEC Perfactory Mini Multi-Lens system is capable of resolving fine detail in the X/Y plane due to its reasonably high resolution. However, it has been found that sub-200 to 300  $\mu\text{m}$  diameter microchannels do not clear well of the uncured resin, and can become blocked if more than 500 to 1000  $\mu\text{m}$  in length. As a result, it is likely that although fully integrated MSL-fabricated devices with hollow microneedles are indeed possible, they probably require a higher resolution MSL system than the EnvisionTEC Perfactory.

## 7.7 Conclusion

The field of microneedles is only a few of decades old, delayed due to the lack of suitable fabrication techniques available. As modern microfabrication techniques such as micromachining have recently evolved to higher resolutions, there is considerable commercial and research interest in developing cheap, pain-free microneedles for medical applications.

In this chapter, we have demonstrated microstereolithography as one potential fabrication technique for both solid and hollow out-of-plane microneedles. A number of microstructure geometries were analysed using FEM computer simulations of stability under axial load, with stepped cone and inverted trumpet geometries showing promise in these tests. It was found that the needle tip radius is a major factor in the overall mechanical strength of these structures, with larger values allowing more stress to be absorbed. However, this must be balanced *in vivo* with the lower force required for skin piercing provided by smaller tip sizes, and our testing in the main modelled the interaction between the needle arrays and a hard, flat surface. Further testing must be carried out to assess effect of the microneedle arrays on skin.

However, it has been shown that the structures produced are able to withstand many times the force required to puncture human skin reported by various papers in the literature. Both FEM analysis of whole arrays and mechanical testing of MSL fabricated arrays showed

sufficient mechanical strength. Arrays of  $9 \times 9$  microneedles in rows were fabricated on the EnvisionTEC Perfactory Mini Multi-Lens rapid manufacturing system, with each needle standing  $400 \mu\text{m}$  from a solid base substrate. The stepped cone geometry was found to be stronger in mechanical testing, with an average failure force of  $0.263 \text{ N}$ , with the inverted trumpet slightly behind at  $0.243 \text{ N}$ . In both cases, the simulation data underestimated the true failure force by a small margin.

Hollow microneedles, identical to the solid structures but with an offset  $80 \mu\text{m}$  lumen were also demonstrated, but not mechanically tested. Although these structures resolved well, it is felt that the limitations of the EnvisionTEC Perfactory system suggest that a fully integrated system built entirely using MSL requires a higher resolution system to fully resolve the microfluidics at the scales required. Such systems already exist commercially, and further work would include work with such technologies.

## 7.8 References

- [1] D. V. McAllister, P. M. Wang, S. P. Davis, J. H. Park, P. J. Canatella, M. G. Allen, and M. R. Prausnitz, "Microfabricated needles for transdermal delivery of macromolecules and nanoparticles: Fabrication methods and transport studies," *Proceedings of the National Academy of Sciences of the United States of America*, vol. 100, pp. 13755-13760, Nov 25 2003.
- [2] B. Stoeber and D. Liepmann, "Fluid injection through out-of-plane microneedles," *Proceedings of the 1st annual International IEEE-EMBS Special Topic Conference on Microtechnologies in Medicine and Biology*, vol. Lyon, France, pp. 224-228, 2000.
- [3] P. Griss and G. Stemme, "Side-opened out-of-plane microneedles for microfluidic transdermal liquid transfer," *Journal of Microelectromechanical Systems*, vol. 12, pp. 296-301, Jun 2003.
- [4] S. P. Davis, B. J. Landis, Z. H. Adams, M. G. Allen, and M. R. Prausnitz, "Insertion of microneedles into skin: measurement and prediction of insertion force and needle fracture force," *Journal of Biomechanics*, vol. 37, pp. 1155-1163, 2004.
- [5] H. J. G. E. Gardeniers, R. Luttge, E. J. W. Berenschot, M. J. de Boer, S. Y. Yeshurun, M. Hefetz, R. van't Oever, and A. van den Berg, "Silicon micromachined hollow microneedles for transdermal liquid transport," *Journal of Microelectromechanical Systems*, vol. 12, pp. 855-862, Dec 2003.
- [6] S. J. Moon and S. S. Lee, "A novel fabrication method of a microneedle array using inclined deep x-ray exposure," *Journal of Micromechanics and Microengineering*, vol. 15, pp. 903-911, May 2005.
- [7] J. W. Gardner, V. J. Varadan, and O. Awadelkarim, "Microsensors, MEMS and Smart Devices," *John Wiley & Sons Ltd, Chichester*, 2001.
- [8] J. E. Mark, "Polymer Data Handbook," *Oxford University Press, Inc.*, 1999.
- [9] F. M. Hendriks, D. Brokken, C. W. J. Oomens, F. P. T. Baaijens, and J. B. A. M. Horsten, "Mechanical properties of different layers of human skin," *MATE internal presentation*, vol. Available online: <http://www.mate.tue.nl/mate/pdfs/249.pdf> [Accessed 10th August 2009], 2000.
- [10] P. Aggarwal and C. R. Johnson, "Geometrical effects in mechanical characterising of microneedle for biomedical applications," *Sensors and Actuators B-Chemical*, vol. 102, pp. 226-234, 2004.

# Chapter 8

---

## 8 Microstereolithography for Active Microfluidic Systems

### 8.1 Introduction

As shown in Chapters 2 and 3 of this thesis, there have been a wide variety of active and passive microfluidic devices produced for controlling the movement of liquids with sub-millilitre volumes. Devices range from simple syringe-type mechanisms [1-4], to those that use hydrodynamic effects to influence fluid motion [5-7]. The range of materials utilised is equally wide. However, the majority of devices found in the literature since the year 2000 [8] use multilayer soft-lithography techniques to shape pumps and valves that use a reciprocating membrane to impart force upon the working fluid. Although multilayer soft-lithography is a versatile technique, excellent for device development where process flexibility is paramount, it is not ideal for the mass production of the final commercial product. This is mainly due to the manual nature of the basic process, although the requirement of expensive cleanroom facilities also makes the process less economically favourable.

The process of microstereolithography, as reviewed in Chapter 4, has a number of similarities with the multilayer soft-lithography process. Each layer of the device being fabricated is created sequentially as a flat slice of a more complex 3D structure, which is then aligned and adhered to the previously fabricated layers. The final device is monolithic, and is impermeable to liquid. Multilayer soft-lithography has a much higher resolution than most SLA systems, limited only by the capabilities of the photocurable mask material used in the soft micromoulds production. However, modern microstereolithography systems are capable of reasonable resolutions, towards sub-micron, and have the advantage of being fully automated from the input of the 3D design data onwards.



The EnvisionTEC Perfactory Mini Multi-Lens SLA system is unique in the market in its projector-based mechanism. Whilst this limits the machine resolution in comparison to the more usual laser-based designs, it does mean that each layer is fabricated in a single step, rather than being created in a raster process. In theory, this makes the system ideal for creating thin horizontal structures in the vertical plane, allowing membranes to be created as part of complex microfluidic systems. In this chapter, this hitherto untested application of the EnvisionTEC Perfactory system will be explored, with the production of microfluidic devices, along with electronic test systems to characterise the said components.

## **8.2 Fabrication of SLA Membranes**

### **8.2.1 Design, Build and Post-Processing Parameters**

A number of test builds were designed and fabricated in order to ascertain the viability of membranes produced using the EnvisionTEC Perfactory Mini Multi-Lens SLA system. These developmental parts were also used to find the ideal build parameters for creating such thin structures, and were designed so that the membranes were formed using the light output from the exposure of a single masked layer. Although thin, membrane-like structures could be created using multiple structures, it was feared that these might not adhere properly and could delaminate, much like the horizontal mesh structures shown in Chapter 7.

It was found during these tests that the use of the default build parameters resulted in many of the membranes being ripped during the build process. As with the microneedle fabrication in the previous chapter, it was assumed that the peeling speed was the critical factor, and indeed a reduction in the “standard” (non burn-in) layers of the peel speed from 1000 to 500  $\mu\text{m}/\text{sec}$  increased the viable membrane yield dramatically. It was also found that the diameter of the membranes was critical. Although different shaped membrane structures are possible, it was decided that circular membranes were preferable, as other shapes have corners that could intensify stress forces upon the membrane during use. Membranes of

between 1 and 10 mm were fabricated. Those below 5 mm in diameter were found to exhibit low incidences of damage during testing, and therefore the maximum diameter for use in the planned devices was set at 5 mm.

The post-processing steps used to remove the excess resin from the devices were also found to affect membrane yields. For standard, bulk components containing internal structures, the parts were immersed in isopropanol for 15 minutes in an un-heated ultrasonic waterbath at room temperature. This time scale is required in order that the solvent dissolves the excess resin trapped within the internal features. However, this was found to be too harsh for components containing small-scale features, and the membranes produced would often break during the cleaning process. It is thought this is in part due to the fact that the standard layers of the SLA build are not fully cured, and the isopropanol can start to leach out the uncured polymer from within the partially cured matrix, weakening the structure. The sonication time was therefore reduced to 5 minutes, which would result in an outwardly resin-free part. Although resin was still trapped inside the component fluidics, in most cases the device designs included integrated pipe fittings, allowing the resin to be manually flushed from the part using a syringe.

One interesting feature of the SLA-fabricated membranes is their behaviour during post-curing in UV lightboxes. It was found that freshly fabricated membranes often took a wrinkled appearance, presumably due to the peeling forces placed upon them during the build process. However, after treatment in the UV lightbox, the membranes appeared flat and smooth. It is noted that an amount of shrinkage is expected from the resin during the resin curing, and a compensation routine is built into the calibration routine of the most recent EnvisionTEC Perfactory RP software. For the membrane to become tight, it is assumed that the membrane must shrink proportionally more than the surrounding bulk material, which would

be sensible considering the much greater thickness of the surrounding material in comparison with the membrane.

### 8.2.2 Membrane Characterisation

Following the optimisation of build and post-processing parameters, a more complex test part was created, shown in *Figure 8.1a*. The part consisted of an internal chamber, topped with a membrane and linked horizontally to an integrated pipe fitting. This allowed a connection to a pneumatic source, which was used to exert force upon the membrane via the internal chamber. The pneumatic pressure was controlled using a manual regulator, and measured using a Honeywell 26PC series silicon pressure sensor. The signal from the pressure sensor was collected using a multimeter, with the input power provided by a standard powerpack. The pressure was varied at arbitrary intervals from around 0.5 PSIG to 3.5 PSIG (3.45 kPa to 24.12 kPa), with the deflection of the centre of the membrane measured using a Tallysurf surface profiler in manual mode. A plot of exerted pressure vs. deflection can be seen in *Figure 8.1b*.

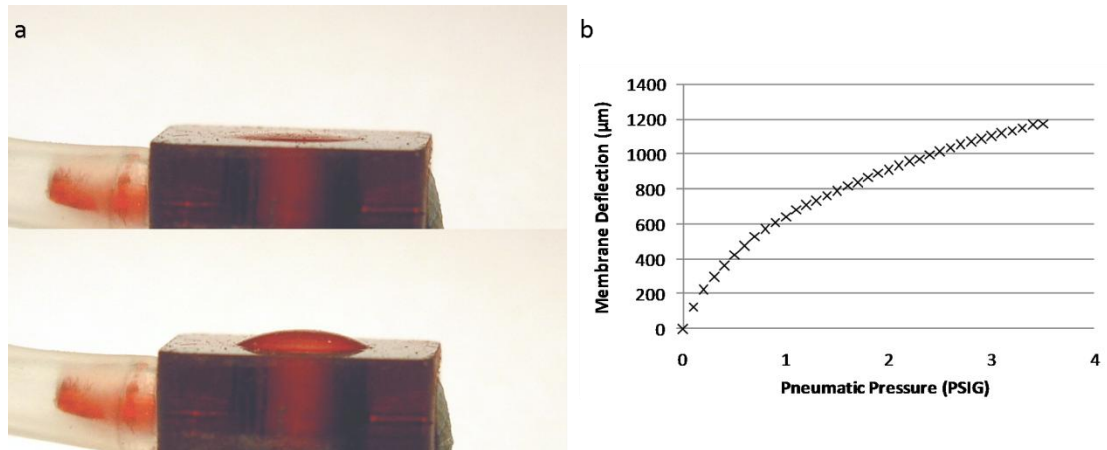


*Figure 8.1 – (a) photograph of test component, showing the membrane in rest (upper) and pressurised (lower) positions; (b) plot of pneumatic pressure vs. membrane deflection measured using a Tallysurf surface profiler in manual mode. A maximum deflection of just less than 1.2 mm was achieved with a pneumatic pressure of 3.5 PSIG (24.12 kPa).*

The same test components were also used for long-term reliability tests of the membrane structures. In order to work in a functioning device, the membranes would have to

cope with a large number of on/off reciprocal pressure cycles. In order to probe their reliability, a simple test system was set up (shown in *Figure 8.2*), comprising of the Honeywell pressure sensor and regulator described previously, a Clippard ESO-3W 12V 3-way solenoid valve, a TiePie Handyscope H3 USB oscilloscope and a National Instruments NI-DAQ 6009 USB data acquisition device. Once again, the power to the pressure sensor was provided by a standard powerpack.

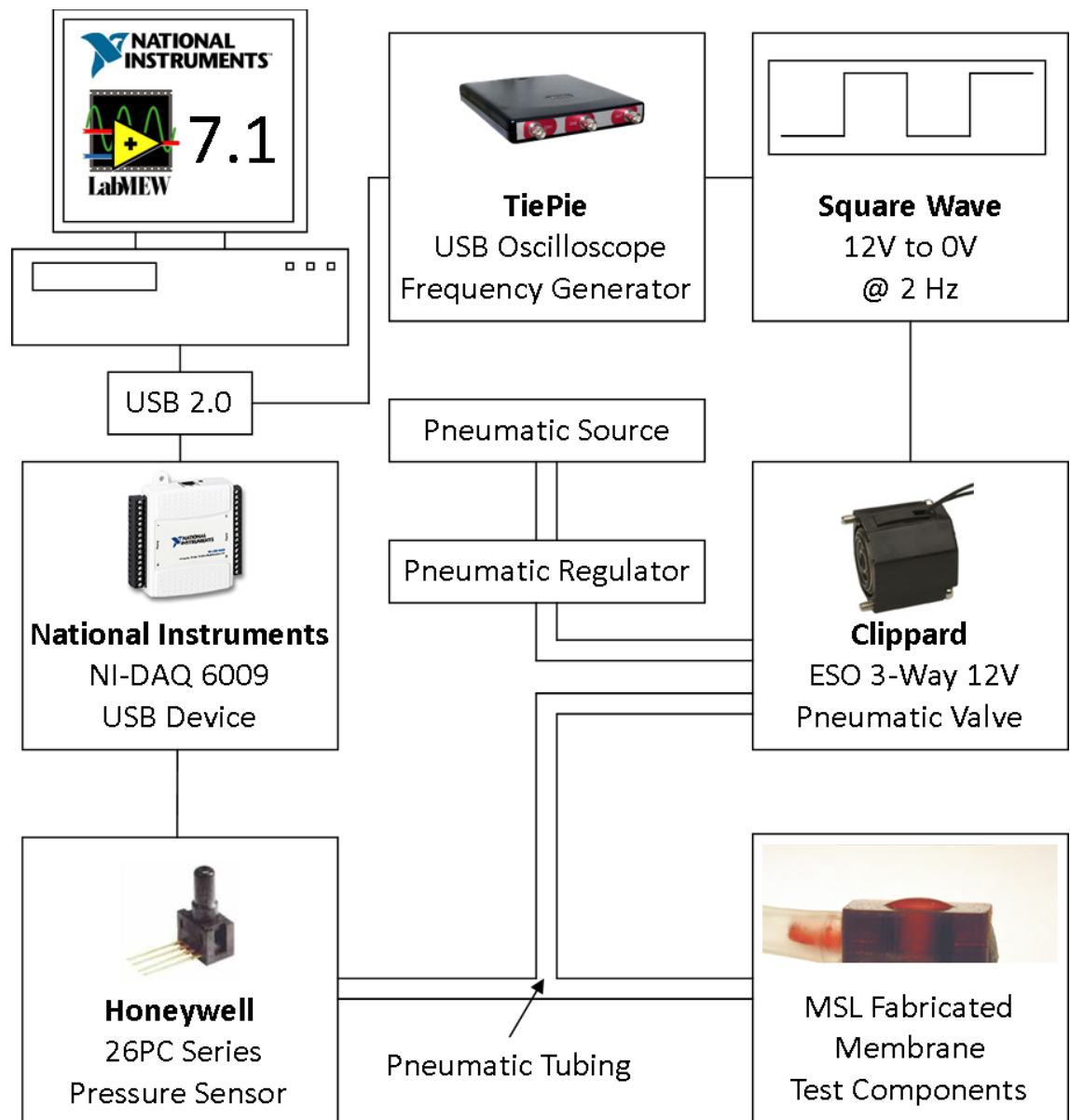


*Figure 8.2 – Schematic of long-term membrane reliability test setup. A 3-way Clippard pneumatic valve was used to digitally (on/atmospheric) control a pneumatic pressure provided by a pressure port and controlled by a regulator. The pressure was read by a Honeywell 26PC-series pressure sensor, which counted the on/off pulses in LabVIEW 7.1 via an NI USB-6009 DAQ device. If a membrane broke during testing, the peak pressure would not reach the set threshold, and the last recorded count number was used to determine the number of cycles reached.*

The NI-DAQ 6009 was connected to a PC running LabVIEW 7.1, set up to monitor the output from the pressure sensor. The Handyscope USB oscilloscope was connected to the same PC, controlled by its own proprietary software. The signal generator from the oscilloscope was employed to directly drive the 12V 3-way valve at a frequency of 1 Hz, switching the valve's output port from the regulator-controlled pressure source to atmospheric pressure. Three identical membrane parts were connected to the valve output, with the pressure sensor connected to a T-junction in the pneumatic tubing between the valve and membranes.

The LabVIEW software was programmed to monitor the pressure sensor output for the peaks and troughs generated by the on/off cycle of the 3-way valve opening and closing. 3 tests were carried out, at 1.0, 2.0 and 3.0 PSIG (6.89, 13.79 and 20.68 kPa). The software counted and wrote to file the number of peaks above a calibrated threshold, allowing the total number of pressure cycles to be counted. Should a membrane break during testing, the cycling would carry on, but the peaks would not be present due to the compromised pneumatic system. Once noticed by the operator, the membrane could be removed and the number of cycles experienced noted, before the test was resumed with only the remaining membranes connected.

At both 1.0 and 2.0 PSIG, no breakages were observed before the number of cycles reached 1,000,000, at which point the test was terminated. At 3.0 PSIG however, one membrane broke at just under 300,000 cycles, the next at around 370,000 cycles, and the final part at just over 700,000 cycles. This attrition suggests the SLA-produced membranes are not suitable for actuation pressures much above 2.0 PSIG, although pressures below this should be safe for long-term device use.

### 8.2.3 Membrane Thickness

In the production of all membranes detailed in this thesis, the EnvisionTEC Perfactory system was set up with a layer thickness of 25  $\mu\text{m}$ . As explained in earlier chapters however, this does not guarantee that the thickness of any overhanging or unsupported features will be exactly 25  $\mu\text{m}$ . In order to adhere each layer to the previous one, a certain amount of over-cure is required to allow cross-linking between layers. In the case of layers with no preceding structure to adhere to, such as membranes, this leads to structures that are thicker than laid out in the original 3D design.

In order to quantify this discrepancy, a small number of test membranes were removed from their support structure and placed on a glass slide. The Tallysurf surface profiler was once again used, but this time in automatic profiler mode, allowing the thickness of the membrane to be accurately measured. The thicknesses measured were found to be relatively consistent, in a region around 60-70  $\mu\text{m}$ . The slight variation can be explained by probable similar variation in the light levels of the projector between build runs, minimised by the calibration procedures detailed in Chapter 4. Although the layer exposure could be reduced in order to reduce the membrane thickness, this can lead to a knock-on effect in the bulk layer adhesion, causing aberrations in the component structure. A thinner membrane would be advantageous in terms of greater flexibility, but this would be balanced by a weakening of the mechanical strength. It was therefore decided to leave the exposure levels at their defaults in further work, although future research with new additive materials could focus on this balancing act.

### 8.3 Selection of Micropump Design and Actuation

#### 8.3.1 Mechanism and Rectification

As mentioned earlier, the reviews found show the large range of micropump and microvalve designs available in the literature for researchers to utilise and improve upon, although the majority of designs rely on a reciprocating displacement mechanism. With the EnvisionTEC Perfactory's strengths lying with the production of thin horizontal membranes, it was clear these designs would be the way forward for microfluidic components built with this technology. This reduced the scope of any reasonable pump mechanisms substantially, but still left a number of options. The first was a multi-membrane peristaltic pump, either in a simple 3-chamber configuration, or with a pair of active membrane valves flanking a pump chamber. Another option was the use of nozzle/diffuser elements, although initial research concluded that these microfluidic elements were most efficient at the higher pump frequencies exhibited by piezoelectric drivers.

#### 8.3.2 Thermopneumatic Actuation

The initial designs investigated were actuated using thermopneumatic principles. Thermopneumatic actuation has the advantage of being a fully integrated solution, relatively simple in terms of design, balanced by a normally relatively low actuation frequency due to the need for the pneumatic chamber to be heated and cooled. The thermopneumatic device designed can be seen in *Figure 8.3*. It consisted of a central pump chamber, flanked by a pair of active membrane valves. The energy requirement for shutting the valves was reduced by the inclusion of collars over the distal fluidics, a feature seen in a number of other published devices [9-16]. The device was fabricated in 4 parts: an upper block, containing the thermopneumatic and working fluid chambers, separated by the actuation membranes; a lower block, containing the distal fluidics and valve collars, along with tight-fit inserts that created the bottom of the working fluid chambers; and a pair of pipe fittings, that slotted into

a pair of square holes on the front edge of the lower part. The device was assembled and then sealed using an acrylate adhesive.

The heating elements were provided by 3 SRL127 devices, consisting of a pair of microhotplates micromachined onto a silicon substrate, mounted on a PCB finger. These devices were originally fabricated to be coated and used as gas sensors, with one microhotplate used to heat the device to operating temperature, while the other was used to monitor the temperature of the sensing substrate during operation. Using a FLIR A20 USB infrared camera, it was ascertained that the temperature of the device was proportional to the resistance measured across the secondary heater meander, and that the device could quickly heat up to over 100 °C with a current of around 5 mA. The time constant of the microhotplate was measured at around 100 ms. The hotplates and PCB finger were inserted into the assembled device, and the thermopneumatic chamber was sealed using silicone sealant.

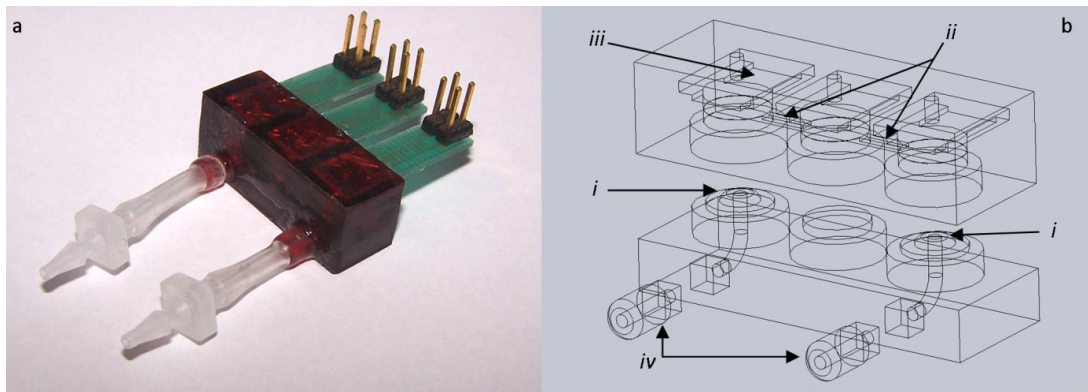


*Figure 8.3 – (a) photograph of initial micropump design, a reciprocating displacement thermopneumatic device rectified by a pair of active membrane valves; (b) wireframe 3D representation of pump, in an exploded view showing the separate components that were built on the SLA machine and later manually assembled, showing the 2 membrane hole valves with (i) collared distal fluidics, the three working fluid chambers linked by (ii) 500 × 300 μm cross-section fluidic channels, the (iii) thermopneumatic actuation chamber, separated from the working fluid chamber by the membrane, and (iv) the separately fabricated MSL pipe fittings. The device measures 28 × 10 × 11 mm, not including heater PCBs and pipe fittings*

The micropump was actuated using the NI-DAQ 6009 USB data acquisition device, using the 5V digital out channels to control 3 IRF3711 MOSFETs regulating the output from a variable power supply, allowing the temperature of the microhotplates to be controlled. The actuation program of the pump is shown in *Figure 8.4*.



During testing with water, the micropump showed initial promise, creating a fluid flow at around 0.5 Hz. However, the flow would quickly break down and stop, and the pump appeared to lock in position. It was found after a period of testing that the problem was almost certainly that the polymer body of the device was not allowing enough heat to escape. This led to the time constant of the thermopneumatic chamber being too high, and the valves were eventually locking down on the valve collars. Although slowing down the pump pattern may have allowed the valves time to unstuck, it was clear that the flow rate was not going to be very large. It was therefore decided to try pneumatic actuation, which does not suffer from such thermal problems, and allows a more direct control over the actuation pressure.

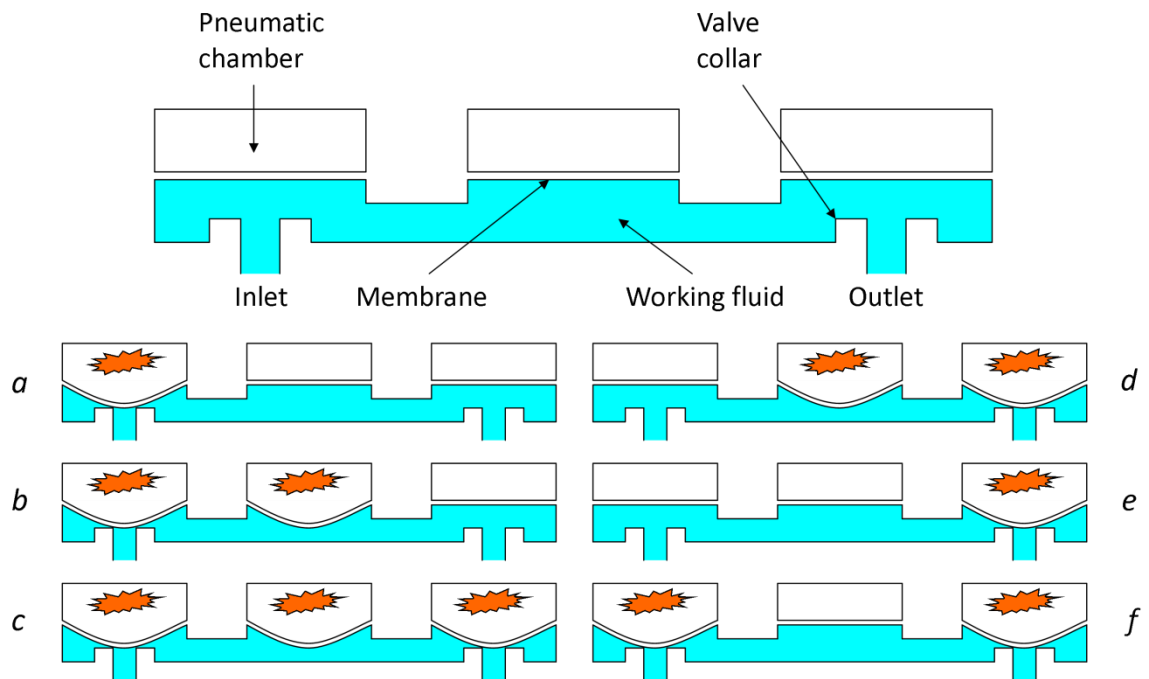


Figure 8.4 – Actuation pattern of thermopneumatic micropump, from (i) to (vi). Although in theory a simpler pattern of (i) to (v) could be used, the step at (vi) makes sure that at no point is the pump in a position where at least one of the valves is not closed, increasing the backpressure created by the actuation motion.

### 8.3.3 Pneumatic Actuation

The previous characterisation of the test membranes, along with the many instances in the literature reviewed in Chapter 2, show that pneumatic actuation is a viable and controllable method for the actuation of a microfluidic device. Most of those devices reported in the literature reported using soft lithography as the fabrication technique. Of these, most

employed the reciprocating membrane with flanking active valves approach seen in the thermopneumatic pump above [8, 17-24], although ball valves [25] and passive flaps [26] have also been used.

One disadvantage of pneumatic actuation is that an external pneumatic is required, making it difficult to compare directly to other fully integrated devices, such as piezoelectric and thermopneumatic actuated micropumps. However, the pressure source can be a standard small-scale pump, powered with a battery, allowing portability. The pneumatic device footprint can also be smaller, and fabrication is simplified. They are also suitable for disposable medical and biological research systems, where the micropump can be integrated as part of a disposable cartridge, with the control electronics and pneumatic source located separately for re-use.

A problem encountered with the multi-part thermopneumatic design, detailed above, is that the assembly introduces a number of difficulties, including the chance of leaks, and the possibility of the glue seeping into microchannels, blocking the pump. It was therefore decided to attempt to build a single-part, monolithic pump. This precludes certain pump designs, such as those that rely on rectification from normally closed passive flap, plug or membrane hole valves. Most of these designs require the membrane or flap to be pressed up against a structure to provide the required force to block flow in a given direction, and building such devices using SLA would simply result in the mobile portion of the valve being fused to the plug. However, active membrane valves are normally open, and are therefore possible.

Another simple concept from a fabrication viewpoint is nozzle/diffuser elements. These microfluidic structures utilise the pressure difference created by flowing fluid through a widening or narrowing tube, and require no moving parts. These elements are relatively common in silicon-based designs, normally using integrated piezoelectric drivers operating at high frequencies [27]. This design has been used in a number of polymer-based devices, mostly

using piezoelectric actuation [28-30], although lower frequency actuation techniques such as electromagnetic [31, 32] and even thermopneumatic [33-36] have been used, suggesting pneumatic actuation with a suitable control valve would be possible.

## 8.4 Initial Pneumatic Micropump Design and Test Rig Development

### 8.4.1 Early Experimentation

An initial single-membrane, pneumatic design was produced, shown in *Figure 8.5a*, features a 4 mm diameter pump membrane, flanked by a pair of pyramidal nozzle diffuser elements, widening from a pinch point of 100  $\mu\text{m}$  to 1 mm over a distance of 5 mm. The minimum width of the nozzle/diffuser elements was decided upon after the examination of the SLA system's capabilities in Chapter 4. A pair of 200  $\mu\text{m}$  wide cleaning holes were also incorporated into the design, into the pneumatic and working fluid chambers, in order to speed up the post processing. The devices were built with the machine parameters described previously, and took around 3 hours to complete.

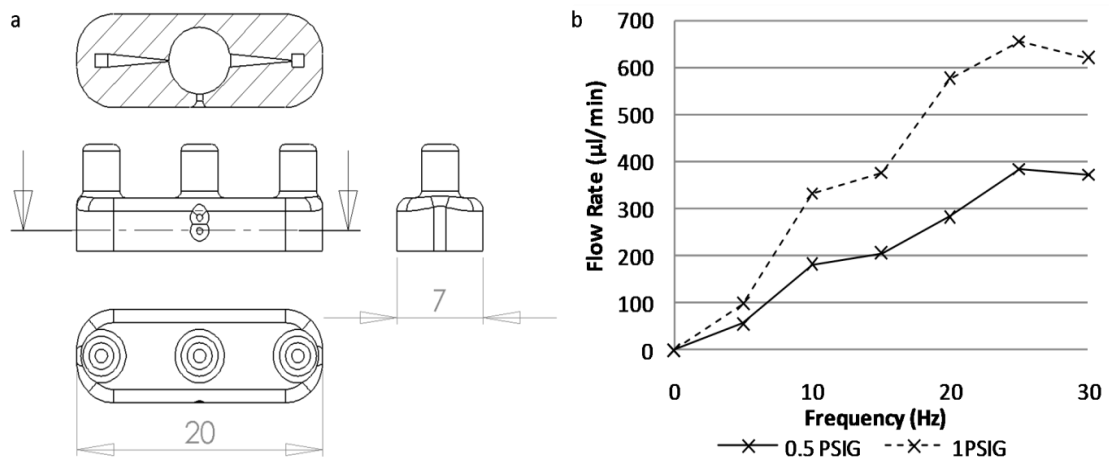


Figure 8.5 – (a) schematic of initial nozzle/diffuser micropump design, produced using the EnvisionTEC Perfactory Mini Multi-Lens SLA system, details in text. (b) initial flowrate vs. frequency test results for this design.

Initial tests were carried out on the first design using a simple actuation and measurement system. The actuation set up was as with the previous long-term tests, using a signal generator to control an N-type MOSFET, switching the valve output from atmospheric

pressure to the pressure from the regulator. However, the pressure sensor was placed on a T-junction between the regulator and the valve, to measure the supply pressure. Flowrate measurements were carried out using ColePalmer Clearflex tubing, stretched horizontally alongside a ruler. The fluid head was timed from point to point, allowing the flowrate at various supply pressures and actuation frequencies to be calculated. This data is shown in *Figure 8.5b*.

The results show a roughly linear rise of flowrate with actuation frequency, indicating levelling off between 25 and 30 Hz. Increasing the actuation pressure also appears to increase flowrate. However, it was obvious that both the method of data collection and the range of data were not of sufficient quality to take any real conclusions, except that the pump design did work and showed promise of reasonable flowrates. There were also problems regarding the reliability of the pump in terms of fabrication yield, as a number of the devices had blocked nozzle/diffuser elements upon being removed from the machine. In the very first batch of pumps fabricated, this was due to the over-cure problem discussed in section 8.2.3, as the “ceiling” layers of the pyramidal nozzle/diffusers were curing through into the fluidic void, blocking the narrow parts of the features.

#### **8.4.2 Test System Setup**

It was decided to build a test rig that could remove as many human elements from the process as possible, and the resultant system is shown in *Figure 8.6*. The system was based on the NI-DAQ 6009 USB data acquisition device used previously, along with the Honeywell 26PC series pressure sensor to monitor the input pneumatic pressure from the regulator. The Lee Co valve used in the previous test setup was replaced with the Clippard ESO-3W 12V 3-way solenoid valve used for the long-term reliability tests, as it was found to have a quicker response time and was therefore able to produce a pulsed pressure at higher frequencies – up to just under 150 Hz as opposed to the 30 Hz of the Lee device.

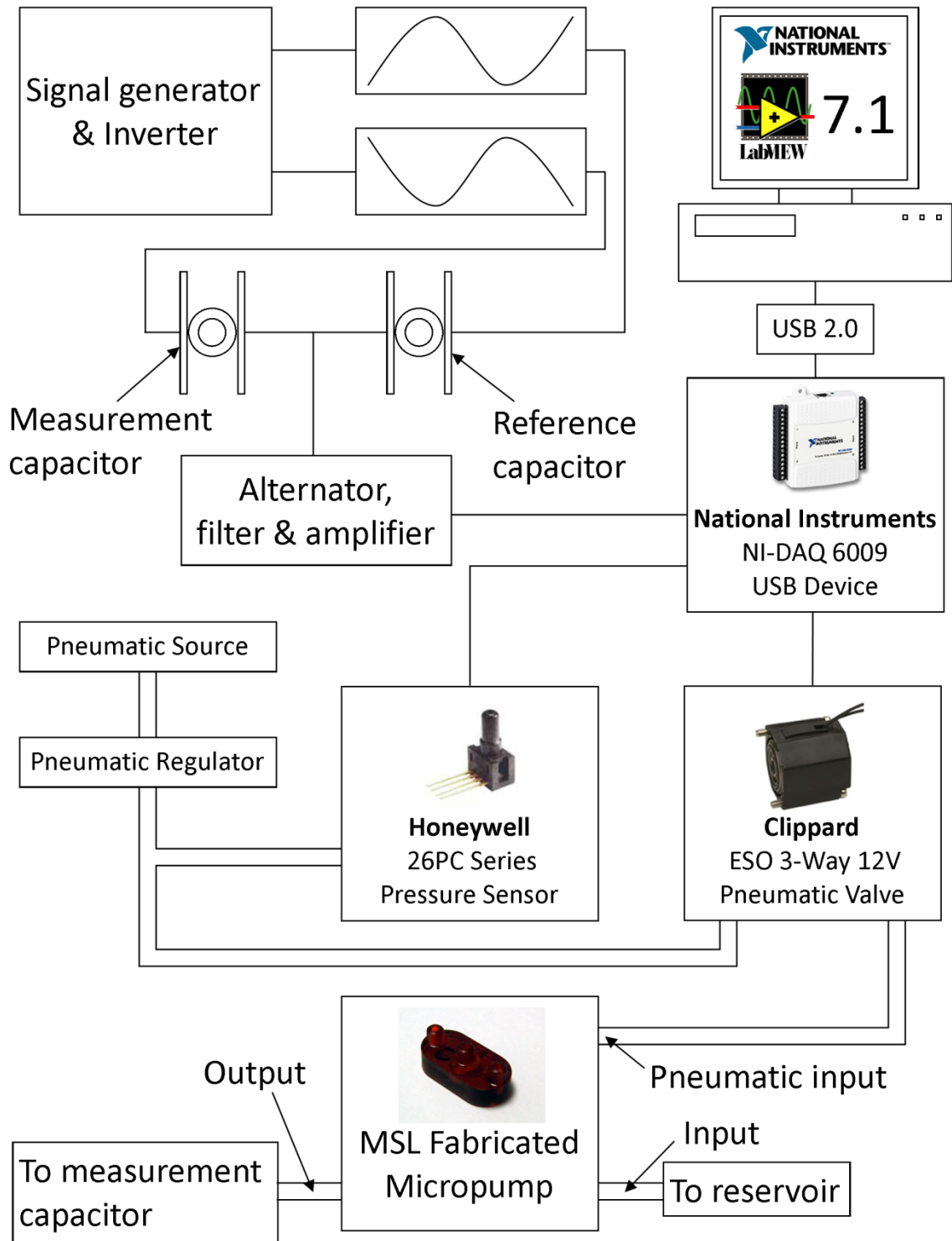


Figure 8.6 – Final test rig used to characterise both the flowrate and backpressure characteristics of the MSL fabricated micropumps. Further details in main text.

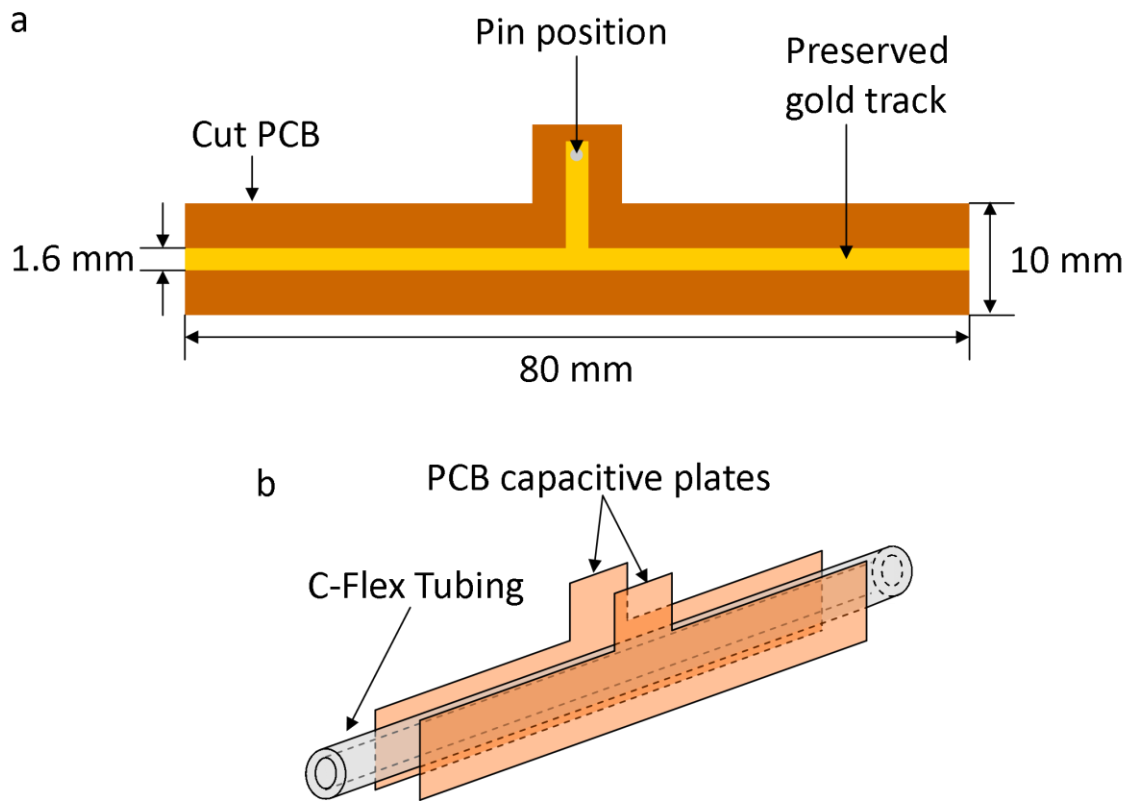


Figure 8.7 – Details of PCB capacitive plates used in final test rig setup. (a) Plate dimensions and layout, including position of soldered pin placed through the PCB facing outwards from the gold strip, allowing connection to the rig electronics. (b) Positioning of plates to form the capacitor, with the C-Flex tubing internal bore (1.6 mm diameter) placed along the horizontal 80 mm gold strip on the plates. This arrangement was held together using a series of customised MSL-fabricated components. Two sets of plates containing the tubing were used, with one connected to the output of the micropump, and the other left dry as a reference device.

It was decided to link the input side of the pump to a large reservoir of deionised water, in order to minimise any backpressure or surface tension effects that might be caused by a smaller input reserve. The output of the pump was connected to a tube of known internal diameter (ColePalmer 1.6 mm ID PTFE tubing), and the movement of the fluid to air boundary would be measured via a pair of capacitive sensors.

Two pairs of capacitive plates, with a gold strip 80 mm long and 1.6 mm wide, were fabricated from a PCB using an automatic router. Connection pins were soldered to tabs integrated on the top of the plates, which were held in place either side of a length of the PTFE tubing using parts fabricated in the SLA machine. The plate design can be seen in more detail

in *Figure 8.7*. One pair of plates was placed either side of the tubing connected to the output of the micropump being tested, and would measure the fluid flow. The other pair would be set up identically, but over a stretch of clean tubing with no fluid in it; this would act as the baseline. In a dual-phase water/air system, the fluid front moves into and through the measuring capacitor. As it does so, the capacitance of the measurement capacitor will change relative to the reference capacitor, allowing the amount of water in the measurement capacitor to be determined. Assuming that the phase change within the tubing has no effect on the movement of the fluid front, and that the working fluid is non-compressible, it is therefore possible to track the movement of the fluid front, and therefore work out the flowrate being generated by the micropump.

In order to measure the relative capacitance of the two capacitors, two circuits were built (see Appendix A). The first circuit uses an oscillator to create a sine wave, which is split and inverted. The original wave is fed into a capacitive plate on the measurement capacitor, whilst the inverted signal is fed into the control. The output signal from the opposite plates of the capacitors are then combined and filtered by the second circuit. In theory, if the two capacitors are identical, the inverted signals combined should cancel each other out, leading to a 0V output signal. However, any difference will create an oscillating output, which is then filtered into a stable output voltage reading, proportional to the difference between the two capacitances. A variable resistor was included in the circuit to control the gain of the output filter, allowing the output to be tailored to the input range of the analogue inputs of the data acquisition device.

Rather than using a signal generator to drive the switching of the valve, control was handed to the NI-DAQ 6009. Due to the limitations of the LabVIEW software and the speed of the PC used, it was not possible to directly drive the valve using the digital out ports. Attempting to do so lead to a slow, often stuttering output signal. However, an analogue port

could be used to output to a voltage-to-square wave convertor (see Appendix A). An LM331 voltage to frequency convertor was configured to output in a range up to 240 Hz linearly with an input voltage range of 0 to 5V. The pulsed output was fed into a 74LS74 Dual D-Type Flip-Flop to produce a square wave at half the pulsed input frequency. This signal was used to switch an N-Type MOSFET in series with the valve, oscillating it between atmospheric and pressurised states.

One disadvantage of this approach is that it is not possible to control the status of the pneumatic valve directly i.e. to turn it on or off from the software. It was found during the initial tests that around half of the data sets showed much lower flowrates at lower frequencies than others. It was discovered that these passes were linked by the tests being started with the membranes in the “on”, pressurised position. It is assumed that the membrane takes time to settle back from the fully inflated position, limiting early flowrates measured from the data. It was therefore decided to check the valve’s status before each test by manually running it at very low frequencies, listening for the distinctive on/off sounds of the valve, stopping the run with the valve in the “off”, atmospheric position.

Another factor that must be checked for is the correct priming of the pump and test fluidics. The nozzle/diffuser designs presented in this chapter are not self-priming, and must be filled manually with a syringe. Even small air bubbles formed during the manual priming are disastrous for pump performance, as the air is compressible and robs the working fluid of energy that would otherwise be used to create flow. In practice it was found that thoroughly drying the test tubing and micropump internal fluidics using the air from the regulator would allow the tube to prime smoothly.

The assembled test rig is shown in *Figure 8.8*. Early testing showed that the capacitive sensors were very sensitive to electrical noise, and they were therefore mounted inside a metal box. A lot of the noise was found to come from the solenoid valve, as it switched quickly



between open and closed states, and therefore both it and its wired connection were shielded to protect other components. The circuitry for the valve control, along with the NI-DAQ device, were also placed in a purpose-built Faraday cage, and the capacitive sensor circuit boards were also mounted in a separate box. It was found that the proximity of the control PC CRT screen also affected the signal noise levels; the computer was therefore positioned at least 2 metres away during testing.

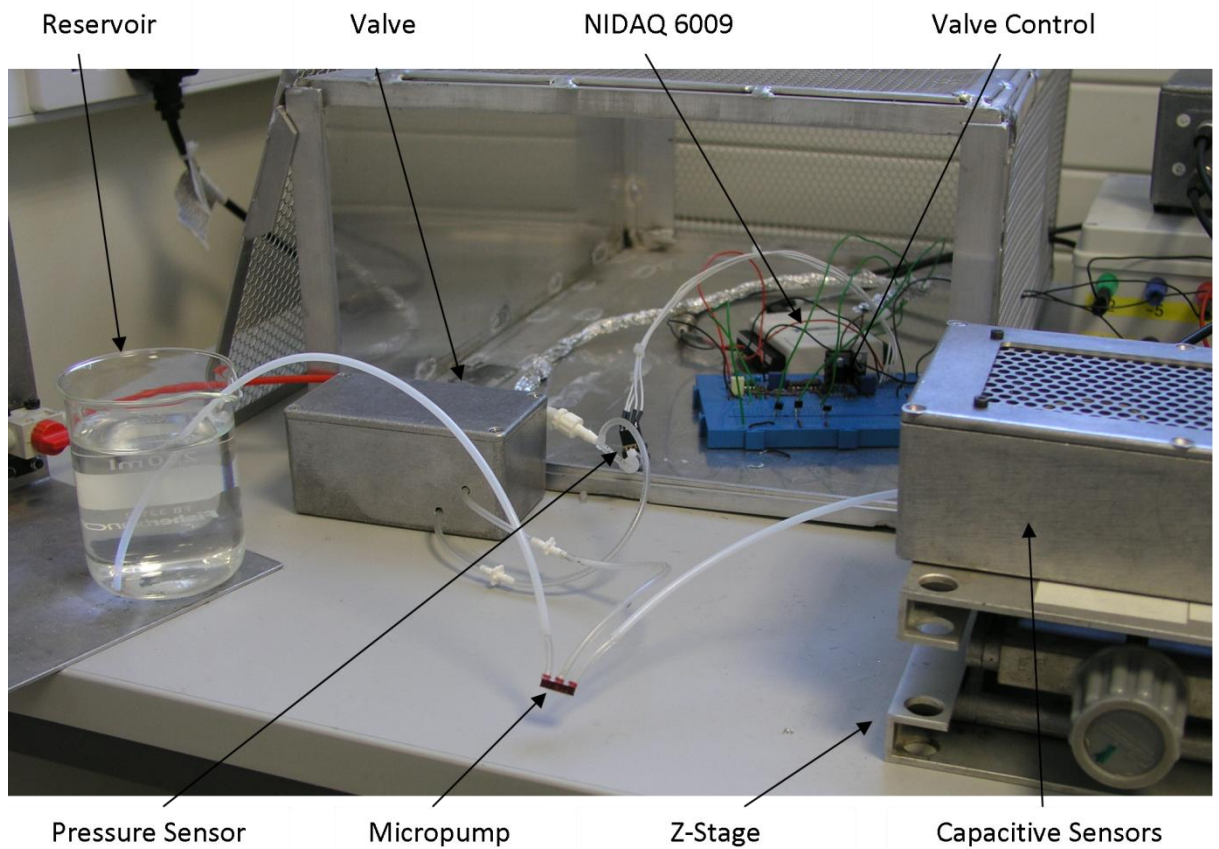


*Figure 8.8 – Test setup used to obtain flowrate data from the pneumatic SLA micropumps. Details of operation in text.*

In order to obtain flowrate readings, tubing through the measurement capacitor must be both horizontal and level with the meniscus of the reservoir, in order to ensure that the flow is subject to zero backpressure. The box containing the capacitive sensors was therefore placed on a Z-stage, allowing it to be moved up and down, and the box was checked using a spirit level. In order to calibrate the Z-height, the tube into the reservoir was gently agitated.

This small amount of force breaks the surface tension on the measurement side. If any flow is observed, the Z-axis can be adjusted to compensate.

The NI-DAQ 6009 device was operated using a custom LabVIEW program, the interface of which is shown in *Figure 8.9*. The software displays using a chart the capacitive sensor voltage over time, along with the input pressure reading. The program has two modes of operation. The first is manual, where the actuation frequency of the micropump can be set either via a slider or input via the keyboard. The second mode sweeps the output voltage from 0V (0 Hz) to 5V (120 Hz). With each cycle of the program, the NI-DAQ is instructed to increase the voltage by a small amount, the value of which is set via the interface. Typically, this would be around 0.01 V, with each cycle lasting around 40 ms. Finally, the values of both the pressure and capacitor voltage signals can be written to a text file, along with a millisecond timer reading for temporal positioning.

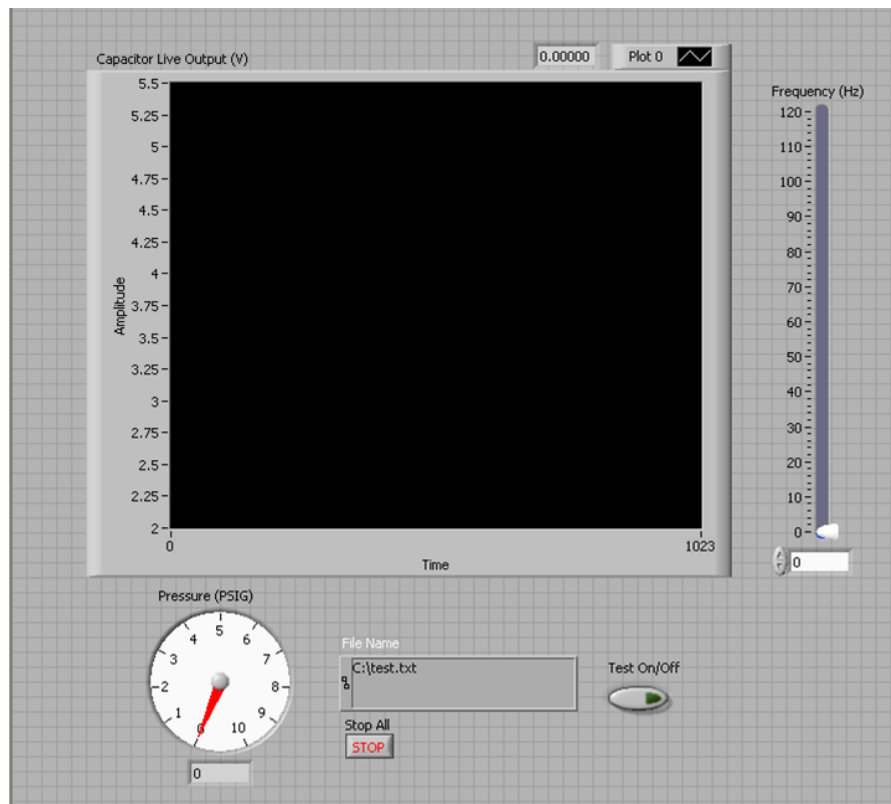


*Figure 8.9 – Interface of LabVIEW 7.1 program used to control the test system and the devices during characterisation. Output indicators for the capacitive sensor voltage and pressure sensor, along with inputs for pump actuation frequency, data file name and test status are visible.*

In order to process this data, the difference between the output voltage of the capacitive sensor circuits when the measurement capacitor is full and empty must be taken. This value can be divided by the length of the capacitor (80 mm) to give a volts-per-millimetre value, normally around 0.0325 V/mm. It was found that the base voltage (empty) and maximum voltage (full) were constant i.e. once the capacitor was empty or full, the reading would not change with any later fluid flow. However, it was found that an amount of sensor drift affected the system, requiring a periodic recalibration of this value.

### **8.4.3 SLA Micropump Reliability – Part 1**

One observation made from the testing to this point was that the membranes integrated into the monolithic micropumps were extremely unreliable, seemingly against the earlier findings in section 8.2.1. The freshly fabricated and post-processed devices would often break their membranes at pressures as low as 1.5 PSIG (10.34 kPa) within a few hundred cycles, an event characterised by the ejection of the water contained within the measurement system by the pneumatic pressure released from behind the now broken membrane.

Initially it was suspected that the water use in testing was damaging the membrane, as this appeared to be the major difference between the long-term test membranes and those micropumps being characterised. It followed therefore that coating the membrane in some form of waterproof layer may help protect the fragile membranes. After considering a number of options, a quick and easy method was to use HPA Conformal Coating. This substance is normally in spray form to protect PCBs and other electronic components against minor environmental damage, such as spillages. The coating was pushed with a syringe through the device fluidics, before being dried with an air jet and left to dry fully. This appeared to solve the reliability problems, although layer thickness consistency was a concern.

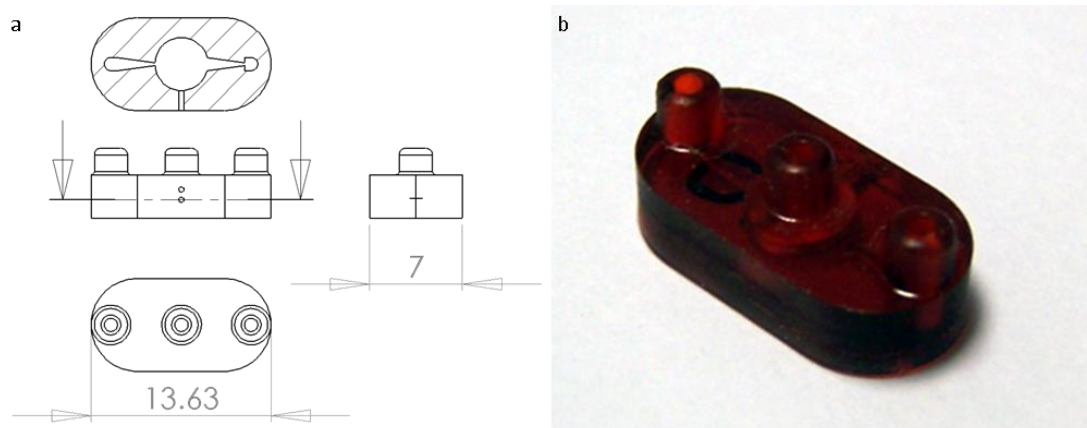


Figure 8.10 – Final single-membrane nozzle-diffuser rectified pneumatic micropump (Mk5) fabricated using the EnvisionTEC Perfactory Mini Multi-Lens SLA system.

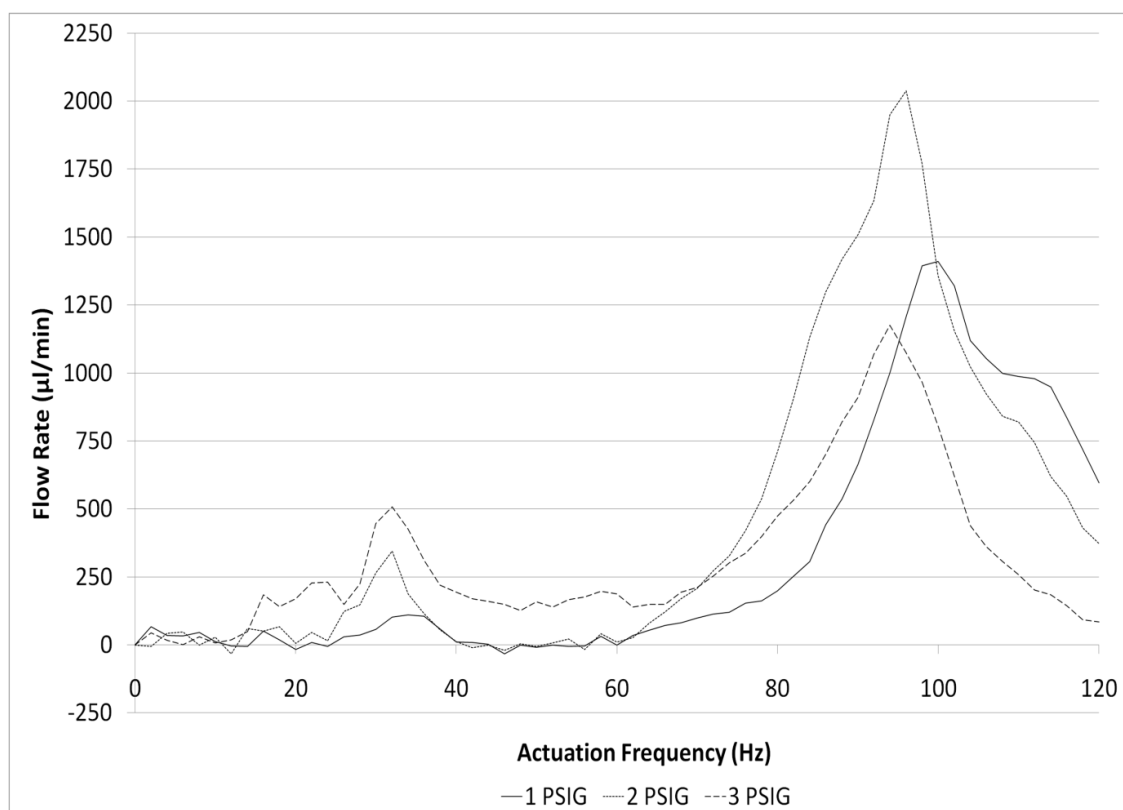


Figure 8.11 – Flowrate data collected from the Mk5 SLA-fabricated micropump using the frequency-sweep mode in the LabVIEW software. This data was published in poster form at Eurosensors '09 [37].

#### 8.4.4 Further Pneumatic Micropump Development

A number of changes were made to the pump to try to increase yield. The nozzle diffusers were made planar (i.e. the cross-section only changes in the X plane, not in the Y) to avoid the over-cure problem, and were defined by their divergent angle ( $8^\circ$  from centreline, see Kar *et al* [29]) rather than their length. This resulted in a shorter nozzle/diffuser footprint, making the pump itself smaller – from 20 mm long to 13.77 mm, which would allow 6 devices to be built instead of 3 on the  $28 \times 21$  mm build area. The narrowest part of the nozzle/diffuser structure was doubled in size to 200  $\mu\text{m}$  to avoid blockages forming during the fabrication process, caused by particles of dust or stray cured resin from previous builds. Finally, the integrated pipe fittings were reduced in height, still allowing a connection yet reducing the fabrication time by 30 minutes.

The resulting device (known as the Mk5) is shown in *Figure 8.10*. The micropump was tested using the test rig outlined in *Figure 8.8*, using the swept-frequency mode. This technique in theory allows the flowrates to be collected across the entire system spectrum in a single test, allowing a greater number of devices to be characterised in a shorter amount of time. Data was collected from a single device, creating a time and capacitive voltage data stream. This stream was split into short, equal segments over a given arbitrary frequency. Using the time and positional data, the flow rate for that short section could be calculated. This data was then subjected to a moving average in order to remove much of the remaining noise. The resulting device flowrate profile can be seen in *Figure 8.11*.

The data shows a small peak in flowrate at around 30 Hz, followed by a much larger peak at around 90 to 100 Hz. It was assumed at the time the dead zone between the two peaks was caused by resonances within the pump membrane, or perhaps within the oscillating pneumatic valve. The graph also shows an optimum actuation pressure of 2 PSIG (13.79 kPa), with an increase or decrease of 1 PSIG (6.89 kPa) leading to a drop in peak performance. The

data was published as part of a poster presentation at the Eurosensors '09 conference in Lausanne, Switzerland [37].

#### 8.4.5 Backpressure Measurements

The backpressure of a pump can be defined by the distance vertically that a pump can raise a column of fluid, and is indicative of the work being done on the liquid by the device. This is normally measured using a manometer, which consists of a U-shaped loop of tubing containing a discrete volume of fluid. With both sides of the U-bend subjected to the same pressure, the meniscus height in both vertical portions of the tube should be identical. Applying a different pressure to one end of the tube causes the fluid to move; the difference in height between the two menisci can be converted into a pressure value.

The flowrate test setup described above can be used to measure the backpressure of a given device. The capacitive plates can be raised at a known angle by mounting the box they are mounted in on a sine table. The table angle can be varied by using precision metal slips under one end of the table. With the reservoir on one side of the pump and the measurement tubing on the output side, the system can be regarded as a one-sided manometer – the reservoir is sufficiently large compared to the measurement tube volume that it is unlikely the vertical height of the reservoir will change. This makes the backpressure calculation simpler, as the final value is dependant only on the vertical height of the water column in the measurement tube, compared to the rest value.

As with the flowrate data collection, full and empty values must be periodically taken to calibrate the position data. However, a third “equilibrium” value must also be taken, to pinpoint the 0 backpressure position. As with the calibration of the Z-stage, the reservoir outlet tube must be agitated in order to allow the fluid in the measurement tube to move to its equilibrium position. The level of the reservoir can then be altered to raise or lower this equilibrium point, normally so it rests around 10 mm above the bottom of the capacitor plates.

Should the maximum backpressure of the pump at a given actuation pressure and frequency take the fluid front beyond the capacitive plates, the sine table angle can be increased by adding further slips, or even clamped vertically to provide a greater backpressure range.

One problem demonstrated by the calibration procedures is that there are surface tension effects at play in the measurement system, requiring agitation of the reservoir tubing in order for the system to reach equilibrium. Although larger tubing could be used to reduce the meniscus/air/tubing interactions, this increases the distance between the capacitive plates, in practice greatly reducing the signal strength. Practically these effects mean that the swept-frequency technique does not work, as although the pump can overcome this effect when in action, any drop in backpressure will not result in a backward movement of the fluid head. Therefore the testing must be carried out in manual, single-frequency mode. Although this takes more time, and requires that the fluid head be returned to its equilibrium position using a manual syringe, it does allow a flowrate vs. backpressure comparison to be made in reasonable detail.

In order to process the data, a similar process was used as with the swept-frequency data, with the data stream split into small segments in order to calculate flowrate at a given position. However, that position can also be converted via simple trigonometry into a vertical position relative to the equilibrium point, and therefore into a backpressure. This results in a graph showing the linear relationship expected between backpressure and flowrate, as shown in *Figure 8.12*. Maximum backpressure and flowrate values can be calculated by finding the Y- and X-axis intercepts of a linear trend line respectively. The error analysis methods used are outlined in *Appendix B*.

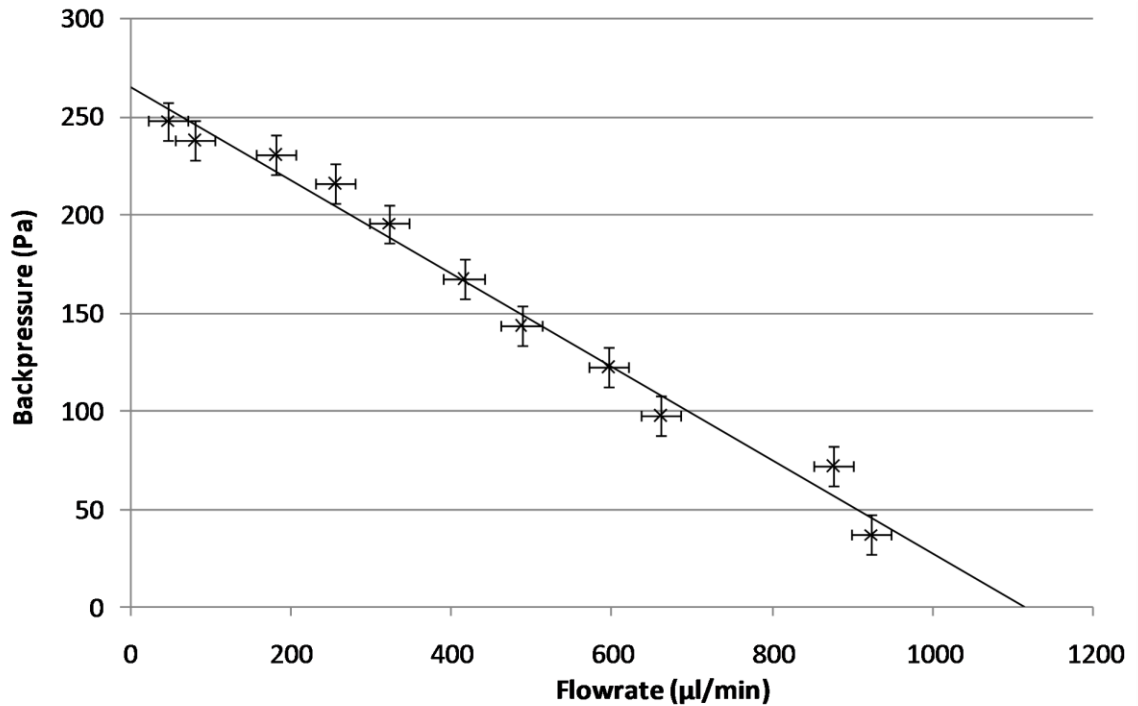


Figure 8.12 – Typical backpressure and flowrate data collected using the test setup described in section 8.3.5.

## 8.5 Data and Device Reliability

### 8.5.1 Swept-Frequency Flowrate Data Reliability

Although the data presented in *Figure 8.11* initially appeared reliable, subsequent backpressure measurements did not match the flowrates calculated, producing a completely different profile versus actuation frequency. It was therefore decided to re-characterise the original device using the flowrate and backpressure data purely from the angled-capacitor setup. The results are shown in *Figures 8.13* and *8.14*.

The difference between the two flowrate data sets is stark. Rather than dual peaks at 30 and 90 to 100 Hz, the former much smaller than the latter, a large peak is visible at 60-70 Hz, with higher actuation pressures also exhibiting flow at around 110-120 Hz. A “dead zone” is still found, but at 100 Hz. It is clear that something in the swept-frequency method causes some form of shift in the data collected.



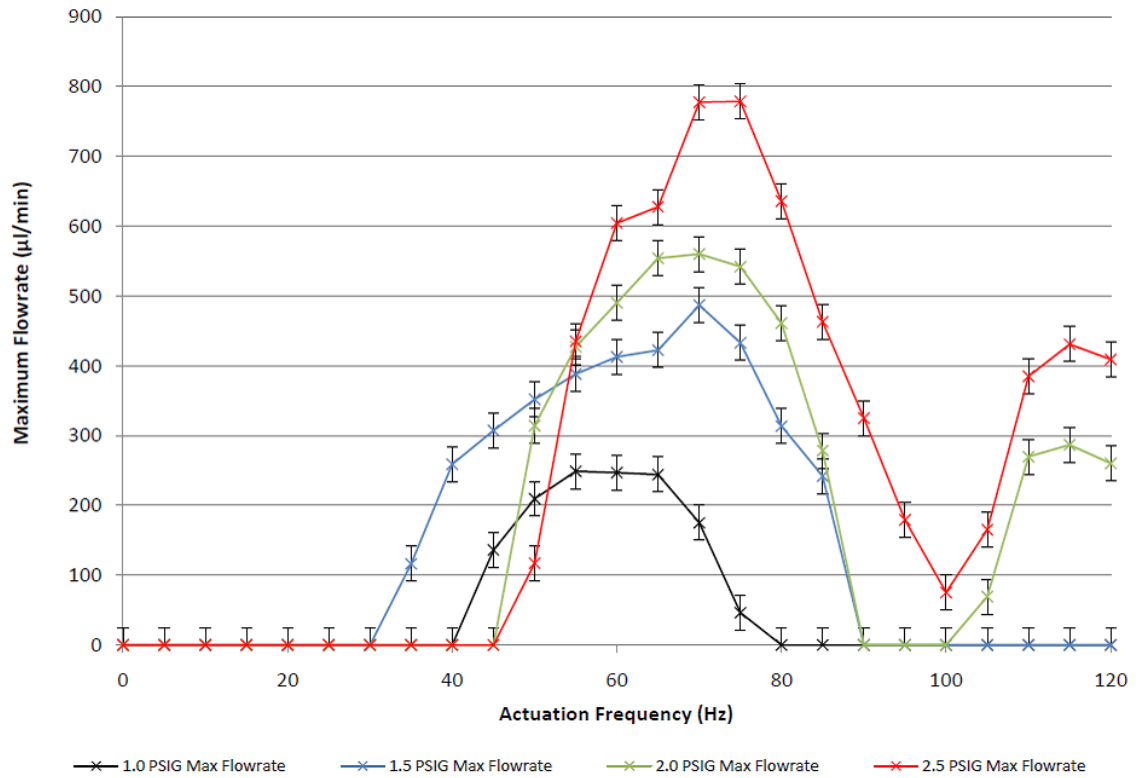


Figure 8.13 - Data collected from the original Mk5 device via manual, single-frequency flowrate measurements, in comparison to the flowrate data collected via the swept-frequency method shown in Figure 8.8.

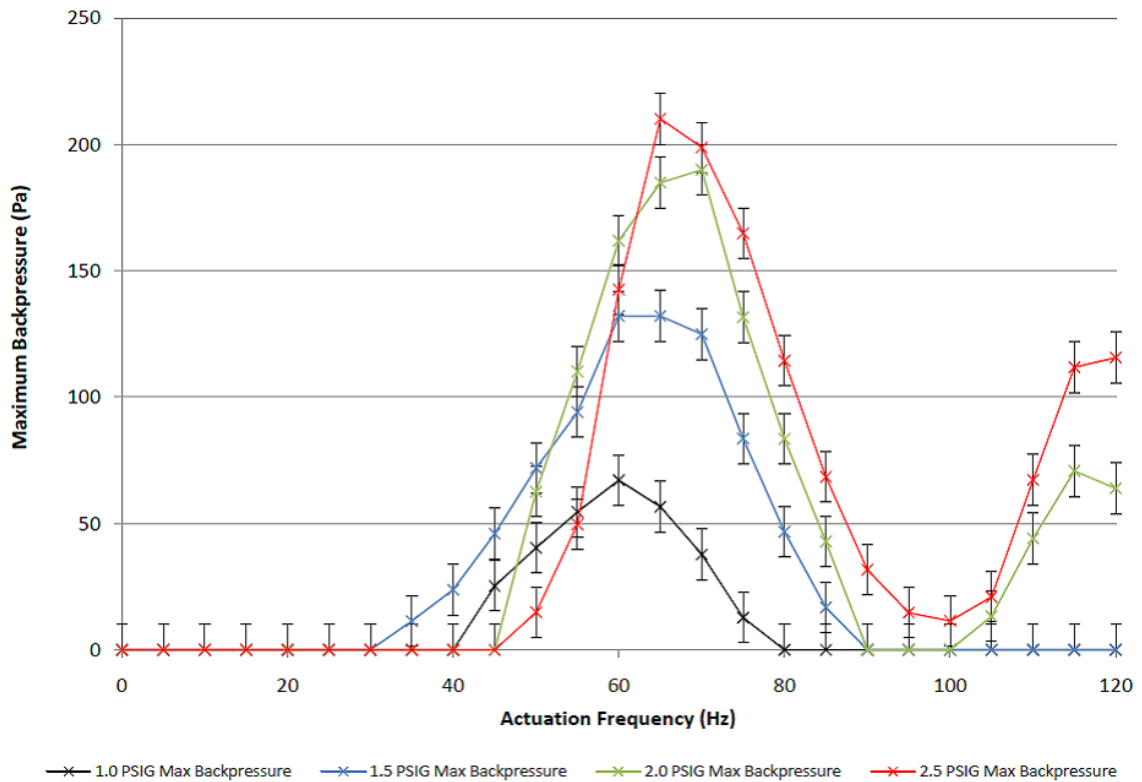


Figure 8.14 – Backpressure data collected from the original Mk5 SLA-fabricated micropump via the manual, single-frequency method.

There are a number of possible causes of this effect. It is assumed that the manually collected flowrate results shown in *Figure 8.10* are more reliable, as each measurement is taken under exactly the same initial conditions. The automatically-collected swept-frequency results however measure the transient flowrate at a given frequency, which may not give the membrane time to reach any characteristic resonant frequencies. Additionally, the ramping up of the frequency sweep was constant across the frequency range, potentially underestimating the early, low-frequency flowrate measurements by not allowing the flowrate time to stabilise. It is also obvious that the automatic technique overestimates the actual maximum flowrate by a factor of 2, probably because the fluid column is not at rest at the point before the flowrate at a given frequency is measured. Although not particularly satisfactory, it was decided to characterise future devices using the manual approach.

### **8.5.2 SLA Micropump Reliability – Part 2**

Although the SLA micropump's reliability had increased greatly since the decision to coat the device internal fluidics and membrane with conformal coating, further tests were carried out to confirm the efficacy of the technique. 6 identical devices were fabricated – 3 were coated, 3 were left after post-processing. The devices were left to dry over a weekend, simply due to the schedule at the time of the experiment. After drying for 3 days, the uncoated devices were tested, and were found to not exhibit the reliability issues of their predecessors.

It was clear that leaving the devices for around 48-72 hours after post-processing helped strengthen the membranes fabricated monolithically within a device. It is assumed, although not proven, that the rest period either allows the membranes to cure more fully in the ambient light, or allows the evaporation of solvents from the device material. It is more likely that the former is the case, due to the lack of reliability issues found with either the test membranes or the thermopneumatic pump. The thermopneumatic design was exposed to water during testing, and showed no reliability issues beyond those attributed to the thermal

properties of the device. It was decided that although the 3 day waiting time was not ideal, it was preferable to the potentially uneven coating procedure. All further devices were therefore fabricated using the 2-3 day waiting period. Further research could be useful in order to empirically characterise the effect of the drying time on membrane reliability.

## **8.6 MSL Micropump – Final Designs**

### **8.6.1 Mk5 Single-Membrane - Manual Data**

A new 6-device batch of Mk5 micropumps was produced. Of these devices, 2 were damaged during the fabrication process, but 4 identical pumps were found to be in working order after the 3 day drying period. Each was characterised using the manual backpressure/flowrate measurement process described above. The data collected was then averaged to form the graphs shown in *Figures 8.15* and *16*.

The data in *Figures 8.15* and *8.16* show some interesting patterns, especially in comparison with the coated micropumps characterised in *Figures 8.13* and *14*. The flowrates of the non-coated micropumps in *Figure 8.15* are much higher at the lower frequencies than those of the coated devices, perhaps suggesting that the coating limits membrane flexibility. However, at higher actuation pressures, above 1.5 PSIG (10.34 kPa), flow rate drops markedly at lower frequencies. It was found under these conditions that the devices would produce an initial flow, but this would quickly stop and even reverse using the angled backpressure test setup. This suggests that the more flexible uncoated membranes are “bottoming out” – being pushed too far by the higher pressure over the longer period afforded by the lower actuation frequencies, and then not returning to their original position sufficiently far enough before the next actuation stroke.

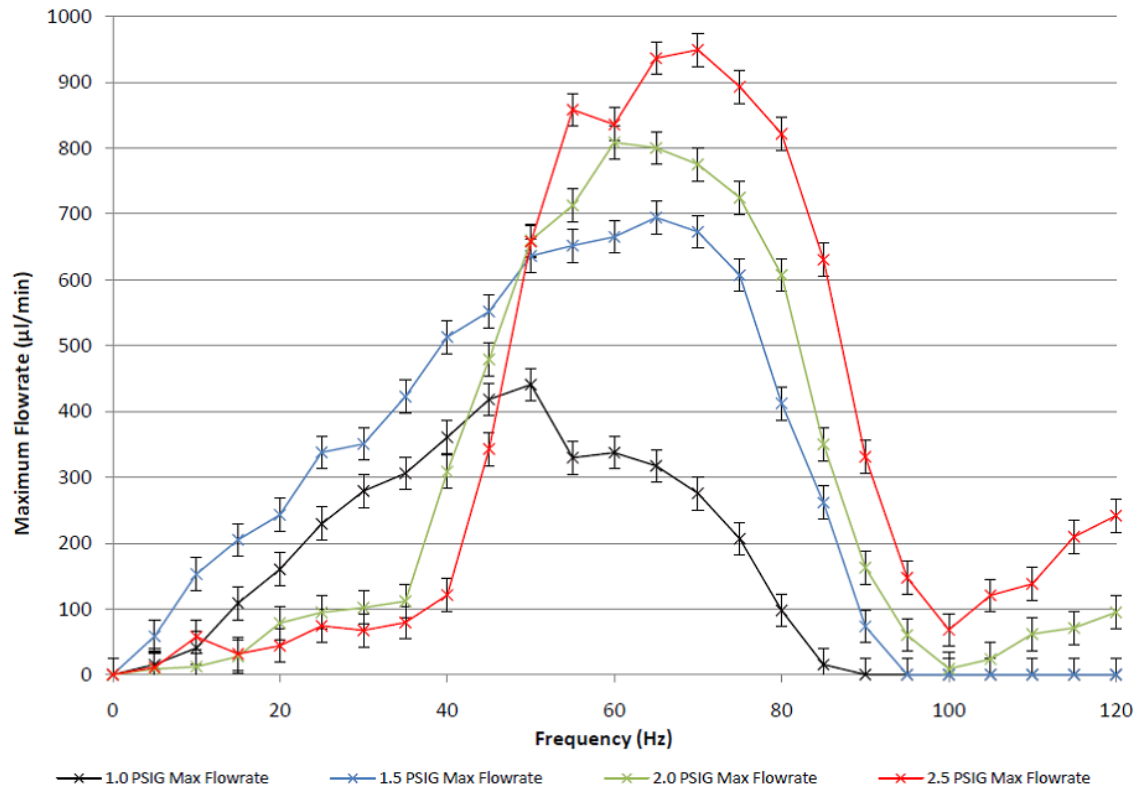


Figure 8.15 – Averaged flow rate data collected from 4 identical Mk5 pneumatic single-membrane nozzle/diffuser micropumps. The devices were post-processed using the drying period described in the main text, rather than the use of conformal coating.

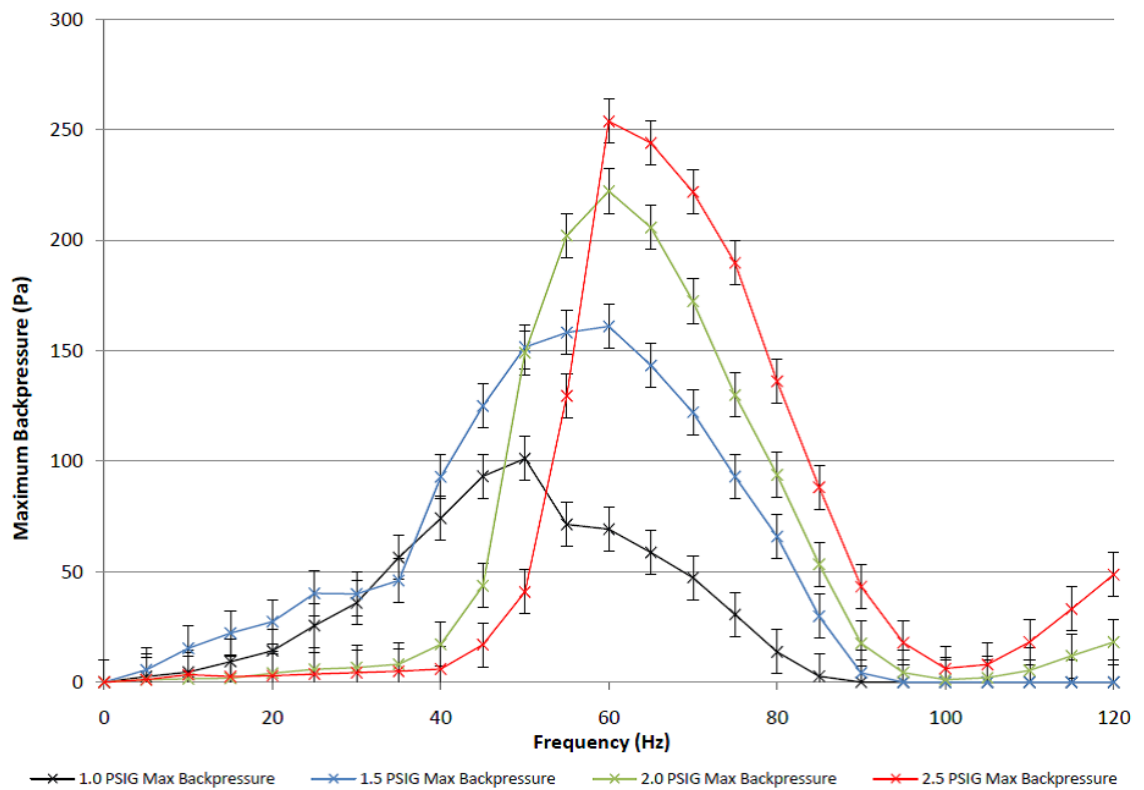


Figure 8.16 – Averaged backpressure data collected from 4 identical Mk5 pneumatic single-membrane nozzle/diffuser micropumps. The devices were post-processed using the drying period described in the main text, rather than the use of conformal coating.

One feature common to both sets of data is the general increase in flowrate and backpressure with actuation pressure. Peak device performance also generally shifts further up the frequency scale with increasing pressure. Finally, with both sets of devices, higher frequencies allow a secondary flow peak at between 110 and 120 Hz, and it is possible that the pump performance could carry on increasing outside the range of the test setup. It was apparent from the data that the uncoated devices offered both greater peak performance, along with better performance over the full range of actuation frequencies.

### 8.6.2 Beyond Single Membranes for Nozzle/Diffuser Designs

One idea investigated was the use of multiple membranes on a single micropump device. A pair of designs were developed: the Mk6, with a pair of parallel membranes acting on a single working fluid chamber; and the Mk7, which was essentially a pair of Mk5 mechanisms placed in parallel on a single device. These designs are shown in *Figure 8.17* and *8.18* respectively.

The first device to be built was in fact the Mk7, due to it being easier to fabricate, not requiring the additional support structures used for the Mk6. The device was treated as per the uncoated Mk5 devices during fabrication and post-processing. However, it was found that it was nearly impossible for the device to be properly primed, mainly due to the liquid filling one branch of the fluidics, but not the other. Further development was therefore halted, especially in light of the more promising results from the initial Mk6 tests.

Data was collected from 3 identical Mk6 devices, averaged and plotted in *Figures 8.19* and *8.20*. A number of observations can be made from the data. Although the flow rates reported are actually lower than those reported for the single-membrane devices, the maximum backpressures achieved are actually higher for any given actuation frequency. In general, maximum flowrate increases with actuation pressure, although there appears to be a levelling off of this trend between 2.0 and 2.5 PSIG (13.79 and 17.24 kPa). The “dead-zone”

seen in other devices at around 100 Hz is less apparent using the “boxer” parallel membrane design. Finally, the low flowrates seen at the higher actuation pressures and lower frequencies due to membrane “bottom-out” is not present, with a relatively linear ramp up of flowrate and backpressure seen across the actuation pressure range.

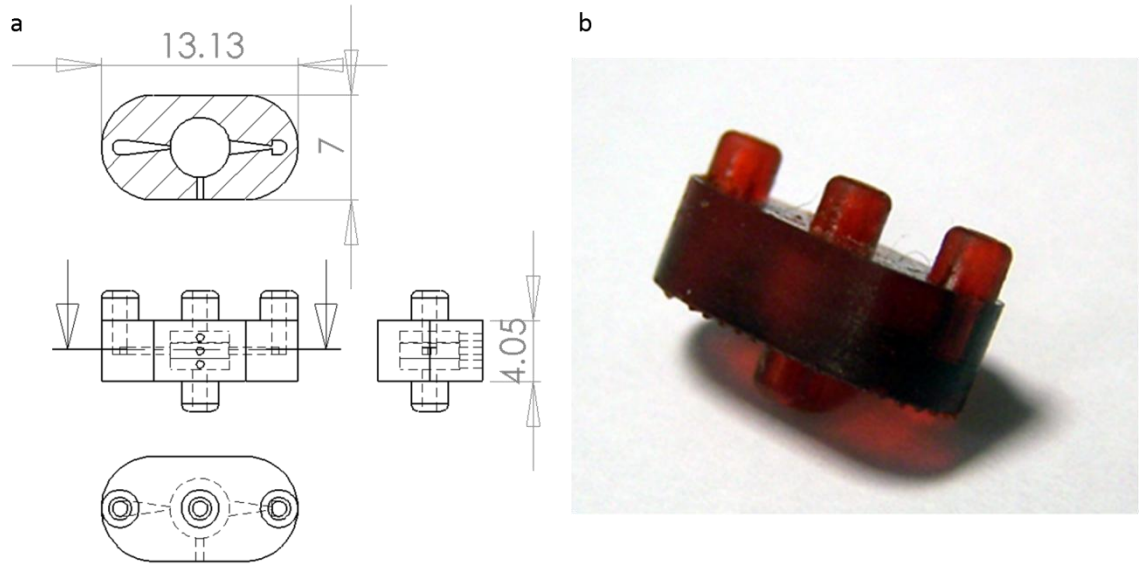


*Figure 8.17 – Dual-membrane “boxer” nozzle-diffuser rectified pneumatic micropump (Mk6) fabricated using the EnvisionTEC Perfactory Mini Multi-Lens SLA system. This device required support structures (concept described in Chapter 4) attached to the bottom surface in order to build – the slight roughness visible on the bottom surface either side of the central pneumatic port are where the support teeth met the device before being removed during post-processing.*

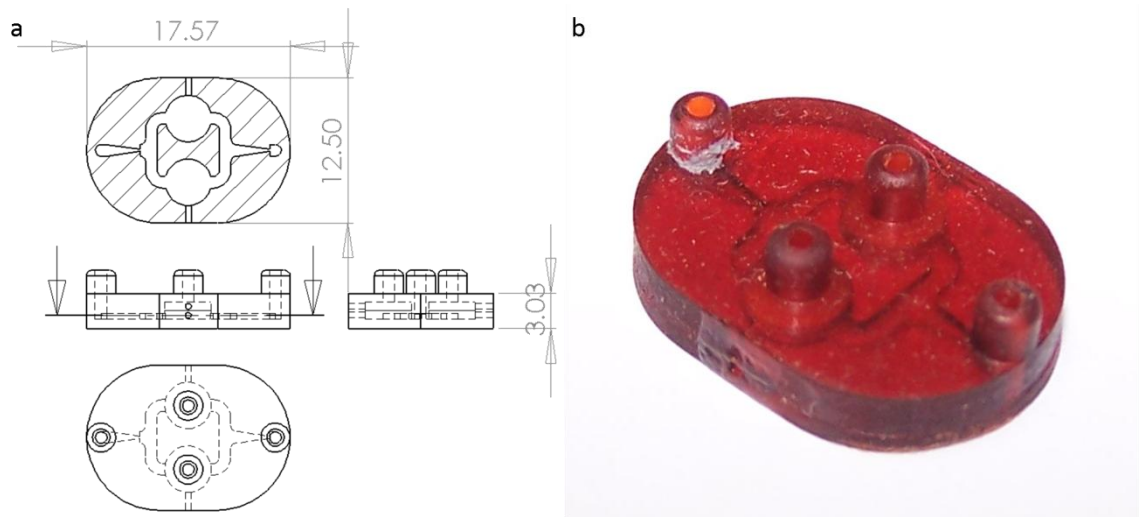


*Figure 8.18 – Dual-membrane nozzle-diffuser rectified pneumatic micropump (Mk7) fabricated using the EnvisionTEC Perfactory Mini Multi-Lens SLA system.*

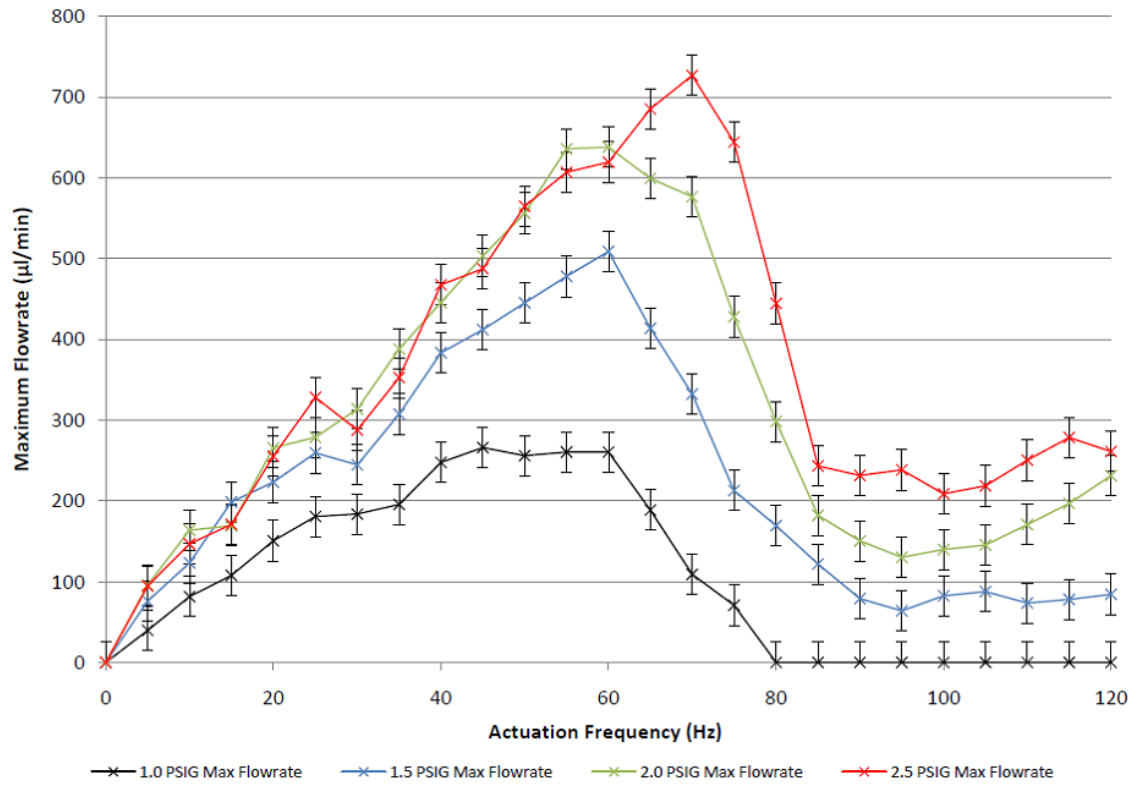


Figure 8.19 – Averaged flow rate data collected from 3 identical Mk6 pneumatic dual-membrane nozzle/diffuser micropumps. The devices were post-processed using the drying period described in the main text, rather than the use of conformal coating.

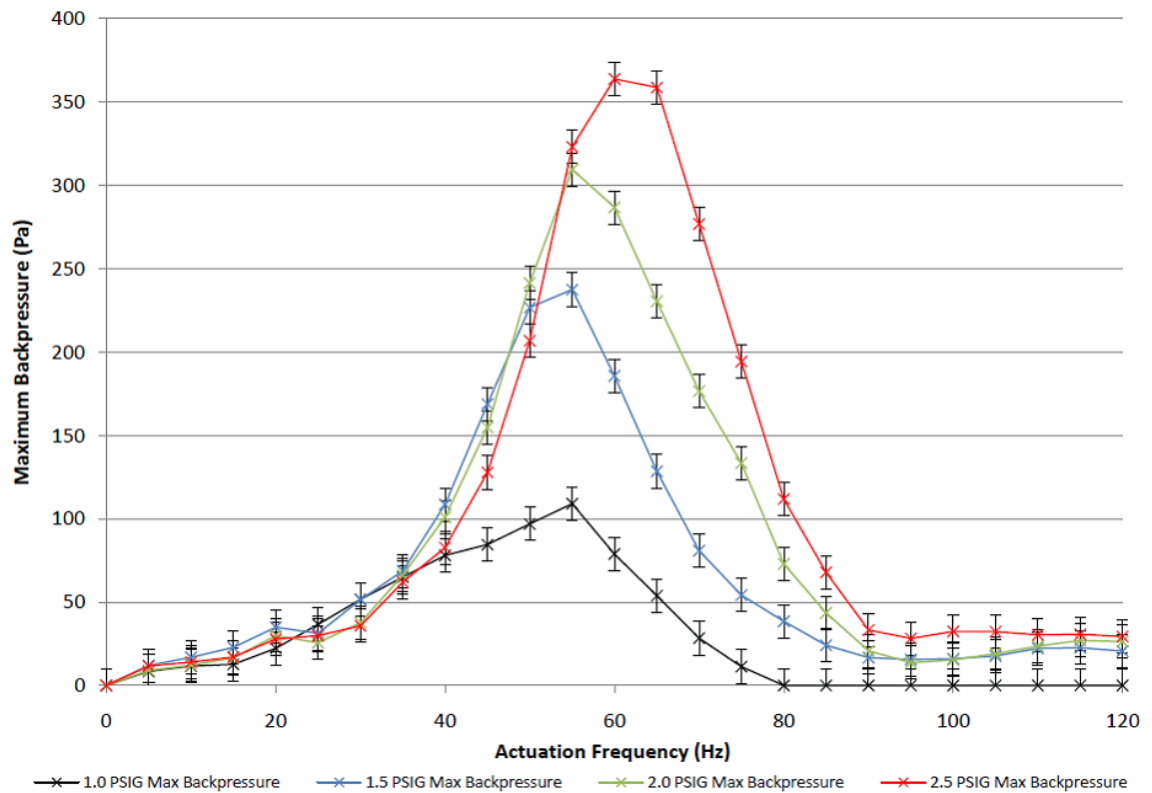
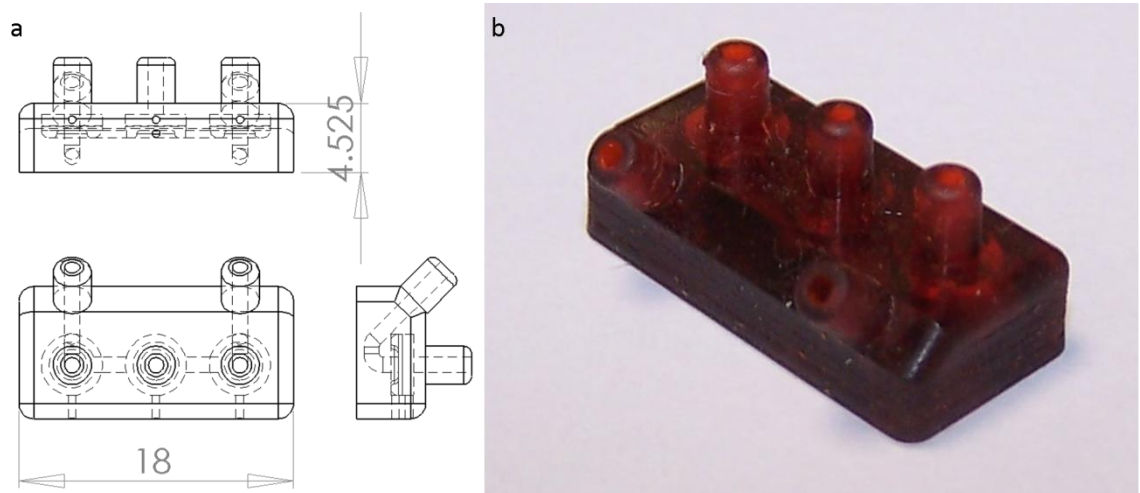


Figure 8.20 – Averaged backpressure data collected from 3 identical Mk6 pneumatic dual-membrane nozzle/diffuser micropumps. The devices were post-processed using the drying period described in the main text, rather than the use of conformal coating.

### 8.6.3 Multi-Membrane Self-Priming Designs

In theory, multiple-membrane active-valve designs such as the thermopneumatic pump outlined previously have a number of advantages over nozzle/diffuser flow rectification. Due to the active closing of the flanking active membrane valves, the maximum backpressure achievable is several orders of magnitude higher. The devices are also more flexible, being able to create flow in both directions and allowing the pumping of air, allowing self-priming.

A monolithic design based on the earlier described thermopneumatic device was developed, shown in *Figure 8.21*. In initial testing, reliability and fabrication yield issues were very much apparent. It is surmised that this is mainly due to the increased number of membranes required for the device operation. During the fabrication of the Mk5 single-membrane pumps, it was found even after optimisation of the build parameters that 1 to 2 of every batch of 6 pumps would have a broken, ripped membrane. This 16-33% loss of yield, if treated on a per-membrane basis, could suggest that on average each 3-membrane device will have at least 1 defective membrane. A number of 2-device batches were fabricated and processed, until a suitable device was found for testing.



*Figure 8.21 – 3-membrane pneumatic SLA-fabricated micropump, consisting of a pair of active membrane valves sandwiching a central pump membrane.*



A number of design and testing problems were found during the initial pump runs. A new LabVIEW program had to be created in order to control the 3 Clippard 3-way valves required to control the pressure to the individual membranes. The device programming itself was identical to that of the thermopneumatic device, as shown in *Figure 8.4*, except pneumatic pressure was employed. Additionally, the much greater backpressure created by the active membrane valves, in comparison to that possible using nozzle/diffuser rectification, meant that the 80 mm capacitive sensors were too small, even when mounted vertically. Therefore, maximum flowrate and backpressure readings had to be taken separately. The flowrates were taken using the capacitive sensors, mounted horizontally in manual measurement mode. Backpressures were taken by suspending a length of ColePalmer C-Flex clear rubber tubing against a vertically mounted metal 1 metre ruler. The device was set at a given actuation frequency, and the fluid column was allowed to stabilise. The height of the fluid column was then measured off the ruler, allowing conversion into a backpressure value. The flowrate and backpressure data is shown in *Figure 8.22*.

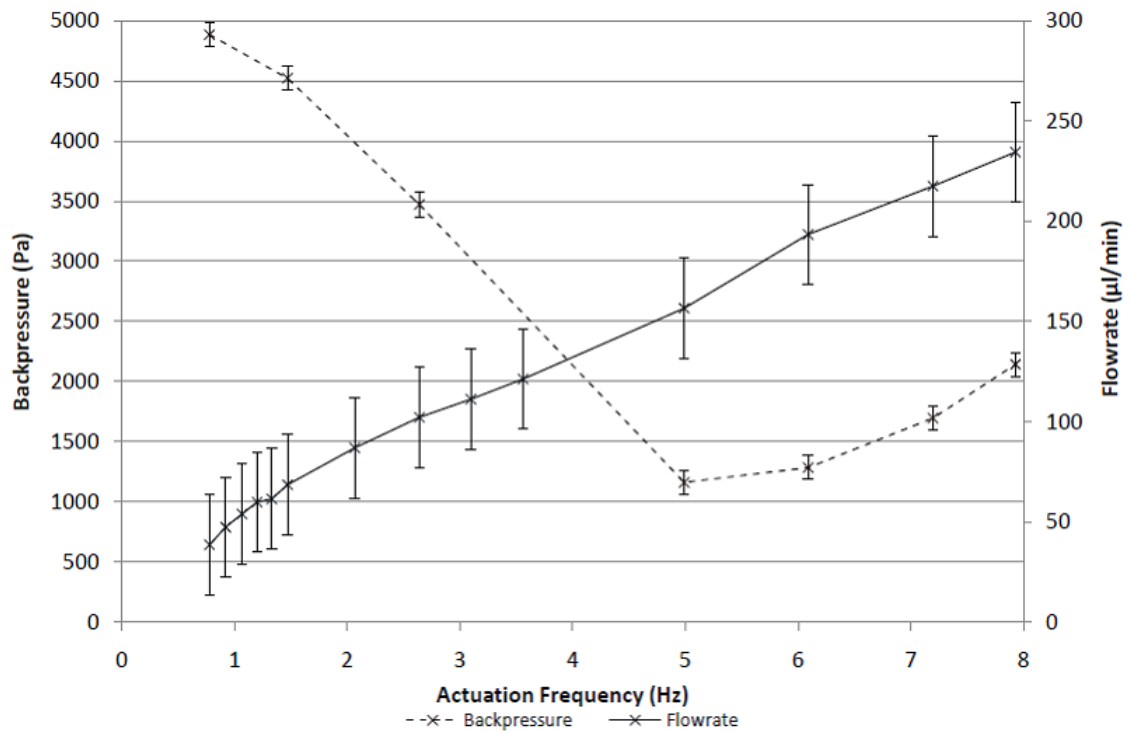


*Figure 8.22 – Backpressure and flowrate data from Mk9, a monolithic 3-membrane pneumatic SLA-fabricated micropump.*

Early reliability issues were encountered, as it was found that quite high pneumatic pressures of around 3 to 4.5 PSIG (20.68 to 27.58 kPa) were often required in order to fully close the valves. The valve membranes when activated rest against a collar, helping to prevent the membrane from becoming over-stressed and breaking, but the central pump membrane was able to expand unimpeded into the pump chamber, often leading to it breaking.

In order to counter these problems, two design changes were made. First, the valve collars were made taller, reducing the pressure required to press the membranes against them and close the valve. Secondly, a cylinder of material was included in the pump chamber, in order to help prevent the pump membrane over stretching and breaking. Although the latter design change appeared to work as expected, the former led to an unexpected side effect: the pump would lock up, much like the thermopneumatic device had done previously. It was found that the valves using the higher collars did require less pressure to close, but would not move far enough for the membrane to produce enough elastic force to move it back into position and open the valve. It is thought that surface tension effects may contribute to the locking effect, as it was not observed when pumping air during priming. The final 3-membrane micropump design therefore included the pump chamber cylinder, but reverted to the 250  $\mu\text{m}$  collar-to-membrane gap, as opposed to the locking 150  $\mu\text{m}$  space.

The multi-membrane design has an interesting backpressure pattern, due to the working mechanism of the active membrane valves. At lower frequencies, the membrane is pushed into the collar for longer, creating a better seal and therefore higher backpressure. Over the range of frequencies tested, the flowrate varies linearly with increasing frequency. This multi-membrane design shows great potential for integration into more complex devices, as its ability to pump in both fluidic directions and self-prime allows a greater flexibility in application. However, the flow created by the pump is comparatively rough compared to the nozzle/diffuser at higher frequencies, and the maximum flowrate obtained was inferior. It

therefore follows that a system containing both devices may exhibit the best qualities of both devices, and this could form part of future research.

### 8.7 Nozzle/Diffuser Optimisation

Although the Mk5 device design had given promising results, it was decided to attempt to optimise the nozzle/diffuser design to improve pump performance. Towards this aim a simple steady-state FEA model was created using the COMSOL Multiphysics package. A 2D cross-section of the Mk5 internal fluidics was exported from SolidWorks 2009 in DXF format. This file was imported into COMSOL, the walls and domains defined, meshed and the simulation run. This process is summarised in *Figure 8.23*. In the initial model, a small square domain was placed at the centre of the pump chamber, with its 4 walls defined as inlets. However, it was found that the side walls facing the nozzle/diffuser elements were producing a stream that was heading straight into the nozzle/diffusers, potentially effecting the simulation. It was therefore decided to define the curved walls of the pump chamber as the inlets, with the end walls of the post nozzle/diffuser fluidics were defined as zero-pressure outlets.

The inlets were defined by a velocity condition, whilst the main subdomain was given the properties of water, with a density of  $1000 \text{ kg/m}^3$  and a dynamic viscosity of  $0.001 \text{ Pa.s}$ . The remaining walls were defined as being non-slip surfaces. Finally, the velocity of the inlet was set at a pair of arbitrary speeds ( $0.0025$  and  $0.005 \text{ m/s}$ ) and the simulation run on a number of different fluidic designs, with nozzle/diffuser divergent angles ranging from  $3$  to  $10$  degrees from the centreline. The fluidic speed was read from the outlets on both sides, and the difference between the maximum velocities calculated. This difference was then plotted on *Figure 8.24*.

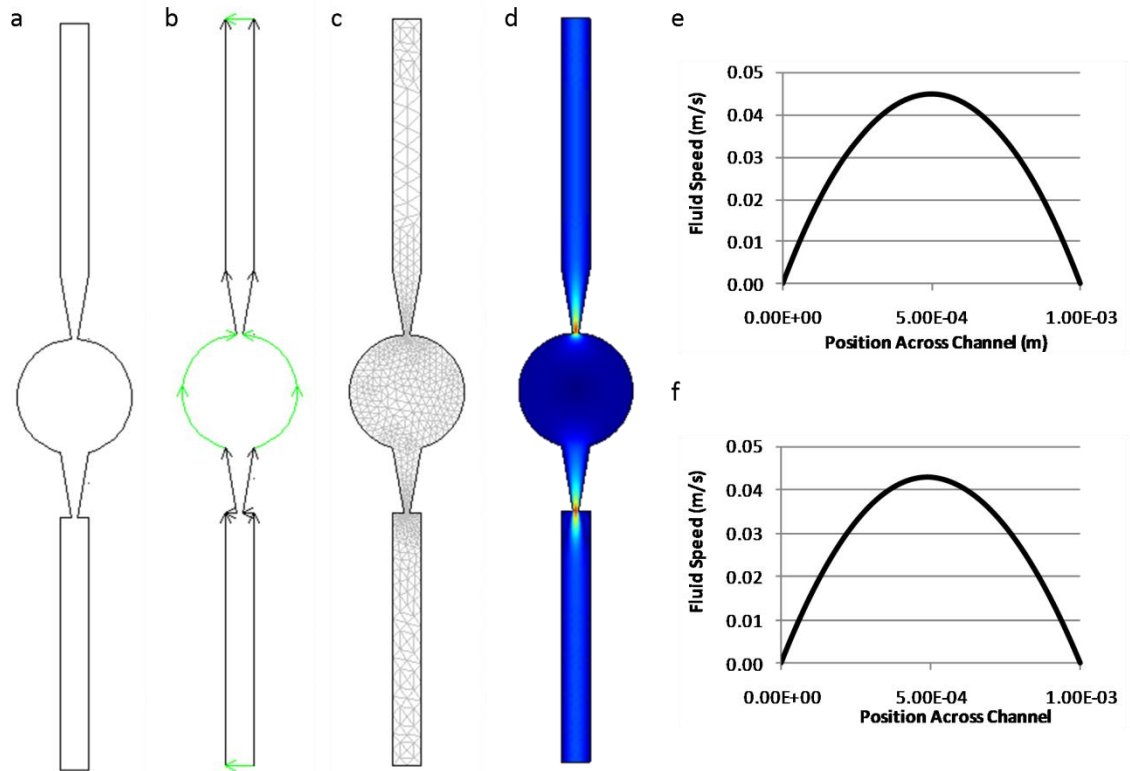


Figure 8.23 – Simulation process: (a) DXF 3D CAD file exported from SolidWorks of device fluidics; (b) model walls and subdomains defined, with the curved pump chamber walls defined as velocity inlets, the end walls (top and bottom) defined as zero-pressure outlets, and the remaining surfaces defined as non-slip. The subdomain was defined as having a density of  $1000 \text{ kg/m}^3$  and a dynamic viscosity of  $0.001 \text{ Pa.s}$ ; (c) the subdomain was meshed (8640 elements per model); (d) the result of the simulation, expressing high pressure as red to low pressure in dark blue. The upper element is the diffuser (pump outlet) and the lower the nozzle (pump inlet); (e) velocity data collected from diffuser side-outlet; (f) velocity data collected from nozzle-side outlet, showing the fluid leaving the device faster on the diffuser side, as expected.

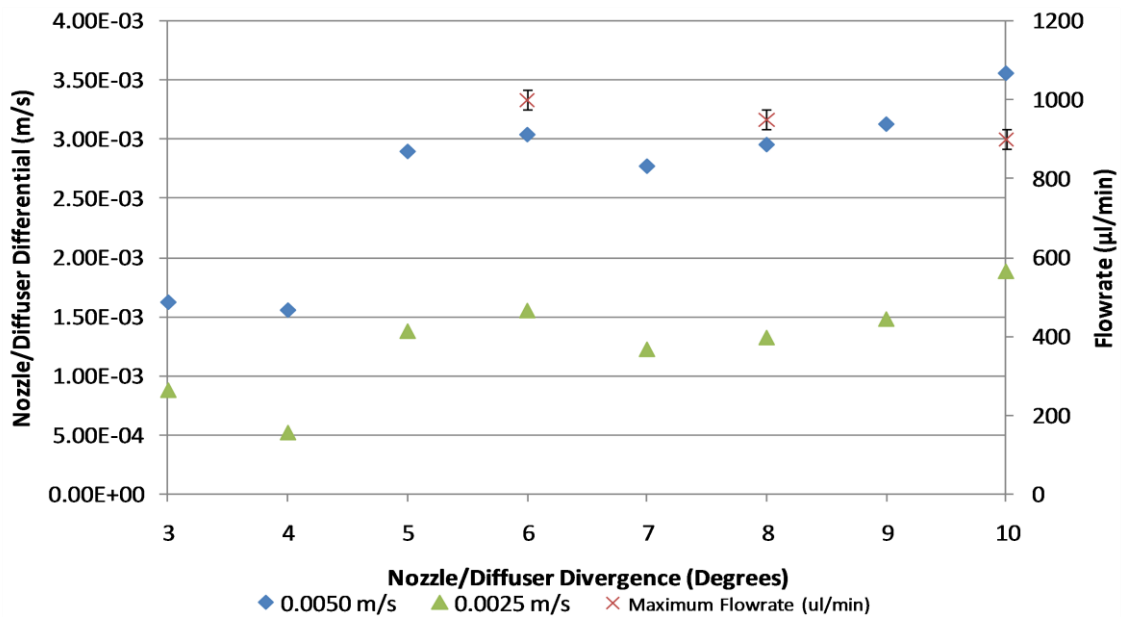


Figure 8.24 – Simulation results, plotting maximum velocity differential between nozzle and diffuser outlets against the nozzle/diffuser centreline divergence, along with the maximum flowrate found for Mk5 pumps using  $6^\circ$ ,  $8^\circ$  and  $10^\circ$  divergence.

In order to validate the simulation, versions of the Mk5 design were produced with nozzle/diffuser elements with  $6^\circ$  and  $10^\circ$  centreline divergence, to compare to the data collected from the  $8^\circ$  original device. The data collected is shown in *Figures 8.25 to 28* inclusive. The maximum flowrates reported were plotted along with the simulation data in *Figure 8.24*.

The data shown in *Figure 8.24* are not conclusive, but have some promise. Although the proportional difference between the  $6^\circ$  and  $8^\circ$  devices in terms of maximum flowrate/fluid velocity is comparable with the real data, the  $10^\circ$  device data does not fit the simulation. It is possible this is an anomaly in the collected data, although it is more likely that the simulation is too simple as a steady-state model to be accurate. Further testing would be required to fully validate the model, including the production and testing of further devices using other divergence angles. Finally, a transient model could be produced, as this could more accurately model the effect of the reciprocating motion of the pump membrane.

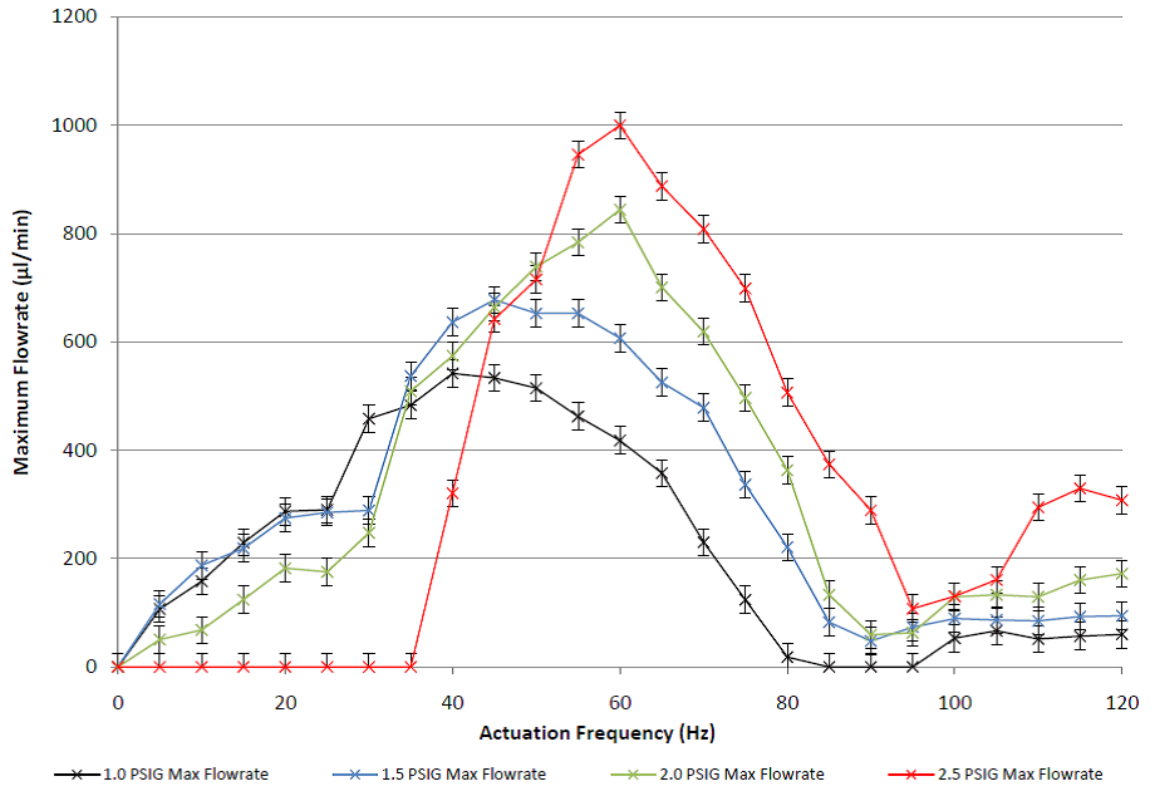


Figure 8.25 – Flowrate collected from Mk5 nozzle/diffuser micropump with nozzle/diffuser elements with  $6^\circ$  centreline divergence. The maximum flowrate of  $995 \mu\text{l}/\text{min}$  was reported at 60 Hz and an actuator pressure of 2.5 PSIG (17.23 kPa).

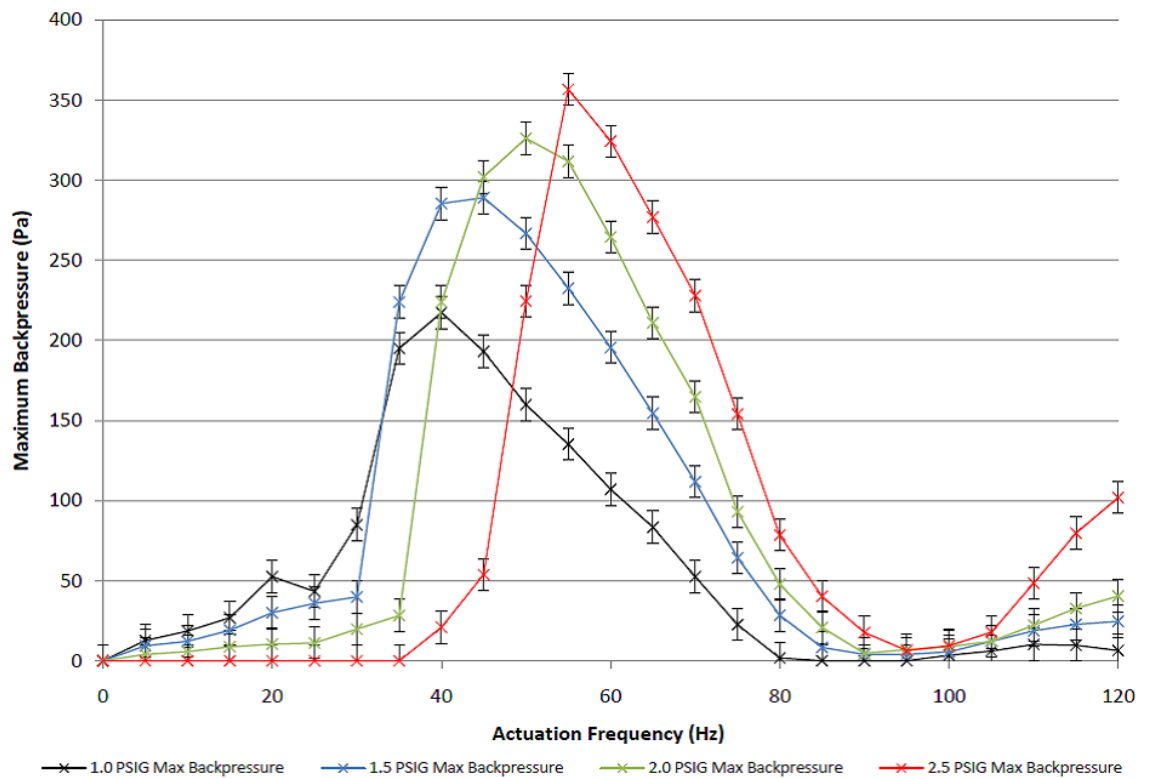


Figure 8.26 – Backpressure collected from Mk5 nozzle/diffuser micropump with nozzle/diffuser elements with  $6^\circ$  centreline divergence.

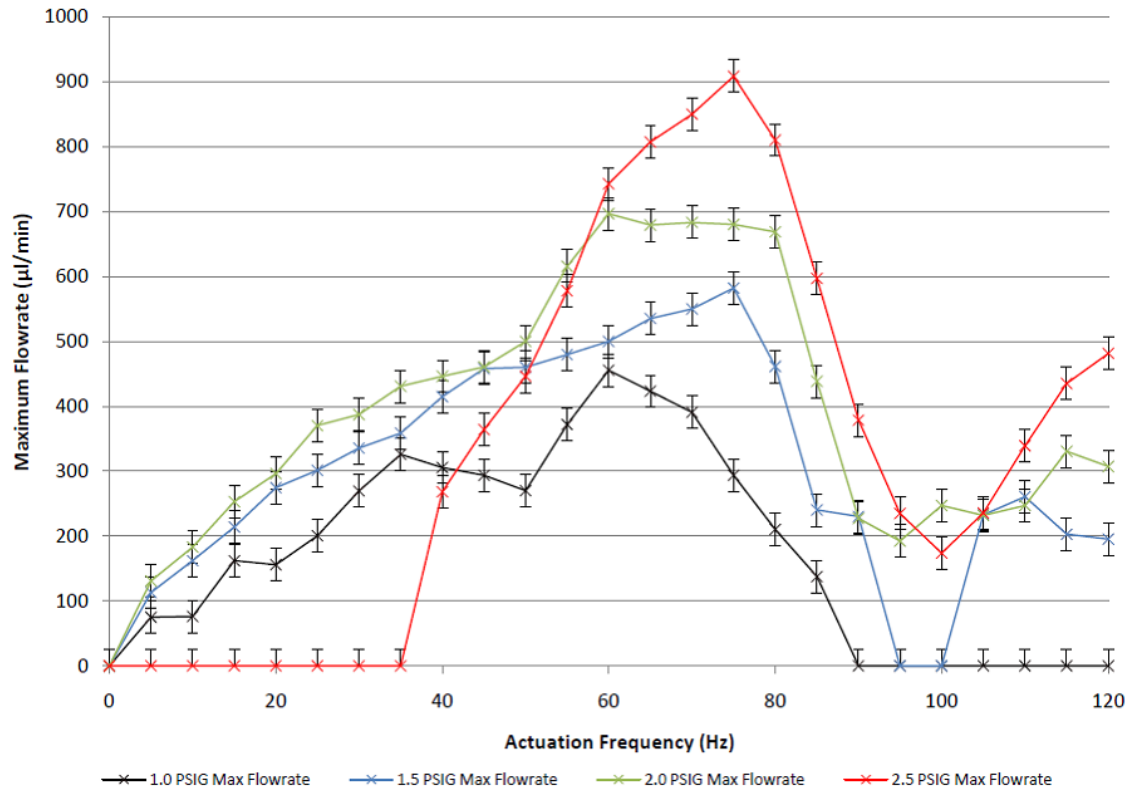


Figure 8.27 - Flowrate data collected from Mk5 nozzle/diffuser micropump with nozzle/diffuser elements with 10° centreline divergence. The maximum flowrate of 802 µl/min was reported at 75 Hz and an actuator pressure of 2.5 PSIG (17.24 kPa).

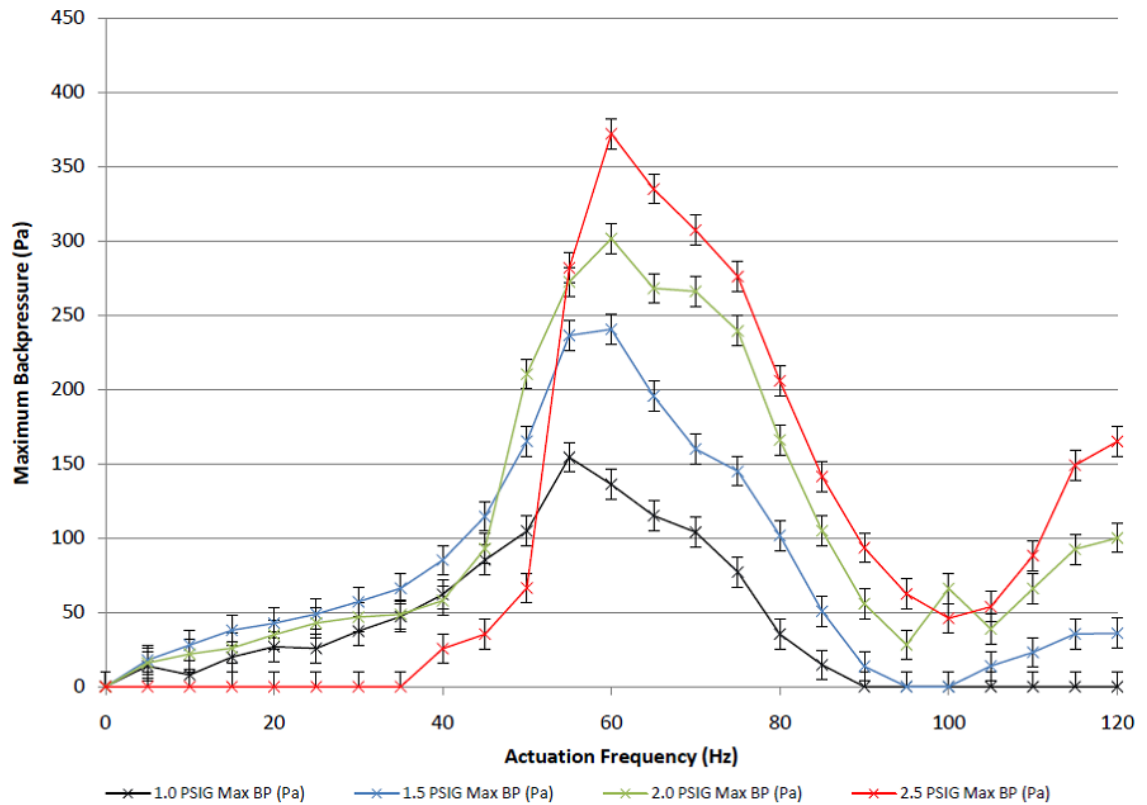
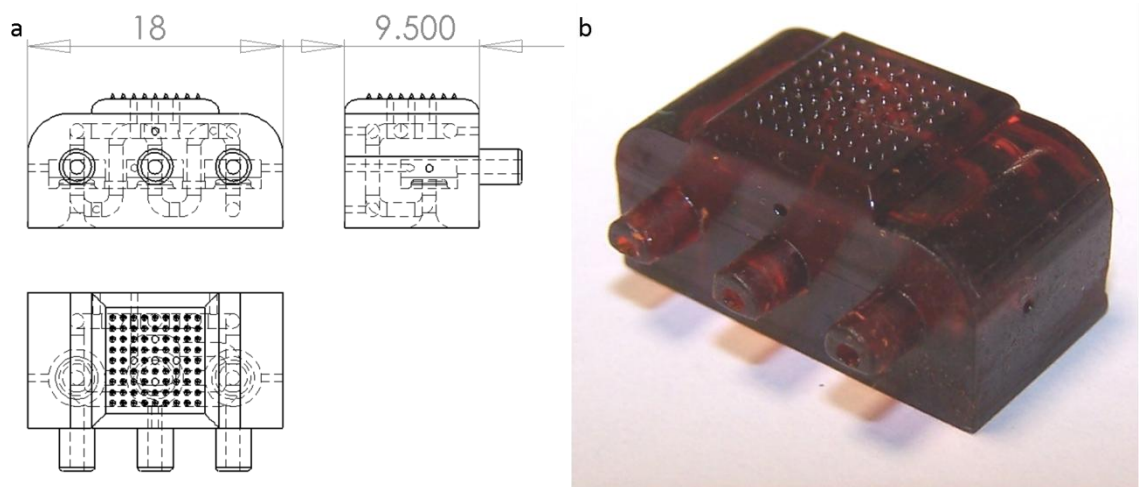


Figure 8.28 - Backpressure data collected from Mk5 nozzle/diffuser micropump with nozzle/diffuser elements with 10° centreline divergence.

## 8.8 Towards an Integrated SLA Microfluidic System

Although the devices presented in this thesis were developed separately, in reality it is most likely they would be used as part of an integrated system. One potential application is in the acquisition and processing of blood samples. To show the potential of SLA systems in the production of complex, 3D integrated microfluidic systems, a test component was fabricated, including a microneedle array, internal fluidic channels and an integrated 3-membrane pneumatic micropump. The test device is shown in *Figure 8.29*.



*Figure 8.29 – Test device fabricated using the EnvisionTEC Perfactory Mini Multi-Len SLA system, featuring a solid microneedle array positioned over an internal chamber, 1 mm deep. 4 0.5 mm diameter holes lead from the array to the chamber. The chamber is connected to an integrated 3-membrane pneumatic micropump by a serpentine channel. The device could be used in the analysis of blood coagulation.*

Although obviously further work would be required, the device presented could be used in the analysis of whole blood samples. Blood let by the microneedle array could be pulled into the device by the self-priming micropump, and pulled along the fluidic channel. If the channel were coated in either a negatively-charged substance such as glass particles or an appropriate clot-forming enzyme, the distance the blood sample travels along the channel before coagulating could be used to measure the clotting ability of a patient.



## 8.9 Conclusion

In this chapter, the development of a series of SLA-fabricated micropumps has been outlined, along with a test system for the characterisation of said devices. Initial work has centred on thermopneumatic actuation of a multi-membrane design. This actuation technique was found to be unreliable due to the insulating properties of the acrylate SLA material. The focus was then shifted to pneumatic actuation. The devices developed could be split into 2 main categories – those rectified with nozzle/diffuser elements, and those rectified using active membrane valves. A range of single-membrane nozzle/diffuser micropumps was produced, with a maximum flowrate of just under 1000  $\mu\text{l}/\text{min}$  achieved using 6° centreline-divergent nozzle/diffuser elements with a backpressure of around 320 Pa. A dual-membrane “boxer” design was also developed. This did not reach the same flowrate, with a maximum of 730  $\mu\text{l}/\text{min}$ . However, the backpressure produced by the device was higher at around 360 Pa.

Work was carried out to optimise the design of the pumps to improve performance, and a simple FEA model was created for this aim. Although the model was not validated fully by the physical data produced, further work could be done to refine the simulation. It should be noted however that for devices built using SLA technology, the lead time for developing the simulation is likely to be far beyond that of simply building a range of devices and testing them.

The ultimate goal of the work was to outline the potential of SLA systems for the production of microfluidic components. It has been shown that membrane-based reciprocating micropumps and active membrane valves can be produced reliably using the system. It has also been shown that such devices can also be integrated along with other SLA-fabricated fluidic components, such as microneedles and microchannels, to form a complex system. Further research could lead to highly complex but easily created devices for use in a range of potential applications.

## 8.10 References

- [1] D. T. Eddington and D. J. Beebe, "A valved responsive hydrogel microdispensing device with integrated pressure source," *Journal of Microelectromechanical Systems*, vol. 13, pp. 586-593, Aug 2004.
- [2] B. T. Good, C. N. Bowman, and R. H. Davis, "Modeling and verification of fluid-responsive polymer pumps for microfluidic systems," *Chemical Engineering Science*, vol. 59, pp. 5967-5974, Dec 2004.
- [3] P. Griss, H. Andersson, and G. Stemme, "Liquid handling using expandable microspheres," *Fifteenth IEEE International Conference on Micro Electro Mechanical Systems, Technical Digest*, pp. 117-120, 2002.
- [4] P. Griss, H. Andersson, and G. Stemme, "Expandable microspheres for the handling of liquids," *Lab on a Chip*, vol. 2, pp. 117-120, 2002.
- [5] A. Furuya, F. Shimokawa, T. Matsuura, and R. Sawada, "Fabrication of fluorinated polyimide microgrids using magnetically controlled reactive ion etching (MC-RIE) and their applications to an ion drag integrated micropump," *Journal of Micromechanics and Microengineering*, vol. 6, pp. 310-319, Sep 1996.
- [6] T. Hasegawa, S. Toga, M. Morita, T. Narumi, and N. Uesaka, "Micro-flow control and micropump by applying electric fields through a porous membrane," *Jsme International Journal Series B-Fluids and Thermal Engineering*, vol. 47, pp. 557-563, Aug 2004.
- [7] T. E. McKnight, C. T. Culbertson, S. C. Jacobson, and J. M. Ramsey, "Electroosmotically induced hydraulic pumping with integrated electrodes on microfluidic devices," *Analytical Chemistry*, vol. 73, pp. 4045-4049, Aug 15 2001.
- [8] M. A. Unger, H. P. Chou, T. Thorsen, A. Scherer, and S. R. Quake, "Monolithic microfabricated valves and pumps by multilayer soft lithography," *Science*, vol. 288, pp. 113-116, Apr 7 2000.
- [9] R. Boden, M. Lehto, U. Simu, G. Thornell, K. Hjort, and J. A. Schweitz, "Polymeric paraffin micropump with active valves for high-pressure microfluidics," *Transducers '05, Digest of Technical Papers, Vols 1 and 2*, pp. 201-204, 2005.
- [10] G. S. Chung and K. B. Han, "Characteristics of a micromachined piezovalue combined with a multilayer ceramic actuator," *Microelectronics Journal*, vol. 38, pp. 690-694, Jun-Jul 2007.
- [11] P. Dario, N. Croce, M. C. Carrozza, and G. Varallo, "A fluid handling system for a chemical microanalyzer," *Journal of Micromechanics and Microengineering*, vol. 6, pp. 95-98, Mar 1996.
- [12] J. Fahrenberg, W. Bier, D. Maas, W. Menz, R. Ruprecht, and W. K. Schomburg, "A Microvalve System Fabricated by Thermoplastic Molding," *Journal of Micromechanics and Microengineering*, vol. 5, pp. 169-171, Jun 1995.
- [13] S. Haeberle, N. Schmitt, R. Zengerle, and J. Ducree, "A centrifugo-magnetically actuated gas micropump," *MEMS 2006: 19th IEEE International Conference on Micro Electro Mechanical Systems, Technical Digest*, pp. 166-169, 2006.
- [14] S. Haeberle, N. Schmitt, R. Zengerle, and J. Ducree, "Centrifugo-magnetic pump for gas-to-liquid sampling," *Sensors and Actuators a-Physical*, vol. 135, pp. 28-33, Mar 30 2007.
- [15] T. Rogge, Z. Rummeler, and W. K. Schomburg, "Polymer micro valve with a hydraulic piezo-drive fabricated by the AMANDA process," *Sensors and Actuators a-Physical*, vol. 110, pp. 206-212, Feb 1 2004.
- [16] C. K. L. Tan, M. C. Tracey, J. B. Davis, and I. D. Johnston, "Continuously variable mixing-ratio micromixer with elastomer valves," *Journal of Micromechanics and Microengineering*, vol. 15, pp. 1885-1893, Oct 2005.
- [17] A. Dodge, E. Brunet, S. L. Chen, J. Goulpeau, V. Labas, J. Vinh, and P. Tabeling, "PDMS-based microfluidics for proteomic analysis," *Analyst*, vol. 131, pp. 1122-1128, 2006.
- [18] W. H. Grover, A. M. Skelley, C. N. Liu, E. T. Lagally, and R. A. Mathies, "Monolithic membrane valves and diaphragm pumps for practical large-scale integration into glass microfluidic devices," *Sensors and Actuators B-Chemical*, vol. 89, pp. 315-323, Apr 1 2003.
- [19] C. W. Huang, S. B. Huang, and G. B. Lee, "Pneumatic micropumps with serially connected actuation chambers," *Journal of Micromechanics and Microengineering*, vol. 16, pp. 2265-2272, Nov 2006.

- [20] W. Inman, K. Domansky, J. Serdy, B. Owens, D. Trumper, and L. G. Griffith, "Design, modeling and fabrication of a constant flow pneumatic micropump," *Journal of Micromechanics and Microengineering*, vol. 17, pp. 891-899, May 2007.
- [21] H. Y. Tseng, C. H. Wang, W. Y. Lin, and G. B. Lee, "Membrane-activated microfluidic rotary devices for pumping and mixing," *Biomedical Microdevices*, vol. 9, pp. 545-554, Aug 2007.
- [22] C. H. Wang and G. B. Lee, "Automatic bio-sampling chips integrated with micro-pumps and micro-valves for disease detection," *Biosensors & Bioelectronics*, vol. 21, pp. 419-425, Sep 15 2005.
- [23] C. H. Wang and G. B. Lee, "Pneumatically driven peristaltic micropumps utilizing serpentine-shape channels," *Journal of Micromechanics and Microengineering*, vol. 16, pp. 341-348, Feb 2006.
- [24] C. H. Weng, W. M. Yeh, K. C. Ho, and G. B. Lee, "A microfluidic system utilizing molecularly imprinted polymer films for amperometric detection of morphine," *Sensors and Actuators B-Chemical*, vol. 121, pp. 576-582, Feb 20 2007.
- [25] A. Sin, C. F. Reardon, and M. L. Shuler, "A self-priming microfluidic diaphragm pump capable of recirculation fabricated by combining soft lithography and traditional machining," *Biotechnology and Bioengineering*, vol. 85, pp. 359-363, Feb 5 2004.
- [26] J. Kim, J. Baek, K. Lee, Y. Park, K. Sun, T. Lee, and S. Lee, "Photopolymerized check valve and its integration into a pneumatic pumping system for biocompatible sample delivery," *Lab on a Chip*, vol. 6, pp. 1091-1094, 2006.
- [27] E. Stemme and G. Stemme, "A Valveless Diffuser/Nozzle-Based Fluid Pump," *Sensors and Actuators a-Physical*, vol. 39, pp. 159-167, Nov 1993.
- [28] N. B. Justis, D. Y. Zhang, and Y. H. Lo, "Integrated dynamic fluidic lens system for in vivo biological imaging," *Proceedings of the 26th Annual International Conference of the IEEE Engineering in Medicine and Biology Society, Vols 1-7*, vol. 26, pp. 1256-1259, 2004.
- [29] S. Kar, S. McWhorter, S. M. Ford, and S. A. Soper, "Piezoelectric mechanical pump with nanoliter per minute pulse-free flow delivery for pressure pumping in micro-channels," *Analyst*, vol. 123, pp. 1435-1441, Jul 1998.
- [30] J. H. Kim, C. J. Kang, and Y. S. Kim, "A disposable polydimethylsiloxane-based diffuser micropump actuated by piezoelectric-disc," *Microelectronic Engineering*, vol. 71, pp. 119-124, Feb 2004.
- [31] M. Khoo and C. Liu, "A novel micromachined magnetic membrane microfluid pump," *Proceedings of the 22nd Annual International Conference of the IEEE Engineering in Medicine and Biology Society, Vols 1-4*, vol. 22, pp. 2394-2397, 2000.
- [32] C. Yamahata, C. Lotto, E. Al-Assaf, and M. A. M. Gijs, "A PMMA valveless micropump using electromagnetic actuation," *Microfluidics and Nanofluidics*, vol. 1, pp. 197-207, Jul 2005.
- [33] J. H. Kim, K. H. Na, C. J. Kang, D. Jeon, and Y. S. Kim, "A disposable thermopneumatic-actuated microvalve stacked with PDMS layers and ITO-coated glass," *Microelectronic Engineering*, vol. 73-74, pp. 864-869, Jun 2004.
- [34] J. H. Kim, K. H. Na, C. J. Kang, and Y. S. Kim, "A disposable thermopneumatic-actuated micropump stacked with PDMS layers and ITO-coated glass," *Sensors and Actuators a-Physical*, vol. 120, pp. 365-369, May 17 2005.
- [35] J. C. Yoo, Y. J. Choi, C. J. Kang, and Y. S. Kim, "A novel polydimethylsiloxane microfluidic system including thermopneumatic-actuated micropump and Paraffin-actuated microvalve," *Sensors and Actuators a-Physical*, vol. 139, pp. 216-220, Sep 12 2007.
- [36] J. C. Yoo, M. C. Moon, Y. J. Choi, C. J. Kang, and Y. S. Kim, "A thermopneumatic-actuated polydimethylsiloxane microfluidic system," *2006 1st IEEE International Conference on Nano/Micro Engineered and Molecular Systems, Vols 1-3*, pp. 1379-1383, 2006.
- [37] P. H. King and J. A. Covington, "A Novel Monolithic Microactuator Fabricated by 3D Rapid Direct Manufacture," *Proceedings of the Eurosensors XXIII Conference, Lausanne*, pp. 1163-1166, 2009 2008.

# Chapter 9

---

## 9 Conclusions and Future Work

### 9.1 Conclusions

Stereolithography, and ALM systems in general, have developed in the last 20 years from academic curiosities into commercially successful technologies. Although their industrial use is relatively limited, due in part to their cost, it is a matter of time before they become commonplace in manufacturing roles, as they are capable of building complex monolithic structures that are simply not possible using traditional machining techniques. Resolution has increased to the point that nanostereolithography systems are now under development, with microstereolithography systems already being seen as an alternative in some applications to silicon micromachining techniques [1].

The purpose of this thesis was to examine the capabilities and applications of microstereolithography systems, with particular emphasis on microfluidic components and microneedles and a goal of moving towards an integrated microfluidic system incorporating both features. The EnvisionTEC Perfactory Mini Multi-Lens SLA system was found to be capable of the production of complex devices with micro-scale internal components, along with high-resolution surface features down to a few tens of microns in cross section.

### 9.2 Microneedles

The field of microneedles was reviewed, and a range of microneedle array designs were proposed for fabrication. This range was narrowed using FEA modelling, resulting in two geometries being selected for fabrication. The stepped cone and inverted trumpet designs were 300  $\mu\text{m}$  in diameter, 400  $\mu\text{m}$  tall with 90  $\mu\text{m}$  diameter tips. These designs were then fabricated, with the factory-default build parameters of the SLA system being found to exert too much stress

on the microneedle structures, damaging them reducing the layer peeling speed by 50% allowed the microneedle structures to resolve well and reliably.

Further FEA modelling was used to optimise the designs, revealing the balancing act between the requirement that the needle tip be small in order to pierce the skin, and that this size reduction also reduces the needle's mechanical strength under axial load. For example, a stepped cone geometry with a 15  $\mu\text{m}$  diameter tip was found during FEA modelling to fail structurally at a force of 0.21 N; doubling the diameter to 30  $\mu\text{m}$  increases the mechanical strength by a factor of 4. Mechanical testing was performed in parallel with FEA modelling to determine the failure force of  $9 \times 9$  arrays of the microneedle structures. The stepped cone geometries were slightly stronger than the inverted trumpet designs, failing at 0.269 and 0.243 N respectively. The simulations underestimated this force by around 20%. At the point of failure, it was calculated from the mechanical test results that the needle tips would have been exerting a pressure of around 30 to 32 MPa, some 10 times more than that required to pierce average human skin [2]. However, further work on the biocompatibility of the materials is needed before such structures could be used on patients.

### 9.3 Active Microfluidic Components

A large review of the field of micropumps and microvalves was carried out, with particular emphasis on the use of polymeric materials. This allowed suitable designs and working principles to be selected. The range of devices fabricated and tested can be seen summarised in *Table 9.1*. Two actuation techniques were tested – thermopneumatic and pneumatic. Both of these techniques simply use changes in air pressure to deform a thin polymeric membrane. The first device fabricated was a 3-membrane thermopneumatic micropump, assembled from 3 separate SLA-fabricated components. The device also required 3 PCB-mounted microhotplates. Although flow was achieved using this method, it was found that the device was unreliable, most probably due to the insulating properties of the polymeric SLA material. Although the thermopneumatic

chamber was able to heat up to perform the “down” membrane stroke, it was not able to cool down in a sufficiently quick time in order to produce a meaningful flow, and the membranes would eventually lock down if the actuation frequency was too high.

The focus of research was therefore shifted to pneumatic actuation, which avoids such problems. Although pneumatic actuation requires an external pressure source, meaning the devices themselves are less well integrated, it does allow the device to be more compact. Additionally, the use of such devices in medical or biological research applications may require the device to be disposable, and the lack of electronic components directly integrated into the system allows for easier disposal or incineration, with the control and pneumatic components kept separate for re-use.

Two main pump designs were considered: a pneumatic version of the 3-membrane thermopneumatic design; and devices with flow rectification provided by nozzle/diffuser elements. Initial results showed flow rates of up to 650  $\mu\text{L}/\text{min}$  with an actuation pressure of 1.0 PSIG (6.89 kPa), rising relatively linearly. However, this data was collected manually, and it was clear that a more automated approach was required.

An electronic test rig was developed, based on LabView controlling a NI-DAQ 6009 device. Central to the function of the system was a capacitive measurement arrangement, allowing precise measurement of the position of a fluidic front. Actuation pressure and temporal data was also collected. Micropump control was integrated into the test software, with an output voltage being used to control a voltage-to-frequency circuit, controlling a 3-way valve that cycled the micropump pneumatic supply from atmospheric to regulator pressure. For the 3-membrane design, this was replaced by directly controlling 3 3-way valves in a predetermined pattern.

Table 9.1—Summary of active microfluidic devices presented in this thesis. Dimensions are of device body, without pipe fittings.

Device	Dimensions (mm)	Actuation	Rectification	Max Flowrate ( $\mu\text{l/min}$ )	Max Back-pressure (Pa)	Description
Thermopneumatic	28 × 10 × 11	Thermopneumatic	Active membrane valves	-	-	Original design; thermal issues prevented reliable flow
Mk1	14 × 7 × 4	Pneumatic	Nozzle/Diffuser 10:1.5 mm	650	-	Initial pneumatic design
Mk5 (Coated)	13.63 × 7 × 3.28	Pneumatic	Nozzle/Diffuser 5:1.8°	770	215	Device fluidics coated with conformal coating
Mk5 (Uncoated)	13.63 × 7 × 3.28	Pneumatic	Nozzle/Diffuser 5:1.8°	950	250	As above, but using improved post-processing in place of coating
Mk5 6°	13.63 × 7 × 3.28	Pneumatic	Nozzle/Diffuser 5:1.6°	1000	360	As Mk5, with 6° divergent nozzle/diffuser; exhibited improved flowrate performance
Mk5 10°	13.63 × 7 × 3.28	Pneumatic	Nozzle/Diffuser 5:1.10°	900	375	As Mk5, with 10° divergent nozzle/diffuser; exhibited de-graded flowrate performance
Mk6	13.63 × 7 × 4.05	Pneumatic	Nozzle/Diffuser 5:1.8°	730	360	Dual-membrane “boxer” design; exhibited improved back-pressure performance
Mk7	17.57 × 12.50 × 3.03	Pneumatic	Nozzle/Diffuser 5:1.8°	-	-	Dual-membrane, parallel design; failed due to problems with priming
3-membrane	18 × 8.65 × 4.525	Pneumatic	Active membrane valves	230	4900	Self-priming; slow flow rates but much greater backpressures than nozzle/diffuser devices

Initial data was collected from this system using a “swept frequency” method, which automatically measured the flowrate across the frequency range for a given actuation pressure. It was later found however that the swept-frequency method lead to distortions of the device characteristics, and an overestimation of the flowrate. A manual, single-frequency method was therefore settled on, and the data produced using this method was deemed to be more reliable, as each reading was taken from the same starting positions, rather than the constantly changing baseline of the automatic readings.

A single-membrane monolithic nozzle/diffuser rectified device was fabricated, and was found to produce a maximum flowrate of 940  $\mu\text{l}/\text{min}$  with a backpressure of 260 Pa. It showed good flow rates over a range of frequencies, with a dead zone around 100 Hz. One problem found was an area of low flow rate at low frequencies and higher actuation pressures – it is assumed this is due to the membrane “bottoming out” when not given enough time to recover between cycles.

A dual-membrane “boxer” nozzle/diffuser pump was also produced. This design is bigger in volume, and cannot produce the flowrates of the single-membrane devices, reaching a maximum of around 730  $\mu\text{l}/\text{min}$ . However, the backpressure was higher at around 360 Pa, suggesting this design could be optimised further.

To try to optimise the nozzle/diffuser elements, a simple steady-state analysis was carried out. This suggested that both 6° and 10° divergence from the centreline would be more efficient than the original 8° device. In practice however, the 10° was found to have a lower maximum flowrate of around 900  $\mu\text{l}/\text{min}$ , although the 6° was more efficient at 1,000  $\mu\text{l}/\text{min}$ . This leaves the model as yet not validated, although further work could be carried out to ascertain if the 10° result was reliable.

The 3-membrane monolithic device was also designed for pneumatic actuation. Although in comparison it produced a much rougher and slower flow than the nozzle/diffuser devices, its



major strength was in its self-priming. The seal created by the active membrane valves allowed a backpressure of around 4.7 kPa to be obtained, although this dropped off quick as the pump cycle frequency and flowrate increased. Regardless, this device shows great potential for integration into more complex microfluidic systems.

To show this, a test device was produced incorporating a 3-membrane pump, a stretch of complex internal microfluidics and a microneedle array. Although the device was never tested, it does prove the ability of the SLA system to produce complex active microfluidic components. It is hoped that further research will develop this application further and into commercial production.

## 9.4 Future Work

The research in this thesis could be developed further in the following areas:

- More work could be carried out on the SLA-fabricated microneedles in order for this technique to become truly viable for the production of devices for use on patients. The main areas of advancement required are in the biocompatibility of the materials and the resolution of the SLA system. Mechanical testing with skin or a synthetic equivalent would also be useful. Similar structures fabricated on existing laser-based systems may allow a small enough internal lumen within hollow microneedle arrays to be resolved without destroying the needle structure or weakening it.
- Work could be carried out to optimise the nozzle/diffuser structures outlines in Chapter 8 to allow greater micropump efficiency. A starting point could be found in the computer models presented in this thesis, which are currently of a relatively basic level and need further work to improve their accuracy.
- An investigation could be carried out into the possibility of producing multi-component systems, rather than monolithic parts. Certain structures such as pre-stressed normally-closed passive valves, of either float or membrane-hole type (see Chapter 3) are not possible using monolithic SLA, as the touching components would be bonded to each

other rather than free moving. Research could centre on the shrinkage of components during post-curing, which can make it difficult to produce several components that fit together without leakage during use.

- Research could be carried out into the applications of the active microfluidic devices presented in Chapter 8, focusing on their use in SLA-fabricated complex and integrated microfluidic systems. In particular a hybrid device comprised of both multi-membrane (for self-priming) and nozzle/diffuser (for smooth flow) devices could be investigated.
- Work could be carried out using laser-based systems to ascertain their efficacy in the production of the membranes used in this thesis.
- More work should be carried out on the long-term biocompatibility of the acrylate resins used. Alternative photosensitive materials could be sought to overcome any problems that arise. Other material properties could be of interest for the future development of the devices and structures presented in this thesis. For example, stronger materials would be advantageous for fabricating microneedles. On the other hand, more flexible materials, possibly approaching the material properties of PDMS, would be very useful in the fabrication of the membranes used in the micropump devices.
- More research needs to be carried out to increase the fabrication yield of components with micro-scale structures. It is possible that work with laser-based systems, which inherently place less strain on microstructures during fabrication, could be favourable in this respect. Ultimately, dual-photon systems would theoretically reduce fabrication stresses further, although these techniques require more complex photosensitive materials.
- Research could be carried out into the prospects for SLA systems for mass-production of components. This could be based around lab-on-a-chip devices or some other component that is not easily produced using conventional machining techniques.

- More research needs to be carried out into the long-term performance of SLA materials in general, including exposure to environmental conditions. The focus on prototyping within the industry has lead to materials being developed with initial finish and aesthetics in mind, with long-term stability sometimes not given consideration. On the other hand, materials that break down in a controlled fashion could be useful in terms of biodegradability and for environmental concerns, or for the production of bio-scaffolds for use in tissue engineering.

## 9.5 References

- [1] J. W. Gardner, V. J. Varadan, and O. Awadelkarim, "Microsensors, MEMS and Smart Devices," *John Wiley & Sons Ltd, Chichester*, 2001.
- [2] P. Aggarwal and C. R. Johnson, "Geometrical effects in mechanical characterising of microneedle for biomeidcal applications," *Sensors and Actuators B-Chemical*, vol. 102, pp. 226-234, 2004.

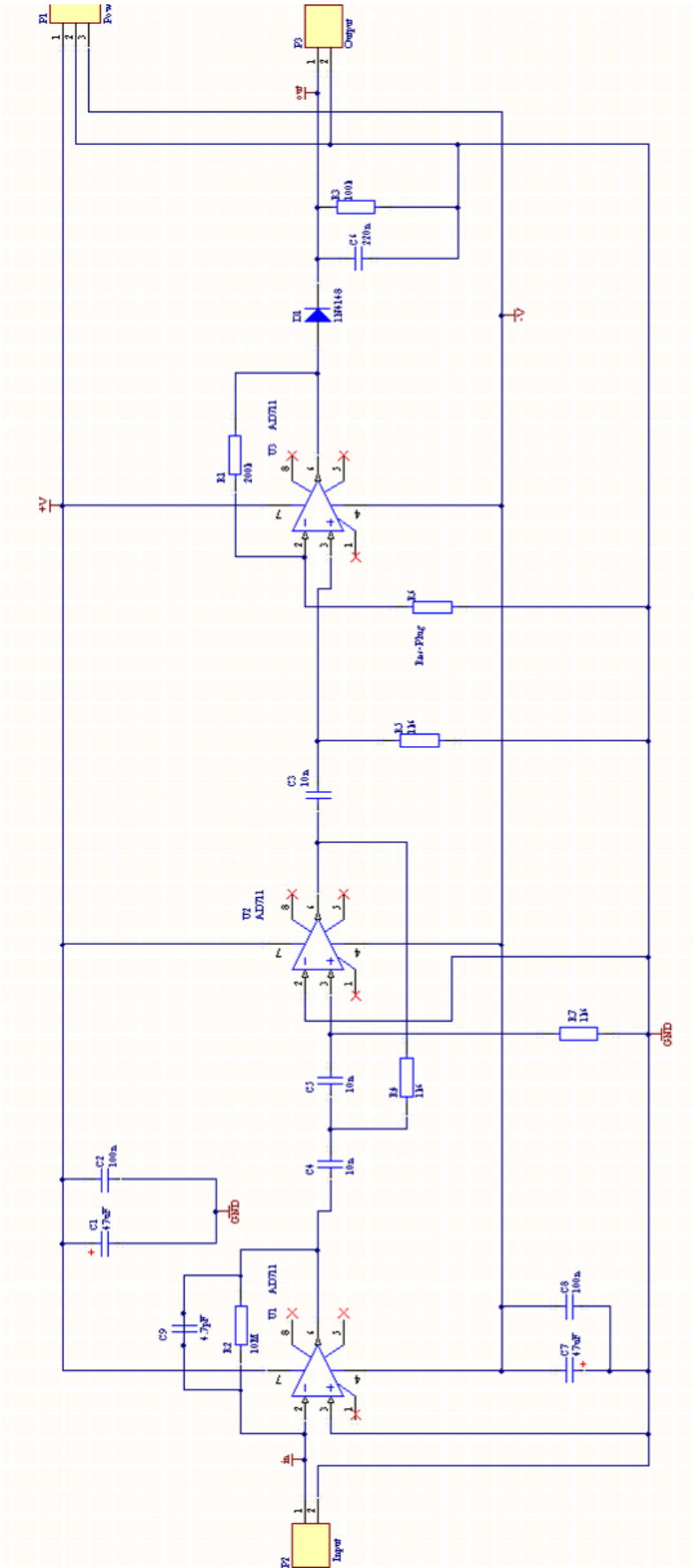
# Appendix A

---

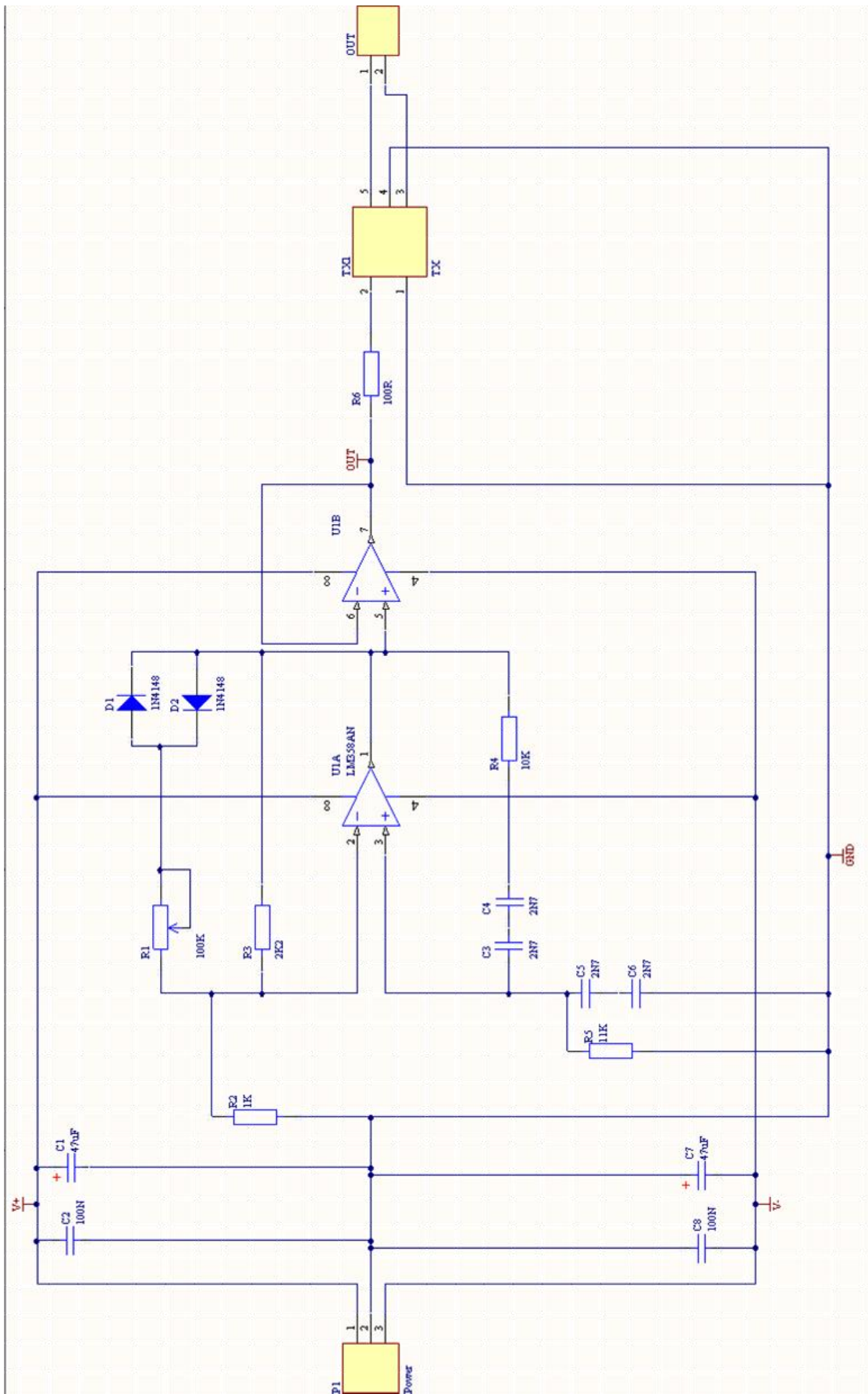
## **A     Circuit Diagrams**

On the following pages the circuit diagrams for the electronics used in the pump electronic test system are shown. The first is the oscillator circuit (A1) used to provide the signal to the capacitive sensors. The second (A2) is the filter used to process the return signal and output a voltage proportional to the difference in capacitance between the measurement capacitor and a reference device. The third (A3) is the voltage-to-frequency circuit used to control the nozzle/diffuser micropumps.

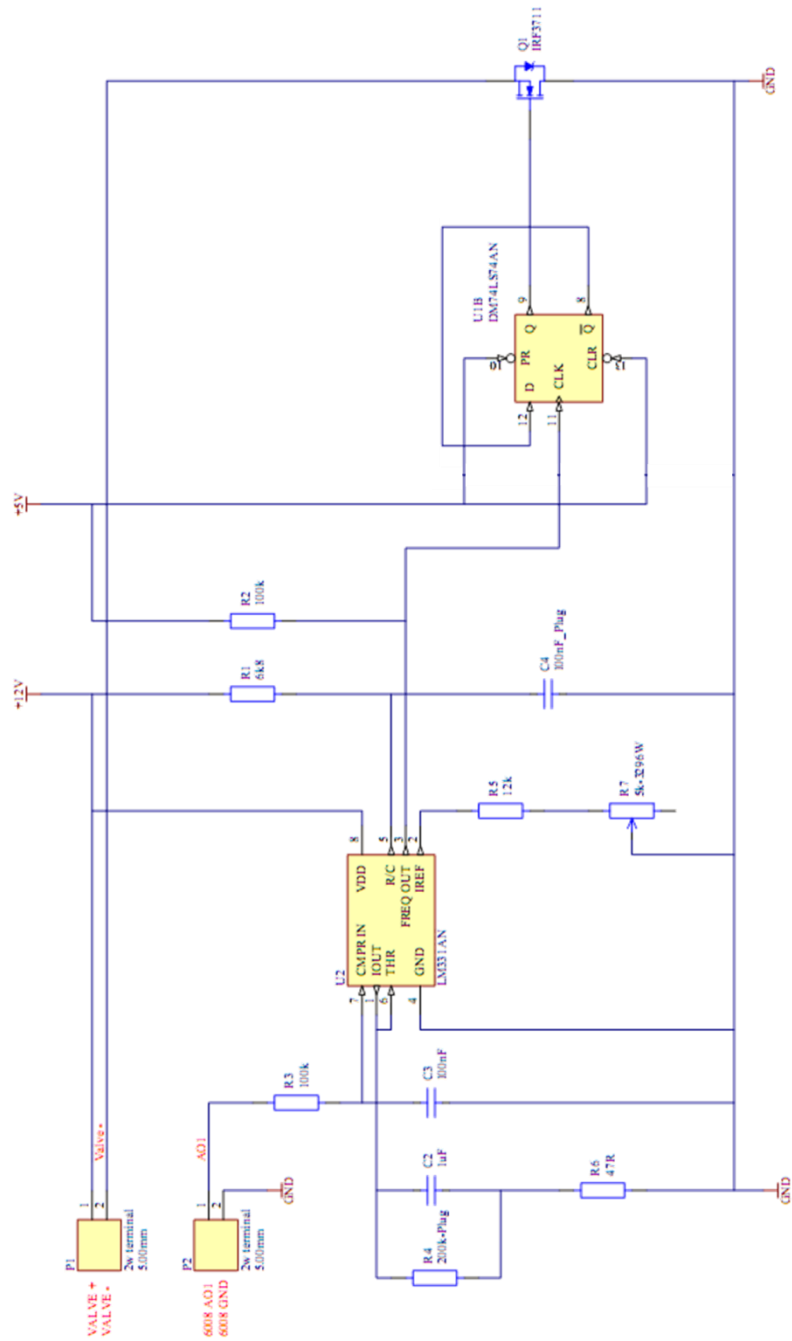
A.1 Capacitive Sensor - Oscillator Circuit



A.2 Capacitive Sensor - Filter Circuit



A.3 Micropump Control - Voltage-to-Frequency Convertor



# Appendix B

---

## B Error Analysis

For addition or subtraction of data values:

$$s_x = \sqrt{s_a^2 + s_b^2 + s_c^2 + \dots}$$

For multiplication or division of data values:

$$s_x = x \cdot \sqrt{\left(\frac{s_a}{a}\right)^2 + \left(\frac{s_b}{b}\right)^2 + \left(\frac{s_c}{c}\right)^2 + \dots}$$

Where:	$x$	=	result of calculation;
	$a \ b \ c$	=	numbers used in calculation;
	$s_x$	=	uncertainty in result;
	$s_a \ s_b \ s_c$	=	uncertainty in numbers used in calculation.